

UCLA

UCLA Electronic Theses and Dissertations

Title

Computational investigations of new bioorthogonal cycloadditions and organic semiconducting materials

Permalink

<https://escholarship.org/uc/item/4x2073x9>

Author

Lopez, Steven Alexander

Publication Date

2015

Peer reviewed|Thesis/dissertation

UNIVERSITY OF CALIFORNIA

Los Angeles

Computational investigations of new bioorthogonal cycloadditions and
organic semiconducting materials

A dissertation submitted in partial satisfaction of the requirements for the degree of Doctor of
Philosophy in Chemistry

by

Steven Alexander Lopez

2015

ABSTRACT OF THE DISSERTATION

Computational investigations of new bioorthogonal cycloadditions and organic semiconducting materials

by

Steven Alexander Lopez

Doctor of Philosophy in Chemistry

University of California, Los Angeles, 2015

Professor Kendall N. Houk

The first part of this thesis describes how quantum mechanical calculations using density functional theory (DFT) have been used to understand mechanisms, reactivities, and stereoselectivities of cycloadditions for applications in organic synthesis. Cycloadditions are among the most important tools to synthetic organic chemists, because complex natural products can be constructed efficiently and with high atom economy. These reactions have emerged as tools by which chemical biologists can label biomolecules (*i.e.* lipids, sugars, nucleic acids) with fluorophores rapidly and selectively. The second part of the thesis describes my contributions to morphology (molecular dynamics) and hole mobility simulations of organic semiconducting materials.

Chapter 1 describes the origin of the *exo*-stereoselectivities of a series of norbornenes towards phenyl azide. The *exo*-stereoselectivities arise from alkene pyramidalization, which causes the alkene to more closely resemble the *exo* transition state than the *endo* transition state. Chapter 2 builds upon the previous studies of predistorted alkenes to include *concave*-stereoselective cycloadditions to an oxabicyclo[3.3.0]octene in collaboration with Gais *et al.* The

alkene moiety of the oxabicyclo[3.3.0]octene is pre-distorted in the *convex* direction, resulting in a preference for concave addition. Calculations on a Pd-catalyzed (3+2) cycloaddition mechanism reveal that the rate- and stereodetermining step is the addition of the π -complex to the oxabicyclo[3.3.0]octene. Chapter 3 illustrates the concept of mutually orthogonal bioorthogonal reactions; the origin of this extraordinary selectivity is determined with DFT calculations. The azide–dibenzocyclooctyne and *trans*-cyclooctene–tetrazine cycloadditions are both inert to biological media and mutually orthogonal: *trans*-cyclooctene derivatives greatly prefer to react with tetrazines rather than azides, while dibenzocyclooctyne derivatives react with azides but not with tetrazines. Dibenzocyclooctyne chemoselectivity is controlled by distortion energy, and *trans*-cyclooctene chemoselectivity is controlled by interaction energy. Chapter 4 describes a mutually orthogonal bioorthogonal pair of isomeric 1,3-disubstituted and 3,3-disubstituted cyclopropenes that are chemoselective for reactions with tetrazines (Diels-Alder cycloaddition) and nitrile imines (1,3-dipolar cycloaddition), respectively. Prescher *et al.* discovered that 3,3-disubstituted cyclopropenes react exclusively with nitrile imines over tetrazines because of unfavorable steric clashes in the alkene-tetrazine transition state (distortion energy control), whereas 1,3-disubstituted cyclopropenes react exclusively with tetrazines because of more favorable orbital interactions in the transition state (interaction energy control). Chapter 5 describes calculations on enamine-azide cycloadditions. The reactions are concerted, and the high regioselectivities are controlled by interaction energy. Chapter 6 extends our understanding of enamine-azide cycloadditions for a wide scope of perfluoroarylazides (PFAAs) towards acetophenone- and phenylacetaldehyde-derived enamines in collaboration with Yan *et al.* Enamines undergo cycloadditions several orders of magnitude faster with perfluoroarylazides than with phenyl azide, because PFAAs have relatively low-lying LUMOs. The 1,3-dipolar

cycloadditions of norbornene and DIBAC also show increased reactivity towards PFAAs over phenyl azide, but are slower than enamine-azide cycloaddition. Chapter 7 is a theoretical study of 4π -electrocyclic ring-opening reactions of *N*-substituted-2-azetines, for a wide range of substituents from π acceptors (e.g., CHO, CN) to π donors (NMe₂, OMe). Reactivity is controlled by a reactant state effect; acceptor substituents delocalize the nitrogen lone pair and stabilize the reactant state of 2-azetines. Torquoselectivities are controlled by a favorable $n_N-\pi^*_{CC}$ orbital interaction upon inward rotation of the *N*-substituent. The torquoselectivities and reactivities of 4-fluoroalkyl-oxetenes are considered in Chapter 8 in collaboration with Mikami *et al.* The torquoselectivities are controlled by the interplay of closed-shell repulsions and a favorable through-space orbital interaction between the breaking σ_{CO} orbital and the σ^*_{CF} orbital of the fluoroalkyl substituent. The electronic character of the substituent of 4-substituted oxetenes controls oxetene electrocyclic ring opening rates.

The last two chapters of the thesis focus on studies of the factors that control the performance of extended π -conjugated materials in organic field-effect transistors (OFETs). Chapter 9 outlines how a multiscale method is used to extract hole mobilities for 2,5-bis(3-tetradecylthiophen-2-yl)thieno[3,2-b]-thiophene (BTTT) semiconducting materials. Briseño *et al.* report that BTTT monomers and dimers bearing alkyl side chains have hole mobilities of $\sim 10^{-3}$ cm²/Vs, while the unsubstituted BTTT monomer has undetectable hole mobilities. Molecular dynamics simulations suggest that alkyl side chains improve crystal packing because of inter alkyl chain dispersive interactions. Chapter 10 explores the photooxidation of rubrene to the corresponding *endo*-peroxide. DFT calculations of the cycloaddition and subsequent acid-catalyzed rearrangement mechanism are included.

The dissertation of Steven Alexander Lopez is approved.

Neil Kamal Garg

Jorge R. Barrio

Kendall N. Houk, Committee Chair

University of California, Los Angeles

2015

DEDICATION

To my wife, Ashley, and the people I talk to on Saturdays, you know who you are

TABLE OF CONTENTS

Abstract.....	iii
Committee page.....	vi
Dedication	vii
Acknowledgements.....	xiii
List of figures	xiv
List of tables.....	xvii
List of schemes.....	xviii
Biographical sketch.....	xxi

Chapter 1. Alkene distortion energies and torsional effects control reactivities and stereoselectivities of azide cycloadditions to norbornene and substituted norbornenes

1.1 Abstract.....	1
1.2 Introduction.....	1
1.3 Computational Details.....	2
1.4 Results and Discussion	
1.4.1 Pyramidalization of norbornenes.....	3
1.4.2 (3+2) Alkene-Azide transition structures.....	5
1.4.3 <i>Exo</i> -stereoselectivities of cycloadditions to norbornenes.....	7
1.4.4 Relationship between reactivity and pyramidalization.....	13
1.4.5 Relationship between reactivity and reaction energy.....	14
1.5 Conclusions.....	15
1.6 References.....	16

Chapter 2. How torsional effects cause attack at sterically crowded concave faces of bicyclic alkenes

2.1 Abstract.....	19
2.2 Introduction.....	19
2.3 Computational Details.....	23
2.4 Results and Discussion	
2.4.1 Conformational analysis of oxabicyclo[3.3.0]octenone.....	25
2.4.2 Origin of stereoselectivities of diazomethane-alkene cycloadditions.....	28
2.4.3 Mechanism of in methylenecyclopropane acetal cycloadditions.....	34
2.4.4 Origin of stereoselectivities in methylenecyclopropane acetal cycloadditions.....	37
2.4.5 Mechanism of Pd-catalyzed methylenecyclopropane cycloadditions.....	40
2.4.6 Origin of stereoselectivities of Pd-catalyzed (3+2) cycloadditions.....	43
2.5 Conclusions.....	44
2.6 References.....	45

Chapter 3. Control and design of mutually orthogonality in bioorthogonal cycloadditions

3.1 Abstract.....	49
3.2 Introduction.....	50
3.3 Computational Details.....	51
3.4 Results and Discussion	
3.4.1 Transition structures of mutually orthogonal bioorthogonal cycloadditions.....	54
3.4.2 Origins of mutual chemoselectivities: Distortion/interaction analysis.....	56
3.5 References.....	61

Chapter 4. Isomeric cyclopropenes exhibit unique bioorthogonal reactivities

4.1 Abstract.....	65
4.2 Introduction.....	65
4.3 Results and Discussion	
4.3.1 Origins of chemoselectivities.....	67
4.3.2 Reaction rates of isomeric cyclopropenes with tetrazines and nitrile imines.....	71
4.6 References.....	76
Chapter 5. Mechanisms and transition states of 1,3-dipolar cycloadditions of phenyl azide with enamines: A computational analysis	
5.1 Abstract.....	78
5.2 Introduction.....	78
5.3 Computational Details.....	80
5.4 Results and Discussion	
5.4.1 Mechanisms of azide-cycloadditions to piperidine enamines.....	81
5.4.2 Transition structures of azide-enamine cycloadditions.....	83
5.4.3 Activation free energy methods benchmarking.....	86
5.4.4 Origin of regioselectivities.....	91
5.4.5 Extent of charge separation in transition enamine-azide transition structures.....	92
5.5 Conclusions.....	94
5.6 References.....	95

Chapter 6. 1,3-Dipolar cycloaddition reactivities of perfluorinated aryl azides with enamines and strained dipolarophiles

6.1 Abstract.....	97
6.2 Introduction.....	98
6.3 Computational Details.....	99
6.4 Results and Discussion	
6.4.1 Acetophenone-derived enamine cycloadditions with aryl azides.....	100
6.4.2 Phenylacetaldehyde-derived enamine cycloadditions with aryl azides.....	101
6.4.3 Origin of rate enhancement for perfluoroaryl azide-enamine cycloadditions.....	108
6.4.4 1,3-dipolar cycloadditions of norbornene and perfluoroaryl azides.....	109
6.4.5 DIBAC-perfluoroaryl azide cycloadditions.....	112
6.5 Conclusions.....	117
6.6 Experimental Methods.....	118
6.7 References.....	121

Chapter 7. Substituent effects on rates and torquoselectivities of electrocyclic ring openings of *N*-substituted-2-azetines

7.1 Abstract.....	125
7.2 Introduction.....	125
7.3 Computational Details.....	128
7.4 Results and Discussion	
7.4.1 2-azetine ground state optimized geometries.....	129
7.4.2 Origin of reactivities.....	135
7.4.3 Origin of torquoselectivities.....	138
7.5 Conclusions.....	143
7.6 References.....	144

Chapter 8. Mono-, di-, and trifluoroalkyl substituent effects on the torquoselectivities of cyclobutene and oxetene electrocyclic ring openings	
8.1 Abstract.....	147
8.2 Introduction.....	148
8.3 Computational Details.....	151
8.4 Results and Discussion	
8.4.1 Ring opening transition structures of model cyclobutenes and oxetenes.....	151
8.4.2 Ring opening transition structures of 2-phenyl oxetenes.....	153
8.4.3 Ring opening transition structures of 4,4-disubstituted 2-phenyl oxetenes.....	156
8.5 Conclusions.....	157
8.6 References.....	158
Chapter 9. How alkyl sidechains on BTTT materials control OFET hole mobilities	
9.1 Abstract.....	164
9.2 Introduction.....	165
9.3 Results and Discussion	
9.3.1 UV-Vis spectra of 1-H , 1-C₆ , 2-H , 2-C₆	169
9.3.2 Crystal structure packing of 1-H , 1-C₆ , 2-C₆	171
9.3.3 Origins of <i>Anti-Anti</i> conformation of 1-H	174
9.3.4 Origins of <i>Syn-Syn</i> conformation of 1-C₆	172
9.3.5 Computed torsional potential of 1-H and 1-Me	175
9.3.6 Origin of device performance disparity between 1-H and 1-C₆	185
9.4 Conclusions.....	190
9.5 References.....	191

ACKNOWLEDGEMENTS

I would like to thank Professor Houk for his commitment and support during my PhD and the ADSE enterprise. I will always remember his kind words and our research discussions during our individual meetings; he is a role model as a scientist and as a mentor. Through Professor Houk, I have interacted closely with other scientists that have unofficially served as mentors during my time at UCLA. Professor Alejandro Briseño has been an incredible scientific collaborator and friend. Professor Martin Breugst is an amazing chemist and went above and beyond to shape my development during graduate school. Dr. Ilhan Yavuz is an absolutely brilliant physicist; he has been the backbone of the Houk organic photovoltaics subgroup.

I must also thank my first research mentor Dr. Jim Canary at New York University for believing in me as a young chemist and recommending me to begin my graduate career at UCLA. I acknowledge the hard work of our collaborators, Professors Mingdi Yan and Olof Ramström, Professor Koichi Mikami, Professor Jennifer Prescher, Professor Morton Munk, Professor Hans-Joachim Gais, and Professor Alejandro Briseño. It has been a pleasure to work with them and the student co-authors. I wish them and their groups the best success in the future.

My friends are the best, in particular, Dr. Christian Gonzalez, Dr. Christina Rotsides, Dr. Crystal Valdez, and Dr. Ashay Patel.

LIST OF FIGURES

Figure 1.1. Series of norbornenes studied.....	2
Figure 1.2. Optimized minima of 3–6 with θ_{dih}	4
Figure 1.3. Optimized transition structures of the 1,3-dipolar cycloaddition of phenyl azide to alkenes 1–7	5
Figure 1.4. Newman projections for the cycloadditions of phenyl azide to the <i>exo</i> 3x-TS (top row) and 3n-TS <i>endo</i> faces of norbornene.	7
Figure 1.5. Plot of activation energies and distortion energies of the reactions of phenyl azide and dipolarophiles 1–7	11
Figure 1.6. Plot of activation enthalpy (kcal mol ⁻¹) vs. θ_{dih} (°).....	13
Figure 1.7. Plot of activation enthalpies and reaction enthalpies of the reactions of phenyl azide and dipolarophiles 1–7	14
Figure 2.1. Pentalenolactone and pentalenolactone F.....	20
Figure 2.2. 3,4-Fused cyclopentenes studied by Danishefsky and Overman.....	22
Figure 2.3. The structures of 1 and 1-down with Newman projections.....	25
Figure 2.4. The optimized transition structures for concave and convex attack of CH ₂ N ₂ on 1	26
Figure 2.5. Newman projections looking down the alkene-allylic C-C bonds of TS1-conc and TS1-conv	28
Figure 2.6. Overlaid geometries of reactants 1 and 1a	29
Figure 2.7. Transition structures for the 1,3-dipolar cycloaddition of CH ₂ N ₂ and 1a	30
Figure 2.8. Overlay of 1b and 1c with an overlay of 1 and 1c	31
Figure 2.9. 1,3-Dipolar cycloaddition transition structures for the reactions of diazomethane with 1b and 1c	32
Figure 2.10. Computed free energy profile for the stepwise pathway of concave and convex additions to 1	35
Figure 2.11. The geometries of methylenecyclopropane acetal 3 , ring opening transition state [TS(3→4)], and reactive intermediate 4	36
Figure 2.12. Stepwise transition structures for the addition of 4 and 1 and corresponding zwitterionic intermediates.	37
Figure 2.13. Newman projections of TS(1→5-conc) and TS(1→5conv)	38
Figure 2.14. Free energy profile for the mechanism for the Pd-catalyzed (3+2) cycloaddition of 1 with 2 and Pd(PMe ₃) ₂	41
Figure 2.15. Computed geometries for the oxidative and nucleophilic addition steps.....	42
Figure 2.16. Newman projections of TS(7+1)-conc and TS(7+1)conv	43
Figure 3.1. Transition structures of MeN ₃ -cycloadditions.....	54
Figure 3.2. FMO diagram for the cycloadditions of <i>trans</i> -cyclooctene with methyl azide and dimethyltetrazine.	57
Figure 3.3. Space-filling models of dibenzocyclooctyne, methyl azide, dimethyltetrazine, and transition states TS5 and TS6	58

Figure 4.1. 1,3-Disubstituted cyclopropenes (top) react with tetrazines via IED-DA reactions. 3,3-Disubstituted scaffolds (bottom) react with 1,3-dipoles to afford covalent adducts.	67
Figure 4.2. Transition structures of diphenyl-substituted nitrile imine (NI) and tetrazine (Tz) to 1,3- and 3,3-dimethylcyclopropene.....	69
Figure 4.3. Cycloaddition kinetics of tetrazine and nitrile imine cycloadditions to isomeric cyclopropenes.....	71
Figure 4.4. Gel analysis of all cycloadditions and control cycloadditions.....	74
Figure 5.1. Regioselective enamine cycloadditions observed by Munk <i>et al.</i>	80
Figure 5.2. Concerted mechanism of cycloadditions of PhN ₃ to enamines 1a–c and stepwise pathway for formation of 3a–c	81
Figure 5.3. Concerted mechanism of cycloadditions of PhN ₃ to enamines 2 and stepwise pathway for formation of 5	82
Figure 5.4. Three possible transition structures for the reactions of 1a–c and 2 with Ph.....	83
Figure 5.5. Optimized structures of zwitterionic 7a and 8	83
Figure 5.6. Potential energy diagram for the cycloadditions of 1a and 2 with PhN ₃	85
Figure 5.7. Dihedral angle scan of the ring closing from 7 and 8	86
Figure 5.8. Comparison of computed activation free energies those determined experimentally.....	88
Figure 5.9. Frontier molecular orbitals and their energies of 1a , 2 , and PhN ₃	91
Figure 5.10. Transition structures of 1b and 1c with PhN ₃	93
Figure 6.1. Amidines isolated experimentally.....	102
Figure 6.2. The concerted transition structures for the (3+2) cycloaddition of PFAAs and PhN ₃ to 5	106
Figure 6.3. Graph of activation, distortion, and interaction energies for TS-a5 , TS-b5 , and TS-g5	108
Figure 6.4. Computed LUMOs of azides a , b , g and the HOMO of enamine 5	108
Figure 6.5. The transition structures for the (3+2) cycloadditions of a , b , and g to norbornene.....	111
Figure 6.6. Graph of activation, distortion, and interaction energies for TS-a9 , TS-b9 , TS-g9	111
Figure 6.7. The lowest energy conformer of dibenzocyclooctyne deriv/ative.....	115
Figure 6.8. The <i>syn</i> and <i>anti</i> transition structures for the cycloadditions of PhN ₃ to the dibenzocyclooctyne derivative.....	116
Figure 6.9. Graph of activation, distortion, and interaction energies for TS-a11 , TS-b11 , and TS-g11	117
Figure 7.1. The optimized geometries of <i>N</i> -substituted-2-azetines.....	129
Figure 7.2. Electrocyclic conrotatory ring opening lone-pair-in, substituent-out transition structures.....	131
Figure 7.3. Electrocyclic conrotatory ring opening lone-pair-out, substituent-in transition structures.....	133
Figure 7.4. 2-azetine “out” and “in” transition structures are overlaid with cyclobutene “out” and “in” transition structures.....	134

Figure 7.5. Plot of $\Delta G_{\text{out}}^{\ddagger}$ and $\Delta G_{\text{in}}^{\ddagger}$ vs. σ_{R}^0 for 2-azetines.	136
Figure 7.6. Computed $\Delta G_{\text{out}}^{\ddagger}$ and $\Delta G_{\text{in}}^{\ddagger}$ vs. σ_{R}^0 for 3-substituted cyclobutenes.....	138
Figure 7.7. Activation barrier difference plotted against Taft σ_{R}^0 values for the electrocyclic ring opening of 3-substituted cyclobutenes and <i>N</i> -substituted-2-azetines.....	139
Figure 7.8. Computed activation free energies vs. reaction free energies for the ring opening of 2-azetines.....	141
Figure 8.1. Transition structures of model cyclobutenes and oxetenes.....	152
Figure 8.2. Transition structures for electrocyclic ring openings of selected mono-substituted cyclobutenes and oxetenes.....	155
Figure 8.3. Transition structures for the electrocyclic ring opening reactions of selected disubstituted oxetenes.	159
Figure 9.1. Normalized UV-Vis spectra of BTTT derivatives in chloroform.....	169
Figure 9.2. Crystal packing of 1-H	171
Figure 9.3. Crystal packing of 1-C₆	172
Figure 9.4. Gas phase DFT-optimized structure of 1-H compared to experimental solid-state structure.....	174
Figure 9.5. Three possible gas phase DFT-optimized structure of 1-H	175
Figure 9.6. Crystal structure of 1-C₆	176
Figure 9.7. The optimized gas phase conformers of 1-Et	178
Figure 9.8. Torsional potentials along the SCCS torsion for 1-H and 1-Me	181
Figure 9.9. GIXD images and corresponding packing cartoons of oligothiophenes on Si substrates by spin-casting from chloroform solution: 1-H , 1-C₆ , and 2-C₆	182
Figure 9.10. The transfer/square root of current characteristics of 1-C₆ , and 2-C₆ ; output characteristics of 1-C₆ , and 2-C₆ BG-BC thin film transistors.....	184
Figure 9.11. Crystal structures of 1-H , 1-C₆ , and 2-C₆ with principal electron transport direction indicated in red.....	186
Figure 9.12. Snapshot crystal configurations before and after simulating thermal disorder for 1-H , 1-C₆ , 2-C₆	187
Figure 9.13. Plot of site energies for 1-H , 1-C₆ , 2-C₆	188

LIST OF TABLES

Table 1.1. $\Delta G_{\text{expt}}^{\ddagger}$, values derived from experimental rate constants for the reactions of phenyl azide with dipolarophiles 2 , 3 , and 7 as calculated by M06-2X/6-311G(d,p), and [SCS-MP2/6-311G(d,p)//M06-2X/6-311G(d,p)].	9
Table 1.2. M06-2X/6-311G(d,p) activation free energies and enthalpies of activation, electronic energies of activation, distortion energies, and interaction energies for the reactions of phenyl azide and dipolarophiles 1–7 .	10
Table 3.1. M06-2X/6-311+G(d,p) Computed activation free energies in the gas phase and in water (G_{gas} and G_{water} , in kcal mol ⁻¹), Relative rate constants (k_{rel} , based on G_{water} at 298 K), and activation, distortion, and interaction energies (E_{act} , E_{dist} , and E_{int} , in kcal mol ⁻¹)	55
Table 4.1. Second-order rate constants for the cyclopropene-tetrazine ligation (15% DMSO/PBS).	72
Table 5.1. Rate constants reported by Munk <i>et al.</i> and the derived $\Delta G_{\text{expt}}^{\ddagger}$ values with reported errors. ΔG^{\ddagger} computed using M06-2X/6-311+G(d,p), B97D/6-311+G(d,p), and SCS-MP2/6-311+G(d,p)//M06-2X/6-311G+(d,p) IEF-PCM: CHCl ₃ .	86
Table 5.2. M06-2X/6-311G+(d,p) IEF-PCM:CHCl ₃ . Electronic activation (ΔE^{\ddagger}) energies, distortion energies ($\Delta E_{\text{d}}^{\ddagger}$) interaction energies ($\Delta E_{\text{i}}^{\ddagger}$) for the reactions of phenyl azide and enamines 1a and 2 .	89
Table 5.3. ΔG^{\ddagger} and for the three possible transition structures and the charge separation (NBO) in the transition structures.	92
Table 5.4. ΔE^{\ddagger} , $\Delta E_{\text{d}}^{\ddagger}$, $\Delta E_{\text{i}}^{\ddagger}$, and ΔG^{\ddagger} for the morpholine and pyrrolidine enamine cycloaddition reactions with phenyl azide.	94
Table 6.1. Rate constants (k_{c}) for the (3+2) cycloadditions of (a–d , g , and h) to 1 .	101
Table 6.2. Rate constants (k_{c}) for the (3+2) cycloadditions of azides (a–h) and phenylacetaldehyde piperidine enamine 5 .	104
Table 6.3. Rate constants of the cycloadditions of a and b with 5–8 .	105
Table 6.4. Azide-norbornene (3+2) cycloaddition rate constants and corresponding activation free energies.	110
Table 6.5. Azide-DIBAC (10) cycloaddition rate constants ^a and corresponding activation free energies.	114
Table 6.6. The activation free energies for the cycloadditions involving a , b , and g to 11 .	115
Table 7.1. Activation free energies for both diastereomeric transition structures of the electrocyclic ring opening reactions of azetines.	135
Table 7.2. The reaction energies for 2-azetines ring opening reactions.	140
Table 9.1. Optical properties, electrochemical data, and DFT calculated energies.	171
Table 9.2. The computed free energies for the three conformers of 1-H , 1-Me , and 1-Et .	179
Table 9.3. The two SCCS dihedral angles (ϕ_1 and ϕ_2) of the three computed conformers of 1-H , 1-Me , and 1-Et .	180
Table 9.4. Experimental computed hole mobilities reorganization energy and electronic coupling of 1-H , 1-C₆ , and 2-C₆ .	189

LIST OF SCHEMES

Scheme 2.1. Experimental conditions and product ratios for the (3+2) cycloadditions with diazomethane, methylenecyclopropane 2 , silylmethylallyl acetate, and methylenecyclopropane acetal 3	21
Scheme 2.2. Theoretical reaction of 1a with CH ₂ N ₂	29
Scheme 2.3. The product ratios found for the reactions of 1b and 1c with CH ₂ N ₂	31
Scheme 2.4. a) Disrotatory electrocyclic ring opening reaction. b) Stepwise pathway involving zwitterionic intermediate 5	34
Scheme 2.5. Computed mechanism of Pd-catalyzed (3+2) cycloaddition.....	40
Scheme 3.1. Azide-cyclooctyne (3+2) cycloaddition and <i>trans</i> -cyclooctene-tetrazine (4+2) cycloaddition reactions.....	51
Scheme 3.2. Selectivity of bioorthogonal cycloadditions	52
Scheme 3.3. Prediction of mutual orthogonality of two new bioorthogonal reagents in azide and tetrazine cycloadditions.....	59
Scheme 4.1. Synthesis of disubstituted cyclopropenes.	70
Scheme 4.2. Disubstituted cyclopropenes undergo 1,3-dipolar cycloadditions with nitrile imines to generate stable cycloadducts.	73
Scheme 5.1. Scope of enamine dipolarophiles (1a–c) and 2 studied by Munk work.....	79
Scheme 6.1. Scope of azides and dipolarophiles for the (3+2) cycloadditions with enamines...99	99
Scheme 6.2. Cycloadditions of PFAAs and acetophenone enamines.	100
Scheme 6.3. Reaction of PFAAs (a–f) and phenylacetaldehyde enamines (5–8) result in triazolines [(a–c)-(1–4)] that lose N ₂ to form amidines.....	102
Scheme 6.4. (3+2) cycloadditions of PhN ₃ and BnN ₃ to norbornene.....	109
Scheme 6.5. Some cyclooctynes DIBO, DIBAC, DIFO, and DIBO known to participate in bioorthogonal reactions.	112
Scheme 6.6. The regioisomeric products resulting from the reaction of 10 with PFAAs or PhN ₃	113
Scheme 7.1. Inward rotation of the lone pair (n) on nitrogen. Outward rotation of the lone pair on nitrogen.....	127
Scheme 7.2. Natural products synthesized using 1-azadienes in inverse electron-demand Diels-Alder reactions.	128
Scheme 8.1. 4π-Electrocyclic ring opening of carbocyclic and heterocyclic four membered rings.....	149
Scheme 8.2. Orbital interactions upon inward rotation of the fluoroalkyl substituent.....	150
Scheme 8.3. Synthesis of oxetenes via a [2+2] cycloaddition and subsequent ring opening reaction.....	150
Scheme 8.4. Mono- and di-substituted cyclobutene and oxetene derivatives.....	151
Scheme 9.1. Synthetic route for dimer synthesis of 2-C₆ , 1-H , and 2-H	167

Scheme 9.2. 1-R monomers (R=H, Me, Et) in three possible planar conformations.....174

References and Notes

1. Eyring, H. *J. Chem. Phys.* **1935**, *3*, 107–115.
2. Evans, M. G.; Polanyi, M. *Trans. Faraday Soc.* **1935**, *31*, 875–894.
3. Marcus, R. A.; Sutin, N. *Biochem. Biophys. Acta* **1985**, *811*, 265–322.
4. Taft, R. W.; Lewis, I. C. *J. Am. Chem. Soc.* **1958**, *80*, 2436.

VITA

Educational History

- June 2015 University of California, Los Angeles
Department of Chemistry & Biochemistry
Doctoral Candidate
- June 2013 University of California, Los Angeles
Department of Chemistry & Biochemistry
M.S. in Chemistry
- May 2010 New York University, New York
College of Arts and Sciences
Bachelor of Science, Chemistry, Minor in Mathematics

Honors and Awards

- 2006 American Chemical Society (ACS) Scholar
- 2008 College of Arts and Science Research Scholar, 2008 – 2009
- 2010 Isidore Rubin Award for Organic Chemistry Research
- 2010 NYSAS Undergraduate Student Research Award
- 2014 UCLA Diversity, Inclusion, and Equity Award
- 2015 Bouchet Graduate Honor Society Scholar

Grants Awarded

- 2006 American Chemical Society Scholar
- 2010 New York University Undergraduate Research Grant, June 2010
- 2011 Gordon Research Conference Diversity Travel Grant, July 2011
- 2012 UCLA Chemistry Department Travel Grant for ACS National Meeting: San Diego, March
2012
- 2012 ACS Division of Organic Chemistry Travel Grant, June 2012
- 2012 Gordon Research Conference Diversity Travel Grant, July 2012
- 2012 FASEB-MARC Travel Award, SACNAS National Conference, October 2012
- 2014 UCLA Chemistry Department Travel Grant for ACS National Meeting: Dallas, TX March
2014
- 2014 Center for Selective C-H Functionalization Outreach Grant (\$9000)
- 2014 AGEP Professional Development Award

Research Experience

- 2008-2010 *Research Intern for Prof. James Canary, New York University, Department of Chemistry*
New York University, New York, May 2008-May 2010
Developed methionine-based chiroptical sensors for the detection of toxic metals such as mercury.
- 2010-present *Graduate Student with Prof. Kendall N. Houk, Winstein Chair in Organic Chemistry*
University of California, Los Angeles, CA July 2010-Present
Used quantum mechanical (DFT) calculations to study the mechanisms, reactivities, and stereoselectivities of pericyclic reactions. These studies have immediate applications in chemical biology and organic synthesis. Molecular dynamics (MD) simulations using the AMBER program were utilized to simulate disordered thin-film mobilities. Kinetic Monte Carlo simulations using the VOTCA program were used to rationalize and predict the charge-carrier dynamics of promising materials used in organic electronic devices.

Teaching and Mentoring

- Tutor, NYU Metro Education Center, Bronx, NY, May 2007- May 2009*
Tutored economically disadvantaged high school students to pass NY State Regents exams in Mathematics and Science.
- Chemistry and Math Instructor, Upward Bound, New York, NY, May 2007 - July 2010*
Constructed a science curriculum, as well as taught an annual class, for economically disadvantaged high school students who were required to retake courses to graduate high school.
- Teaching Fellow, University of California, Los Angeles, Los Angeles, CA September 2010-Present*
Served as a teaching assistant for a graduate-level Physical Organic Chemistry (course 243A) during Winter 2015. Instructed a group of twenty students. Taught a weekly discussion section, was responsible for midterm and final exams.
- Instructed two quarters of Organic Chemistry lecture (course 30C), which consisted of three groups of twenty students per quarter. Two office hours per week, graded midterm and final exams. Incorporated problem-based learning to teach a variety of organic chemistry topics.
- Served as a teaching assistant for Organic Chemistry lab (course 30BL) for four quarters. Instructed two groups of twenty students per quarter. Held two office hours per week, wrote and graded weekly quizzes and lab reports.
- Instructor, Center for Excellence in Engineering, University of California, Los Angeles, Los Angeles, CA September 2012 – September 2013*
Taught a general chemistry course (CHEM 20A) during the summers of 2012 and 2013. My responsibilities included preparing lectures for thirty students for five hours weekly for three weeks. I wrote and graded a midterm and final exam.

Leadership and Community Service

President, Organization for Cultural Diversity in Chemistry (OCDC), Los Angeles, CA January 2011 – January 2014

Primary responsibilities include organizing a lecture series sponsored by Procter & Gamble and presiding over monthly meetings. Established monthly lunch seminars at UCLA consisting of members presenting their research and personal history. Spearheaded an outreach program for community college students to increase awareness of research careers in the physical sciences, while highlighting the importance of diversity. Raised approximately \$20,000 in additional funding for the organization and established collaborations with inter-campus organizations such as the Center for Community College Partnerships (CCCP), the Undergraduate Research Center (URC), Graduate Division, and the Society for the Advancement of Native Americans and Chicanos in Science (SACNAS).

President and co-founder, Alliance for Diversity in Science and Engineering (ADSE), United States May 2014-present

Current responsibilities include overseeing new chapters, writing proposals for NCDS funding, and organizing diversity symposia at American Chemical Society (ACS) national meetings. Hosted a symposium entitled, “*Diversity in Chemistry: Uniting Our Differences For A Common Scientific Future*” featuring chemists from the University of California system attended during the SACNAS (Society for the Advancement of Native American and Chicanos in Science) conference with funds from the NSF Center for C–H Functionalization (CCHF).

Associate, Committee for Minority Affairs, American Chemical Society, United States January 2015–present

Active elected associate of CMA and member of the communications subcommittee. Within the subcommittee, I contribute to *ChemDiversity*, a blog describing the many successful implementations of programs to increase diversity in chemistry. Organized a CMA-sponsored symposium at the 249th national American Chemical Society meeting in Denver, CO. The symposium will showcase academic and industrial chemists that have profoundly increased the diversity and inclusivity of chemistry.

Can read and write in Spanish and Italian

Publications

1. “Multi-mode Selective Detection of Mercury by Chiroptical Fluorescent Sensors Based on Methionine/Cysteine” Carney, P.; **Lopez, S. A.**; Mickley, A.; Grinberg, K.; Zhang, W.; Dai, Z.; *Chirality* **2011**, *23*, 916–920.
2. “Origins of Bioorthogonal and Orthogonal Cycloadditions: Distortion, LUMO Energies, and Steric Effects” Liang, Y; Mackey, J.; **Lopez, S. A.**; Liu, F.; Houk, K. N. *J. Am. Chem. Soc.* **2012**, *134*, 17904–17907.
3. “Alkene Distortion Energies and Torsional Effects Control Reactivities and Stereoselectivities of Azide Cycloadditions to Norbornenes” **Lopez, S. A.**; Houk, K. N. *J. Org. Chem.* **2013**, *78*, 1778–1783.
4. “Mechanisms and Transition States of 1,3-Dipolar Cycloadditions of Phenyl Azide with Enamines: A Computational Analysis” **Lopez, S. A.**; Munk, M. E.; Houk, K. N. *J. Org. Chem.* **2013**, *78*, 1576–1582.
5. “Isomeric Cyclopropenes Exhibit Unique Bioorthogonal Reactivities” Kamber, D. N.; Nazarova, L. A.; Liang, Y.; **Lopez, S. A.**; Patterson, D. M.; Shih, H-W.; Houk, K. N.; Prescher, J. A. *J. Am. Chem. Soc.* **2013**, *135*, 13680–13683.

6. “Substituent Effects on Rates and Torquoselectivities of Electrocyclic Ring Openings of *N*-substituted-2-Azetines” **Lopez, S. A.**; Houk, K. N. *J. Org. Chem.* **2014**, *79*, 6189–6195.
7. “How torsional effects cause attack at sterically crowded concave faces of bicyclic alkenes” **Lopez, S. A.**; Pourati, M.; Gais, H.-J.; Houk, K. N. *J. Org. Chem.* **2014**, *79*, 8304–8312.
8. “1,3-Dipolar Cycloaddition Reactivities of Perfluorinated Aryl Azides with Enamines and Strained Dipolarophiles” Xie, S.*; **Lopez, S. A.***; Ramström, O.; Yan, M. *J. Am. Chem. Soc.* **2014**, *137*, 8, 2958–2966. (*First authorship shared)

Presentations

1. **Lopez, S. A.**; Dai, Z.; Canary, J. “Design and Development of a Methionine-Based Mercury Sensor” *Inquiry*, New York University publication about the URC
2. **Lopez, S. A.**; Houk, K. N. “Role of Distortion Energies on 1,3-Dipolar Cycloadditions of Strained Alkenes” Poster presentation at the Gordon Research Conference: Physical Organic Chemistry, Holderness, NH July 2011.
3. “Role of Distortion Energy on 1,3-dipolar cycloadditions to strained alkenes” **Lopez, S. A.**; Houk, K. N. *Abstracts of Papers*, 243rd ACS National Meeting & Exposition, San Diego, CA.
4. **Lopez, S. A.**; Houk, K. N. “Pyramidalization and Distortion Energies Control Rates of 1,3-Dipolar Cycloadditions with Phenyl Azide” Poster presentation at Gordon Research Conference: Computational Chemistry, Mt. Snow, VT, July 2012.
5. “Origins of Selectivity of Bioorthogonal Cycloadditions: The Role of Distortion, LUMO energies, and Steric Effects” Oral Presentation, **Lopez, S. A.**; Houk, K. N. SACNAS National Conference, Seattle, WA, October 2012.
6. “Torquoselectivities of Electrocyclic Ring opening Reactions of 2-azetines” Oral presentation, **Lopez, S. A.**; Houk, K. N. *Abstracts of Papers*, 247th ACS National Meeting & Exposition, Dallas, TX, March 2014.
7. “1,3-Dipolar Cycloadditions of Perfluorophenyl azides to Enamines and the Decomposition of Triazolines: A Computational Study” (invited oral presentation), **Lopez, S. A.**; Xie, S.; Ramström, O.; Yan, M.; Houk, K. N. Reaction Mechanism Conference, Davis, CA, June 2014.
8. “How torsional effects cause attack at sterically crowded concave faces of bicyclic alkenes” Oral presentation, **Lopez, S. A.**; Pourati, M.; Gais, H.-J.; Houk, K. N. *Abstracts of Papers*, 248th ACS National Meeting & Exposition, San Francisco, CA, August 2014.
9. “Multi-scale simulations of morphology and charge-transport in oligothiophenes” Oral presentation, **Lopez, S. A.**, Yavuz, I.; Zhang, L.; Cherniawski, B.; Briseno, A. L.; Houk, K. N. *Abstracts of Papers*, 249th ACS National Meeting & Exposition, Denver, CO, March 2015.

Chapter 1

Alkene Distortion Energies and Torsional Effects Control Reactivities and Stereoselectivities of Azide Cycloadditions to Norbornene and Substituted Norbornenes^a

ABSTRACT: The transition structures for 1,3-dipolar cycloadditions of phenyl azide to norbornene derivatives were located with quantum mechanical methods. Calculations were carried out with M06-2X/6-311G(d,p) and SCS-MP2/6-311G(d,p)//M06-2X/6-311G(d,p) methods. The calculated activation barriers strongly correlate with transition state distortion energies (ΔE_d^\ddagger) but not with the reaction energies. Strain-promoted reactions are accelerated because it is easy to distort the strained reactants to a pyramidalized transition state geometry; a correlation of cycloaddition rates with substrate distortion was found for the bicyclic and tricyclic alkenes studied here. The stereoselectivities of reactions of norbornene derivatives are controlled primarily by torsional effects that also influence alkene pyramidalization. These reactions are distortion-accelerated.

INTRODUCTION

The unusual reactivity and high *exo* stereoselectivity of norbornene in cycloadditions has long been of great mechanistic interest¹ and has recently led to useful bioorthogonal chemistry involving norbornenes.^{2,3} Huisgen and co-workers first observed the unexpectedly high reactivity of norbornene and its derivatives along with a great preference for *exo* cycloadditions of phenyl azide and other 1,3-dipoles; other groups have confirmed these observations.⁴ After accounting for factors such as strain by calculating hydrogenation energies using MM2 computations, Huisgen found that the *exo* activation barriers are 1–3 kcal mol⁻¹ lower than expected. He attributed this reduced activation energy to “factor X”.⁵ Our group discovered that “factor X” is

^a Reprinted with permission from *J. Org. Chem.* **2013** 78, 1778. Copyright 2012 American Chemical Society. Authors are Steven Alexander Lopez and K. N. Houk

due to exceptionally favorable torsional effects in the *exo* transition state.⁶ We have now investigated the transition states for 1,3-dipolar cycloadditions of strained, pyramidalized alkenes with phenyl azide, an ambiphilic 1,3-dipole, and a common substrate in Sharpless' Click chemistry.⁷ We report computed transition structures and activation barriers for cycloadditions to a number of norbornenes and to the simple alkenes, *cis*-2-butene (**1**) and cyclohexene (**2**). In addition to norbornene, tricyclic hydrocarbons with norbornene fused to cyclopropene or cyclobutene (**4** and **5**), *syn*-sesquinorbornene (**6**), and *anti*-sesquinorbornene (**7**) were studied. These compounds are shown in Figure 1. The unstrained planar alkenes (**1** and **2**) are used as a standard to which the reactivity of pyramidalized alkenes (**3–6**) can be compared.

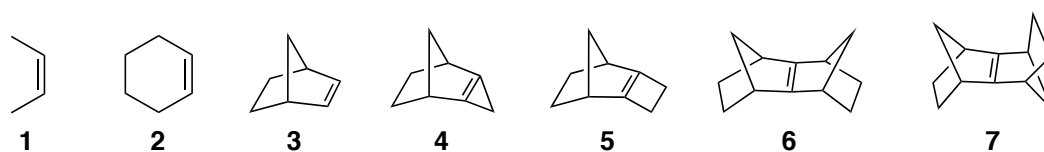


Figure 1. Series of alkenes studied.

Computational Methods

All computations were carried out with the Gaussian 09⁸ series of programs. The stationary points were located using M06-2X⁹/6-311G(d,p), and frequency calculations on these stationary points provide activation enthalpies and free energies. Vibrational analysis confirmed all stationary points to be first-order saddle points or minima with no imaginary frequencies. The *ab initio* method MP2 included the spin-component-scaled (SCS) correction, which uses standard parameters with the application of frozen-core approximation for nonvalence-shell electrons. SCS-MP2¹⁰/6-311G(d,p) single points used the M06-2X/6-311G(d,p)-optimized geometries to give independent estimates of barrier heights and reaction energies. (Energies given in the

Supporting Information.) Solvation corrections were computed on gas-phase geometries with M06-2X/6-311G(d,p). On the basis of the results of a study performed by our group,¹¹ the corrections used the CPCM model¹² using UAKS radii for two solvents (CCl₄ and Et₂O) and more accurately reproduce experimental conditions. A quasiharmonic correction was applied during the entropy calculation by setting all frequencies that are less than 100 cm⁻¹ to 100 cm⁻¹.¹³ Both SCS-MP2 and M06-2X predict 2–5 kcal mol⁻¹ higher barriers than experiment, likely due to overestimation of $-T\Delta S^\ddagger$ for these bimolecular reactions in solution. A benchmarking study on the 1,3-dipolar cycloaddition of 48 different dipoles to ethylene and acetylene was done by our group.¹⁴ G3B3 was adopted as the standard method for predicting activation barriers, and M06-2X and SCS-MP2//B3LYP were found to predict activation barriers closest to those from G3B3.¹⁴

Results

Pyramidalization of Norbornenes

Previous studies have shown that ring strain and ground-state angle distortion contribute greatly to the extent of alkene pyramidalization.¹⁵ Second-order Jahn–Teller distortion leads to stabilization resulting from mixing of 2s orbitals of the alkene carbons with p orbitals which form the π bond.¹⁶ Pyramidalization occurs in the *endo* direction for norbornene derivatives to minimize torsional strain.¹⁷ The optimized structures of alkenes 3–6 are shown in Figure 2. The ideal bond angle for sp²-hybridized carbons is 120°, while sp³ carbons have an ideal bond angle of 109.5°; consequently, the smaller C–C=C angles in strained alkenes reduce the force constants for out-of-plane bending. We use θ_{dih} to quantify the degree of pyramidalization in these alkenes. The torsional angle, θ , designated by the green atoms of **3** in Figure 3 is subtracted from 180° to obtain the out-of-plane bending angle, θ_{dih} . $\theta_{\text{dih}} = 0^\circ$ when $\theta = 180^\circ$.

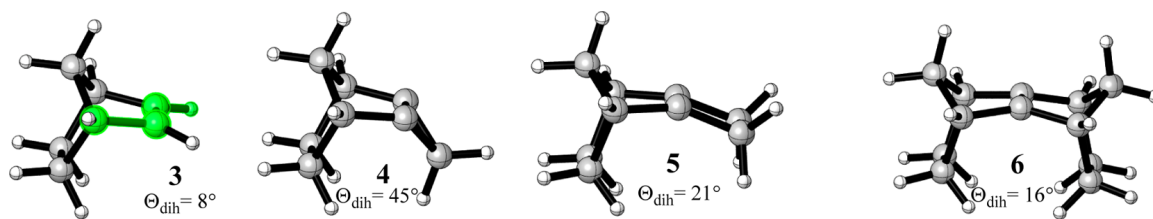


Figure 2. Optimized minima of **3–6** as calculated by M06-2X/6-311G(d,p). The green atoms in **3** define θ_{dih} .

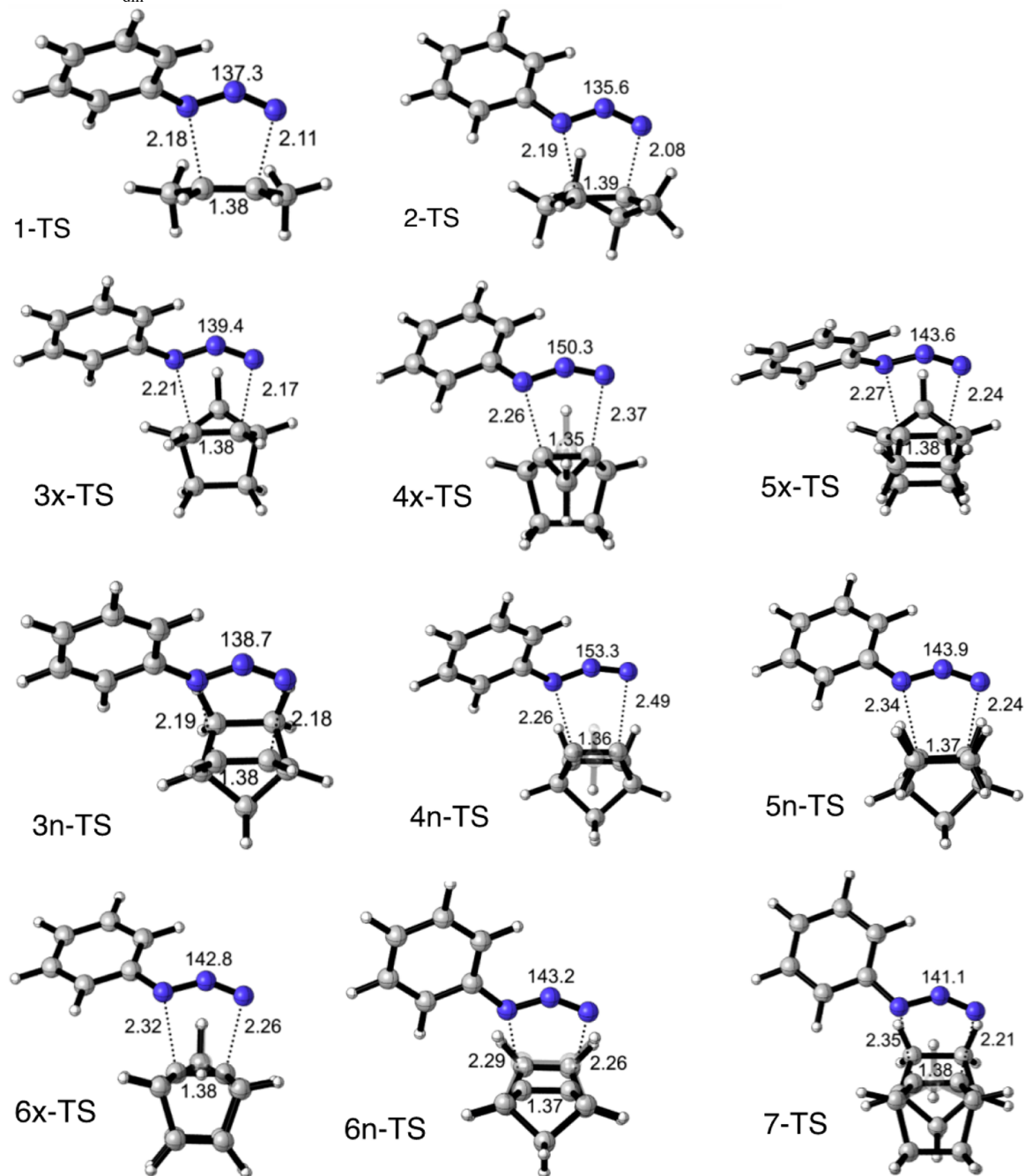


Figure 3. Optimized transition structures of the 1,3-dipolar cycloaddition of phenyl azide to alkenes **1–7** as calculated by M06-2X/6-311G(d,p). Bond lengths are reported in Å.

This value is identical to the “butterfly angle” (ψ), as described by Williams.¹⁸ θ_{dih} is 60° for a perfectly sp^3 -pyramidalized alkene. Our high-level DFT calculations compare well with previous results by Vazquez,¹⁹ Williams,^{15b} and our group.⁶ We report θ_{dih} of 8° , 45° , 21° , 16° , and 0° for alkenes **3**, **4**, **5**, **6**, and **7**; they report 7° , 44° , 18° , 16° , and 0° for the same alkenes.

Transition Structures. The optimized transition structures of the reactions of dipolarophiles (**1–7**) with phenyl azide are shown in Figure 3. The reactions are concerted, but the transition structures show that bond formation is slightly asynchronous. The dipolarophiles in the transition states all have nearly identical alkene bond lengths (1.35–1.39 Å). However, the $\angle\text{NNN}$ and forming bond distances between the dipole and dipolarophile vary significantly through the series, $136\text{--}153^\circ$ and 2.08–2.49 Å, respectively. The partial bond to the more electrophilic (unsubstituted) terminus of phenyl azide is somewhat shorter than the partial bond to the more nucleophilic terminus.

The transition structures for the planar alkenes *cis*-2-butene (**1**) and cyclohexene (**2**) are very similar, with $\angle\text{NNN}$ of 137° and 136° , respectively. Both have average forming C–N bond lengths of 2.14 Å. *anti*-Sesquinorbornene is planar and has an earlier transition state, the result of increased steric clashes in the transition structure between the ethylene bridges of *syn*-sesquinorbornene. The *exo* transition structures for the norbornenes **3–6** have $\angle\text{NNN}$ that increase with θ_{dih} in the reactants; this correlates with the lower activation barriers and earlier transition states as θ_{dih} increases. The *exo* transition structures for the reactions of **3**, **5**, and **4** with phenyl azide have $\angle\text{NNN} = 139^\circ$, 144° , and 150° , respectively, and correspond to increasingly early transition states.

Stereoselectivities. The *exo*-stereoselectivities of these reactions results from different torsional effects in *exo* and *endo* transition states. Figure 4 shows Newman projections along the 1,2 and 3,4 bonds in the 1,3-dipolar cycloaddition transition states of norbornene and phenyl azide. These torsional effects are representative of all of the pyramidalized alkenes discussed here.

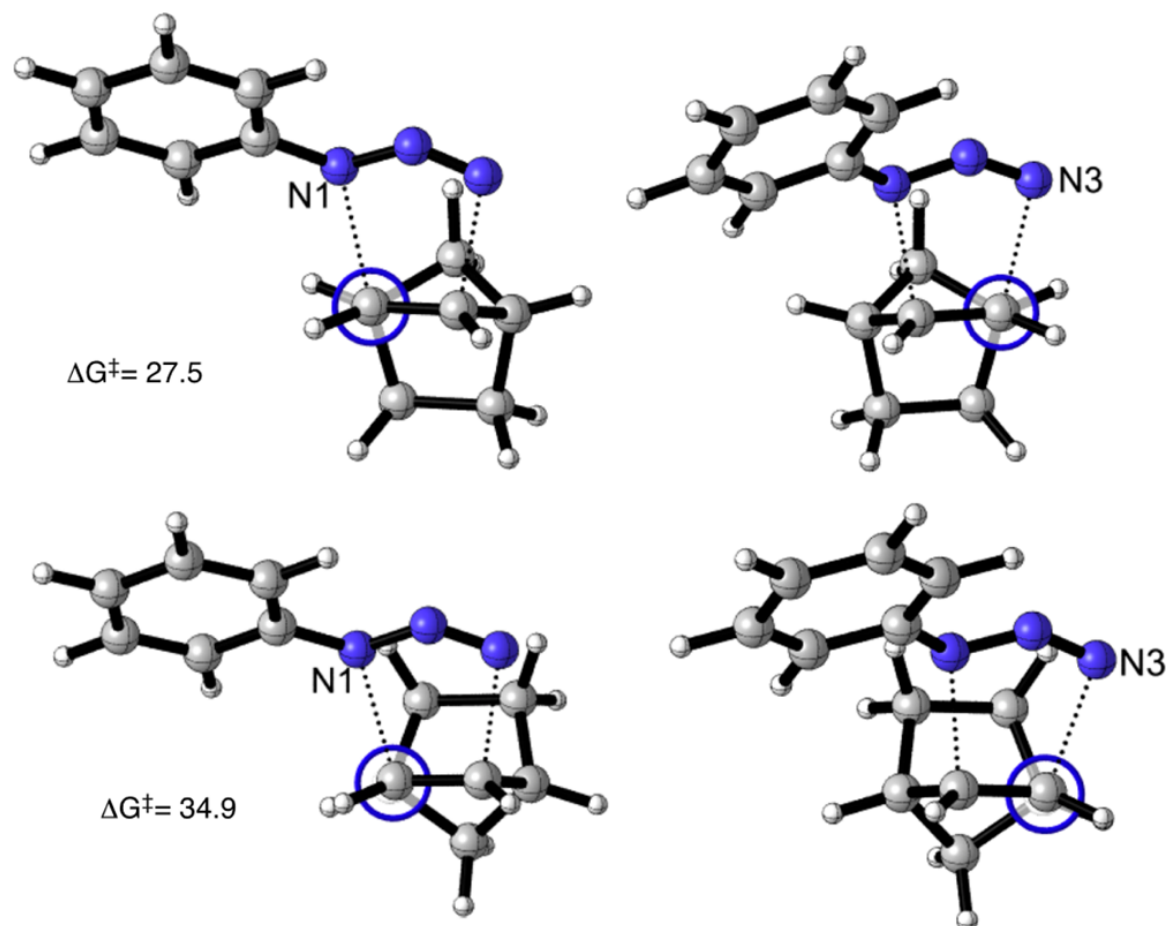


Figure 4. Newman projections for the cycloadditions of phenyl azide to the *exo* **3x-TS** (top row) and **3n-TS** (bottom row) *endo* faces of norbornene. ΔG^\ddagger values (kcal mol⁻¹) are shown below the Newman projections.

A nearly perfect staggered conformation about the C-1, C-2 bond can be seen for the *exo* transition structure (**3x-TS**) on both termini of phenyl azide. The Newman projections for **3n-TS** shows the partially formed C–N bonds and the vicinal HCCH bonds suffer some eclipsing, while the HCC_{bridged}H eclipsing is severe, a factor noted originally by Schleyer for norbornyl

solvolysis.²⁰ The distortion/interaction model²¹ is an approach to dissect activation barriers (ΔE^\ddagger) into distortion energy (ΔE_d^\ddagger) and interaction energy (ΔE_i^\ddagger). Distortion energy is the amount of energy required to bend phenyl azide and the dipolarophile into the transition state geometries without allowing interaction. The interaction energy results from closed-shell (steric) repulsion, charge transfer from occupied-vacant orbital interactions, electron transfer, and polarization effects. The distortion/interaction model was used to analyze the reactivities and *exo* stereoselectivities of these 1,3-dipolar cycloadditions. Since the dipolarophile is “pre-distorted” into the geometry of the *exo* transition state, the distortion energy is smaller for the *exo* transition states. This control of reactivity by distortion energies has been used to understand and design catalysts for palladium-catalyzed allylic alkylations.²² Bickelhaupt has developed the activation strain model²³ to explain S_N2 reactions and the enhanced reactivity of predistorted catalytically active transition-metal complexes.²⁴ Our group describes this as the distortion/interaction model and been applied to Diels–Alder reactions and 1,3-dipolar cycloadditions.

We first established that computed activation free energies correspond reasonably well to experimental values, when available. Table 1 shows a comparison of the experimental activation barriers to the computed barriers using M06-2X/6-311G(d,p) and SCS-MP2/6-311G(d,p)//M06-2X/6-311G-(d,p).

Table 1. $\Delta G_{\text{expt}}^{\ddagger}$ ^a, values derived from experimental rate constants. $\Delta G_{\text{comp}}^{\ddagger}$ energies include solvation by CPCM^{CCl4} or CPCM^{Et2O}. The reactions of phenyl azide with dipolarophiles **2**, **3**, and **7** as calculated by M06-2X/6-311G(d,p), and [SCS-MP2/6-311G(d,p)//M06-2X/6-311G(d,p)]. Linear regressions are shown below the table.^c

alkene	Solvent	T (°C)	$10^7 k_2$ (M ⁻¹ s ⁻¹)	$\Delta G_{\text{expt}}^{\ddagger}$ ^{a,b} (kcal mol ⁻¹)	$\Delta G_{\text{M06-2X}}^{\ddagger}$ (kcal mol ⁻¹)	$\Delta G_{\text{SCS-MP2}}^{\ddagger}$ (kcal mol ⁻¹)
2 ²⁵	CCl ₄	25°	0.03	29.0	33.1	32.1
3 ³⁵	CCl ₄	25°	188	23.9	28.2	29.0
7 ²⁶	Et ₂ O	30°	270	23.6	27.4	25.3

^a Calculated from $k_2 = 6 \times 10^{12} e^{(-\Delta G_{\ddagger}^{\ddagger}/RT)}$ ^b Computed free energies in solution are for the standard state of 1M. ^{a,a} ^c Linear Regression between $\Delta G_{\text{calc}}^{\ddagger}$ and $\Delta G_{\text{expt}}^{\ddagger}$ for M06-2X and SCS-MP2 methods. M06-2X/6-311G(d, p) $\Delta G_{\text{calc}}^{\ddagger} = 1.01 \Delta G_{\text{expt}}^{\ddagger} + 3.72$; $R^2 = 0.99$ and SCS-MP2/6-311G(d,p)//M06-2X/6-311G(d,p) $\Delta G_{\text{calc}}^{\ddagger} = 0.97 \Delta G_{\text{expt}}^{\ddagger} + 4.05$; $R^2 = 0.75$.

Table 1 shows that M06-2X predicts activation barriers better than SCS-MP2. Both predict higher activation barriers than $\Delta G_{\text{expt}}^{\ddagger}$. Both give the correct order of reactants, but M06-2X gives an experimentally good correlation. Table 2 gives the computed activation barriers (ΔG^{\ddagger} , ΔH^{\ddagger} , ΔE^{\ddagger}) distortion and interaction energies, and the \angle NNN in each transition structure studied here.

Table 2. M06-2X/6-311G(d,p) activation free energies and enthalpies of activation, electronic energies of activation, distortion energies, and interaction energies for the reactions of phenyl azide and dipolarophiles **1–7**. (x=*exo*, n=*endo*) \angle NNN is the azide bond angle in each respective transition structure.

Alkene	ΔG^\ddagger	ΔH^\ddagger	ΔE^\ddagger	ΔH_{rxn}	$\Delta E_{\text{d}}^\ddagger$	$\Delta E_{\text{d}}^\ddagger$	$\Delta E_{\text{d}}^\ddagger$ Total	$\Delta E_{\text{i}}^\ddagger$	\angle NNN ($^\circ$)
					Alkene	PhN ₃			
1	32.8	19.6	19.1	-29.2	7.6	23.4	31.1	-12.0	137
2	32.2	19.6	19.2	-26.8	8.2	25.1	33.3	-14.1	136
3x	27.5	14.7	14.4	-38.1	4.6	20.5	25.0	-10.7	139
3n	34.9	21.7	21.1	-36.5	10.8	21.1	31.9	-10.8	139
4x	16.0	3.3	3.1	-68.6	0.9	10.6	11.5	-8.4	150
4n	21.6	9.3	9.0	-71.9	9.0	8.2	17.2	-8.2	153
5x	22.1	8.7	8.3	-51.0	2.5	16.4	18.9	-10.6	144
5n	30.8	17.6	17.2	-53.7	12.6	15.1	27.7	-10.5	144
6x	26.2	12.1	11.7	-33.4	3.9	21.2	25.1	-13.4	139
6n	40.3	27.1	27.2	-41.3	22.6	15.7	38.3	-11.1	143
7	26.4	13.8	17.6	-46.5	6.7	17.7	29.0	-11.4	141

There is a large range of activation energies, ΔE^\ddagger (3–27 kcal mol⁻¹), and a similarly large range of distortion energies, $\Delta E_{\text{d}}^\ddagger$ (12–38 kcal mol⁻¹), but a relatively small range of interaction energies, $\Delta E_{\text{i}}^\ddagger$ (8–14 kcal mol⁻¹). The distortion energies of the alkenes control barrier heights (Table 1), while the interaction energies are nearly constant. The range of alkene distortion energies (2–23 kcal mol⁻¹) is notably larger than the range of distortion energies of phenyl azide (15–25 kcal mol⁻¹), although the latter are generally larger than the former. Figure 5 shows a plot of ΔE^\ddagger vs. $\Delta E_{\text{d}}^\ddagger$ for the seven reactions studied.

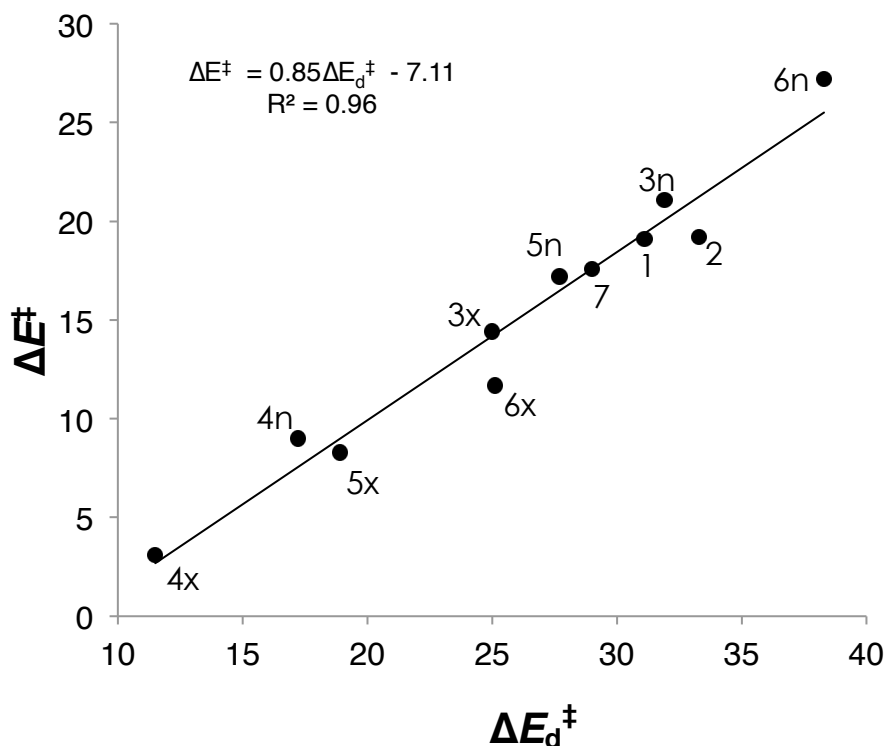


Figure 5. Plot of activation energies and distortion energies of the reactions of phenyl azide and dipolarophiles **1-7**, calculated by M06-2X/6-311G(d,p). Values in kcal mol⁻¹.

There is an excellent linear correlation between distortion energy and activation energy ($r^2 = 0.96$). Similar relationships have been observed for the cycloadditions of many dipoles and dienes with simple alkenes²⁷ and for related reactions by Bickelhaupt and coworkers.²⁸ It was previously shown with 1,3-dipolar cycloadditions of acetylene and ethylene with many dipoles the distortion of the 1,3-dipole comprises ~80% of the distortion energy.²⁹ This portion of the total distortion energy is referred to as dipole distortion energy in this work and is defined as the energy required to bend the dipole into its transition structure geometry from its equilibrium geometry. In the azide cycloaddition studied here with unstrained **1** and **2**, dipole distortion energies comprise 75% of the total distortion energy. In the series of strained alkenes, dipole distortion energy makes up 40–90% of the total distortion energy.

Despite the rather remarkable fit in Figure 3, two outliers, **6x** and **6n** are apparent. The activation barriers for the 1,3-dipolar cycloaddition of *syn*-sesquinorbornene deviate because of severe steric clashes in the *endo* transition structures (Figure 3). This effect appears in the distortion energy as well. Pyramidalization plays a key role in the reactivities and stereoselectivities of these strained cycloalkenes undergoing 1,3- dipolar cycloadditions. The extent of pyramidalization (θ_{dih}) of the disubstituted alkenes (**1–5**) is first described, followed by the tetrasubstituted alkenes (**6–7**). Norbornene (**3**) is the least pyramidalized alkene ($\theta_{\text{dih}} = 8^\circ$), and the ΔE^\ddagger of **3x-TS** is 14 kcal mol⁻¹, the highest among pyramidalized alkenes. The distortion energy of phenyl azide is similar for both transition states, but the large difference between alkene distortion energies favors the *exo* transition state (4.6 vs. 10.8 kcal mol⁻¹).

The θ_{dih} of **5** is 21°, and the ΔE^\ddagger drops to 8.3 kcal mol⁻¹. The lowered activation barrier is due to reduced distortion energy of the alkene and phenyl azide. The reduced distortion energy of phenyl azide results from the earlier transition state involving the distorted alkene. The largest θ_{dih} is seen in the optimized structure of **4**, and the smallest $\Delta E_{\text{d}}^\ddagger$ and ΔE^\ddagger occur with **4x-TS** (11.5 and 3.1 kcal mol⁻¹, respectively). A remarkably small 0.9 kcal mol⁻¹ is required to distort **4** into the *exo* transition state geometry, and 10.6 kcal mol⁻¹ is required to distort phenyl azide into the NNN of 150° in the transition structure. *syn*-Sesquinorbornene (**6**) has $\theta_{\text{dih}}=16.8^\circ$; the distortion energy of **6x-TS** is 3.9 kcal mol⁻¹ and for **6n-TS** is 22.6 kcal mol⁻¹. The steric clashes of the hydrogens at carbons 3, 4, 8, and 9 with the azide contribute to the large difference in distortion energy, $\Delta\Delta E_{\text{d}}^\ddagger$ (13.2 kcal mol⁻¹). *anti*-Sesquinorbornene is planar like *cis*-2-butene and cyclohexene, but the transition state shows a greater \angle NNN than those of **1-TS** and **2-TS**. As a result, the dipole distortion energy is 6.0 kcal mol⁻¹ lower than that of **1-TS**. The relatively early transition state requires less bending of phenyl azide, which results in a lower activation barrier.

The ΔE^\ddagger for the reaction of tetramethylethylene with phenyl azide is 5.3 kcal mol⁻¹ higher than for the reaction of *anti*-sesquinorbornene with phenyl azide. The strained nature of the *anti*-sesquinorbornene compared to tetramethylethylene results in the lower distortion energy. Figure 6 correlates pyramidalization (θ_{dih}) to reactivity (ΔH^\ddagger) for the stereochemically-preferred reactions of **1–6** with phenyl azide.

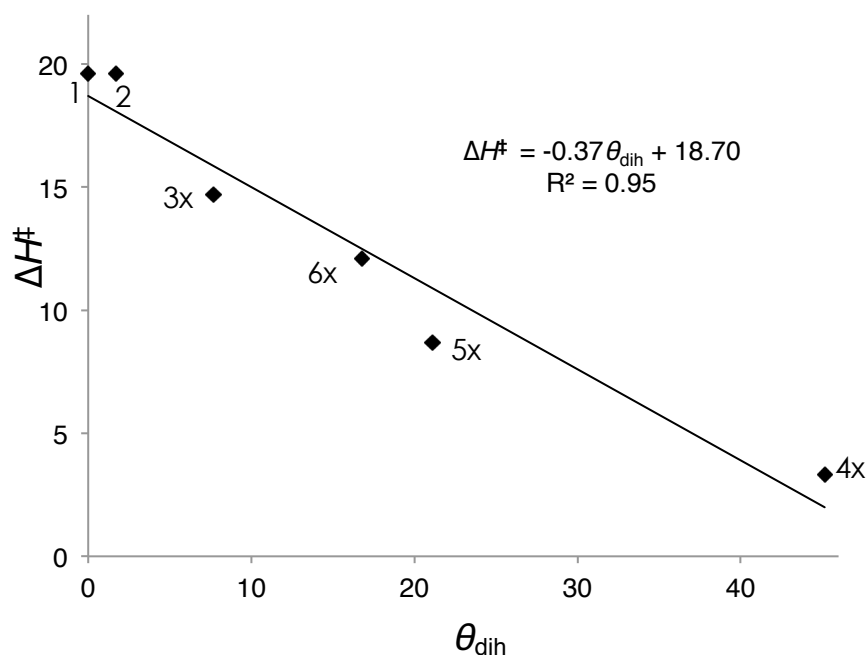


Figure 6. Plot of activation enthalpy (kcal mol⁻¹) vs. θ_{dih} (°), calculated with M06-2X/6-311G(d,p)

The planar alkenes, **1** and **2** have nearly identical activation enthalpies. It is apparent that even slight pyramidalization of alkenes can greatly accelerate 1,3-dipolar cycloadditions. When $\theta_{\text{dih}} = 4^\circ$, ΔH^\ddagger is lowered by 1.4 kcal mol⁻¹, which corresponds to an order of magnitude acceleration at 25 ° C. ΔH^\ddagger is 0 kcal mol⁻¹ when the $\theta_{\text{dih}} = 51^\circ$. For comparison, perfectly pyramidal sp³ carbon has a corresponding θ_{dih} of 60°. It is notable that *endo* attack is also accelerated in the cases of high pyramidalization, compared to the unstrained alkenes. The degree of bending is an

indication of the ease of out-of-plane bending and the magnitude of distortion energies. The role of strain release in controlling reactivity was investigated by comparing ΔH^\ddagger vs. ΔH_{rxn} in Figure 7.

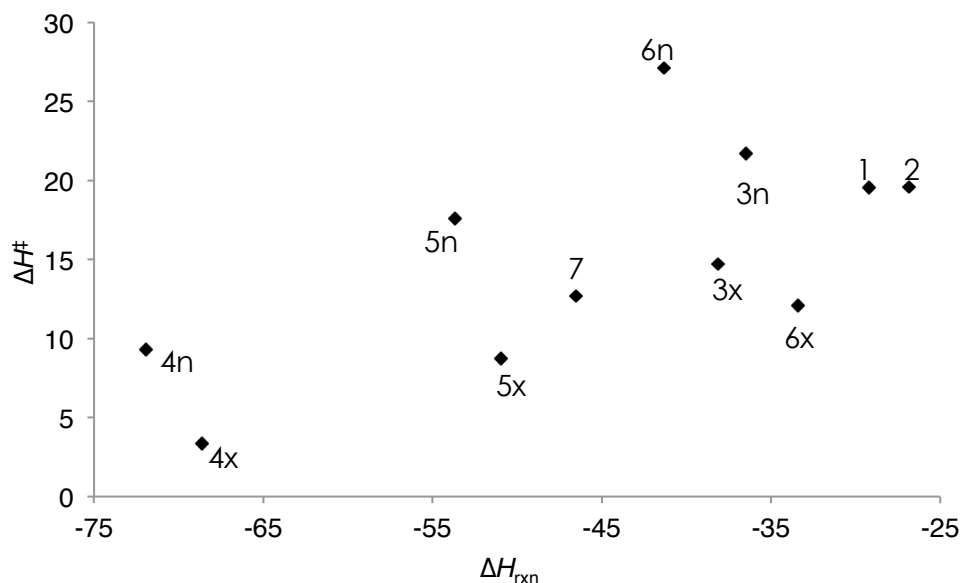


Figure 7. Plot of ΔH^\ddagger vs. ΔH_{rxn} , calculated by M06-2X/6-311G(d,p). $\Delta H^\ddagger = 0.30\Delta H_{\text{rxn}} + 28.61$; $R^2=0.43$.

The energies of reaction used in this plot are shown in Table 1. There is no significant correlation of these quantities and $r^2= 0.43$. Consequently, there is no clear Dimroth, Brønsted, Evans–Polanyi, or Marcus relationship,³⁰ where the differences in activation barriers are about one-half of the differences in reaction energies. Strain release, as measured by the change of energy upon reaction, shows only a qualitative relationship to reaction rates. In Figure 7, the most strain is released with the substrates on the left side of the graph, but only **4x** shows unusually high reactivity. The lack of relationship between activation barrier and strain release indicates that the enhanced reactivities of these strained alkenes are not “strain-promoted”. We have shown instead that they are distortion-accelerated when the ease of distortion to the

transition-state geometry is lowered.

Conclusion

The computations reported for a series of highly strained alkenes demonstrate the powerful effect that distortion and pyramidalization have on 1,3-dipolar cycloadditions of alkenes. Pyramidalization is a form of predistortion that causes the alkene to geometrically resemble the *exo* transition structure. Less distortion energy is required to achieve this transition state, and the activation energy is correspondingly lessened. Alkenes with planar double bonds such as *cis*-2-butene and cyclohexene have much higher barriers, since the dipolarophiles and phenyl azide must undergo significant distortion to achieve the transition-state geometry. A strained cycloalkene with a pyramidalization of just 4° accelerates the reaction by an order of magnitude. While reactions of this type are often called strain-promoted, this study and others by our group³¹ indicate that reduction of distortion energy controls rates of cycloaddition. This can be manifested in predistortion as in **3–6** discussed here or in reduction of distortion energies caused by angle strain as in cyclopropene.³² The reactions are distortion-accelerated, subtly different from strain-promoted. The strain results in a predistortion of the alkene, which resembles the transition structure. Reduced distortion energy results in distortion-accelerated reactions.

Acknowledgements

K. N. Houk was the project director. We thank the National Science Foundation (NSF CHE-1059084) for financial support of this research. The computations were performed on the UCLA IDRE Hoffman2 cluster.

References

- ¹ Vazquez, S.; Camps, P. *Tetrahedron* **2005**, *61*, 5147–5208.
- ² Sletten, E. M.; Bertozzi, C. R. *Acc. Chem. Res.* **2011**, *44*, 666.
- ³ Han, H.-S.; Devaraj, N. K.; Lee, J.; Hilderbrand, S. A.; Weissleder, R.; Bawendi, M. G. *J. Am. Chem. Soc.* **2010**, *132*, 7838.
- ⁴ (a) Huisgen, R.; Moebius, L.; Mueller, G.; Stangl, H.; Szeimies, G.; Vernon, J. M. *Chem. Ber.* **1965**, *98*, 3992. (b) Gutsmedl, K.; Wirges, C. T.; Ehmke, V.; Carell, T. *Org. Lett.* **2009**, *11*, 2405. (c) Hansell, C. F.; Espeel, P.; Stamenovic, M. M.; Barker, I. A.; Dove, A. P.; Du Prez, F. E.; O'Reilly, R. K. *J. Am. Chem. Soc.* **2011**, *133*, 13828. (d) Watson, W. H.; Galloy, J.; Bartlett, P. D.; Roof, A. A. M. *J. Am. Chem. Soc.* **1981**, *103*, 2022.
- ⁵ Huisgen, R.; Ooms, P. H. J.; Mingin, M.; Allinger, N. L. *J. Am. Chem. Soc.* **1980**, *102*, 3951.
- ⁶ Rondan, N. G.; Paddon-Row, M. N.; Caramella, P.; Mareda, J.; Mueller, P. H.; Houk, K. N. *J. Am. Chem. Soc.* **1982**, *104*, 4974.
- ⁷ Kolb, H. C.; Finn, M. G.; Sharpless, K. B. *Angew. Chem., Int. Ed.* **2001**, *40*, 2004.
- ⁸ Frisch, M. J. et al. (see complete reference in the Supporting Information). Gaussian 09, revision A.1; Gaussian Inc.: Wallingford, CT, 2009.
- ⁹ Zhao, Y.; Truhlar, D. G. *Theor. Chem. Acc.* **2008**, *120*, 215.
- ¹⁰ (a) Grimme, S. J. *J. Chem. Phys.* **2003**, *109*, 3067. (b) Grimme, S. *J. Chem. Phys.* **2003**, *118*, 9095. (c) Greenkamp, M.; Grimme, S. *Chem. Phys. Lett.* **2004**, *392*, 229.
- ¹¹ Takano, Y.; Houk, K. N. *J. Chem. Theor. Comput.* **2005**, *1*, 70.
- ¹² (a) Klamt, A.; Schürmann, G. *J. Chem. Soc., Perkin Trans. 2* **1993**, 799. (b) Andzelm, J.; Kolmel, C.; Klamt, A. *J. Chem. Phys.* **1995**, *103*, 9312. (c) Barone, V.; Cossi, M. *J. Phys. Chem. A* **1998**, *102*, 1995. (d) Cossi, M.; Rega, N.; Scalmani, G.; Barone, V. *J. Comput. Chem.* **2003**, *24*,

669.

¹³ (a) Zhao, Y.; Truhlar, D. G. *Phys. Chem. Chem. Phys.* **2008**, *10*, 2813. (b) Ribeiro, R. F.; Marenich, A. V.; Cramer, C. J.; Truhlar, D. G. *J. Phys. Chem. B.* **2011**, *115*, 14556.

¹⁴ Lan, Y.; Zou, L.; Cao, Y.; Houk, K. N. *J. Phys. Chem. A* **2011**, *115*, 13906.

¹⁵ (a) Houk, K. N.; Rondan, N. G.; Brown, F. K.; Jorgensen, W. L.; Madura, J. D.; Spellmeyer, D. *C. J. Am. Chem. Soc.* **1983**, *105*, 5980. (c) Holthausen, M. C.; Koch, W. J. *Phys. Chem.* **1993**, *97*, 10021.

¹⁶ Volland, W. V.; Davidson, E. R.; Borden, W. T. *J. Am. Chem. Soc.* **1979**, *101*, 533.

¹⁷ Williams, R. V.; Colvin, M. E.; Tran, N.; Warrener, R. N.; Margetić, D. *J. Org. Chem.* **2000**, *65*, 562.

¹⁸ Williams, R. V.; Margetić, D. *J. Org. Chem.* **2004**, *69*, 7134.

¹⁹ Fernandez, J. A.; Vazquez, S. *Eur. J. Org. Chem.* **2007**, *27*, 4493.

²⁰ Schleyer, P.; von, R. *J. Am. Chem. Soc.* **1964**, *86*, 1854.

²¹ Ess, D. H.; Houk, K. N. *J. Am. Chem. Soc.* **2007**, *129*, 10646.

²² Wassenaar, J.; Jansen, E.; Zeist, W-J. v.; Bickelhaupt, F. M.; Siegler, M. A.; Spek, A. L.; Reek, J. N. H. *Nature Chem.* **2010**, *2*, 417.

²³ de Jong, G. T.; Bickelhaupt, F. M. *ChemPhysChem* **2007**, *8*, 1170.

²⁴ Zeist, W-J. v.; Visser, R.; Bickelhaupt, F. M. *Chem. Eur. J.* **2009**, *15*, 6112.

-
- ²⁵ Huisgen, R.; Moebius, L.; Mueller, G.; Stangl, H.; Szeimies, G.; Vernon, J. M. *Chem. Ber.*, **1965**, *98*, 3992.
- ²⁶ Watson, W. H.; Galloy, J.; Bartlett, P. D.; Roof, A. A. M. *J. Org. Chem.* **1985**, *50*, 4093.
- ²⁷ Jones, G. O.; Houk, K. N. *J. Org. Chem.* **2008**, *73*, 1333. (b) Paton, R. S.; Kim, S.; Ross, A. G.; Danishefsky, S. J.; Houk, K. N. *Angew. Chem., Int. Ed.* **2011**, *50*, 10366.
- ²⁸ (a) Fernandez, I.; Cossio, F. P.; Bickelhaupt, F.; Matthias. *J. Org. Chem.* **2011**, *76*, 2310. (b) Fernandez, I.; Bickelhaupt, F.; Matthias. *J. Comput. Chem.* **2012**, *33*, 509.
- ²⁹ Gordon, C.; Mackey, J. L.; Jewett, J. C.; Sletter, E. M.; Houk, K. N.; Bertozzi, C. R. *J. Am. Chem. Soc.* **2012**, *134*, 9199.
- ³⁰ Dimroth, O. *Angew. Chem.* **1933**, *46*, 571. (b) Evans, M. G.; Polanyi, M. *Trans. Faraday Soc.* **1936**, *32*, 1340. (c) Marcus, R. A. *J. Chem. Phys.* **1956**, *24*, 966.
- ³¹ Hayden, A.; Houk, K. N. *J. Am. Chem. Soc.* **2009**, *131*, 4084. (b) Osuna, S.; Houk, K. N. *Chem. Eur. J.* **2009**, *15*, 13219. (c) Cheong, P. H.-Y.; Paton, R. S.; Bronner, S.; Im, G-Yoon, J.; Garg, N. K.; Houk, K. N. *J. Am. Chem. Soc.* **2010**, *132*, 126.
- ³² (a) Thalhammer, F.; Wallfahrer, U.; Sauer, J. *Tetrahedron Lett.* **1990**, *31*, 3851. (b) Sauer, J.; Bäuerlein, P.; Ebenbeck, W.; Gousetis, C.; Sichert, H.; Troll, T.; Utz, F.; Wallfahrer, U. *Eur. J. Org. Chem.* **2001**, 2629. (c) Yang, J.; Seckute, J.; Cole, C. M.; Devaraj, N. K. *Angew. Chem., Int. Ed.* **2012**, *51*, 7476.

Chapter 2

How torsional effects cause attack at sterically crowded concave faces of bicyclic alkenes^a

Abstract: Cycloadditions of 1,3-dipoles and related species to a *cis*-oxabicyclo[3.3.0]octenone occur on the more sterically crowded concave face. These cycloadditions were studied experimentally by Gais and coworkers in 1998 (*Eur. J. Org. Chem.* **1998**, 257-273), and have now been studied computationally with Density Functional Theory (DFT). Transition states have been computed for various types of (3+2) cycloadditions, including diazomethane 1,3-dipolar cycloadditions, a thermally promoted methylenecyclopropane acetal cycloaddition, and a Pd-catalyzed cycloaddition of methylenecyclopropane to an oxabicyclo[3.3.0]octenone. The concave stereoselectivities arise from alkene predistortion that leads to torsional steering in the transition state.

Introduction

The pentalenolactone family includes natural products with antibiotic, antiviral, and antitumor activities.¹ Gais and coworkers undertook the synthesis of pentalenolactone F, a precursor in the biosynthesis of other members of the pentalenolactone family (Figure 1).^{2a} The Binger- and Trost-type palladium-catalyzed cycloadditions^{3,4} were used to generate tricyclic quinanes.

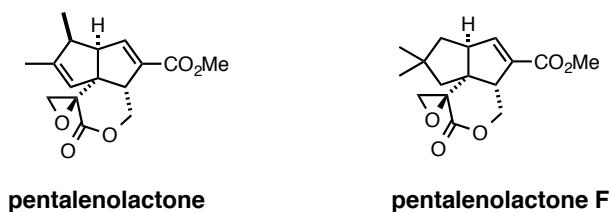
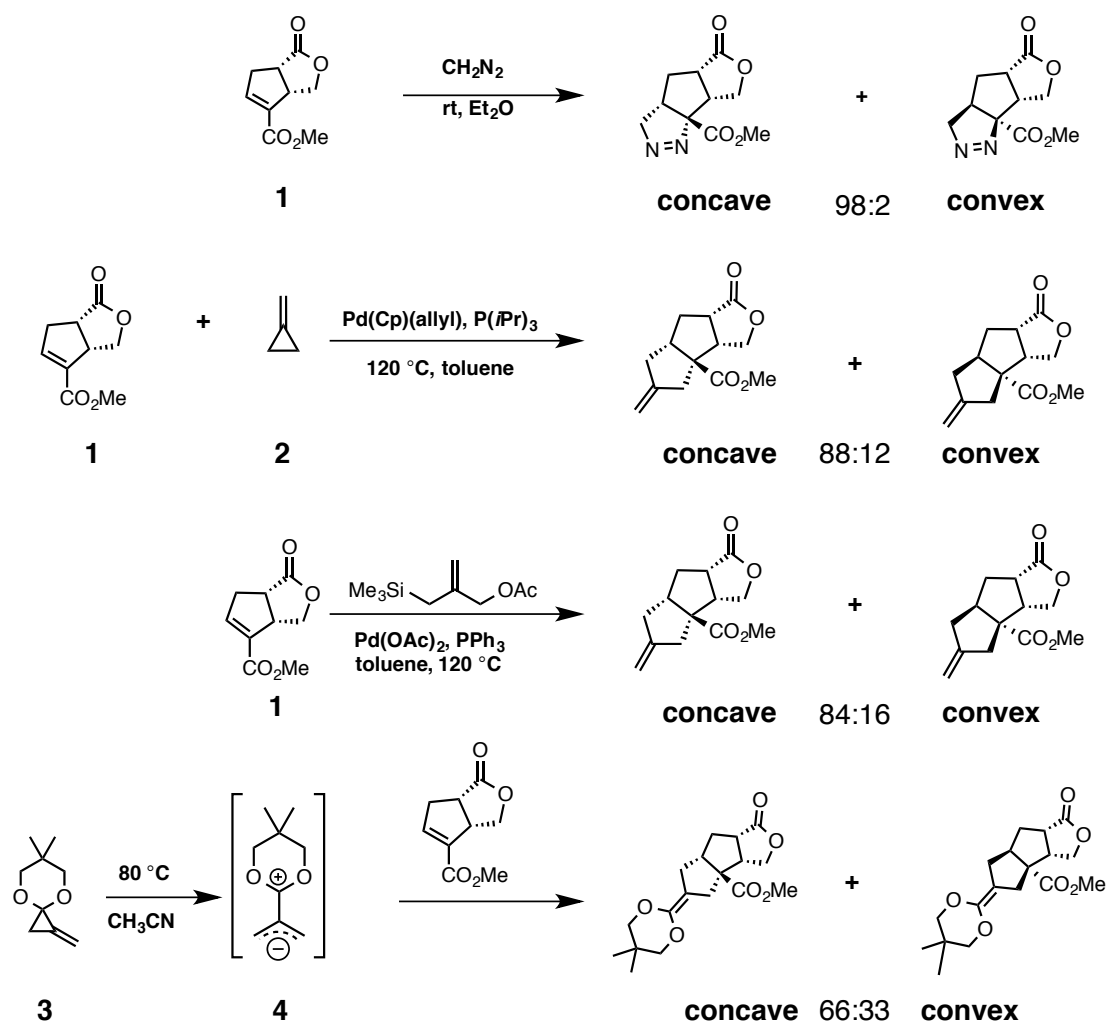


Figure 1. Pentalenolactone and pentalenolactone F.

^a Reprinted with permission from *Journal of Organic Chemistry* **2014**, 79, 8304–8312. Copyright 2013 American Chemical Society. Authors are Steven Alexander Lopez, M. Pourati, H-J. Gais, and K. N. Houk

Gais and coworkers report that the contra-steric product was unexpectedly formed for many of the reactions they performed.^{2a} Scheme 1 shows the reactions of CH₂N₂, silylmethylallyl acetate, **2**, and **4** with **1** as well as reported product distributions reported by Gais and coworkers. They proposed that the stereoselectivity associated with the CH₂N₂ cycloaddition resulted from electrostatic stabilization only possible in concave transition states.^{2a} We have used quantum mechanical calculations to probe the origins of the stereoselectivities, and have evaluated these factors and others that lead to stereoselectivity in spite of obvious steric barriers to reaction

Scheme 1. Experimental conditions and product ratios for the (3+2) cycloadditions with diazomethane (first row), methylenecyclopropane **2** (second row), silylmethylallyl acetate (third row), and methylenecyclopropane acetal **3** (fourth row).^{2a}



The selectivity typically arises from favorable torsional effects (staggering) in one transition structure and unfavorable torsional effects (eclipsing) in the other. Felkin proposed this for nucleophilic additions to carbonyls,⁵ and transition state calculations have revealed the importance of these effects for stereoselective hydride reductions of ketones,⁶ and other types of nucleophilic attack,⁷ and reactions of electrophiles,⁸ radicals,⁹ as well as concerted cycloadditions.^{15a,10} Torsional effects have been shown to influence the manner by which a reagent adds to an unsymmetrical π bond.^{8a} Norbornene is a bicyclic hydrocarbon featuring a cyclopentene fixed in a pronounced envelope conformation. Huisgen discovered strong *exo*-

stereoselectivity and rate acceleration associated with cycloadditions to the strained alkene.¹¹ Our group explained that the *exo*-stereoselectivity resulted from torsional steering.¹²

The additions to conformationally flexible cyclopentenes are more complicated, but addition is generally preferred to the concave face of the envelope cyclopentene.¹³ Overman reported a contra-steric OsO₄ dihydroxylation that occurs from the concave face of a [3.3.0] bicycle, and our group determined that torsional effects direct that and related concave dihydroxylations.¹⁴ Figure 2 shows 3,4-fused cyclopentenes studied by Danishefsky (epoxidations)¹³ and Overman (OsO₄).¹⁴

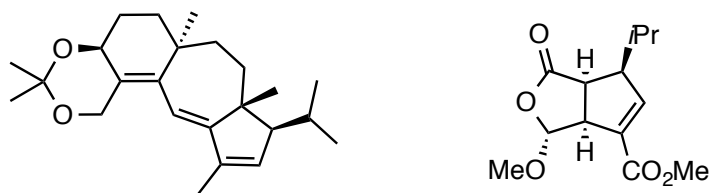


Figure 2. 3,4-Fused cyclopentenes studied by Danishefsky and Overman.

Computational Methods

All computations were carried out with the GAUSSIAN 09 series of programs.¹⁵ Stationary points for the Pd-catalyzed (3+2) cycloadditions were computed using the M06¹⁶ level of theory with the LANL2DZ¹⁷ pseudopotential for Pd and the 6-31G+(d,p) basis set for all other atoms in the gas phase. Single point energy calculations on these geometries were performed using M06/6-311+G(d,p). The single point calculations include solvation by toluene using the integral equation formalism polarizable continuum model (IEF-PCM).¹⁸

The stationary points corresponding to the CH₂N₂ and methylenecyclopropane acetal cycloadditions were optimized employing M06-2X¹⁹ and the double- ζ split-valence 6-31+G(d,p) basis set. Some transition states for the methylenecyclopropane acetal could not be located with gas phase calculations. It has been shown that polarizable continuum models are sometimes necessary to locate stationary points in polar media; it does not significantly alter frequencies.²⁰ Therefore, M06-2X/6-31+G(d,p) IEF-PCM^{MeCN} was utilized for optimizations for the computations involving methylenecyclopropane acetal. Single point energy calculations on the diazomethane and methylenecyclopropane acetal stationary points were carried out using M06-2X/6-311+G(d,p) IEF-PCM^{Et₂O} and M06-2X/6-311+G(d,p) IEF-PCM^{MeCN}, respectively.

All optimizations used tight convergence criteria, and an ultrafine grid was used throughout this work for numerical integration of density.²¹ Vibrational analysis confirmed all stationary points to be minima (no imaginary frequencies) or first-order saddle points (one imaginary frequency). Thermal corrections were computed from unscaled frequencies for a standard state of 298.15 K and 1 atm. Truhlar's quasiharmonic approximation correction was applied to all optimizations, which sets frequencies less than 100 cm⁻¹ to 100 cm⁻¹ for thermal corrections and entropies.²²

Results/Discussion

The computed structures of the global minimum, a conformer of bicyclic lactone **1**, and the crystal structure^{2a,23} **1-CS** are shown in Figure 3. The C₄ of the cyclopentene moiety is “up” in the global minimum and “down” in conformer **1-down**. The dihedral angle formed by C₁C₂C₃C₄ is constrained to 10° below the plane of the cyclopentene moiety. Figure 3 shows Newman projections of fully optimized **1** and a constrained **1-down** looking down the highlighted bond. **1-down** is not the global minimum, since it produces eclipsing along the green bond.

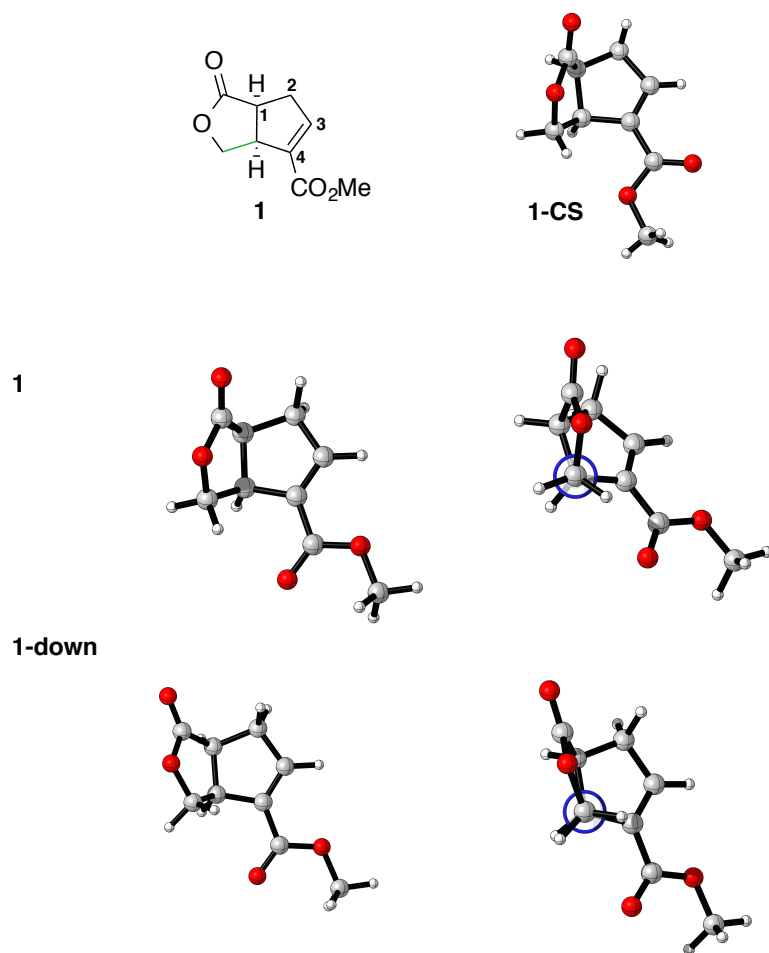


Figure 3. The geometries of **1** and **1-down** are shown on the left. Newman projections looking down the highlighted bond for **1** and **1-down** are shown on the right. Computed at the M06-2X/6-31+G(d,p) level of theory.

1-down is 3.5 kcal mol⁻¹ higher in energy than **1**, and collapses to **1** upon unconstrained optimization. The global minimum shows the sp² vinylic carbons attached to the ester are pyramidalized by 4° in the convex direction. The structure of **1** was determined by X-ray crystallography, and the alkene is indeed pyramidalized 4° in the convex direction.^{2a} The computed structure is nearly identical to that resolved by X-ray crystallography, but the crystal structure shows the ester and alkene in an *s-cis* configuration. We compute the *s-cis* configuration of **1** to be 0.3 kcal mol⁻¹ above the *s-trans* configuration.

The transition structures for addition of CH₂N₂ to the concave and convex faces of **1** were located (**TS1-conc** and **TS-conv**, respectively), and the transition structures involve nucleophilic attack of the diazomethane carbon terminus on the β-carbon of the α,β-unsaturated ester. The other regioisomeric transition structures were located, but are much higher in energy. Figure 4 shows the lowest energy transition structures and the computed activation free energies.

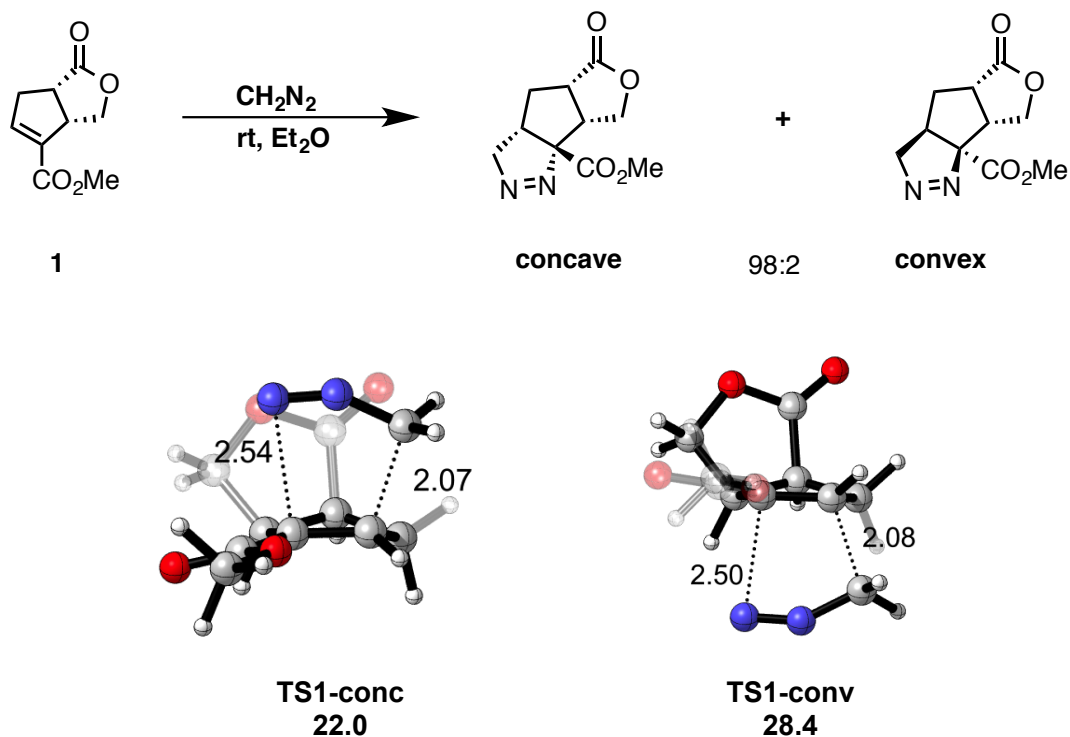


Figure 4. The optimized transition structures for concave and convex attack of CH_2N_2 on **1** are shown. Bond lengths are reported in Å. Computed at the M06-2X/6-311+G(d,p) IEF-PCM^{Et₂O}//M06-2X/6-31+G(d,p) level of theory. The activation free energies are reported in kcal mol⁻¹.

The transition structures reflect the polar nature of the ester on the double bond of **1**; they are concerted, but asynchronous. Both concave transition structures have shorter forming C-C bondlengths than C-N bondlengths (2.07 and 2.08 Å vs. 2.54 and 2.50 Å, respectively). **TS1-conc** is lower in free energy than **TS1-conv** by 6.4 kcal mol⁻¹. This is an overestimation of the concave : convex product ratio (98 : 2), but the calculations do reflect substantial concave stereoselectivity.

The distortion/interaction model was used to analyze the origins of stereoselectivity for this 1,3-dipolar cycloaddition. The activation energy (ΔE^\ddagger) is dissected into distortion energy (ΔE_d^\ddagger) and interaction energy (ΔE_i^\ddagger).²⁴ Distortion energy is the energy required to distort each of the reactants into their respective transition state geometries without interaction between the

distorted fragments. The interaction energy is the energy of interaction between the destabilized cycloaddends. It is often a net stabilizing quantity that results from charge transfer from occupied-vacant orbital interactions, electron transfer, polarization, and closed-shell (steric) repulsions.

The distortion energies of **TS1-conc** and **TS1-conv** are 24.6 and 26.1 kcal mol⁻¹, respectively. The interaction energies are -18.8 kcal mol⁻¹ and -13.4 kcal mol⁻¹, respectively. The $\Delta\Delta E_i^\ddagger$ is larger than the $\Delta\Delta E_d^\ddagger$, and mainly responsible for the stereoselectivity. We evaluated torsional effects in **TS1-conc** and **TS1-conv** using Newman projections, which are shown in Figure 5.

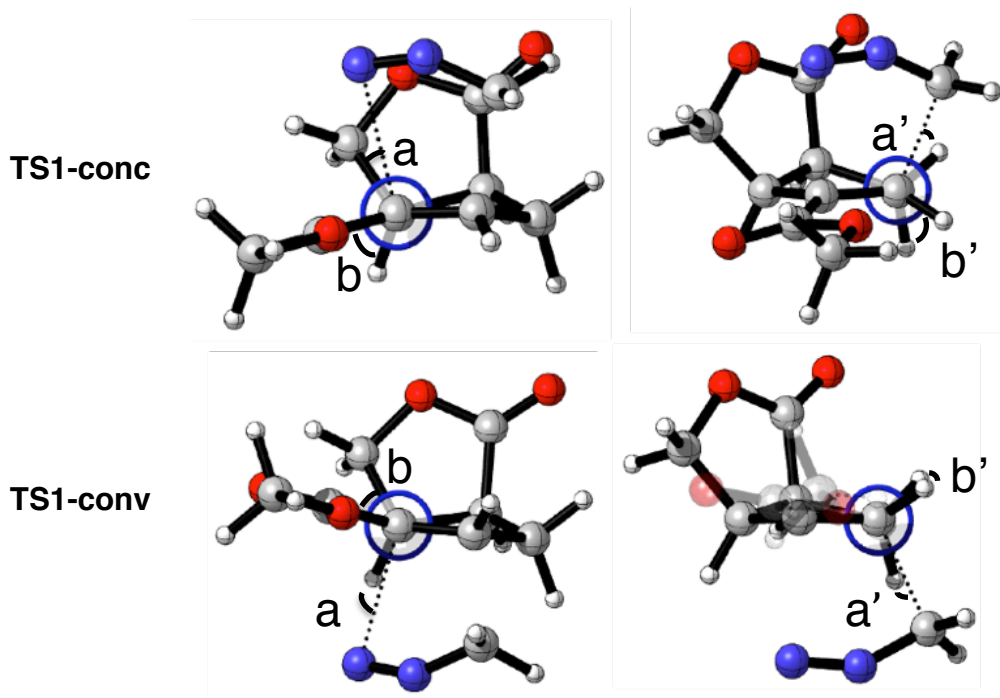
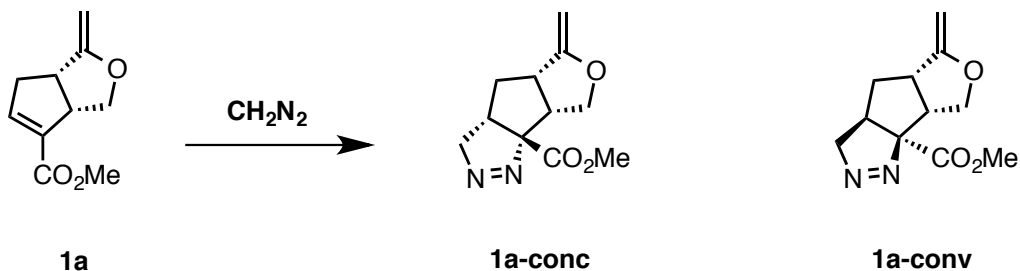


Figure 5. Newman projections looking down the alkene-allylic C-C bonds of **TS1-conc** are shown in the top row and those for **TS1-conv** are shown in the bottom row. Computed at the M06-2X/6-31+G(d,p) level of theory.

The Newman projections of **TS1-conc** show partially staggered newly forming C–N and C–C bonds (a and $a' = 20^\circ$ and 26° , respectively). The newly-forming C–N bonds are almost perfectly eclipsed in **TS1-conv** (a and $a' = 9^\circ$ and 10° , respectively). This torsional strain in **TS1-conv** manifests itself as reduced interaction energy because the eclipsing occurs between the two reacting cycloaddends (-18.8 vs. -13.4 kcal mol $^{-1}$, respectively). The vicinal ester-CC-CH $_2$ and HCCH bonds are staggered in **TS1-conc**, (b and $b' = 56^\circ$ and 48°), while these are nearly eclipsed in **TS1-conv** (b and $b' = 47^\circ$ and 15°). Since **1** must distort into a conformation with eclipsed vicinal C–H bonds to reach the convex transition structures, this torsional strain is reflected as increased distortion energy (24.6 and 26.1 kcal mol $^{-1}$).

Gais and coworkers proposed that electrostatic interaction between the nucleophilic carbon terminus of CH $_2$ N $_2$ and the electrophilic lactone carbon in **1** stabilizes **TS1-conc** and not **TS1-conv**.^{2a} We have evaluated this hypothesis by computing the reaction of **1a** with CH $_2$ N $_2$ (Scheme 2). **1a** differs from **1** only in that the carbonyl oxygen in **1** is replaced with a methylene group in **1a**. The global minima of **1** (red) and **1a** (blue) are overlaid in Figure 6 to compare their ground state structures.

Scheme 2. Theoretical reaction of **1a** with CH $_2$ N $_2$.



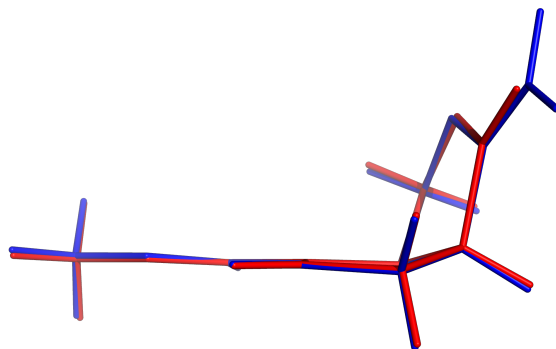


Figure 6. Overlaid geometries of reactants **1** (red) and **1a** (blue). Computed at the M06-2X/6-31+G(d,p) level of theory.

These structures are nearly identical and are in a fixed envelope conformation. The vinyl ester is pyramidalized in the convex direction by 4° in both **1** and **1a**. Figure 7 shows the transition states for attack of CH_2N_2 on the concave and convex faces of **1a**. The activation free energies are shown below each structure.

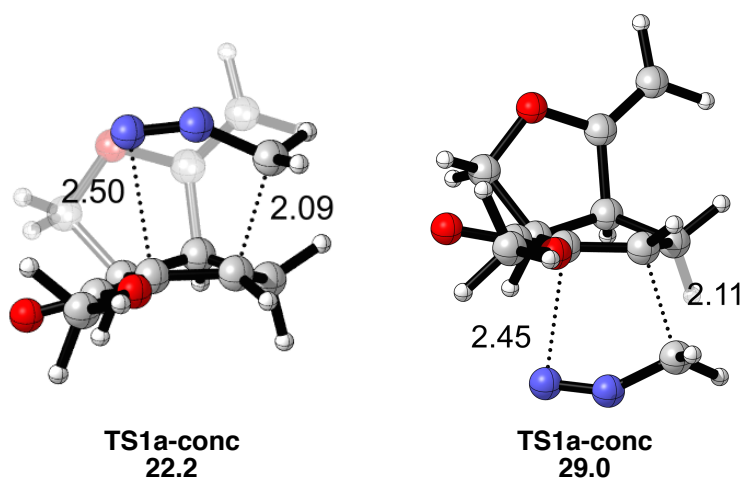


Figure 7. Transition structures for the 1,3-dipolar cycloaddition of CH_2N_2 and **1a**. Activation free energies are computed at the M06-2X/6-311+G(d,p) IEF-PCM^{Et₂O}//M06-2X/6-31+G(d,p) level of theory. Values are activation free energies are reported in kcal mol⁻¹. Bond lengths are given in Ångstroms.

Despite greatly reducing the electrophilicity of the lactone carbon (**1a**), the reaction is still predicted to be highly concave-stereoselective ($\Delta\Delta G^\ddagger = 6.7 \text{ kcal mol}^{-1}$). Our computations show that electrostatic stabilization of the concave transition structures is not responsible for concave stereoselectivity, but torsional effects do explain stereoselectivity. Gais and coworkers found that the reactions of CH_2N_2 with hemiacetal **1b** and acetal **1c** are non-stereoselective (Scheme 3).^{2a} We have computationally investigated the origins of the low selectivities of CH_2N_2 cycloadditions to **1b** and **1c**.

Scheme 3. The product ratios found for the reactions of **1b** and **1c** with CH_2N_2 .^{2a}

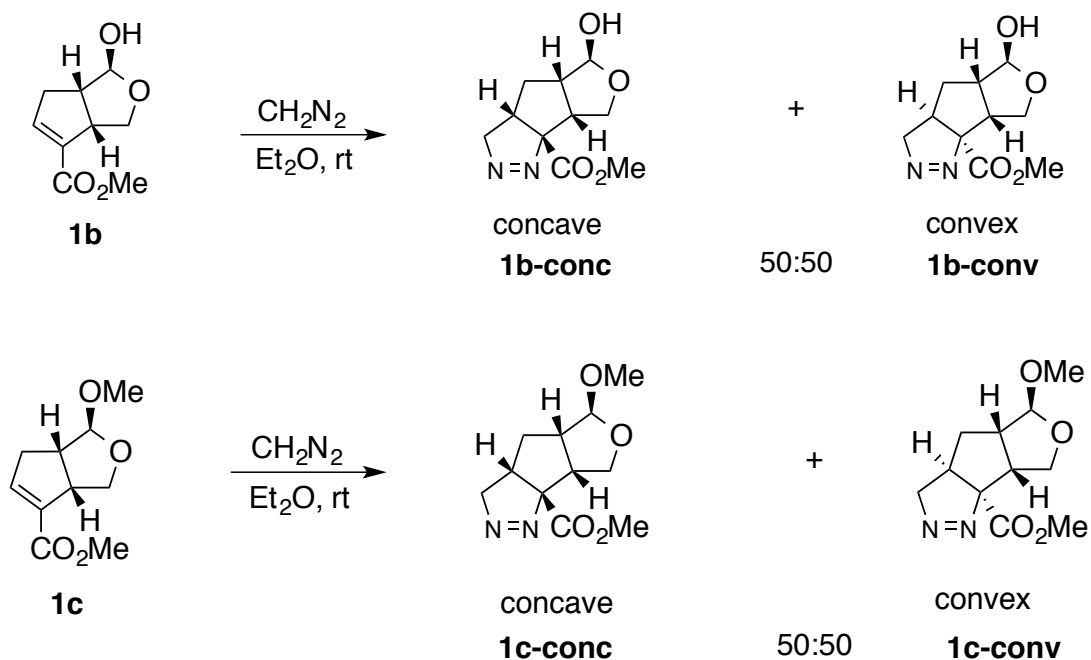


Figure 8 shows an overlay of the global minima of **1b** (orange) and **1c** (green) and another overlay compares the structures of **1c** (green) and **1** (red).

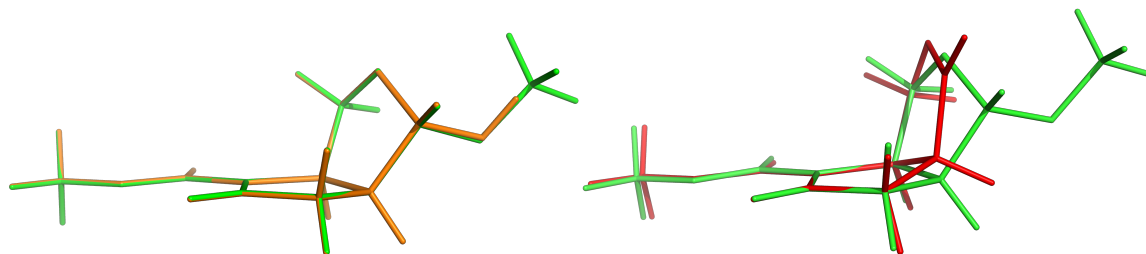
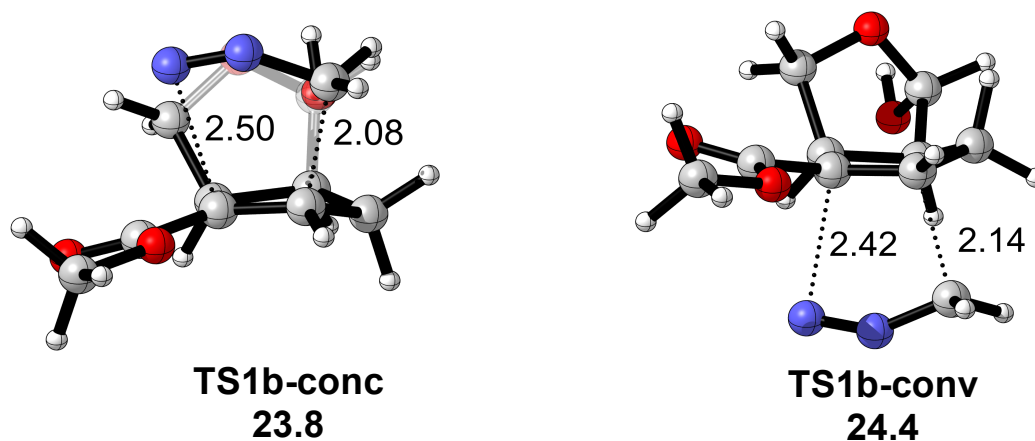


Figure 8. Overlay of **1b** (orange) and **1c** (green) are shown on the left side and overlay of **1** (red) and **1c** (green) is shown on the right side. Computed at the M06-2X/6-31+G(d,p) level of theory.

Figure 8 shows that **1b** and **1c** are nearly identical in structure and feature planar cyclopentene moieties. **1** prefers an envelope conformation, a predistortion that makes it resemble the concave addition. Figure 9 shows the transition structures for the 1,3-dipolar cycloadditions of CH_2N_2 with **1b** and **1c**. We also computed the transition structures for two other configurations of OH and OMe in **1b** and **1c**, respectively (coordinates and energies can be found in the supporting information). These structures are 1.7–3.1 kcal mol⁻¹ higher in energy than those shown in Figure 9.



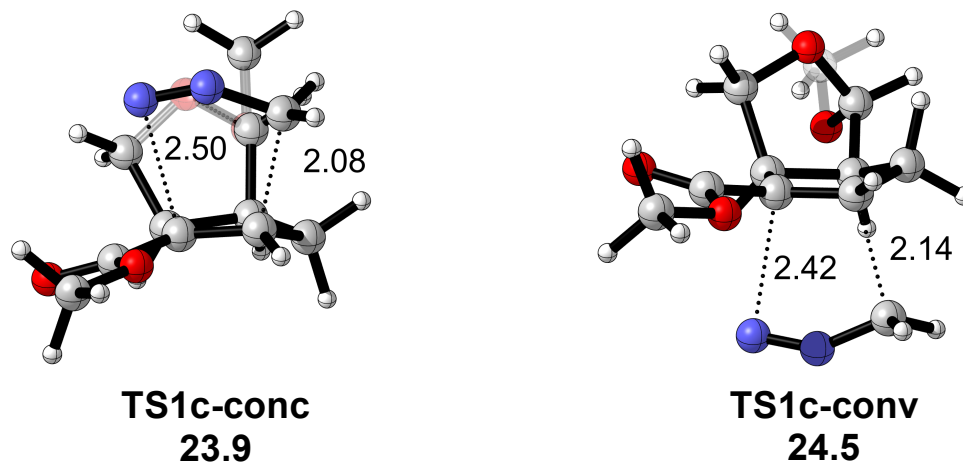


Figure 9. 1,3-Dipolar cycloaddition transition structures for the reactions of diazomethane with **1b** and **1c**. Bond lengths are reported in Ångstroms. Activation free energies computed at the M06-2X/6-311+G(d,p) IEF-PCM^{Et2O} //M06-2X/6-31+G(d,p) level of theory. Energies are reported in kcal mol⁻¹.

The computed activation free energies show a preference for cycloadditions to the concave face for **1b** and **1c** of only 0.6 kcal mol⁻¹ in both cases. Although these results suggest a slight preference for attack on the concave face of **1b** and **1c**, the $\Delta\Delta G^\ddagger$ are very small.

Methylenecyclopropane Acetal Cycloadditions

Cycloadditions of methylenecyclopropane acetals were first performed by Yamago and Nakamura in 1989.²⁵ Thermolysis causes a 2π disrotatory electrocyclic ring opening²⁶ of methylenecyclopropane acetals to generate the zwitterionic 1,3-dipole **4**. Previous computational studies showed that the most stable form of the dipole is the closed-shell singlet species.²⁷ Experimentally, the cycloadditions follow the “endo rule”, and a highly polar transition state has been proposed.²⁸ Scheme 4a shows the electrocyclic ring opening of **3** to form **4** and Scheme 4b

shows the subsequent stepwise addition of **4** to **1**. Gais and coworkers report that the concave:convex product ratio is 2:1.^{2a}

Scheme 4. a) Disrotatory electrocyclic ring opening reaction. b) Stepwise pathway involving zwitterionic intermediate **5**.

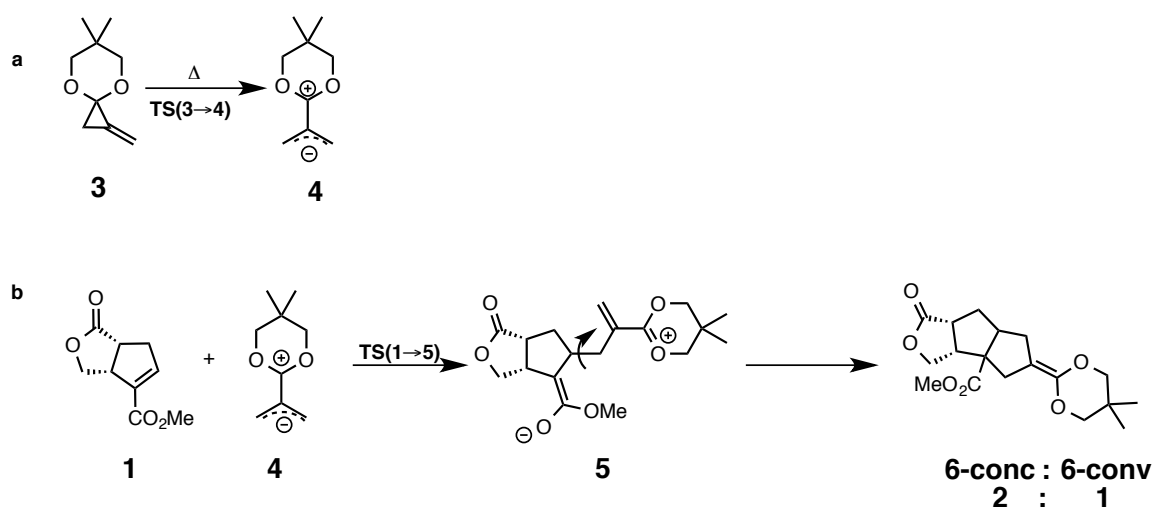


Figure 10 shows the free energy profile for the mechanism shown in Scheme 4. The energies are relative to separated reactants (**1** and **3**). The computed structures of relevant species from Scheme 4 are shown in Figures 1 and 12.

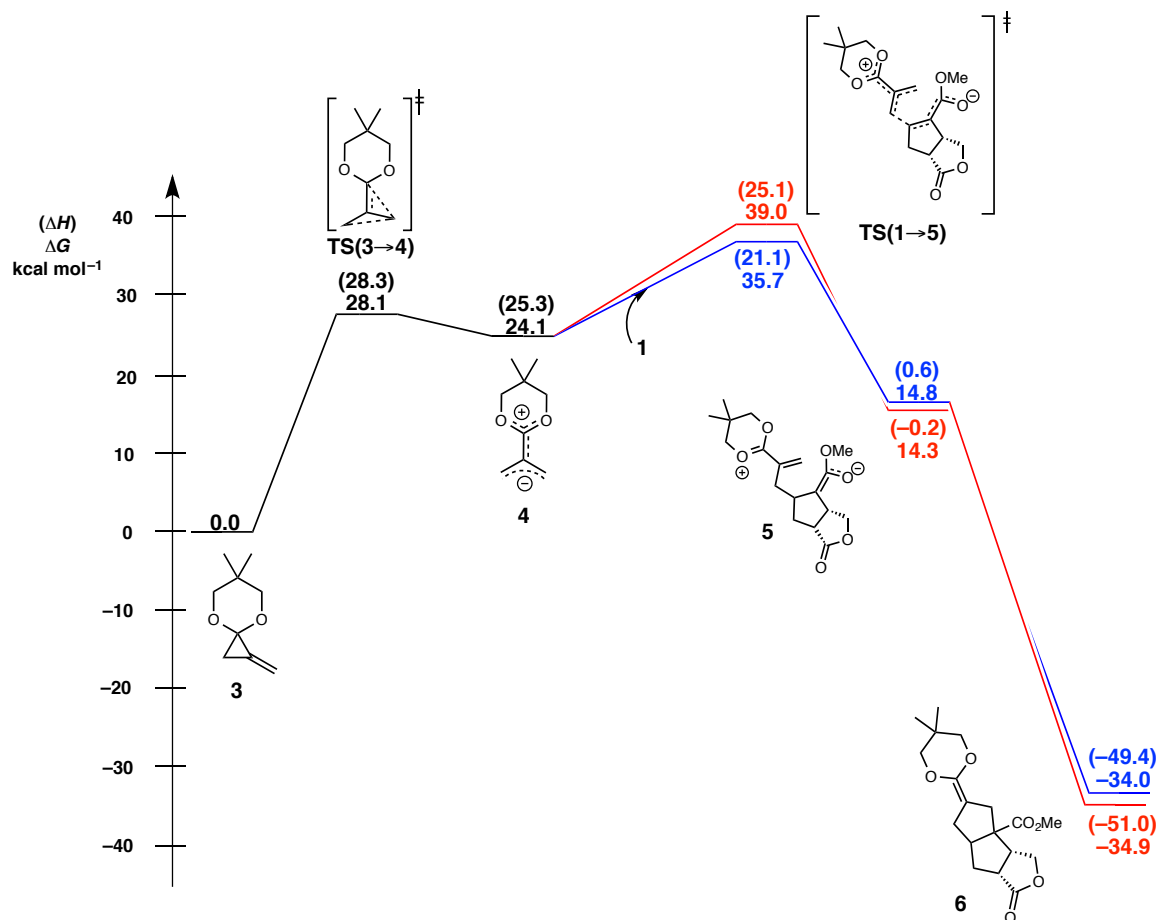


Figure 10. Computed free energy profile for the stepwise pathway of concave (blue) and convex (red) additions to **1**. The energies reported in black correspond to the ring opening of **3**. Free energies and enthalpies are reported in kcal mol⁻¹ and are relative to **1** and **3**. Computed at the M06-2X/6-311+G(d,p) IEF-PCM^{MeCN}//M06-2X/6-31+G(d,p) IEF-PCM^{MeCN} level of theory.

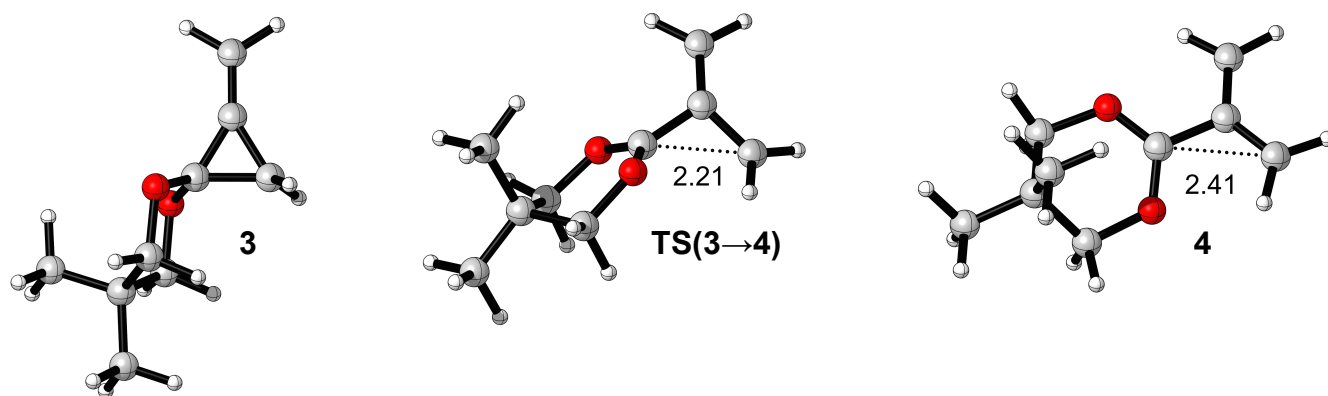


Figure 11. The geometries of methylenecyclopropane acetal **3**, ring opening transition state [TS(**3**→**4**)], and reactive intermediate **4**. Bond lengths are reported in Ångstroms. Computed at the M06-2X/6-31+G(d,p) IEF-PCM^{MeCN} level of theory.

The formation of reactive intermediate **4** is highly endergonic ($\Delta G = 24.1 \text{ kcal mol}^{-1}$). No transition states for a concerted cycloaddition of **4** and **1** at various levels were located. In line with this, a two dimensional relaxed scan of the potential energy surface suggested the concerted process was barrierless. This is because of the negative enthalpic barriers for TS(**1**→**5-conc**) and TS(**1**→**5-conv**), -4.2 and $-0.2 \text{ kcal mol}^{-1}$, respectively. Therefore, a variational transition state treatment is required to determine the $\Delta\Delta G^\ddagger$ for this reaction more accurately.

Transition structures corresponding to the stepwise addition of **4** to **1** [TS(**1**→**5-conc**) and TS(**1**→**5-conv**)] were located and are found to be only 11.6 and $14.9 \text{ kcal mol}^{-1}$ higher in free energy than **4** and **1**, respectively, and in fact lower in ΔH than separated reactants **4** and **1**. The stepwise addition to the concave face is preferred ($35.7 \text{ kcal mol}^{-1}$) to the convex face addition ($39.0 \text{ kcal mol}^{-1}$). The $\Delta\Delta G^\ddagger$ between TS(**1**→**5-conc**) and TS(**1**→**5-conv**) is $3.3 \text{ kcal mol}^{-1}$, a significant overestimation of $\Delta\Delta G^\ddagger$ that corresponds to the experimentally observed

concave: convex product ratio (2:1). These computed transition structures and the resulting zwitterionic intermediates (**5-conc** and **5-conv**) are shown in Figure 12.

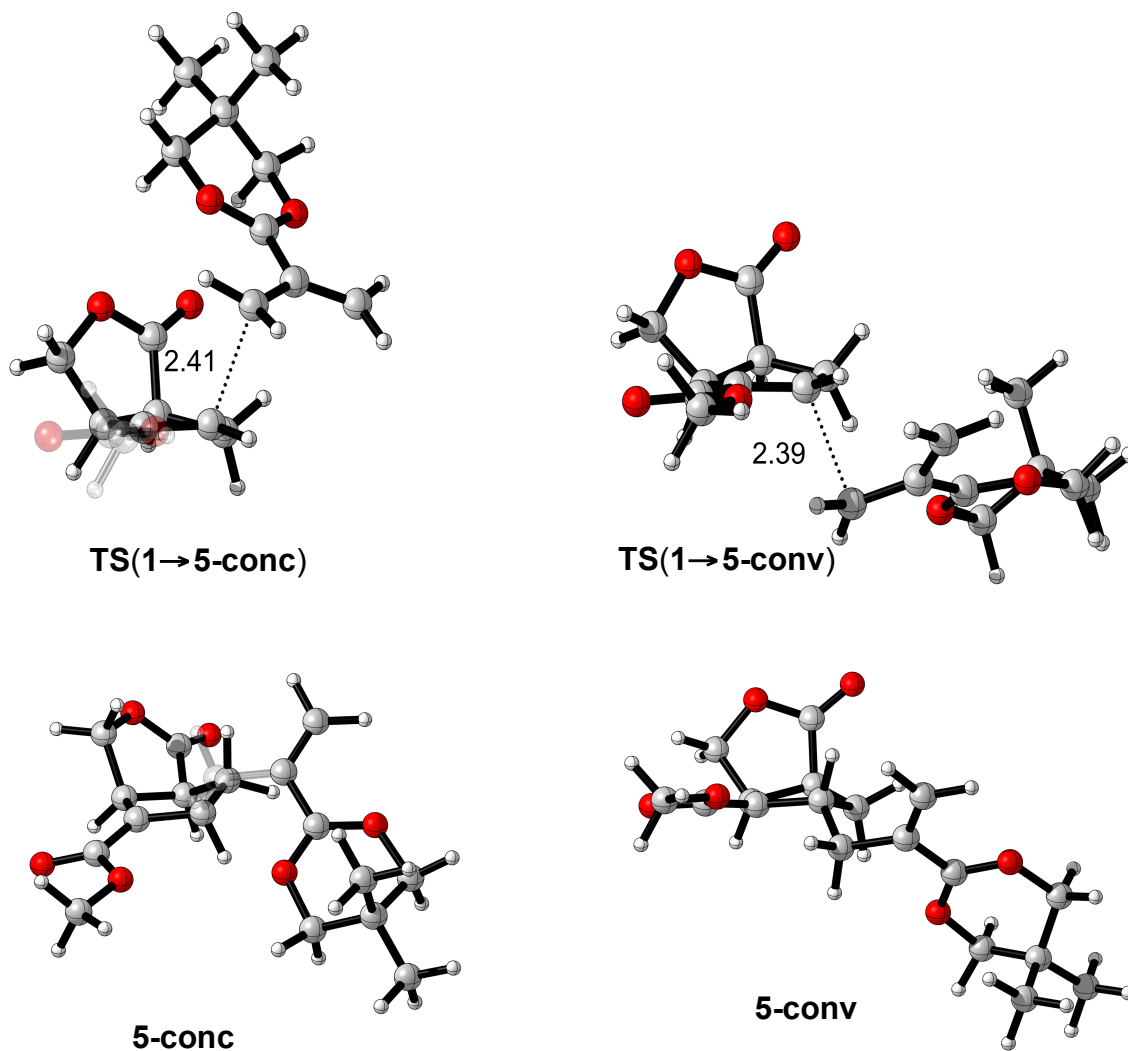


Figure 12. Stepwise transition structures for the addition of **4** and **1** and corresponding zwitterionic intermediates. The bond lengths are reported in Ångstroms. Computed at the M06-2X/6-31+G(d,p) IEF-PCM^{MeCN} level of theory.

TS(1→5-conc) and **TS(1→5-conv)** have newly forming C-C bond lengths of 2.41 and 2.39 Å, respectively. We evaluated torsional effects in **TS(1→5-conc)** and **TS(1→5-conv)** using Newman projections looking along the C₂-C₃ bond of the cyclopentene moiety (Figure 13).

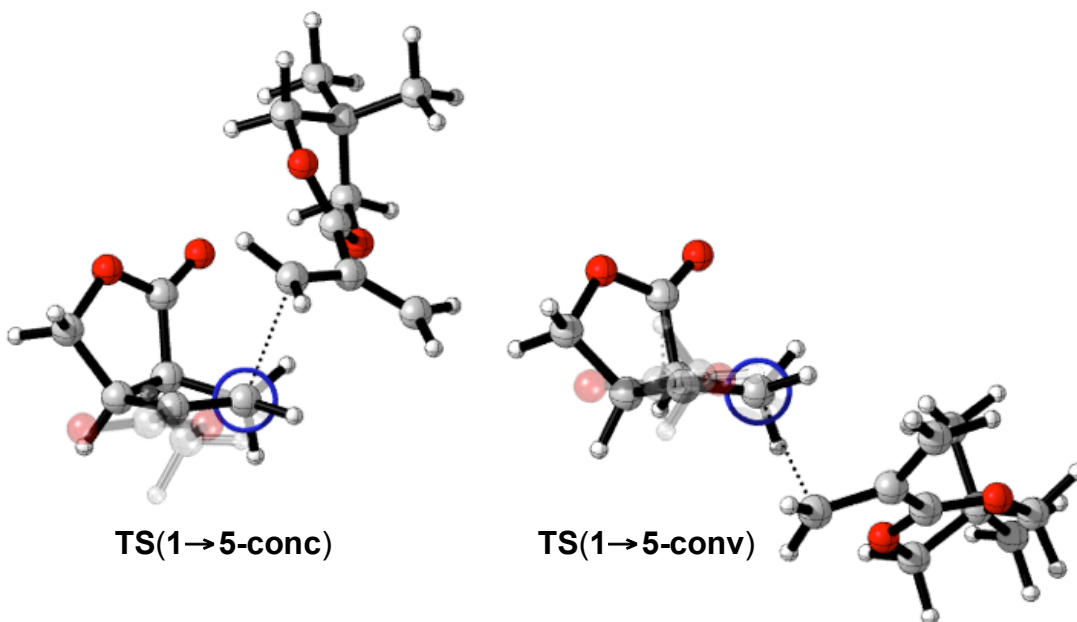


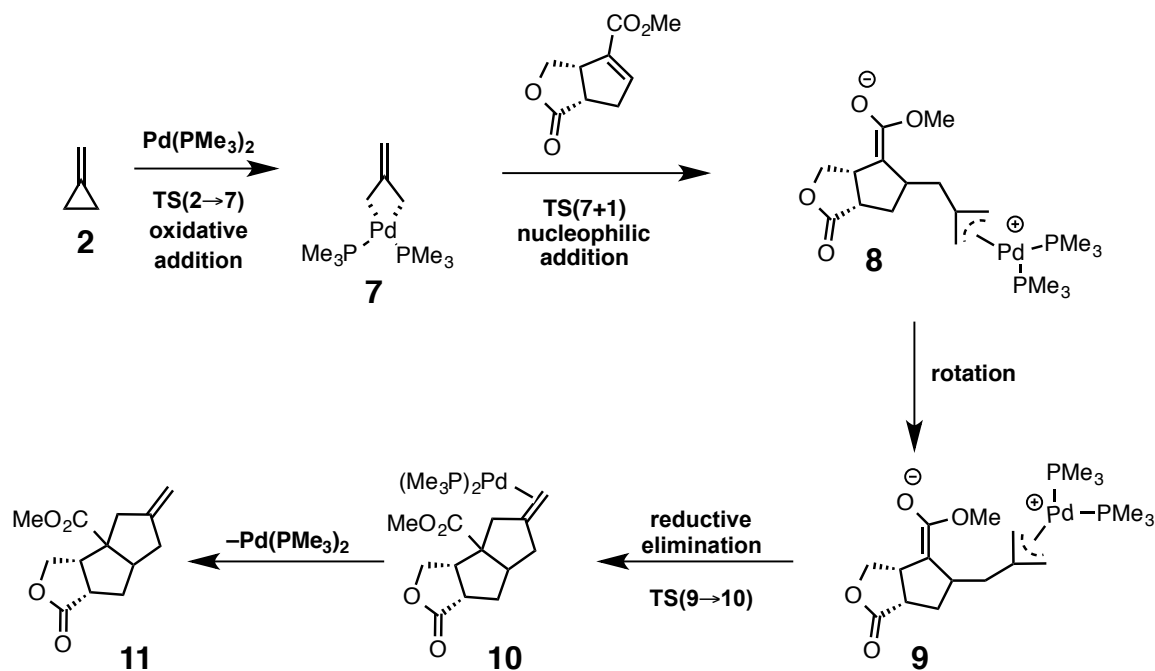
Figure 13. Newman projections of **TS(1→5-conc)** and **TS(1→5conv)**. Calculated at the M06-2X/6-31+G(d,p) level of theory. The methyl ester is hidden for clarity.

Figure 13 shows staggering of HCCH bonds (vinyl H-methylene H) in **TS(1→5-conc)** and eclipsing of the same bonds in **TS(1→5-conv)**. Despite the increased size and mechanistic complexity of this reaction as compared to the CH₂N₂ cycloaddition, torsional effects are responsible for concave stereoselectivity.

Pd-Catalyzed (3+2) Cycloaddition

Pd-catalyzed (3+2) reactions involving methylenecyclopropane **2** affords synthetically useful fused cyclopentanes²⁹ The cycloadditions of methylenecyclopropanes with electron deficient alkenes have been shown to be catalyzed by Pd and Ni.^{4,30} Previous computational mechanistic studies of intramolecular Pd-catalyzed (3+2) cycloadditions were done by Cárdenas *et al.* and include an alternate mechanism involving a σ -allyl palladium complex.³¹ Those results guided our computations that lead to the most favorable mechanism (Scheme 5). Our computational results utilize PMe_3 instead of the experimental ligand, $\text{P}(i\text{Pr})_3$; this approximation does not change the conclusions of this study. A mechanism involving coordination to the enolate oxygen of **9** was found to be higher in energy and was discarded. The geometries and energies of relevant stationary points for the alternate mechanism are given in the supporting information.

Scheme 5. Mechanism of Pd-catalyzed (3+2) cycloaddition computed here.



Gais and coworkers generated the catalyst by treating $[\text{Pd}(\text{Cp})(\text{allyl})]$ with $\text{P}(i\text{Pr}_3)$ at $-78\text{ }^\circ\text{C}$.^{2a} Fujimoto reported that Pd(0) preferentially oxidatively inserts into the distal σ bond of methylenecyclopropane to form TMM-PdL₂ complex **7**.³² Figure 14 shows the free energy profile for the mechanism shown in Scheme 5. The reported energies correspond to stationary points resulting from concave additions. The $\Delta\Delta G^\ddagger$ between the concave and convex nucleophilic addition transition states will be discussed to continue our investigations of stereoselectivity.

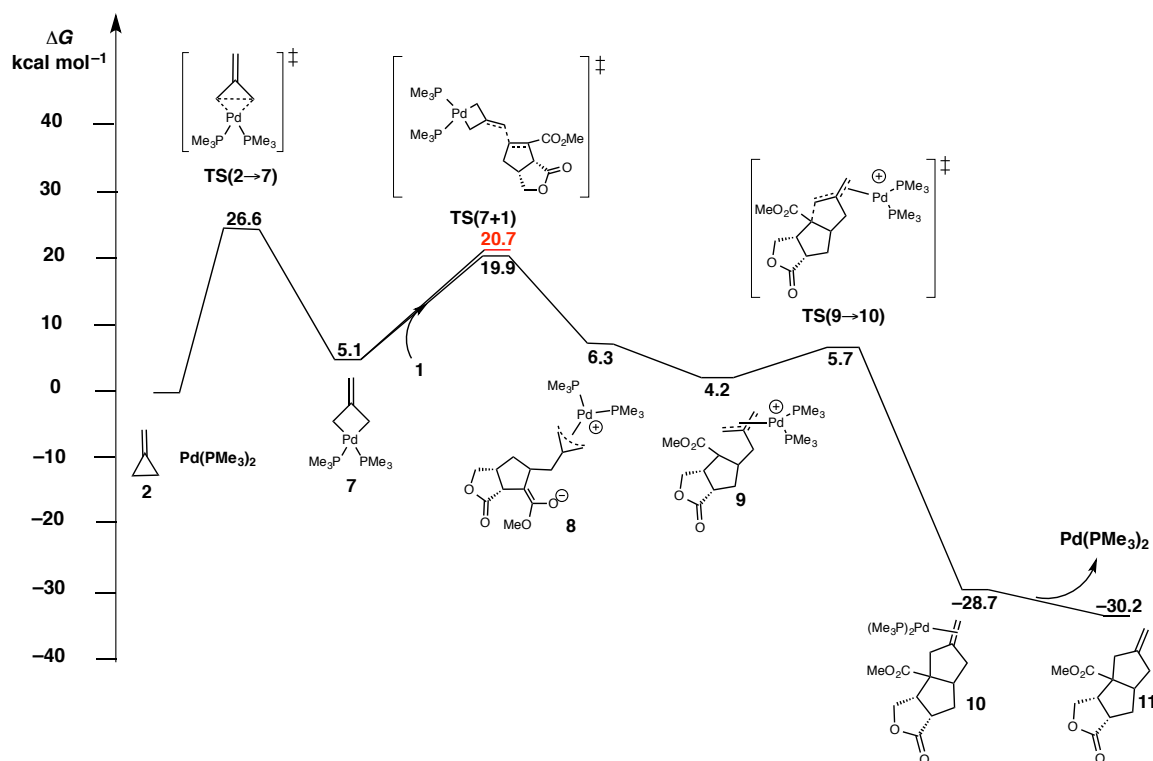


Figure 14. Free energy profile for the mechanism for the Pd-catalyzed (3+2) cycloaddition of **1** with **2** and Pd(PMe₃)₂. Values are reported in kcal mol⁻¹ and are relative to separated **1**, **2**, and Pd(PMe₃)₂. All energies are computed at the M06/LANL2DZ-/6-311+G(d,p) IEF-PCM^{toluene}//M06/LANL2DZ-6-31+G(d,p) level of theory.

The oxidative addition step is rate-determining ($\Delta G^\ddagger = 28.9$ kcal mol⁻¹) and the four-membered palladacycle **7** is formed endergonically ($\Delta G = 5.1$ kcal mol⁻¹). Then **7** adds nucleophilically to the concave or convex face of **1**, [TS(7+1)-*conc* and TS(7+1)-*conv*, respectively]. TS(7+1)-*conc* is lower in energy than TS(7+1)-*conv* by 0.8 kcal mol⁻¹. This $\Delta\Delta G^\ddagger$ is a slight underestimation of the concave : convex product (7:1) ratio observed by Gais and coworkers.^{2a} The large exergonicity of the overall reaction indicates that product formation is irreversible and the selectivity is under kinetic control. The stationary points leading up to and including the stereo-determining step are shown in Figure 13. The free energies are relative to **1**, **2**, and Pd(PMe₃)₂ and are shown below each structure.

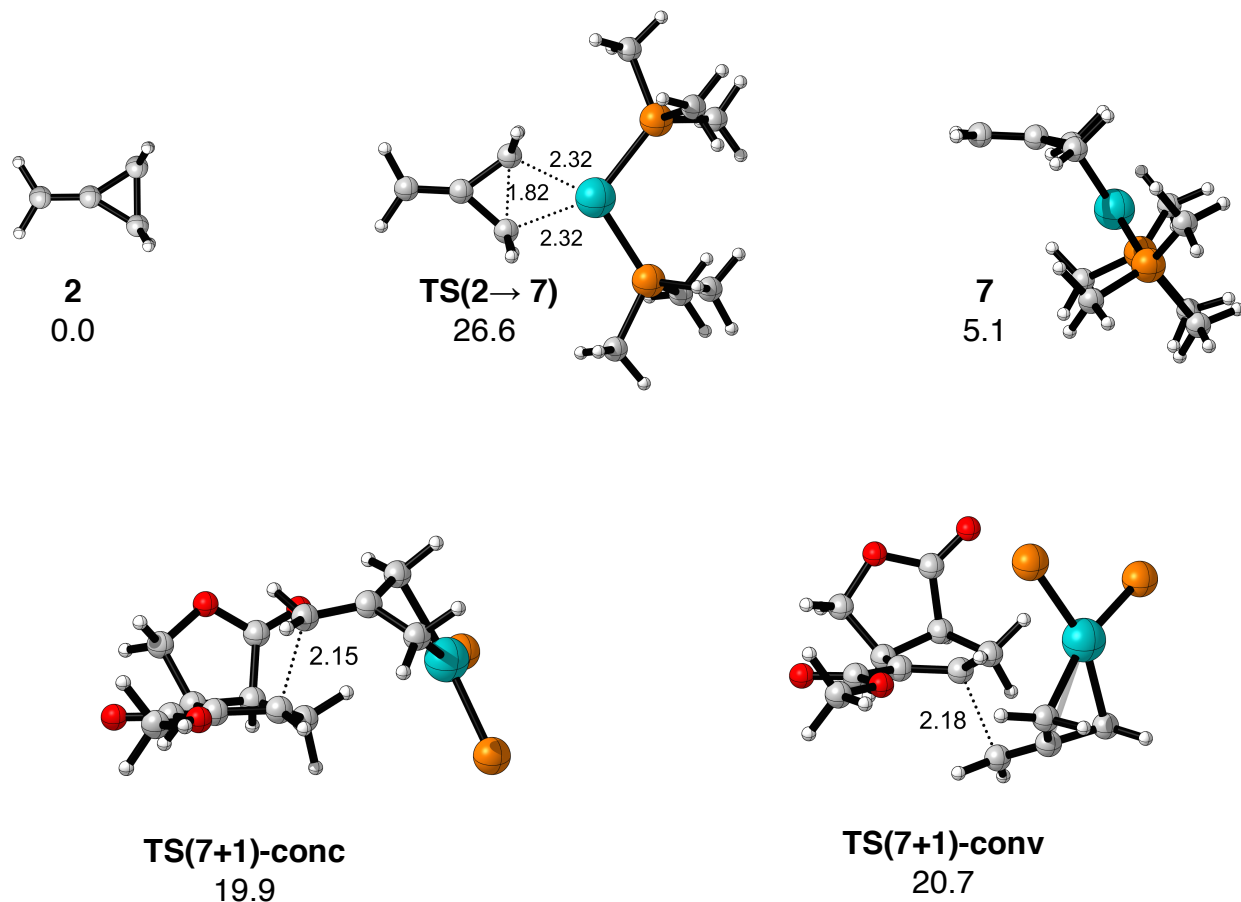


Figure 15. Computed geometries for the oxidative and nucleophilic addition steps. Computed at the M06/LANL2DZ-6-31+G(d,p) level of theory. Bond lengths are reported in Ångstroms. Values are free energies and are reported in kcal mol⁻¹. -Me₃ groups are hidden for clarity.

We utilized Newman projections to evaluate torsional effects in **TS(7+1)-conc** and **TS(7+1)-conv** to probe the origins of the concave stereoselectivity for this reaction. Figure 16 shows the Newman projections looking down the C₂-C₃ bond of **1** in **TS(7+1)-conc** and **TS(7+1)-conv**.

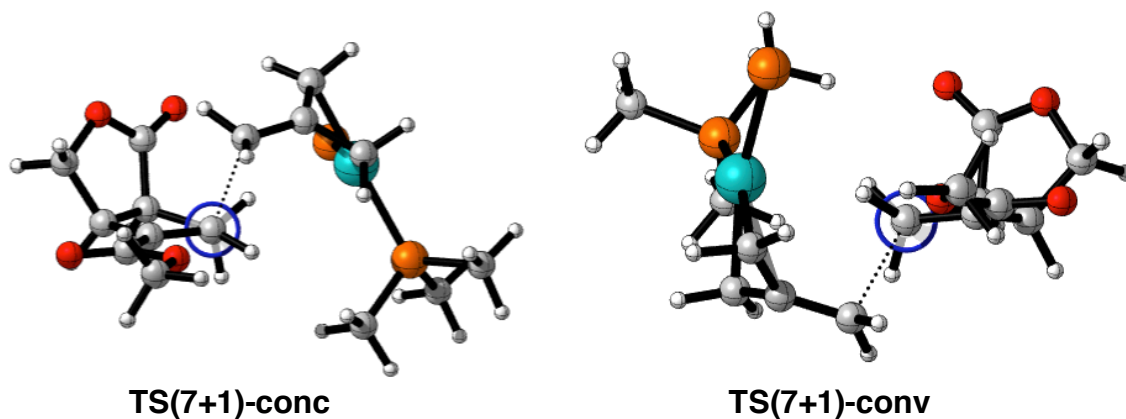


Figure 16. Newman projections of **TS(7+1)-conc** and **TS(7+1)-conv**. Calculated at the M06/LANL2DZ-6-31+G(d,p) level of theory. One of the PMe_3 groups is hidden for clarity in each structure.

The Newman projection for **TS(7+1)-conc** shows both allylic **C-H bonds** and newly forming C-C bonds are almost perfectly staggered. Conversely, **TS(7+1)-conv** shows some eclipsing of both allylic **C-H bonds** and newly forming C-C bonds. The torsional strain is visible in the Newman projection of **TS(7+1)-conv** indicates that the concave stereoselectivity arises from torsional effects in the transition state.

Conclusion

We have determined the origins of concave stereoselectivity for cycloadditions to an oxabicyclo[3.3.0]octenone. The torsional effects are different on the two faces when the alkene is in a rigid envelope conformation.^{8a} The π bond of **1** is pyramidalized 4° in the convex direction, which causes alkene predistortion. Less distortion energy is required to reach the geometry of the concave-attack transition structures, a result of favorable torsional effects. The convex transition structures are disfavored because the alkene must undergo additional distortion to overcome predistortion and achieve the geometries of convex-attack transition structures. In addition, qualitative inspection of the convex transition structures shows that torsional strain that manifests itself as both decreased interaction energy and increased distortion energies in these transition structures. This effect is general to the three types of reactions studied experimentally by Gais *et al.*, and here through quantum mechanical calculations.

Acknowledgements

K. N. Houk and H-J. Gais were the project directors. M. Pourati performed calculations on the diazomethane–**1** cycloaddition reactions. Steven Alexander Lopez performed the rest of the calculations, oversaw the work of M. Pourati and wrote the manuscript. We thank the National Science Foundation (NSF CHE- 1059084) for financial support of this research. The computations were performed on the UCLA IDRE Hoffman2 cluster.

References

-
- ¹ (a) Lambeir, A. M.; Loiseau, A. M.; Kuntz, D. A.; Vellieux, F. M.; Michels, F. M. Opperdoes, F. R. *Eur. J. Biochem.* **1991**, *198*, 429. (b) Braxenthaler, M.; Pötsch, B.; Fröhlich, K. U.; Dieter, M. *FEMS Microbiol. Lett.* **1991**, *83*, 311. (c) Willson, M.; Lauth, N.; Perie, J.; Callens, M.; Opperdoes, F. R. *Biochem.* **1994**, *33*, 214. (d) Cane, D. E.; Sohng, J.-K. *Biochem.* **1994**, *33*, 6524. (e) Lesburg, C. A.; Lloyd, M. D.; Cane, D. E.; Christianson, D. W. *Protein Sci.* **1995**, *4*, 2436. (f) Fröhlich, K.-U.; Kannwischer, R.; Rüdiger, M.; Mecke, D. *Arch. Microbiol.* **1996**, *165*, 179. (g) Spanevello, R. A.; Pellegrinet, S. C. *Cur. Top. Phytochem.* **2000**, *3*, 225. (h) Testero, S. A.; Spanvello, R. A. *Org. Lett.* **2006**, *8*, 3793. (i) Zhu, D.; Seo, M. J.; Ikeda, H.; Cane, D. E. *J. Am. Chem. Soc.* **2011**, *133*, 2128. (j) Liu, Q.; Yue, G.; Wu, N.; Lin, G.; Li, Y.; Quan, J.; Li, C.-C.; Wang, G.; Yang, Z. *Angew. Chem.* **2012**, *124*, 12238; *Angew. Chem. Int. Ed.* **2012**, *51*, 12072.
- ² (a) Rosenstock, B.; Gais, H.-J.; Herrmann, E.; Raabe, G.; Binger, P.; Freund, A.; Wedemann, P.; Krüger, C.; Linder, H. J. *Eur. J. Org. Chem.* **1998**, 257. (b) Herrmann, E.; Gais, H.-J.; Rosenstock, B.; Raabe, G.; Lindner, H. J. *Eur. J. Org. Chem.* **1998**, 275.
- ³ (a) Trost, B. M. *Pure Appl. Chem.* **1988**, *60*, 1615. (b) Trost, B. M. *Angew. Chem.* **1986**, *98*, 1. (c) Trost, B. M. *Angew. Chem., Int. Ed. Engl.* **1986**, *25*, 1. (d) Trost, B. M.; Lam, T. M.; Herbage, M. A. *J. Am. Chem. Soc.* **2013**, *135*, 2459
- ⁴ Binger, P.; Bücg, H. M.; *Topp. Curr. Chem.* **1987**, *135*, 77.
- ⁵ Cherest, M.; Felkin, H. *Tetrahedron Lett.* **1968**, *9*, 2205.
- ⁶ (a) Houk, K. N.; Paddon-Row, M. N.; Rondan, N. G.; Wu, Y.-D.; Brown, F. K.; Spellmeyer, D. C.; Metz, J. T.; Li, Y.; Loncharich, R. J. *Science* **1986**, *231*, 1108. (b) Mukherjee, D.; Wu, Y.-D.;

Fronczek, F. R.; Houk, K. N. *J. Am. Chem. Soc.* **1988**, *110*, 3328.; (c) Ando, K.; Houk, K. N.; Busch, J.; Menasse, A.; Sequin, U. *J. Org. Chem.* **1998**, *63*, 1761.

⁷ (a) Wu, Y.-D.; Houk, K. N. *J. Am. Chem. Soc.* **1987**, *109*, 908. (b) Ando, K.; Condroski, K. R. Houk, K. N.; Wu, Y.-D.; Lu, S. K. Overman, L. E. *J. Org. Chem.* **1998**, *63*, 3196. (c) Im, G-Y. J.; Bronner, S. M.; Goetz, A. E.; Paton, R. S.; Cheong, P. H.-Y.; Houk, K. N.; Garg, N. K. *J. Am. Chem. Soc.* **2010**, *132*, 17933. (d) Wu, Y.-D.; Houk, K. N.; Paddon-Row, M. N. *Angew. Chem. Int. Ed. Engl.* **1992**, *31*, 1019.

⁸ (a) Wang, H.; Houk, K. N. *Chem. Sci.* **2014**, *5*, 462. (b) Kaori, A.; Green, N. S.; Li, Y.; Houk, K. N. *J. Am. Chem. Soc.* **1999**, *121*, 5334. (c) Lucero, M. J.; Houk, K. N. *J. Org. Chem.* **1998**, *63*, 6973.

⁹ (a) Paddon-Row, M. N. Spellmeyer, D.C. Houk, K. N. *J. Org. Chem.* **1986**, *51*, 2874. (b) Liu, J.; Houk, K. N. *J. Org. Chem.* **1998**, *63*, 8565. (c) Damm, W.; Giese, B.; Hartung, J.; Hasskerl, T.; Houk, K. N. Hueter, O.; Zipse, H. *J. Am. Chem. Soc.* **1992**, *114*, 4067.

¹⁰ (a) Iafe, R. G.; Houk, K. N. *Org. Lett.* **2006**, *8*, 3469. (b) Lopez, S. A.; Houk, K. N. *J. Org. Chem.* **2013**, *78*, 1778.

¹¹ Huisgen, R.; Ooms, P. H. J.; Mingin, M.; Allinger, N. L. *J. Am. Chem. Soc.* **1980**, *102*, 3951.

¹² Rondan, N. G.; Paddon-Row, M. N.; Caramella, P.; Mareda, J.; Mueller, P. H.; Houk, K. N. *J. Am. Chem. Soc.* **1982**, *104*, 4974.

¹³ Cheong H-Y, P.; Yun, H.; Danishefsky, S. J.; Houk, K. N. *Org. Lett.* **2006**, *8*, 1513.

¹⁴ Wang, H.; Kohler, P.; Overman, L. E.; Houk, K. N. *J. Am. Chem. Soc.* **2012**, *134*, 16054.

¹⁵ Frisch, M. J.; et al. *Gaussian 09*, revision C-01; Gaussian Inc.; Wallingford, CT, 2009. (see complete reference in the Supporting Information).

¹⁶ Zhao, Y.; Truhlar, D. G. *Theor. Chem. Acc.* **2008**, *120*, 215.

-
- ¹⁷ Hay, P. J.; Wadt, W. R. *J. Chem. Phys.* **1985**, *82*, 299.
- ¹⁸ Cancès, E.; Mennucci, B.; Tomasi, J. *J. Chem. Phys.* **1997**, *107*, 3032.
- ¹⁹ Zhao, Y.; Truhlar, D. G. *Theor. Chem. Acc.* **2008**, *120*, 215.
- ²⁰ Ribero, R. F.; Marenich, A. V.; Cramer, C. J.; Truhlar, D. G. *J. Phys. Chem. B* **2011**, *115*, 14556.
- ²¹ Wheeler, S. E.; Houk, K. N. *J. Chem. Theory Comput.* **2010**, *6*, 395.
- ²² (a) Zhao, Y.; Truhlar, D. G. *Phys. Chem. Chem. Phys.* **2008**, *10*, 2813. (b) Ribeiro, R. F.; Marenich, A. V.; Cramer, C. J.; Truhlar, D. G. *J. Phys. Chem. B* **2011**, *115*, 14556.
- ²³ Cambridge Crystallographic Data Centre as supplementary publication no. 100846. Copies of the data can be obtained free of charge on application to The Director, CCDC, 12 Union Road, Cambridge CB2 1EZ, UK [fax: (internat.) +44 (0)1223 336033, e-mail: deposit@chemcrys.cam.ac.uk].
- ²⁴ Ess, D. H.; Houk, K. N. *J. Am. Chem. Soc.* **2007**, *129*, 10646.
- ²⁵ Yamago, S.; Nakamura, E. *J. Am. Chem. Soc.* **1989**, *111*, 7285.
- ²⁶ Woodward, R. B.; Hoffmann, R. *J. Am. Chem. Soc.* **1965**, *87*, 395.
- ²⁷ Carpenter, B. K.; Little, R. D.; Berson, J. A. *J. Am. Chem. Soc.* **1976**, *98*, 5723 b) Platz, M. S.; McBride, J. M.; Little, R. D.; Harrison, J. J.; Shaw, A.; Potter, S. E.; Berson, J. A. *J. Am. Chem. Soc.* **1976**, *98*, 5725. c) Siemionki, R.; Shaw, A.; O'Connell, G.; Little, R. D.; Carpenter, B. K.; Shen, L.; Berson, J. A. *Tetrahedron Lett.* **1978**, 3529. d) Nakamura, E.; Yamago S.; Ejiri, S.; Dorigo, A. E.; Morokuma, K. *J. Am. Chem. Soc.* **1991**, *113*, 3183. e) Nakamura, E.; Yamago, S. *Acc. Chem. Res.* **2002**, *35*, 867.
- ²⁸ Ejiri, S.; Yamago, S.; Nakamura, E.; *J. Am. Chem. Soc.* **1992**, *114*, 8707.

²⁹ ^aLautens, M.; Klute, W.; Tam, W. *Chem. Rev.* **1996**, *96*, 49. ^bPaquette, L. A. *Top. Curr. Chem.* **1984**, *119*, 1.

³⁰ Brandi, A.; Cacchi, S.; Cordero, F. M.; Goti, A. *Chem. Rev.* **2003**, *103*, 1213.

³¹ Garcia-Fandiño, R.; Gulias, M.; Mascareñas, J. L.; Cardenas, D. J. *Dalton Trans.* **2012**, *41*, 9468.

³² Suzuki, T.; Fujimoto, H. *Inorg. Chem.* **2000**, *39*, 1113.

Chapter 3

Control and Design of Mutual Orthogonality in Bioorthogonal Cycloadditions^a

Abstract: The azide–dibenzocyclooctyne and *trans*-cyclooctene–tetrazine cycloadditions are both bioorthogonal and mutually orthogonal: *trans*-cyclooctene derivatives greatly prefer to react with tetrazines rather than azides, while dibenzocyclooctyne derivatives react with azides but not with tetrazines under physiological conditions. DFT calculations used to identify the origins of this extraordinary selectivity are reported, and design principles to guide discovery of new orthogonal cycloadditions are proposed. Two new bioorthogonal reagents, methylcyclopropene and 3,3,6,6-tetramethylthiacycloheptyne, are predicted to be mutually orthogonal in azide and tetrazine cycloadditions.

^a Reprinted with permission from *Journal of the American Chemical Society* **2012**, *134*, 17904–17907. Copyright 2014 American Chemical Society. Authors are Yong Liang, Joel L. Mackey, Steven Alexander Lopez, and K. N. Houk

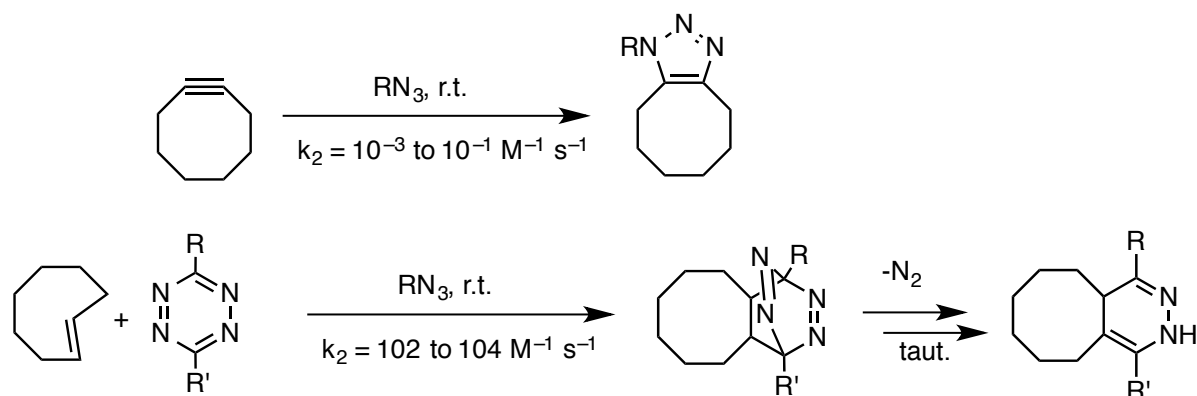
Introduction

Azide and tetrazine cycloadditions have become central reactions in the rapidly developing field of cellular component labeling with bioorthogonal reactions.¹ Bertozzi and co-workers have developed strain-promoted (3+2) cycloaddition reactions between azides and cyclooctynes since 2004 (Scheme 1a).² This reaction proceeds at a rate that is sufficiently high for *in vivo* labeling without the toxic copper(I) catalysts traditionally employed in “click chemistry” involving azide cycloadditions. Several groups have developed structurally varied cyclooctyne derivatives with different chemical reactivities and physical properties.³ Another breakthrough in this area came in 2008 with applications of the inverse electron-demand Diels-Alder reactions of 1,2,4,5-tetrazines and strained alkenes (Scheme 1b).⁴ In particular, the *trans*-cyclooctene-tetrazine (4+2) cycloaddition occurs with an extremely high bimolecular rate constant ($k_2 = 10^2 - 10^4 \text{ M}^{-1} \text{ s}^{-1}$),⁵ much faster than the azide-cyclooctyne (3+2) cycloaddition ($k_2 = 10^{-3} - 1 \text{ M}^{-1} \text{ s}^{-1}$).^{1c} Recently, Hilderbrand and co-workers demonstrated that two bioorthogonal cycloaddition pairs are mutually orthogonal.⁶ As shown in Scheme 2a, *trans*-cyclooctene derivatives greatly prefer to react with tetrazines rather than azides, while dibenzocyclooctyne derivatives react with azides, but not with tetrazines under physiological conditions (Scheme 2b). Based on this discovery, Hilderbrand et al. successfully realized the simultaneous labeling and imaging of two different cancer cell types in biological environments.⁸ At almost the same time, Schultz, Lemke, and co-workers found that *trans*-cyclooctenes show extremely high selectivity toward tetrazines rather than azides in protein labeling experiments.⁷

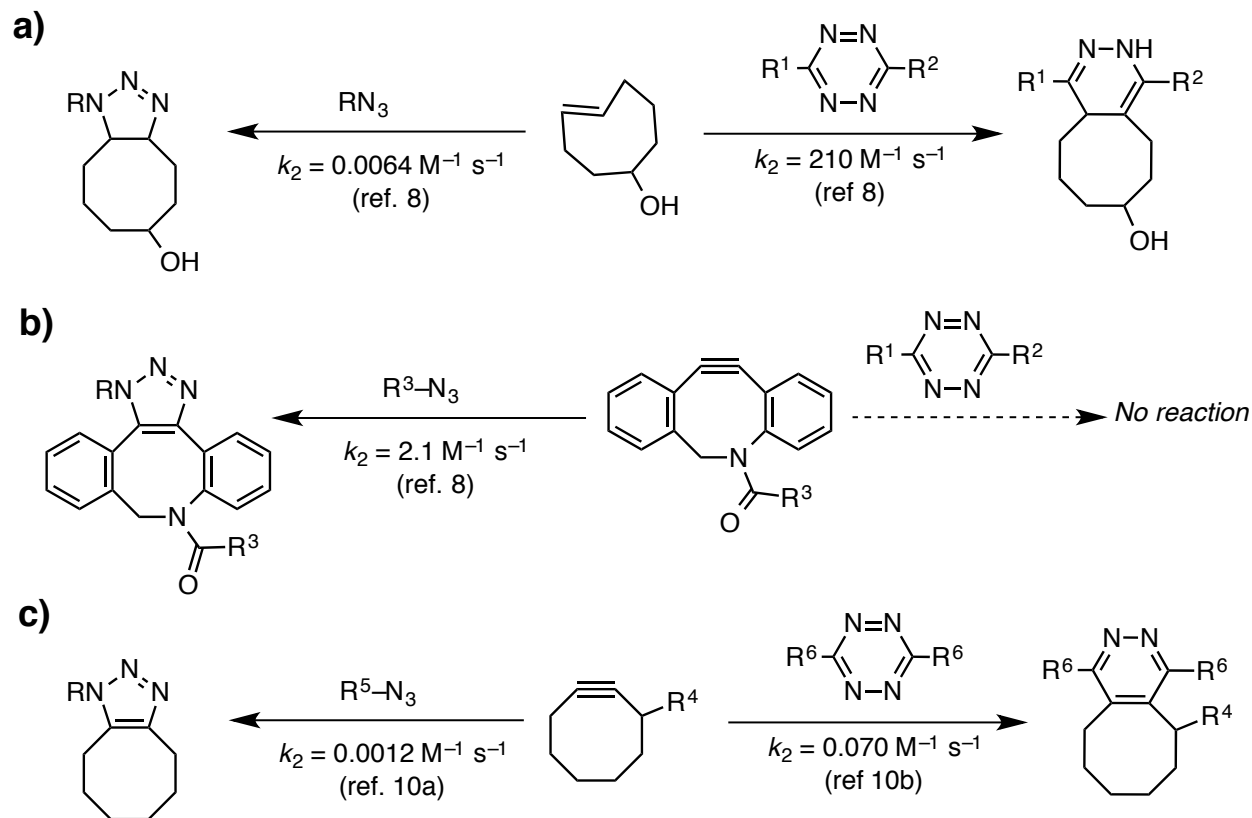
Computational Methodology

All computations were carried out with the Gaussian 09⁸ series of programs. The stationary points were located using M06-2X⁹/6-311+G(d,p), and frequency calculations on these stationary points provide activation enthalpies and free energies. Vibrational analysis confirmed all stationary points to be first-order saddle points or minima with no imaginary frequencies. Solvation corrections (IEFPCM^{H20}) were computed on gas-phase geometries with M06-2X/6-311+G(d,p).

Scheme 1. Azide-cyclooctyne (3+2) cycloaddition and *trans*-cyclooctene-tetrazine (4+2) cycloaddition reactions^a



Scheme 2. Selectivity of bioorthogonal cycloadditions



^a $R-N_3$ = AF647-azide, R^1 = Me, R^2 = $(CH_2)_3NH_2$, R^3 = PEG_4CO_2H , R^4 = $CH_2Ph-(p-CO_2H)$ (for azide-cycloaddition) or H (for tetrazine-cycloaddition), R^5 = Bn, and R^6 = Ph.

However, the cyclooctyne-modified proteins couple with both tetrazine-functionalized and azide-functionalized dyes.⁹ The similar reactivity of cyclooctynes with azides and tetrazines is also demonstrated by separate kinetic studies of the Bertozzi and Wang groups: tetrazines react with cyclooctynes only 1 to 2 orders of magnitude faster than azides do (Scheme 2c).¹⁰ *Trans*-cyclooctene, cyclooctyne, and dibenzocyclooctyne are all highly strained molecules; why do their selectivities toward azides and tetrazines in bioorthogonal cycloadditions differ dramatically? Here we answer this question by DFT calculations, point out the factors that control reactivity patterns of azides and tetrazines, develop a set of design principles to guide discovery of new orthogonal cycloadditions, and predict that two new bioorthogonal reagents,

methylcyclopropene and 3,3,6,6-tetramethylthiacycloheptyne, will be mutually orthogonal in azide and tetrazine cycloadditions.

Results/Discussion

We explored the cycloaddition reactions of *trans*-cyclooctene, cyclooctyne, and dibenzocyclooctyne with both methyl azide (**TS1**, **TS3**, **TS5**) and dimethyltetrazine (**TS2**, **TS4**, **TS6**) using quantum mechanical calculations.¹¹ M06-2X,¹² a density functional that we have shown to give relatively accurate energies for cycloadditions,¹³ is used in this computational study. Figure 1 shows the transition structures (**TS1-6**) for six cycloaddition reactions.

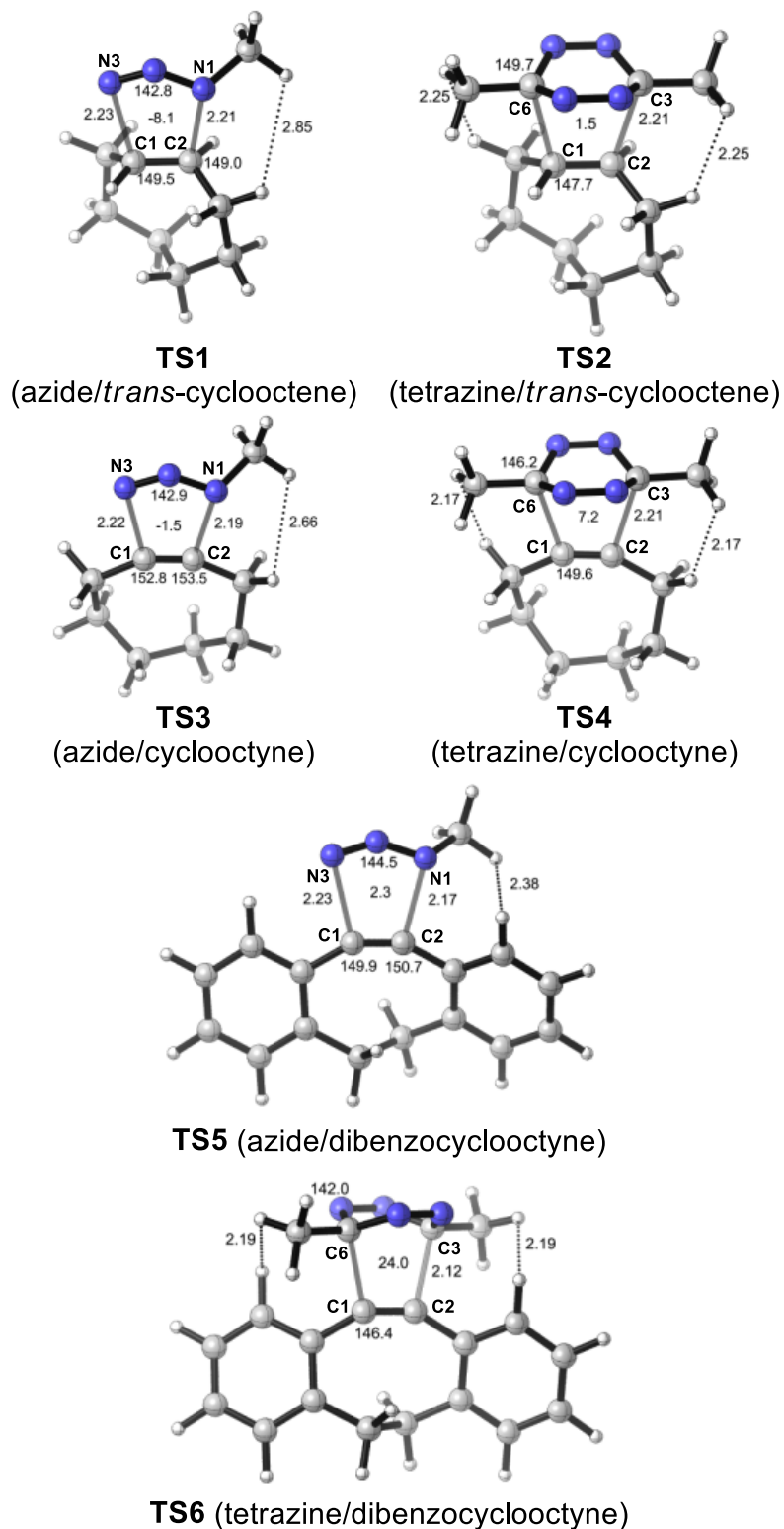


Figure 1. M06-2X/6-311+G(d,p) optimized transition structures of methyl azide-cycloadditions TS1, TS3, and TS5 and dimethyltetrazine-cycloadditions TS2, TS4, and TS6. Distances are given in Å, and angles or dihedral angles are given in degrees.

We also analyzed the activation barriers of these reactions by using the distortion/interaction model.¹⁴ In this model, the activation energy (E_{act}) of a reaction is analyzed in terms of the distortion energy (E_{dist}), the energy required for the geometrical deformation of reactants to achieve their transition state conformations, and the interaction energy (E_{int}), arising from the interactions between two distorted reactants in the transition state. The computed activation free energies, relative rate constants, and the distortion/interaction energies are summarized in Table 1. *Trans*-cyclooctene, cyclooctyne, and dibenzocyclooctyne are all highly reactive, because their distortion energies (3–6 kcal mol⁻¹, **TS1-5**) are much lower than those for unstrained alkenes or alkynes (8–17 kcal mol⁻¹).^{14j,k}

Table 1. M06-2X/6-311+G(d,p) Computed activation free energies in the gas phase and in water (G_{gas} and G_{water} , in kcal mol⁻¹), Relative rate constants (k_{rel} , based on G_{water} at 298 K), and activation, distortion, and interaction energies (E_{act} , E_{dist} , and E_{int} , in kcal mol⁻¹)

	G_{gas}	G_{water}	k_{rel}	E_{act}	E_{dist}	E_{int}
TS1	25.0	26.4	2.0	12.3	20.5 (17.8 ^a)	-8.2
TS2	18.6	17.9	3.4 x 10 ⁶	2.1	19.9 (16.4 ^b)	-17.8
TS3	25.0	26.8	1.0	11.7	20.6 (17.9 ^a)	-8.9
TS4	24.5	24.2	81	8.0	26.0 (20.3 ^b)	-18.0
TS5	21.9	23.9	1.3 x 10 ²	7.7	20.4 (17.1 ^a)	-12.7
TS6	31.4	33.4	1.4 x 10 ⁻⁵	13.7	36.7 (27.8 ^b)	-23.0
TS7	28.7	29.5	1.0 x 10 ⁻²	15.0	24.5 (17.0 ^a)	-9.5
TS8	21.8	21.6	6.5 x 10 ³	5.1	21.3 (12.5 ^b)	-16.2
TS9	19.7	21.7	5.5 x 10 ³	5.7	15.6 (14.3 ^a)	-9.9
TS10	30.9	31.7	2.5 x 10 ⁻⁴	13.2	34.4 (25.6 ^b)	-21.2

^a The data in parentheses are the distortion energies of methyl azide. ^b The data in parentheses are the distortion energies of dimethyltetrazine.

For the cycloadditions of *trans*-cyclooctene, the activation free energy in water with tetrazine (via transition state **TS2**) is lower than that with azide (via **TS1**) by more than 8 kcal mol⁻¹ (Table 1). This accounts for the nearly exclusive tetrazine-selectivity of *trans*-cyclooctenes in the experiments.^{8,9} The distortion/interaction model analysis shows that the distortion energies of transition states **TS1** and **TS2** are nearly identical, but that the favorable interaction energy of **TS2** is much larger than that of **TS1** (-17.8 versus -8.2 kcal mol⁻¹, Table 1). The different electronic properties of tetrazine and azide produce this large interaction energy difference. The frontier molecular orbital (FMO) analysis (Figure 2) indicates that the preferred orbital interaction is between the HOMO of *trans*-cyclooctene and the LUMO of methyl azide, or relevant vacant orbital of dimethyltetrazine.¹⁵ Notably, azide is a much weaker electron acceptor than tetrazine due to its higher LUMO energy (3.39 versus 2.48 eV, Figure 2). The smaller orbital energy gap between *trans*-cyclooctene and tetrazine makes the favorable orbital interaction in **TS2** stronger than that in **TS1**. Therefore, tetrazines are much more reactive than azides in the cycloadditions using *trans*-cyclooctenes, due to their higher electrophilicity.¹⁶

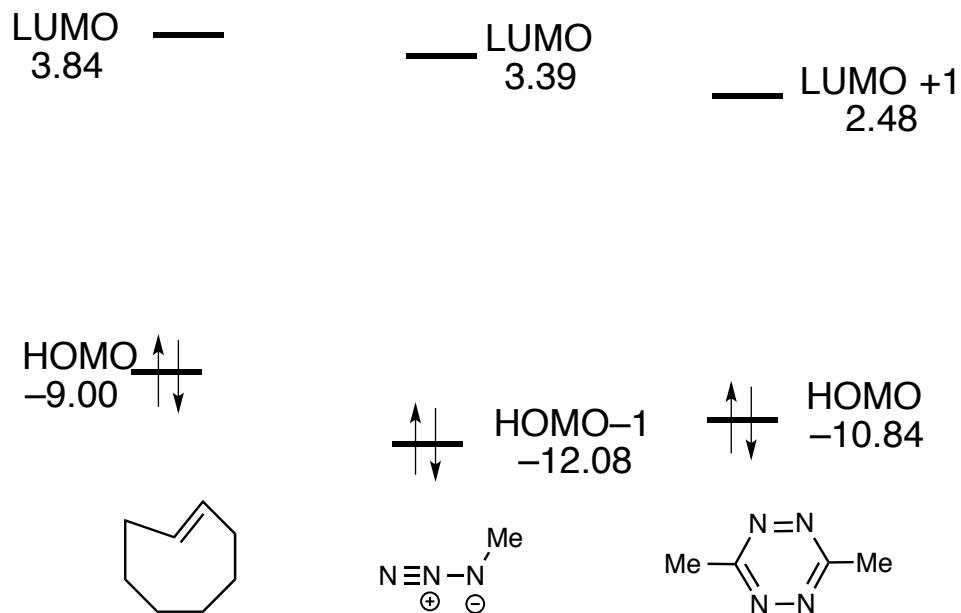


Figure 2. FMO diagram for the cycloadditions of *trans*-cyclooctene with methyl azide and dimethyltetrazine. HF//M06-2X/6-311+G(d,p) computed orbital energies are given in eV.

The cycloaddition of dibenzocyclooctyne with dimethyltetrazine is seven orders of magnitude slower than with methyl azide (Table 1, **TS5-6**), in good agreement with the experimental observation that dibenzocyclooctyne derivatives only react with azides.⁸ The extremely sluggish kinetics of the dibenzocyclooctyne-tetrazine cycloaddition is mainly due to very high distortion energy for this reaction (36.7 kcal mol⁻¹, **TS6**). The transition structure **TS6** (Figure 1) shows that two distances between the methyl hydrogen atoms of tetrazine and the *ortho* hydrogen atoms of the aromatic rings of dibenzocyclooctyne are 2.19 Å, close to the sum (2.20 Å) of their van der Waals radii.¹⁷ This is achieved at the expense of increased distortions of the transition state and the poor orbital overlap, as evidenced by the C₃-C₆-C₁-C₂ dihedral angle of 24° in **TS6**. The effects of the unfavorable steric repulsion and the poor orbital overlap greatly move the transition state **TS6** later along the reaction coordinate. A later transition state means a greater geometrical deformation of reactants, requiring more distortion energy.

These factors are shown in the space-filling models of reactants and transition states (Figure 3).¹⁸ By contrast, the shortest H–H distance between methyl azide and dibenzocyclooctyne is 2.38 Å in **TS5** (Figure 1), suggesting that closed-shell repulsions do not destabilize the transition structure. Moreover, the N₁-N₃-C₁-C₂ dihedral angle in **TS5** is 2.3°, and such a planar geometry ensures the maximum orbital overlap in the cycloaddition transition state. Although the electrophilicity of tetrazine is significantly higher than that of azide, the size of 3,6-disubstituted tetrazine is obviously larger than that of azide. In the case of dibenzocyclooctynes, due to the great steric hindrance caused by two aryl hydrogen atoms *ortho* to the alkyne moiety, the steric effect overwhelms the electronic effect, leading to the exclusive azide-selectivity. For the cycloadditions of cyclooctyne, the activation free energy for the tetrazine (4+2) reaction (via transition state **TS4**) is 2.6 kcal mol⁻¹ lower in water than that for the azide (3+2) reaction (via **TS3**, Table 1). This indicates that the cyclooctyne-tetrazine cycloaddition is only a few orders of magnitude faster than the cyclooctyne-azide cycloaddition.

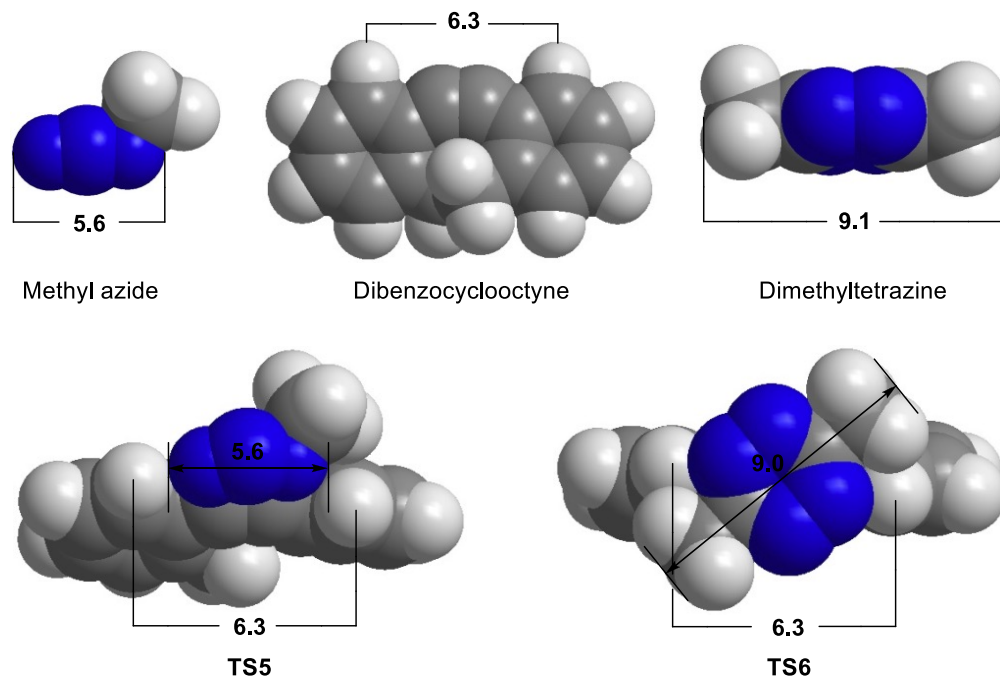


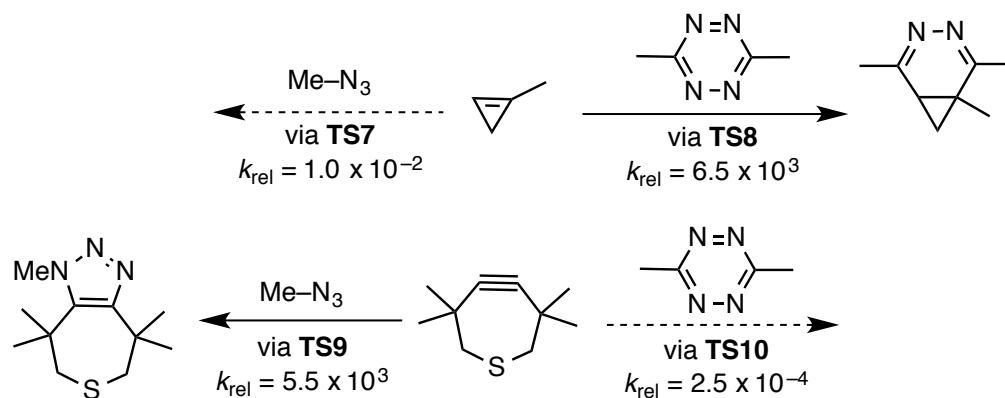
Figure 3. Space-filling models of dibenzocyclooctyne, methyl azide, dimethyltetrazine, and transition states TS5 and TS6. Distances are given in Å.

The interaction energy of **TS4** is 9.1 kcal mol⁻¹ more favorable than that of **TS3** (–18.0 versus –8.9 kcal mol⁻¹) because of the favorable electronic effect of tetrazine, but the distortion energy of **TS4** is 5.4 kcal mol⁻¹ higher than that of **TS3** (26.0 versus 20.6 kcal mol⁻¹) due to steric repulsions between dimethyltetrazine and the propargylic hydrogen atoms of cyclooctyne in **TS4** (Figure 1).

We can now generalize principles for the design of orthogonal reaction pairs in cycloadditions of the same electron-demand type.¹⁸ The electronically more reactive electrophile (or nucleophile) **A** must be sterically more encumbered than the electronically less reactive one **B** (for instance, **A** = dimethyltetrazine; **B** = methyl azide). **A** will react more readily with sterically unencumbered cycloaddition partners, but **B** will react more readily with sterically encumbered ones.

We have used these principles to predict that two new bioorthogonal reagents, methylcyclopropene^{3f} and 3,3,6,6-tetramethylthiacycloheptyne^{2c}, will also be mutually orthogonal in azide and tetrazine cycloadditions (Scheme 3, the relative rate constants shown are predicted for the aqueous solution).

Scheme 3. Prediction of mutual orthogonality of two new bioorthogonal reagents in azide and tetrazine cycloadditions



Methylcyclopropene derivatives show high rates of reaction with tetrazines,^{3f,20} while 3,3,6,6-tetramethylthiacycloheptyne has been found to react readily with azides.^{2c} The sterically encumbered but electronically reactive tetrazine should react much faster than the azide with the sterically unencumbered cyclopropene (Scheme 3a), while the azide should be much more reactive with the sterically encumbered cycloalkyne with four methyl groups adjacent to the alkyne moiety (Scheme 3b). The computed activation free energies, relative rate constants, and the distortion/interaction energies of the corresponding cycloadditions further support our prediction (Table 1, **TS7–10**).²¹ Further computational design of new bioorthogonal and orthogonal cycloadditions is ongoing in our laboratory.

Acknowledgements

K. N. Houk was the project director. Steven Alexander Lopez performed all the calculations involving *trans*-cyclooctene, organized results, and wrote one-third of the manuscript. Y. Liang wrote two-thirds of the manuscript and performed calculations involving the cyclopropenes and thia-cycloheptynes, J. L. Mackey performed calculations on the alkyne systems. Fang Liu wrote the abstract and edited the final work. We thank the National Science Foundation (NSF CHE-1059084) for financial support of this research. The computations were performed on the UCLA IDRE Hoffman2 cluster.

References

¹ (1) For reviews, see: (a) Sletten, E. M.; Bertozzi, C. R. *Angew. Chem., Int. Ed.* **2009**, *48*, 6974. (b) Jewett, J. C.; Bertozzi, C. R. *Chem. Soc. Rev.* **2010**, *39*, 1272. (c) Debets, M. F.; van Berkel, S. S.; Dommerholt, J.; Dirks, A. J.; Rutjes, F. P. J. T.; van Delft, F. L. *Acc. Chem. Res.* **2011**, *44*, 805. (d) Devaraj, N. K.; Weissleder, R. *Acc. Chem. Res.* **2011**, *44*, 816.

(2) For recent examples of the azide cycloaddition, see: (a) Mbua, N. E.; Guo, J.; Wolfert, M. A.; Steet, R.; Boons, G.-J. *ChemBioChem* **2011**, *12*, 1912. (b) Plass, T.; Milles, S.; Koehler, C.; Schultz, C.; Lemke, E. A. *Angew. Chem., Int. Ed.* **2011**, *50*, 3878. (c) de Almeida, G.; Sletten, E. M.; Nakamura, H.; Palaniappan, K. K.; Bertozzi, C. R. *Angew. Chem., Int. Ed.* **2012**, *51*, 2443. (d) Hudak, J. E.; Barfield, R. M.; de Hart, G. W.; Grob, P.; Nogales, E.; Bertozzi, C. R.; Rabuka, D. *Angew. Chem., Int. Ed.* **2012**, *51*, 4161.

(3) For recent examples of the tetrazine cycloaddition, see: (a) Taylor, M. T.; Blackman, M. L.; Dmitrenko, O.; Fox, J. M. *J. Am. Chem. Soc.* **2011**, *133*, 9646. (b) Liu, D. S.; Tangpeerachaikul,

A.; Selvaraj, R.; Taylor, M. T.; Fox, J. M.; Ting, A. Y. *J. Am. Chem. Soc.* **2012**, *134*, 792. (c) Seitchik, J. L.; Peeler, J. C.; Taylor, M. T.; Blackman, M. L.; Rhoads, T. W.; Cooley, R. B.; Refakis, C.; Fox, J. M.; Mehl, R. A. *J. Am. Chem. Soc.* **2012**, *134*, 2898. (d) Lang, K.; Davis, L.; Wallace, S.; Mahesh, M.; Cox, D. J.; Blackman, M. L.; Fox, J. M.; Chin, J. W. *J. Am. Chem. Soc.* **2012**, *134*, 10317. (e) Lang, K.; Davis, L.; Torres-Kolbus, J.; Chou, C.; Deiters, A.; Chin, J. W. *Nat. Chem.* **2012**, *4*, 298. (f) Yang, J.; Seckute, J.; Cole, C. M.; Devaraj, N. K. *Angew. Chem., Int. Ed.* **2012**, *51*, 7476.

² (a) Agard, N. J.; Prescher, J. A.; Bertozzi, C. R. *J. Am. Chem. Soc.* **2004**, *126*, 15046. (b) Sletten, E. M.; Bertozzi, C. R. *Acc. Chem. Res.* **2011**, *44*, 666.

³ (a) Baskin, J. M.; Prescher, J. A.; Laughlin, S. T.; Agard, N. J.; Chang, P. V.; Miller, I. A.; Lo, A.; Codelli, J. A.; Bertozzi, C. R. *Proc. Natl. Acad. Sci. U.S.A.* **2007**, *104*, 16793. (b) Codelli, J. A.; Baskin, J. M.; Agard, N. J.; Bertozzi, C. R. *J. Am. Chem. Soc.* **2008**, *130*, 11486. (c) Ning, X. H.; Guo, J.; Wolfert, M. A.; Boons, G. J. *Angew. Chem., Int. Ed.* **2008**, *47*, 2253. (d) Jewett, J. C.; Sletten, E. M.; Bertozzi, C. R. *J. Am. Chem. Soc.* **2010**, *132*, 3688. (e) Dommerholt, J.; Schmidt, S.; Temming, R.; Hendriks, L. J. A.; Rutjes, F. P. J. T.; van Hest, J. C. M.; Lefeber, D. J.; Friedl, P.; van Delft, F. L. *Angew. Chem., Int. Ed.* **2010**, *49*, 9422. (f) Debets, M. F.; van Berkel, S. S.; Schoffelen, S.; Rutjes, F. P. J. T.; van Hest, J. C. M.; van Delft, F. L. *Chem. Commun.* **2010**, 46, 97.

⁴ (a) Blackman, M. L.; Royzen, M.; Fox, J. M. *J. Am. Chem. Soc.* **2008**, *130*, 13518. (b) Devaraj, N. K.; Weissleder, R.; Hilderbrand, S. A. *Bioconjugate Chem.* **2008**, *19*, 2297.

⁵ Karver, M. R.; Weissleder, R.; Hilderbrand, S. A. *Bioconjugate Chem.* **2011**, *22*, 2263.

⁶ Karver, M. R.; Weissleder, R.; Hilderbrand, S. A. *Angew. Chem., Int. Ed.* **2012**, *51*, 920.

⁷ Plass, T.; Milles, S.; Koehler, C.; Szymanski, J.; Mueller, R.; Wiebler, M.; Schultz, C.; Lemke, E. A. *Angew. Chem., Int. Ed.* **2012**, *51*, 4166.

⁸ Frisch, M. J. et al. (see complete reference in the Supporting Information). Gaussian 09, revision A.1; Gaussian Inc.: Wallingford, CT, 2009.

⁹ Zhao, Y.; Truhlar, D. G. *Theor. Chem. Acc.* **2008**, *120*, 215.

¹⁰ (a) Agard, N. J.; Baskin, J. M.; Prescher, J. A.; Lo, A.; Bertozzi, C. R. *ACS Chem. Biol.* **2006**, *1*, 644. (b) Chen, W.; Wang, D.; Dai, C.; Hamelberg, D.; Wang, B. *Chem. Commun.* **2012**, *48*, 1736.

¹¹ Frisch, M. J.; et al. Gaussian 09, revision C.01; Gaussian, Inc.: Wallingford, CT, 2010.

¹² (a) Zhao, Y.; Truhlar, D. G. *Theor. Chem. Acc.* **2008**, *120*, 215. (b) Zhao, Y.; Truhlar, D. G. *Acc. Chem. Res.* **2008**, *41*, 157.

¹³ (a) Paton, R. S.; Mackey, J. L.; Kim, W. H.; Lee, J. H.; Danishefsky, S. J.; Houk, K. N. *J. Am. Chem. Soc.* **2010**, *132*, 9335. (b) Lan, Y.; Zou, L.; Cao, Y.; Houk, K. N. *J. Phys. Chem. A* **2011**, *115*, 13906.

¹⁴ (a) Ess, D. H.; Houk, K. N. *J. Am. Chem. Soc.* **2007**, *129*, 10646. (b) Ess, D. H.; Houk, K. N. *J. Am. Chem. Soc.* **2008**, *130*, 10187. (c) Hayden, A. E.; Houk, K. N. *J. Am. Chem. Soc.* **2009**, *131*, 4084. (d) Schoenebeck, F.; Ess, D. H.; Jones, G. O.; Houk, K. N. *J. Am. Chem. Soc.* **2009**, *131*, 8121. (e) van Zeist, W.-J.; Bickelhaupt, F. M. *Org. Biomol. Chem.* **2010**, *8*, 3118.

(f) Fernández, I.; Cossío, F. P.; Bickelhaupt, F. M. *J. Org. Chem.* **2011**, *76*, 2310. (g) Lan, Y.; Wheeler, S. E.; Houk, K. N. *J. Chem. Theory Comput.* **2011**, *7*, 2104. (h) Paton, R. S.; Kim, S.; Ross, A. G.; Danishefsky, S. J.; Houk, K. N. *Angew. Chem., Int. Ed.* **2011**, *50*, 10366. (i) Fernández, I.; Bickelhaupt, F. M. *J. Comput. Chem.* **2012**, *33*, 509. (j) Gordon, C. G.; Mackey, J. L.; Jewett, J. C.; Sletten, E. M.; Houk, K. N.; Bertozzi, C. R. *J. Am. Chem. Soc.* **2012**, *134*, 9199. (k) Lopez, S. A.; Houk, K. N. *J. Org. Chem.* **2012**, *78*, 1778.

¹⁵ In the cycloadditions of strained alkynes, FMO analysis showed that charge transfer from the alkyne to methyl azide or dimethyltetrazine also occurs.

¹⁶ Houk, K. N. *Acc. Chem. Res.* **1975**, *8*, 361.

¹⁷ Rowland, R. S.; Taylor, R. *J. Phys. Chem.* **1996**, *100*, 7384.

¹⁸ A second design principle is also being investigated: two cycloadditions with different electron demand (for example, the normal Diels–Alder reaction between a nucleophilic diene and an electrophilic dienophile and the inverse-electron-demand reaction of a nucleophilic dienophile and an electrophilic diene) are mutually orthogonal because of pure electronic effects.

Chapter 4

Isomeric cyclopropenes exhibit unique bioorthogonal reactivities^a

ABSTRACT: Bioorthogonal chemistries have provided tremendous insight into biomolecule structure a function. However, many of the most popular bioorthogonal transformations are incompatible with one another, limiting their utility for studies of multiple biomolecules in tandem. We identified two reactions that can be used concurrently to tag biomolecules in complex environments: the inverse-electron-demand Diels-Alder reaction of tetrazines with 1,3-disubstituted cyclopropenes, and the 1,3-dipolar cycloaddition of nitrile imines with 3,3-disubstituted cyclopropenes. Remarkably, the cyclopropenes used in these reactions differ by the placement of a single methyl group. Such orthogonally reactive scaffolds will bolster efforts in the chemistry and biology communities to monitor multi-component processes in cells and organisms.

Introduction

The bioorthogonal chemical reporter strategy has been widely used to interrogate glycans, lipids, and other biopolymers in living systems.¹ This approach relies on the introduction of a uniquely reactive functional group (*i.e.*, a “chemical reporter”) into a biomolecule of interest. The chemical reporter can be ligated to probes for visualization or retrieval using highly selective (*i.e.*, “bioorthogonal”) chemistries.^{1b,2} While powerful, this two-step strategy has been largely limited to examining one biological feature at a time in live cells and tissues. This is because many bioorthogonal reactions are incompatible with one another and cannot be used in tandem to monitor multiple species.³

^a Reprinted with permission from *Journal of the American Chemical Society* **2013**, *135*, 13680–13683. Copyright 2013 American Chemical Society. Authors are D. Kamber, L. Nazarova, Y. Liang, Steven Alexander Lopez, K. N. Houk, and J. A. Prescher.

Our long-term goal is to identify transformations that can be used concurrently to tag biomolecules in complex environments. As a starting point, we were drawn to the cycloaddition reactions of cyclopropenes. Functionalized cyclopropenes are stable in physiological environments, yet readily reactive with dienes and other biocompatible motifs.⁴ We and others have shown 1,3-disubstituted cyclopropenes can be metabolically incorporated into cellular glycans and selectively ligated via inverse-electron demand Diels-Alder (IED-DA) reactions with tetrazine probes (Figure 1A).^{4b,4c,5} In related work, Lin and colleagues demonstrated that 3,3-disubstituted cyclopropenes can be introduced into recombinant proteins and ultimately detected via 1,3-dipolar cycloaddition with nitrile imines (Figure 1A).^{4d} This reaction, similar to the cyclopropene-tetrazine ligation, proceeds readily in cellular environments and without detriment to living systems.

We were intrigued by cyclopropene IED-DA and dipolar cycloadditions for an additional reason: these reactions had the potential to be orthogonal to one another and, thus, applicable to multi-component biomolecule labeling. In earlier work, we demonstrated that 1,3-disubstituted cyclopropenes react with tetrazines at the least-hindered face of the three-membered ring (*i.e.* the side bearing the C-3 H atom).^{4b} Additional steric bulk at this position (as in the case of 3,3-disubstituted cyclopropenes) would, in theory, impede IED-DA reactivity but not impact cycloadditions with less sterically encumbered reactants (*i.e.* 1,3-dipoles).

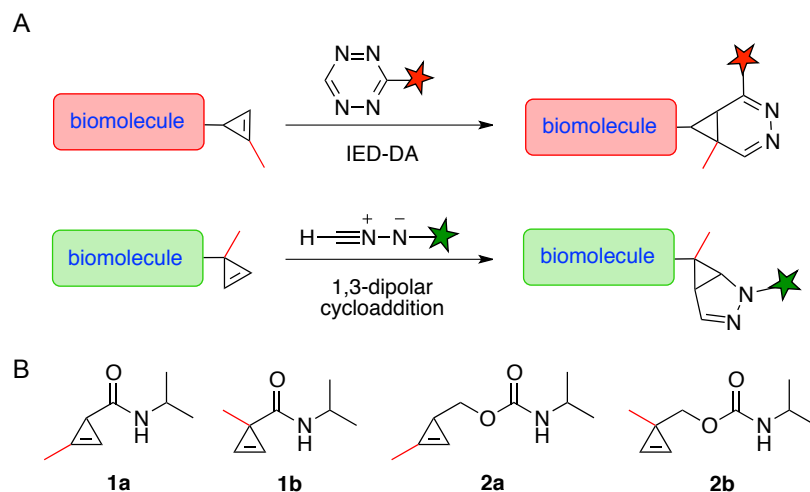


Figure 1. (A) Cyclopropene scaffolds undergo bioorthogonal cycloaddition reactions. 1,3-Disubstituted cyclopropenes (top) react with tetrazines via IED-DA reactions. 3,3-Disubstituted scaffolds (bottom) react with 1,3-dipoles to afford covalent adducts. (B) Panel of disubstituted cyclopropenes examined in this work.

To predict whether cyclopropene reactivity could be tuned by steric modifications at C-3, we explored the reactions of 1,3- and 3,3-dimethylcyclopropene (Cp(1,3) and Cp(3,3)) with diphenyl-substituted nitrile imine (NI) and tetrazine (Tz), using density functional theory (DFT) calculations.⁶ M06-2X,⁷ a density functional that provides relatively accurate energetics for cycloadditions,⁸ was used here.

Results/Discussion

The four transition structures for the reactions are shown in Figure 2. We also analyzed the activation barriers using the distortion/interaction model,⁹ in which the activation energy (E_{act}) is analyzed in terms of the distortion energy (E_{dist}) required for the reactants to achieve their transition-state geometries, and the interaction energy (E_{int}) arising from orbital overlap between the two distorted reactants in the transition state. The computed activation free energies in water

(G_{water}), relative rate constants (k_{rel}), and distortion/interaction energies are shown below the transition structures in Figure 2. Calculations indicate that for the sterically less encumbered nitrile imine, 1,3-dimethylcyclopropene reacts only 2.8 times faster than 3,3-dimethylcyclopropene. The distortion and interaction energies are very close, suggesting that increased steric bulk at C-3 of the cyclopropene does not dramatically influence reactivity with linear 1,3-dipoles. However, for the bulkier tetrazine, placement of a single methyl group at C-3 reduces cyclopropene reactivity by over four orders of magnitude in the IED-DA reaction. In the transition state **TS-Tz-Cp(3,3)**, to avoid steric clashes between the C-3 methyl and tetrazine nitrogens, the dihedral angle between the cyclopropene plane and the C-C bonds-forming plane increases to 120° , about 15° larger than the corresponding value in **TS-Tz-Cp(1,3)**. In the figure below, note how the cyclopropene C-3 and methyl groups are tilted away from the tetrazine. This results in increased distortion energy (24.0 versus 22.0 kcal mol⁻¹) and less favorable interaction energy (-13.7 versus -18.1 kcal mol⁻¹) due to poorer orbital overlap. Similar reactivities were predicted for functionalized cyclopropene and tetrazine probes. Collectively, these data suggest that isomeric cyclopropenes possess unique bioorthogonal reactivities: 3,3-disubstituted cyclopropenes should react readily with nitrile imines, but not tetrazines, under physiological conditions; 1,3-disubstituted cyclopropenes, and should react readily with both.

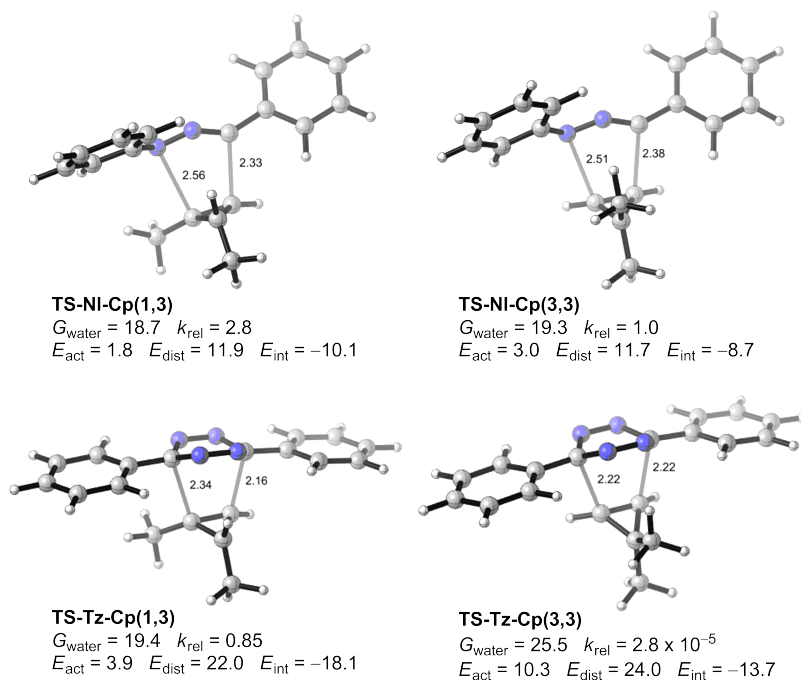
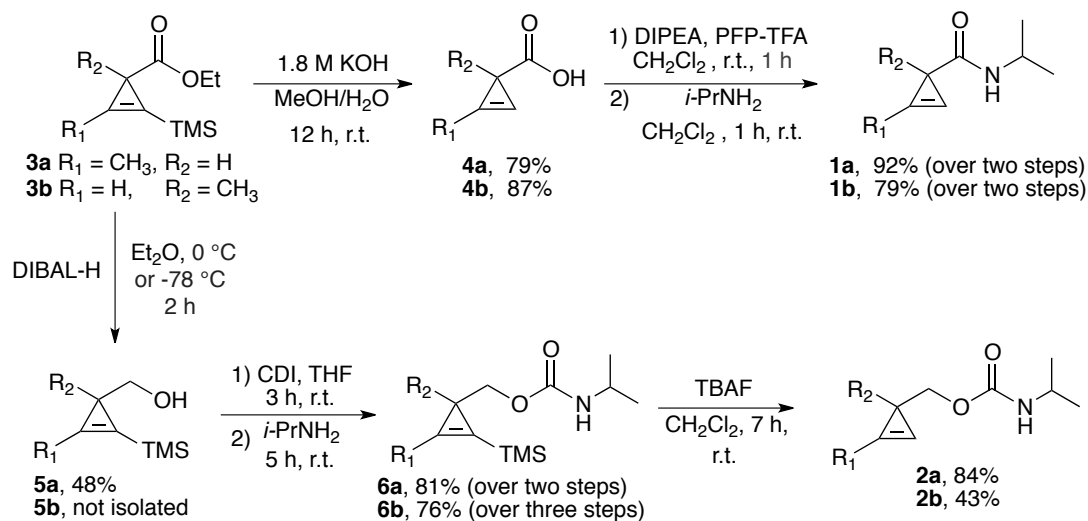


Figure 2. M06-2X/6-31G(d)-optimized transition-state structures for the cycloadditions of 1,3- and 3,3-dimethylcyclopropene [Cp(1,3) and Cp(3,3)] with diphenyl-substituted nitrile imine (NI) and tetrazine (Tz). M06-2X/6-311+G(d,p)//6-31G(d)-computed energies and relative rate constants (distances in Å, energies in kcal mol⁻¹, k_{rel} based on G_{water} at 298 K) are also shown.

To test these predictions, we synthesized a panel of disubstituted cyclopropenes bearing methyl groups at either C-1 or C-3 (Figure 1B). The scaffolds also comprise amide or carbamate groups as these linkages mimic those found in numerous bioconjugates. The amide-functionalized probes **1a-b** were synthesized similarly to previous reports (Scheme 1).^{4b-d} In brief, esters **3a-b** were first subjected to base-catalyzed hydrolysis. The resulting acids (**4a-b**) were subsequently treated with PFP-TFA, followed by isopropylamine to access the desired probes. To prepare the carbamate-functionalized scaffolds, esters **3a-b** were first reduced with DIBAL-H. The reaction with **3b** was prone to cyclopropane formation; over-reduction was avoided at -78 °C. Alcohols **5a-b** were ultimately converted to the desired carbamates (**2a-b**) via CDI-coupling with isopropylamine, followed by TMS removal with TBAF.

Scheme 1. Synthesis of disubstituted cyclopropenes.



With the desired cyclopropenes in hand, we first analyzed their IED-DA reactivity with model tetrazines (Table 1). Tetrazines **7-8** were incubated with excess cyclopropene, and the cycloadditions were monitored by the change in tetrazine absorbance over time. As shown in Figures 3, robust IED-DA reactivity was observed with the 1,3-disubstituted scaffolds **1a** and **2a**, while no reactivity was detected with their 3,3-disubstituted counterparts (**1b** and **2b**). In fact, no reaction between **1b** or **2b** and tetrazine **7** was observed in phosphate buffer even after 24 h at elevated temperature. Minimal IED-DA reactivity with the 3,3-disubstituted probes was only observed in the presence of large amounts of organic solvent, and in these cases, the transformations were quite slow. It should also be noted that the tetrazine-cyclopropene ligations revealed the expected trends, with the more electron-rich carbamates and less sterically hindered tetrazine exhibiting the fastest rates (Table1)¹⁰ Second-order rate constants for all the transformations are shown in Tables 1.

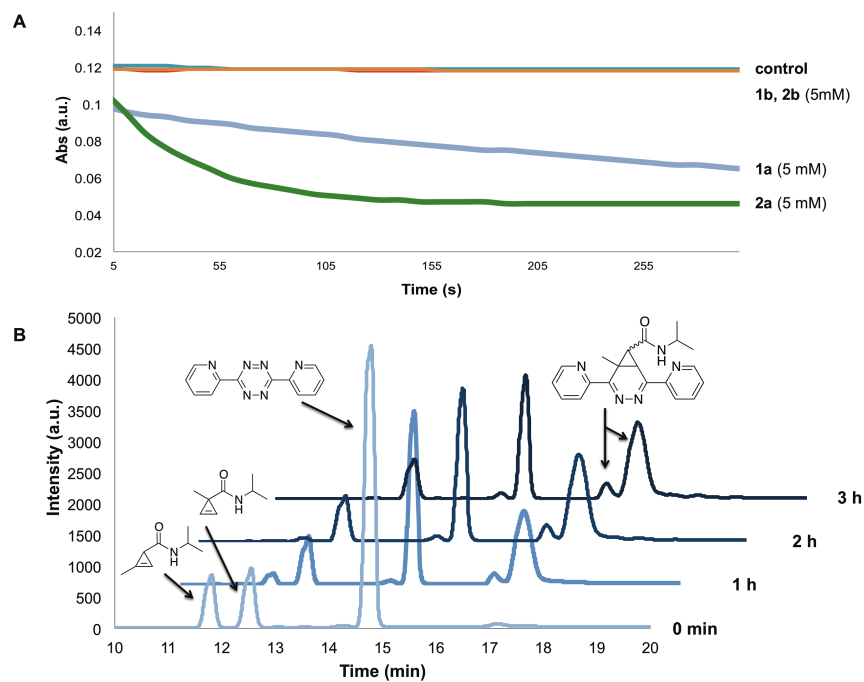


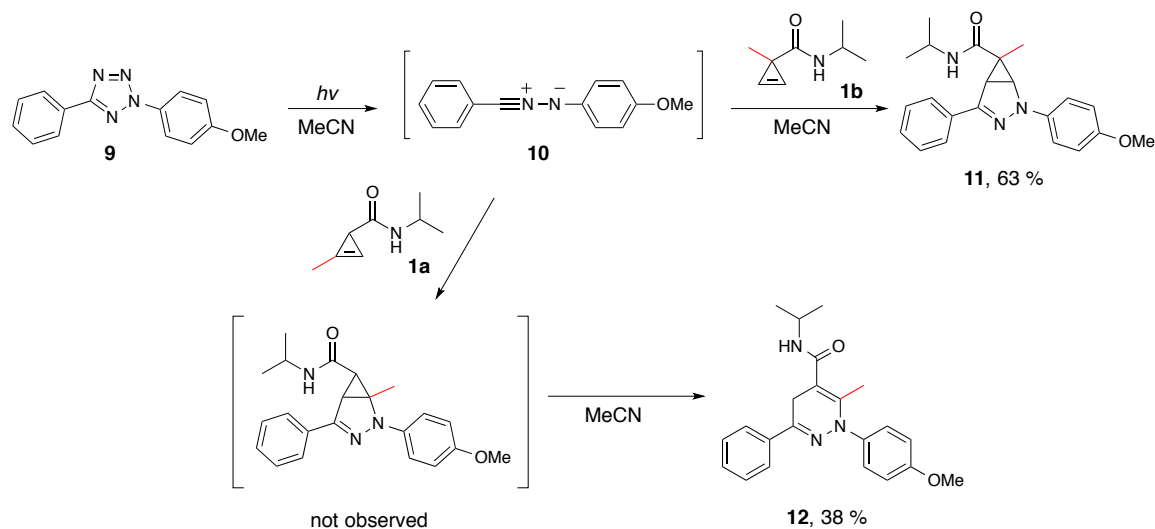
Figure 3. Tetrazines react selectively with 1,3-disubstituted cyclopropenes. (A) Reaction of cyclopropenes **1-2** (5 mM in 15% DMSO/PBS) with tetrazine **7** (0.2 mM) monitored by UV-visible spectroscopy. (B) Reaction of cyclopropenes **1a-b** (5 mM in 15% MeCN/PBS) with tetrazine **7** (10 mM) monitored by HPLC. The initial cycloadduct formed between **1a** and **7** can undergo further intramolecular cyclization in aqueous solution.^{4b}

Table 1. Second-order rate constants for the cyclopropene-tetrazine ligation. All rate constants were measured in 15% DMSO/PBS. *No reaction observed after 90 min.

Entry	Cyclopropene	Tetrazine	k_2 ($\times 10^{-2} \text{ M}^{-1} \text{ s}^{-1}$)
1	1a 	7 	3.19 ± 0.45
2	1b 	7 	N/R*
3	1b 	8 	N/R*
4	2a 	7 	277.8 ± 36.6
5	2b 	7 	N/R*
6	2b 	8 	N/R*

Despite their extremely sluggish reaction kinetics with tetrazines, 3,3-disubstituted cyclopropenes react readily with nitrile imines in “photo-click” reactions.^{4d} Indeed, when micromolar concentrations of **1b** and **9** were subjected to UV light (generating **10** *in situ*), the fluorescent cycloadduct **11** was formed in less than 5 minutes (Scheme 2). The corresponding 1,3-cyclopropene **1a** also reacted rapidly with **10** to provide the rearranged cycloadduct **12**. Similar rearrangements have been observed in 1,3-dipolar cycloadditions with cyclopropenes and nitrile oxides.¹¹ Both ligation products **11** and **12** were found to be stable in aqueous solution for over three days. Importantly, nitrile imine **10** could also be generated in the presence of tetrazine **7** with no observable side reactivity, highlighting the compatibility of these reagents.

Scheme 2. Disubstituted cyclopropenes undergo 1,3-dipolar cycloadditions with nitrile imines to generate stable cycloadducts.



The unique reactivity profiles of 1,3- and 3,3-disubstituted cyclopropenes suggested that the probes could be used in tandem for biomolecule labeling. To test this hypothesis, we functionalized model proteins (BSA and lysozyme) with the isomeric cyclopropenes **13a-b** using standard NHS-ester coupling conditions (Figure 4A). Mass spectrometry analysis was used to verify that equivalent numbers of cyclopropene units were appended to the scaffolds. When the proteins were treated with a tetrazine-rhodamine conjugate (**Tz-Rho**), only samples functionalized with 1,3-disubstituted cyclopropenes (**Cp (1,3)**) showed robust dose- and time-dependent labeling, in agreement with our kinetic data (Figures 4B-C). No labeling above background was observed with proteins outfitted with 3,3-disubstituted cyclopropenes (**Cp (3,3)**). Both **Cp (1,3)** and **Cp (3,3)** samples were covalently modified with nitrile imines using “photo-click” conditions (Figures 4D). The fluorescent intensities of the **Cp (1,3)** adducts were somewhat reduced, though, likely due to the decreased absorption efficiency of the products (**12** versus **11**, Figure S7). When conjugates **Cp (1,3)** and **Cp (3,3)** were subjected to both

cycloaddition reactions (treatment with **Tz-Rho** (100-750 μM), followed by tetrazole **9** and UV photolysis), tetrazine labeling was again only observed for **Cp (1,3)** samples. The **Cp (3,3)** samples, along with unmodified scaffolds on **Cp (1,3)**, were detected following nitrile imine generation (Figures 4E)

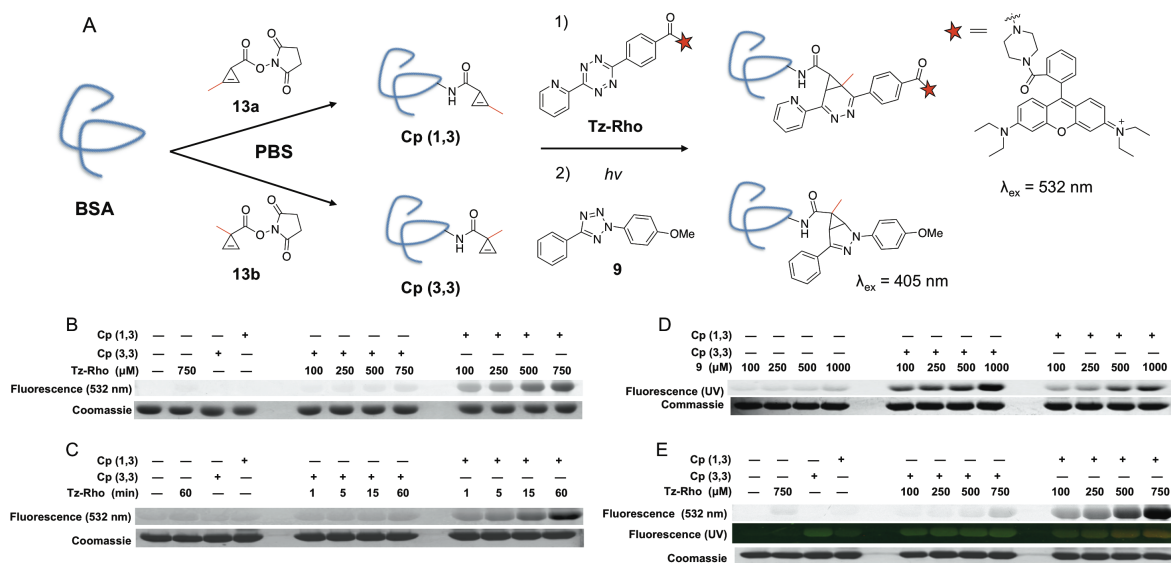


Figure 4. Selective labeling of model proteins with orthogonal cycloaddition reactions. (A) Cyclopropenes **13a-b** were appended to BSA using standard coupling conditions. The modified proteins **Cp (1,3)** and **Cp (3,3)** were subsequently reacted with either a tetrazine-rhodamine conjugate (**Tz-Rho**) or nitrile imine **10** (generated via photolysis of tetrazole **9**). (B) Gel analysis of **Cp (1,3)** or **Cp (3,3)** samples incubated with **Tz-Rho** (100-750 μM) or no reagent (—) for 1 h. (C) Gel analysis of **Cp (1,3)** or **Cp (3,3)** incubated with **Tz-Rho** (500 μM) for 0-60 min. (D) Gel analysis of samples **Cp (1,3)** or **Cp (3,3)** treated with tetrazole **9** (100-1000 μM) and UV irradiation. (E) Samples treated with **Tz-Rho** (100-750 μM) or no reagent (—), followed by **9** (5 mM) and UV irradiation). The gel was scanned at 532 nm (top panel) to visualize rhodamine fluorescence, and also illuminated with UV light (middle panel) to visualize nitrile imine cycloadducts (green). The red color observed in the UV-illuminated gel (middle panel) is due to rhodamine fluorescence. For B-E, protein loading was assessed with Coomassie stain (lower panels)

In sum, we identified a set of cyclopropenes that exhibit unique modes of bioorthogonal reactivity. Computational analyses predicted that 1,3-disubstituted cyclopropenes would undergo facile IED-DA reactions, while 3,3-disubstituted scaffolds would be minimally reactive with tetrazines. Upon synthesis and *in vitro* characterization of a panel of modified cyclopropenes, we discovered that cyclopropenes that differ in the placement of a single methyl group (C-1 vs. C-3) exhibit vastly different IED-DA reaction profiles: 1-methyl cyclopropenes can be selectively ligated with tetrazine probes in the presence of 3-methyl cyclopropenes; the unmodified 3-methyl substituted scaffolds can be efficiently ligated via dipolar cycloaddition reactions. The ability to selectively modify isomeric cyclopropenes paves the way for multi-component imaging studies *in vitro* and in live cells. The cyclopropene scaffold also offers unique opportunities for further biocompatible reaction development, including selective nucleophilic additions and normal-demand Diels-Alder reactions. An arsenal of such orthogonal reactions will provide insight into complex biological systems.

Acknowledgement

D. N. Kamber, L. A. Nazarova, D. M. Patterson, H-W. Shih performed all of the experiments. Y. Liang and S. Lopez carried out the DFT calculations. K. N. Houk and J. A. Prescher were the project directors. We thank the National Science Foundation (NSF CHE- 1059084) for financial support of this research. The computations were performed on the UCLA IDRE Hoffman2 cluster.

References

¹ (a) Chang, P. V.; Prescher, J. A.; Hangauer, M. J.; Bertozzi, C. R. *J. Am. Chem. Soc.* **2007**, *129*, 8400. (b) Prescher, J. A.; Bertozzi, C. R. *Nat. Chem. Biol.* **2005**, *1*, 13. (c) Prescher, J. A.; Dube, D. H.; Bertozzi, C. R. *Nature* **2004**, *430*, 873. (d) Hang, H. C.; Wilson, J. P.; Charron, G. *Acc. Chem. Res.* **2011**, *44*, 699. (e) Haun, J. B.; Devaraj, N. K.; Hilderbrand, S. A.; Lee, H.; Weissleder, R. *Nat. Nanotechnol.* **2010**, *5*, 660.

² Sletten, E. M.; Bertozzi, C. R. *Angew. Chem. Int. Ed.* **2009**, *48*, 6974.

³ (a) Debets, M. F.; van Berkel, S. S.; Dommerholt, J.; Dirks, A. T.; Rutjes, F. P.; van Delft, F. L. *Acc. Chem. Res.* **2011**, *44*, 805. (b) Lang, K.; Davis, L.; Wallace, S.; Mahesh, M.; Cox, D. J.; Blackman, M. L.; Fox, J. M.; Chin, J. W. *J. Am. Chem. Soc.* **2012**, *134*, 10317. (c) Chen, W.; Wang, D.; Dai, C.; Hamelberg, D.; Wang, B. *Chem. Commun.* **2012**, *48*, 1736. (d) Plass, T.; Milles, S.; Koehler, C.; Schultz, C.; Lemke, E. A. *Angew. Chem. Int. Ed.* **2011**, *50*, 3878. (e) Liang, Y.; Mackey, J. L.; Lopez, S. A.; Liu, F.; Houk, K. N. *J. Am. Chem. Soc.* **2012**, *134*, 17904. (f) Sanders, B. C.; Friscourt, F.; Ledin, P. A.; Mbua, N. E.; Arumugam, S.; Guo, J.; Boltje, T. J.; Popik, V. V.; Boons, G. J. *J. Am. Chem. Soc.* **2011**, *133*, 949.

⁴ (a) Zhu, Z.-B.; Wei, Y.; Shi, M. *Chem. Soc. Rev.* **2011**, *40*, 5534. (b) Patterson, D. M.; Nazarova, L. A.; Xie, B.; Kamber, D. N.; Prescher, J. A. *J. Am. Chem. Soc.* **2012**, *134*, 18638. (c) Yang, J.; Seckute, J.; Cole, C. M.; Devaraj, N. K. *Angew. Chem. Int. Ed.* **2012**, *51*, 7476. (d) Yu, Z.; Pan, Y.; Wang, Z.; Wang, J.; Lin, Q. *Angew. Chem. Int. Ed.* **2012**, *51*, 10600. (e) Thalhammer, F.; Wallfahrer, U.; Sauer, J. *Tetrahedron Lett.* **1990**, *31*, 6851.

⁵ Cole, C. M.; Yang, J.; Seckute, J.; Devaraj, N. K. *ChemBioChem* **2013**, *14*, 205.

⁶ Frisch, M. J.; *et al.* *Gaussian 09*, revision C.01; Gaussian, Inc.: Wallingford, CT, **2010**.

⁷ (a) Zhao, Y.; Truhlar, D. G. *Acc. Chem. Res.* **2008**, *41*, 157. (b) Zhao, Y.; Truhlar, D. G. *Theor. Chem. Acc.* **2008**, *120*, 215.

⁸ (a) Lan, Y.; Zou, L.; Cao, Y.; Houk, K. N. *J. Phys. Chem. A* **2011**, *115*, 13906. (b) Paton, R. S.; Mackey, J. L.; Kim, W. H.; Lee, J. H.; Danishefsky, S. J.; Houk, K. N. *J. Am. Chem. Soc.* **2010**, *132*, 9335.

⁹ (a) Ess, D. H.; Houk, K. N. *J. Am. Chem. Soc.* **2007**, *129*, 10646. (b) Gordon, C. G.; Mackey, J. L.; Jewett, J. C.; Sletten, E. M.; Houk, K. N.; Bertozzi, C. R. *J. Am. Chem. Soc.* **2012**, *134*, 9199.

¹⁰ (a) Diev, V. V.; Kostikov, R. R.; Gleiter, R.; Molchanov, A. P. *J. Org. Chem.* **2006**, *71*, 4066. (b) Karver, M. R.; Weissleder, R.; Hilderbrand, S. A. *Bioconjugate Chem.* **2011**, *22*, 2263.

¹¹ Chen, S.; Ren, J.; Wang, Z. *Tetrahedron* **2009**, *65*, 9146.

Chapter 5

Mechanisms and Transition States of 1,3-Dipolar Cycloadditions of Phenyl Azide with Enamines: A Computational Analysis^a

ABSTRACT. The transition structures for the 1,3-dipolar cycloaddition of phenyl azide to enamines derived from acetophenone or phenylacetaldehyde and piperidine, morpholine, or pyrrolidine were located using quantum mechanical methods. These cycloadditions were studied experimentally in 1975 by Meilahn, Cox, and Munk (*J. Org. Chem.* **1975**, *40*, 819–823.) Calculations were carried out with M06-2X/6-311+G(d,p), SCS-MP2/6-311G(d,p)//M06-2X/6-311+G(d,p), and B97D/6-311+G(d,p) methods with the IEF-PCM solvation model for chloroform and ethanol. The distortion/interaction model was utilized to understand mechanisms, reactivities, and regioselectivities.

Introduction

The “click” reaction of azides with terminal alkynes catalyzed by copper catalysts, and the copper free analogs involving azides and strained alkynes, have attracted much attention in the last decade due to a great variety of applications in chemical biology and materials chemistry.^{1,2,3,4,5} These reactions involve two reaction partners, neither of which is electrophilic or nucleophilic with respect to the other. Either copper catalysis or strain-induced activation (distortion-accelerated reactions) are required to achieve acceptable rates.^{6,7}

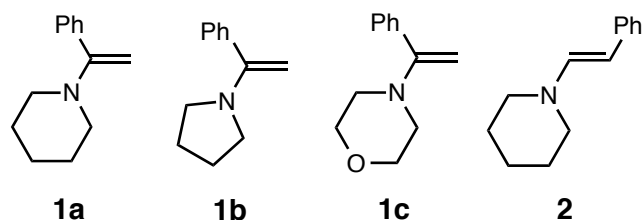
This paper describes a theoretical exploration of a different type of azide cycloaddition, involving very nucleophilic enamines that react rapidly with the relatively electrophilic azides. Through measurements of solvent effects on rate constants, Hammett parameters, and semi-

^a Reprinted with permission from *Journal of Organic Chemistry* **2013**, *78*, 1576–1582. Copyright 2013 American Chemical Society. Authors are Steven Alexander Lopez, Morton E. Munk, and K. N. Houk

empirical Complete Neglect of Differential Overlap (CNDO) molecular orbital calculations, Munk *et al.* deduced that the reactions involve a concerted mechanism with highly asynchronous transition states.⁸

We have employed quantum mechanical calculations to characterize the nature of the transition states and reaction mechanism. We previously investigated simple enamine-azide (3+2) cycloadditions to look for reversible reactions that might be candidates for dynamic combinatorial chemistry.⁹ We now report on the 1,3-dipolar cycloadditions of phenyl azide to the enamines derived from acetophenone and piperidine (**1a**), pyrrolidine (**1b**), and morpholine (**1c**), or phenylacetaldehyde and piperidine (**2**) (Scheme 1).

Scheme 1. Enamine dipolarophiles (**1a–c**) and **2** studied by Munk⁸ and in this work.



The reactions of phenyl azide with 1,1-disubstituted enamines (**1a – 1c**) and *trans*-enamine (**2**) and the possible products are shown in Figure 1. Munk *et al.* performed these reactions and found that **3a–c** and **5** were formed exclusively. The reactions were carried out in chloroform, ethanol, and acetonitrile; the rates are not sensitive to solvent polarity.⁸ We have computationally investigated the mechanisms and regioselectivities of these enamine–azide cycloadditions studied by Munk. The distortion/interaction model has been used to provide a more complete understanding of the mechanisms and factors controlling reactivities in enamine–azide cycloadditions.¹⁰

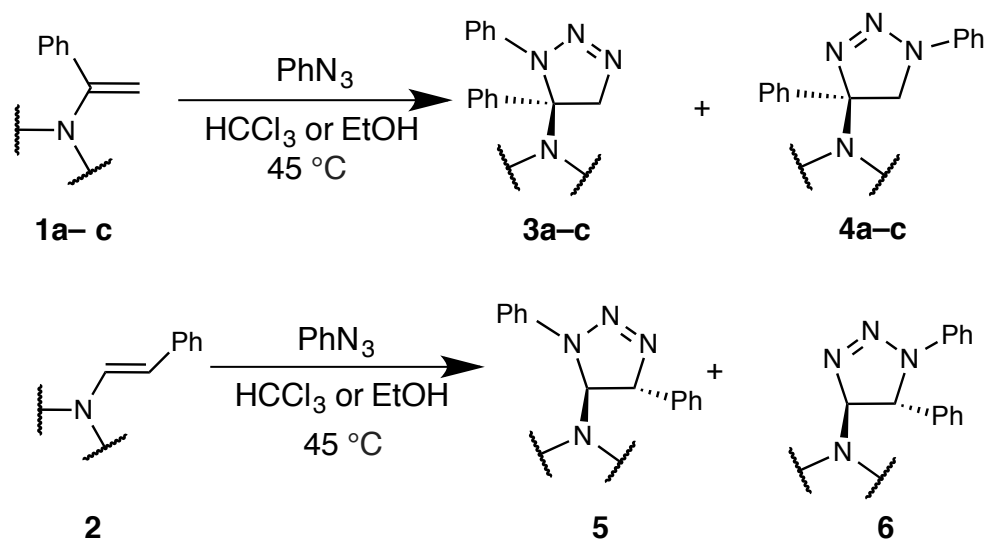


Figure 1. Enamines **1a-c** and **2** undergo reactions with phenyl azide to form **3a-c**, and **5**. **4a-c** and **6** are not observed experimentally.

Computational Methods

All computations were carried out with the GAUSSIAN 09 series of programs.¹¹ Reactants, transition states, and products were optimized with M06-2X¹² and B97D¹³ methods. Vibrational analysis confirmed all stationary points to be minima (no imaginary frequencies) or first order saddle points (one imaginary frequency). An ultrafine grid was used with the M06-2X/6-311+G(d,p) geometry optimization. Frequency calculations on these stationary points provided activation enthalpies and free energies. Additional electronic energies were calculated with SCS-MP2¹⁴/6-311G+(d,p)//M06-2X/6-311G+(d,p). Polarizable continuum model IEF-PCM¹⁵ for solvation by ethanol and chloroform were used for the computations. The use of solvent was critical in locating stationary points for the stepwise transition structures and

intermediates. A quasiharmonic correction was applied during the entropy calculations by setting all frequencies to 100 cm^{-1} when they are less than 100 cm^{-1} .^{16,17}

Results/Discussion

Mechanisms of Azide Cycloadditions to Piperidine Enamines

We have computed both concerted and stepwise paths for the four enamine-azide cycloadditions shown in Figure 1. Both concerted (**a**, Figures 2 and 3) and stepwise (**b**, Figures 2 and 3) pathways were found for formation of observed products **3a-c** and **5**.

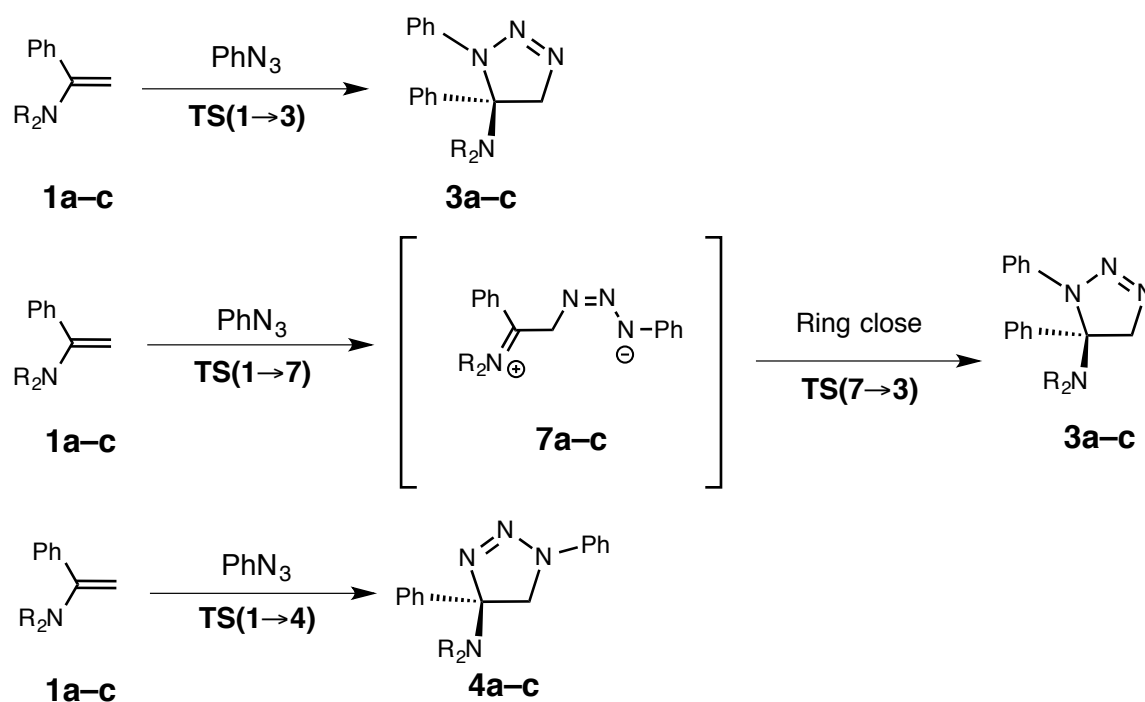


Figure 2. Concerted mechanism of cycloadditions of PhN_3 to enamines **1a-c** and stepwise pathway for formation of **3a-c**.

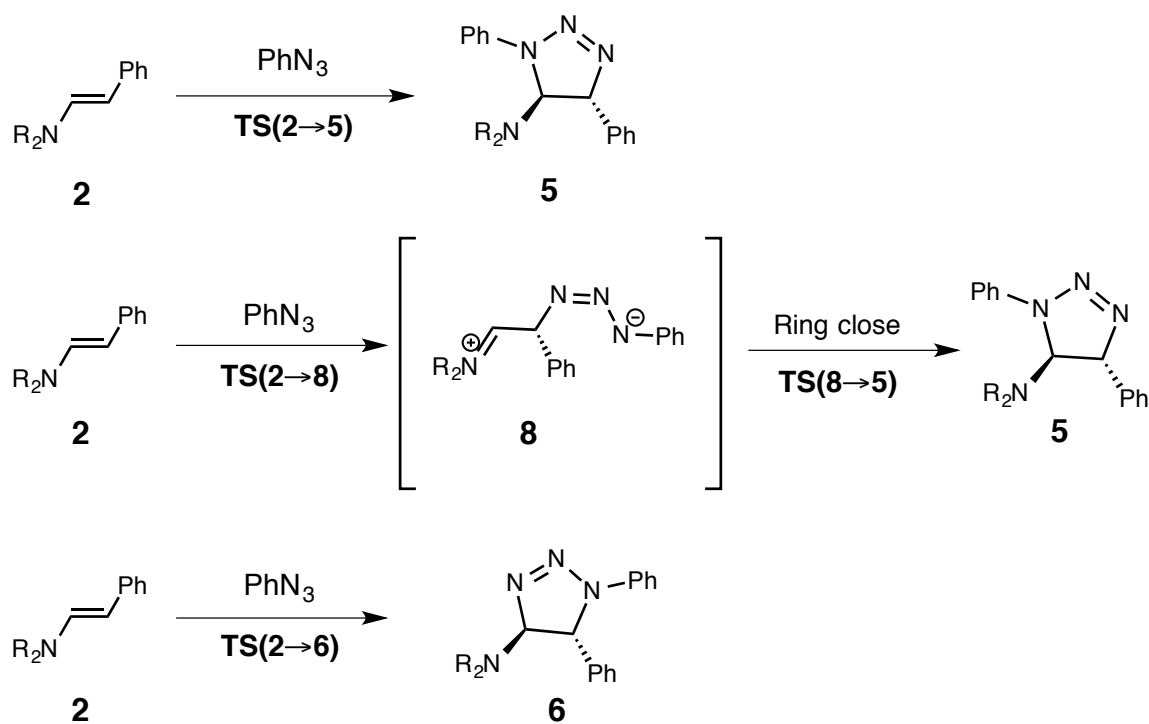


Figure 3. Concerted mechanism of cycloadditions of PhN_3 to enamines **2** and stepwise pathway for formation of **5**.

The transition structures for the reaction of **1a** and **2** with PhN_3 are shown in Figure 4. $\text{TS}(1\mathbf{a} \rightarrow 3\mathbf{a})$ and $\text{TS}(2 \rightarrow 5)$ are concerted, although highly asynchronous and lead to **3a** and **5**. $\text{TS}(1\mathbf{a} \rightarrow 4\mathbf{a})$ and $\text{TS}(2 \rightarrow 6)$ are concerted and quite synchronous but much higher in energy (Figure 6); these lead to the unobserved cycloadducts, **4a** and **6**. The transition structures for the first steps of the stepwise mechanisms $\text{TS}(1\mathbf{a} \rightarrow 7)$ and $\text{TS}(2 \rightarrow 8)$ result in zwitterionic intermediates, **7a** and **8** (Figure 5). These types of zwitterionic intermediates have been reported by Huisgen¹⁸ and recently by Banert.¹⁹ No transition state could be found for the ring closure to the products, **3a** and **5**, presumably because of the very flat surface region of the zwitterionic intermediates.

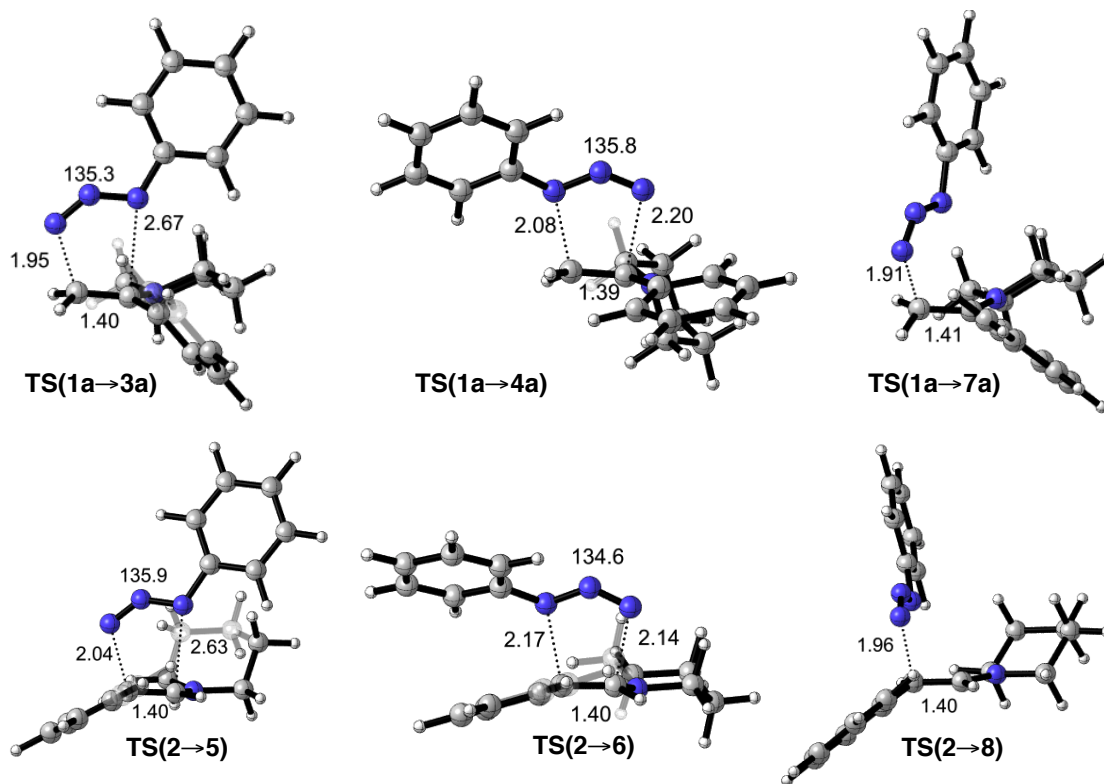


Figure 4. Three possible transition structures for the reactions of **1a–c** and **2** with phenyl azide as calculated by M06-2X/6-311G+(d,p) using IEF-PCM: CHCl₃. Bond lengths are in Ångstroms.

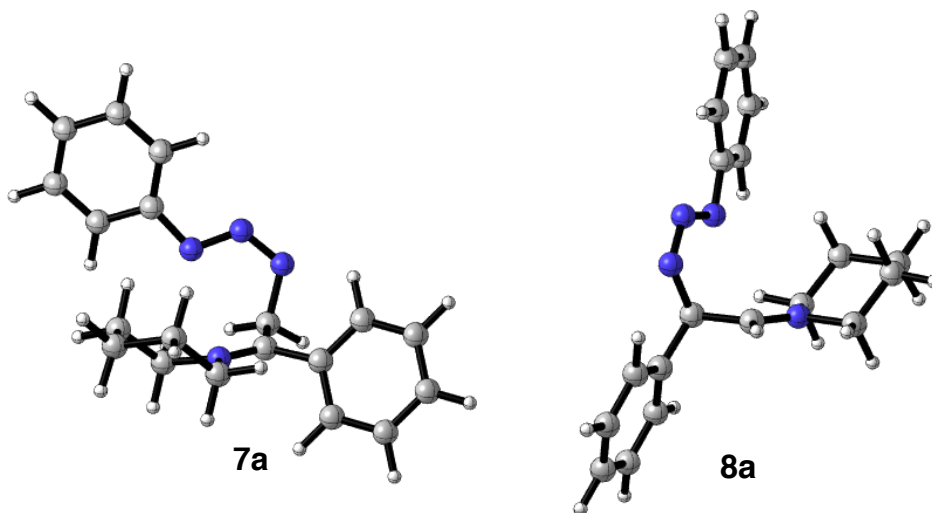
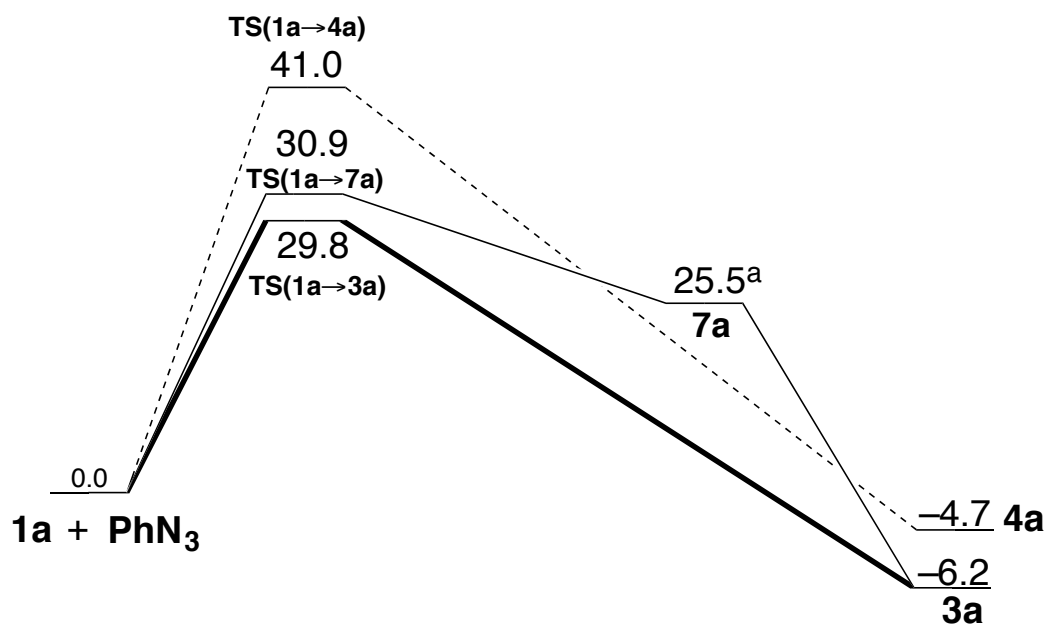


Figure 5. Optimized structures of zwitterionic **7a** and **8**.

The breaking π -bonds of the enamine substructure are very similar in the transition structures shown in Figure 4 (1.39 – 1.41 Å) as are the azide bond angles (135–136°). **TS(1a→3a)** and **TS(2→5)** have transition state bond lengths between the β -carbon and terminal

azide nitrogen (C_2-N_3) that are more developed than the C_1-N_1 bond [1.95 Å vs. 2.67 Å for **TS(1a→3a)** and 2.04 Å vs. 2.63 Å for **TS(2→5)**]. Based on these bond lengths, the corresponding asynchronicities are 0.72 Å and 0.59 Å. The transition states leading to the unobserved cycloadducts [**TS(1a→4a)** and **TS(2→6)**] also have very similar enamine double bond lengths (1.39 Å and 1.40 Å, respectively). These transition states have more synchronous bond formation. **TS(1a→4a)** has a slightly more formed bond between C_2-N_1 (2.08 Å) than does **TS(2→6)** (2.17 Å). The C_1-N_1 bonds are also similar in **TS(1a→4a)** and **TS(2→6)** (2.67 Å and 2.63 Å, respectively).

The bond-forming step in the stepwise pathways **TS(1a→7)** than **TS(2→8)** have relatively short CN bonds (1.91 Å and 1.96 Å, respectively) in line with stepwise cycloadditions. The free energies (kcal mol⁻¹) of transition structures, intermediates, and products resulting from this mechanistic study are shown in Figure 6.



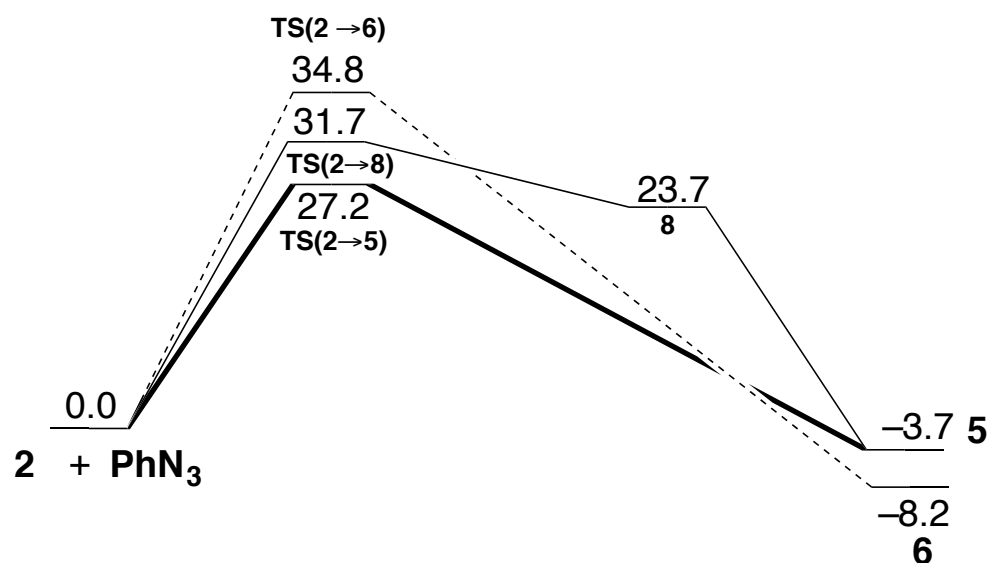


Figure 6. Potential energy diagram for the cycloadditions of **1a** with PhN₃ and **2** with PhN₃.^a The energy of **7a** is calculated using M06-2X/6-311+G(d,p)// M06-2X/6-31+G(d). Values are in kcal mol⁻¹.

The lowest energy transition states for the reactions of enamines **1a** and **2** with phenyl azide are highly asynchronous (Figure 4). **TS(1a→3a)** and **TS(2→5)** are 11.0 and 7.0 kcal mol⁻¹ more stable than **TS(1a→4a)** and **TS(2→6)**, respectively. **TS(1a→7a)** and **TS(2→8)** are disfavored by 1.1 and 4.5 kcal mol⁻¹, respectively and lead to zwitterionic intermediates, **7a** and **8**. Scans of the dihedral angles formed by C₂-C₁-N₃-N₂ in **7a** and **8**, leading to products, **3a** and **5** are shown in Figure 7. The scans reveal that the potential energy surface is relatively flat near zwitterionic intermediates, **7a** and **8**. The zwitterionic mechanism requires the rotation around the dihedral angle (C₂-C₁-N₃-N₂) until the termini of the azide and alkene interact, at which point the energy drops rapidly to form the second C-N bond. Although no ring closing transition state could be found on the potential energy surface, triazoline formation is stepwise.

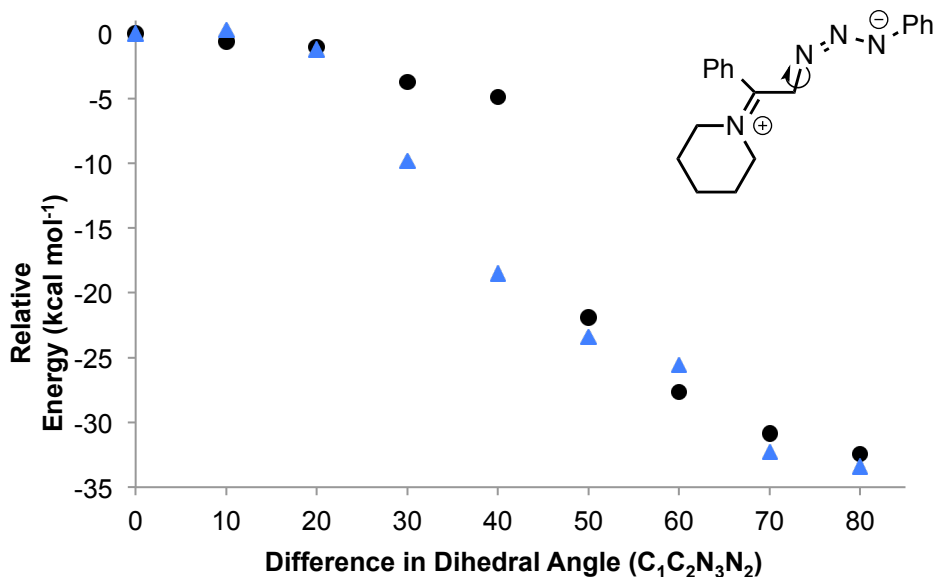


Figure 7. Dihedral angle scan of the ring closing from **7** (black circle) and **8** (blue triangle) to their respective products.

Table 1 shows the activation free energies derived from experimental rate constants for the reactions studied by Munk *et al.* using transition state theory. The computed barriers of those reactions are listed for comparison

Table 1. Rate constants ($M^{-1}s^{-1}$) reported by Munk *et al.* and the derived $\Delta G^{\ddagger}_{\text{expt}}$ values with reported errors. ΔG^{\ddagger} (kcal mol⁻¹) computed using M06-2X/6-311+G(d,p), B97D/6-311+G(d,p), and SCS-MP2/6-311+G(d,p)//M06-2X/6-311G+(d,p) IEF-PCM: CHCl₃. Reactions carried out in chloroform at 44.8 °C.

	$10^7 k_2$	$\Delta G^{\ddagger}_{\text{expt}}$	$\Delta H^{\ddagger}_{\text{expt}}$	$\Delta G^{\ddagger}_{\text{M06-2X}}$	$\Delta H^{\ddagger}_{\text{M06-2X}}$	$\Delta G^{\ddagger}_{\text{SCS-MP2}}$	$\Delta H^{\ddagger}_{\text{SCS-MP2}}$	$\Delta G^{\ddagger}_{\text{B97d}}$
1a	152	25.7 ± 1.2	15 ± 1.2	30.1	15.1	31.6	17.6	18.7
1b	33	$26.6 \pm .02^a$	-	31.1	-	31.8	-	19.8
1c	5167	$23.4 \pm .02^a$	-	27.9	-	28.8	-	16.7
2	1667	24.1 ± 1.2	13 ± 1.2	27.5	12.7	26.9	12.7	19.3

^a Error bars were derived from the report that the maximum error was 1.0%

M06-2X and SCS-MP2 calculations predict activation barriers higher than experimental ones and give the correct order of reactivity. Although B97D incorrectly predicts the order of reactivity if all four reactions in Table 1 are considered, ΔG^\ddagger are in the correct order for the three structurally related acetophenone enamines, **1a–c**. SCS-MP2 and M06-2X predict the correct order of reactivity for **1a–c**. SCS-MP2 and M06-2X incorrectly predict the activation barrier of **1c** to be higher than **2**, but the difference is within experimental error. M06-2X predicts barriers 3-4 kcal mol⁻¹ higher than experiment. This is likely due to overestimation of $-T\Delta S^\ddagger$ for these bimolecular reactions in solution. This is supported by the ΔH^\ddagger of entries 1 and 2 in Table 1 where M06-2X energetics agree quite closely with experimental barriers. Figure 8 shows the $\Delta G_{\text{expt}}^\ddagger$ vs. $\Delta G_{\text{comp}}^\ddagger$ for the three methods used in this work. The discussion refers to the quantum mechanical results using the M06-2X functional.

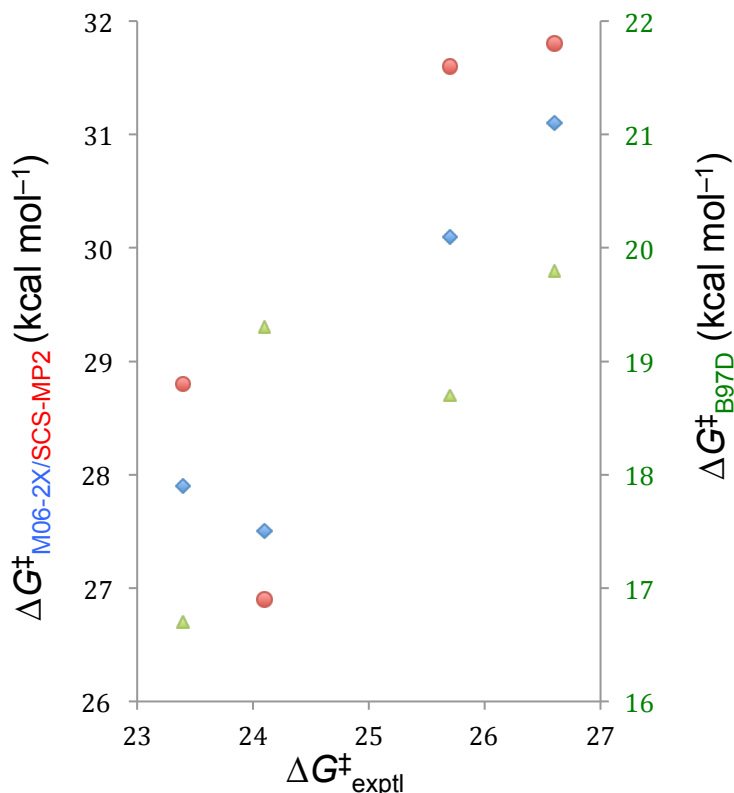


Figure 8. $\Delta G_{\text{exptl}}^{\ddagger}$ values are derived from experimental rate constants. $\Delta G_{\text{comp}}^{\ddagger}$ energies are computed in solvent using IEF-PCM (CHCl_3). The reactions of phenyl azide with **1a–c** and **2** M06-2X/6-311G+(d,p) (blue diamond), and SCS-MP2/6-311+G(d,p)//M06-2X/6-311G+(d,p) (red circle) and B97D/6-31G(d,p) (green triangle).

Regioselectivities

The energetics for formation of the regioisomers were shown in Figure 6. The activation energies for formation of regioisomers **3a** and **5** are 7 and 11 kcal mol⁻¹ lower than the formation of unobserved products, **4a** and **6**. Previous studies by Munk *et al.* and Pocar *et al.* attempted to decrease the regioselectivity of the enamine-azide 1,3-dipolar cycloaddition by utilizing more sterically bulky enamines. Tetrasubstituted enamines were used as dipolarophiles, but only one regioisomer was formed in these studies because of the cited electronic control that results from the electron donation from nitrogen resonance donation.^{20,21}

The distortion/interaction model developed by our group¹⁰ has recently been used to explain reactivities and selectivities of cycloadditions in bioorthogonal reactions,^{22,23} materials chemistry,²⁴ and palladium-catalyzed cross-coupling reactions.²⁵ The distortion/interaction model dissects activation barriers (ΔE^\ddagger) of bimolecular reactions into distortion energies (ΔE_d^\ddagger) and interaction energies (ΔE_i^\ddagger). The distortion energy is the amount of energy required to distort phenyl azide and the enamine into their transition state geometries without allowing the cycloaddition partners to interact. The interaction energy arises from a combination of closed-shell (steric) repulsion, charge transfer involving occupied and vacant orbital interactions, electrostatic interactions, and polarization effects. These results of the distortion/interaction analysis are shown in Table 2.

Table 2. M06-2X/6-311G+(d,p) IEF-PCM:CHCl₃. Electronic activation (ΔE^\ddagger) energies, distortion energies (ΔE_d^\ddagger) interaction energies (ΔE_i^\ddagger) for the reactions of phenyl azide and enamines **1a** and **2**.

	ΔE^\ddagger (kcal mol ⁻¹)	ΔE_d^\ddagger Total (kcal mol ⁻¹)	ΔE_d^\ddagger Dipolarophile (kcal mol ⁻¹)	ΔE_d^\ddagger Azide (kcal mol ⁻¹)	ΔE_i^\ddagger (kcal mol ⁻¹)
TS(1a→3a)	14.6	31.8	7.0	24.8	-17.3
TS(1a→4a)	25.6	34.8	9.8	25.0	-9.2
TS(1a→7)	15.5	33.0	6.9	26.1	-17.6
TS(2→5)	11.8	30.0	6.6	23.4	-18.2
TS(2→6)	19.2	36.7	8.8	27.9	-17.6
TS(2→8)	16.5	34.6	7.9	26.7	-18.1

The distortion energy is comprised of of azide distortion energy and dipolarophile distortion energy. The exclusive formation of **3a** from **1a** results from the lowest energy transition state, **TS(1a→3a)**. **TS(1a→4a)** is less favorable because the interaction is 8.1 kcal mol⁻¹ less stabilizing. This arises from the more favorable HOMO–LUMO interaction as described in early FMO theories of cycloaddition regioselectivity.^{26,27,28,29} Figure 9 shows that the LUMO of PhN₃ is concentrated at the unsubstituted N terminus. This becomes united with the nucleophilic terminus β to the N; the site of the largest HOMO coefficient. The $\Delta\Delta E_d^\ddagger$ is relatively small (3.0 kcal mol⁻¹), the interaction energy controls the reactivity. Distortion energies reinforce the preference controlled by interaction energy, due to the relatively late transition structure (increased distortion energy).

The reaction of **2** with phenyl azide yields only **5**. $\Delta\Delta E_i^\ddagger$ is approximately equal (0.5 kcal mol⁻¹) for **TS(2→5)** and **TS(2→6)**. In this case, the favored product, **5**, is formed because of *distortion* energy control. The azide distortion energy is 4.5 kcal mol⁻¹ higher in **TS(2→6)** than in **TS(2→5)**. Figure 9 show that the HOMO of **2** is quite high and the terminal alkene π coefficients are nearly the same. Both transition states have favorable interaction energies. Figure 4 shows that the phenyl group of phenyl azide is aligned with the azide in **TS(1a→3a)** and **TS(2→5)**, but is bent 38° out of this plane in **TS(2→6)**. **TS(2→6)** allows favorable π stacking to occur, but this is unfavorable compared to the position of the phenyl group in **TS(2→5)**.

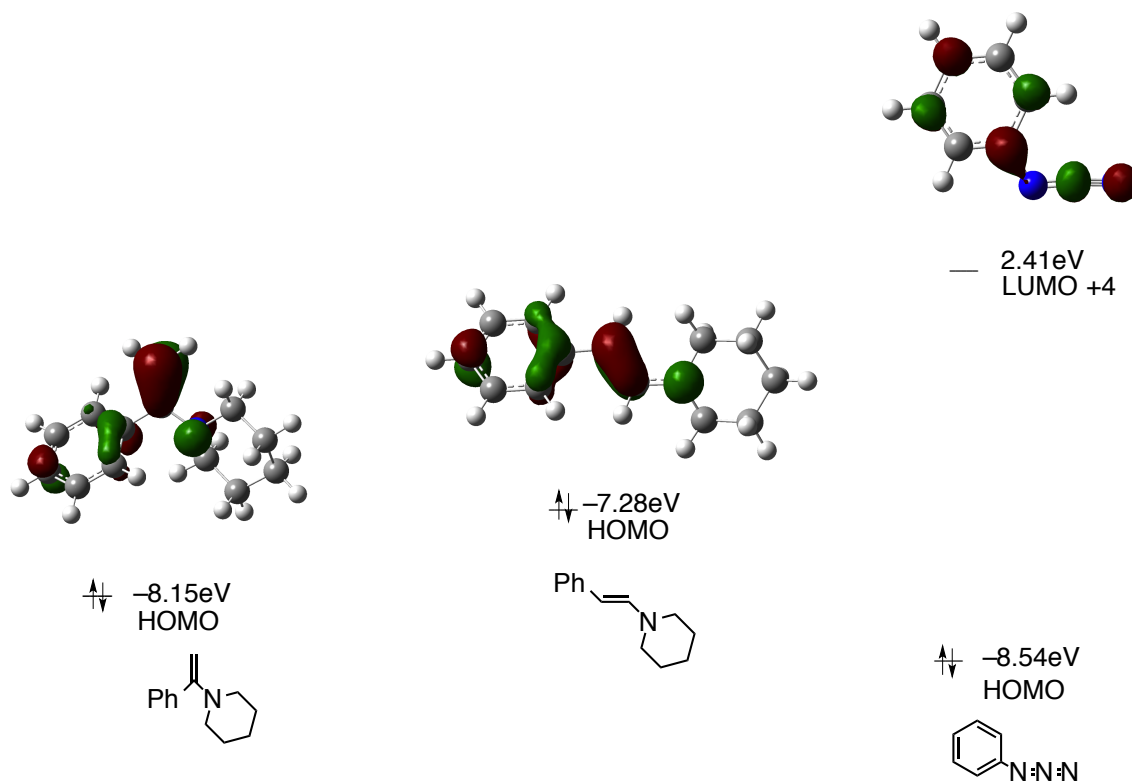


Figure 9. Frontier molecular orbitals and their energies of **1a**, **2**, and phenyl azide.

The polar nature of this reaction was thought to lead a charge-separated transition state. The high-lying enamine HOMO does indeed lead to significant charge transfer from the enamine to the azide. Table 3 lists the extent of charge separation (NBO³⁰) for the transition structures optimized in solvent (ethanol and chloroform). The large charge separation is due to the relatively small HOMO-LUMO gap resulting from the high-lying HOMO of the enamine and the LUMO of phenyl azide. There appears to be a small solvent effect as compared to the gas phase for the greatly charge separated transition states, **TS(1a→3a)** and **TS(2→5)**, but the activation barriers are higher for the disfavored transition states. The CPCM solvation model gave nearly identical results to the ones shown in Table 3. This result is consistent with the similar experimental rates determined by Munk *et al.* in chloroform and ethanol.⁸

Table 3. ΔG^\ddagger and for the three possible transition structures and the charge separation (NBO) in the transition structures.

	ΔG^\ddagger (kcal mol ⁻¹)	$\Delta G^\ddagger_{\text{CHCl}_3}$ (kcal mol ⁻¹)	$\Delta G^\ddagger_{\text{EtOH}}$ (kcal mol ⁻¹)	Charge separation (CHCl ₃)	Charge separation (EtOH)
TS(1a→3a)	32.4	29.8	32.0	0.37e	0.37e
TS(1a→4a)	42.9	43.3	45.0	0.06e	0.06e
TS(1a→7)	–	33.9	32.8	0.46e	0.44e
TS(2→5)	30.1	29.4	29.3	0.36e	0.36e
TS(2→6)	36.1	37.1	37.1	0.17e	0.17e
TS(2→8)	–	33.2	33.0	0.48e	0.46e

Table 3 shows the significant charge separation for the favored (0.36-0.37e) and stepwise transition states (0.46–0.48e), and notably less for the disfavored transition states (0.06e–0.17e). The asynchronicities of the transition states are qualitatively correlated with the amount of charge separation in the transition state. The charge separation for **TS(1a→3a)** in both solvents is 0.37e indicative of a very polar transition state, whereas **TS(1a→4a)** has a charge separation of only 0.06e, more alike to a normal unactivated alkene azide cycloaddition transition state.^{31,32}

Cycloadditions of Pyrrolidine and Morpholine Enamines with Azides

Munk also investigated the cycloadditions of enamines consisting of morpholine and pyrrolidine. The publication states, “*Although piperidine and pyrrolidine are nearly equal in basicity, the acetophenone enamine of the latter amine is 34 times more reactive toward phenyl azide. In sharp contrast the piperidine enamine reacts only 4.5 times faster than the morpholine enamine in spite of the 1000-fold difference in amine basicity.*”⁸ The transition structures for these reactions [(**TS(1b→3b)**) and **TS(1c→3c)**] are shown in Figure 10. As with **TS(1a→3a)** and

TS(2→5), the transition states are quite asynchronous [0.71 Å and 0.68 Å for TS(1b→3b) and TS(1c→3c), respectively].

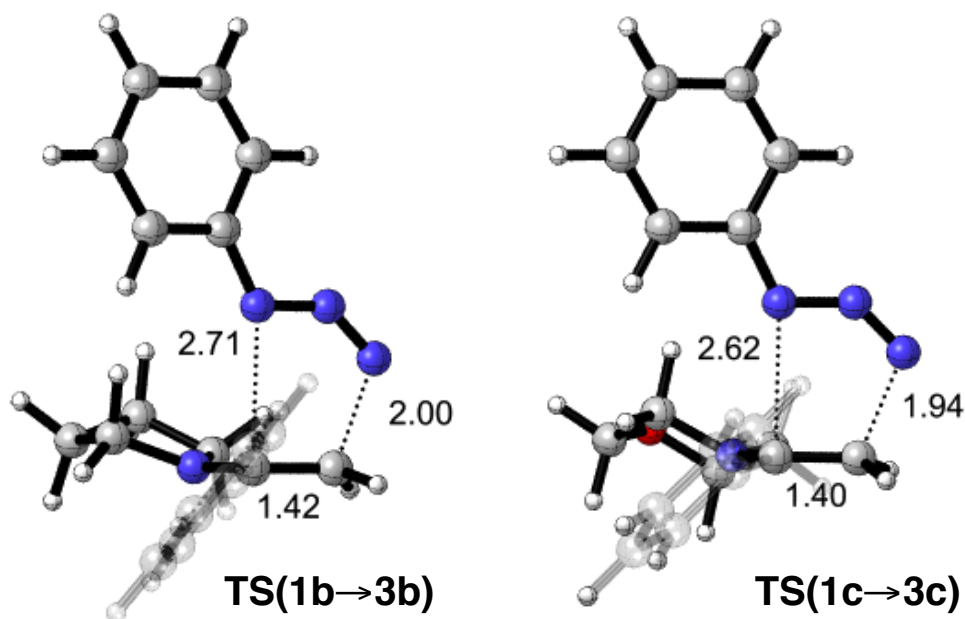


Figure 10. TS(1b→3b) and TS(1c→3c) with phenyl azide as calculated by M06-2X/6-311G+(d,p) using IEF-PCM: CHCl₃. Bond lengths are in Å and the phenyl groups were made transparent for more clear view of the transition states.

Munk *et al.* cite the superior resonance donation of the pyrrolidine relative to piperidine and attribute the greater reactivity of **1b** over **1a** to this.³³ Table 4 shows a small range of interaction energies (−17.6 to −16.3 kcal mol^{−1}), whereas the distortion energies have a larger range (28.7 to 33.0 kcal mol^{−1}). The distortion energy controls the reactivity of the enamines **1a–c** towards PhN₃.

Table 4. ΔE^\ddagger , ΔE_d^\ddagger , ΔE_i^\ddagger , and ΔG^\ddagger for the morpholine and pyrrolidine enamine cycloaddition reactions with phenyl azide. Calculated by M06-2X/6-311+G(d,p)

TS	ΔE^\ddagger (kcal mol ⁻¹)	ΔE_d^\ddagger (kcal mol ⁻¹)	ΔE_i^\ddagger (kcal mol ⁻¹)	ΔG^\ddagger (kcal mol ⁻¹)	$k_2 \times 10^3$ (Lmol ⁻¹ min ⁻¹)
TS(1a→3a)	14.6	31.8	-17.3	29.8	0.91
TS(1b→3b)	12.4	28.7	-16.3	27.6	31.
TS(1c→3c)	15.4	33.0	-17.6	30.7	0.20

The sterically crowded environment of the 1,1-disubstituted enamines (**1a–c**) allows only one of the substituents to become planar with the double bond. The five membered ring of pyrrolidine can planarize more effectively, which results in maximum overlap with reduced distortion energy penalty than piperidine. **TS(1a→3a)** and **TS(1c→3c)** have nearly equivalent distortion energies (31.8 and 33.0 kcal mol⁻¹). **TS(1b→3b)** has reduced distortion energy (28.7 kcal mol⁻¹), which reflects the relative ease with which pyrrolidine is planarizes to the transition state geometry.

Conclusion

We have found that the cycloadditions of enamines with phenyl azide are concerted reactions with asynchronous transition states. Both distortion and interaction energies are influential on determining regioselectivities.

Acknowledgements

K. N. Houk and M. E. Munk were the project directors. We thank the National Science Foundation (NSF CHE- 1059084) for financial support of this research. The computations were performed on the UCLA IDRE Hoffman2 cluster.

References

- ¹ Kolb, H. C.; Finn, M. G.; Sharpless, K. B. *Angew. Chem., Int. Ed.* **2001**, *40*, 2004.
- ² Agard, N. J.; Prescher, J. A.; Bertozzi, C. R. *J. Am. Chem. Soc.*, **2004**, *126*, 15046.
- ³ Chang, P. V.; Prescher, J. A.; Sletten, E. M.; Basin, J. M.; Miller, I. A.; Agard, N. J.; Lo, A.; Bertozzi, C. R. *Proc. Nat. Acad. Sci. U.S.A.* **2010**, *107*, 1821.
- ⁴ Karver, M. R.; Weissleder, R.; Hilderbrand, S. A. *Angew. Chem., Int. Ed.* **2012**, *51*, 920.
- ⁵ Cao, Y.; Houk, K. N. *J. Mater. Chem.* **2011**, *21*, 1503.
- ⁶ Kolb, H. C.; Finn, M. G.; Sharpless, K. B. *Angew. Chem., Int. Ed.* **2001**, *40*, 2004.
- ⁷ Agard, N. J.; Prescher, J. A.; Bertozzi, C. R. *J. Am. Chem. Soc.*, **2004**, *126*, 15046.
- ⁸ Meilahn, M. K.; Cox, B.; Munk, M. E. *J. Org. Chem.* **1975**, *40*, 819.
- ⁹ Jones, G. O.; Houk, K. N. *J. Org. Chem.* **2008**, *73*, 1333.
- ¹⁰ Ess, D. H.; Houk, K. N. *J. Am. Chem. Soc.* **2007**, *129*, 10646.
- ¹¹ Frisch, M. J.; et. al. (see complete reference in the Supporting Information). *Gaussian 09*, revision C-01; Gaussian Inc.; Wallingford, CT, 2009.
- ¹² Zhao, Y.; Truhlar, D. G. *Theor. Chem. Acc.* **2008**, *120*, 215.
- ¹³ Grimme, S. *J. Comp. Chem.* **2006**, *27*, 1787.
- ¹⁴ (a) Grimme, S. *J. Chem. Phys.* **2003**, *109*, 3067. (b) Grimme, S. *J. Chem. Phys.* **2003**, *118*, 9095. (c) Greenkamp, M.; Grimme, S. *Chem. Phys. Lett.* **2004**, *392*, 229.
- ¹⁵ Tomsí, J.; Mennucci, B.; Cancès, E. *Theochem* **1999**, *464*, 211.

-
- ¹⁶ Zhao, Y.; Truhlar, D. G. *Phys. Chem. Chem. Phys.* **2008**, *10*, 2813.
- ¹⁷ Ribeiro, R. F.; Marenich, A. V.; Cramer, C. J.; Truhlar, D. G. *J. Phys. Chem. B.* **2011**, *115*, 14556.
- ¹⁸ Huisgen, R.; Mloston, G.; Langhals, E. *J. Org. Chem.* **1986**, *51*, 4085.
- ¹⁹ Quast, H.; Manfred, B.; Hergenroether, T.; Regnat, D.; Lehmann, J.; Banert, K. *Helvetica Chimica Acta* **2005**, *88*, 1589.
- ²⁰ Kim, Y. K.; Munk, M. E. *J. Am. Chem. Soc.* **1964**, *86*, 2213.
- ²¹ Fusco, R.; Bianchetti, G.; Pocar, D. *Gazz. Chim. Ital.* **1961**, *91*, 849.
- ²² Gordon, C. G.; Mackey, J. L.; Jewett, J. C.; Sletten, E.; Houk, K. N.; Bertozzi, C. R. *J. Am. Chem. Soc.* **2012**, *134*, 9199.
- ²³ Liang, Y.; Mackey, J. L.; Lopez, S. A.; Liu, F.; Houk, K. N. *J. Am. Chem. Soc.* **2012**, *134*, 17904.
- ²⁴ Cao, Y.; Houk, K. N. *J. Mater. Chem.* **2011**, *21*, 1503.
- ²⁵ Schoenebeck, F.; Houk, K. N. *J. Am. Chem. Soc.* **2010**, *132*, 2496.
- ²⁶ Houk, K. N. *J. Am. Chem. Soc.* **1972**, *94*, 8953.
- ²⁷ Houk, K. N.; Sims, J.; Duke Jr., R. E.; Strozier, R. W.; George, J. K. *J. Am. Chem. Soc.* **1973**, *95*, 7287.
- ²⁸ Houk, K. N.; Sims, J.; Watts, C. R.; Luskus, L. J. *J. Am. Chem. Soc.* **1973**, *95*, 7301.
- ²⁹ Sustman, R.; Trill, H. *Angew. Chem., Int. Ed. Engl.*, **1972**, *11*, 838.
- ³⁰ Foster, J. P.; Weinhold, F.; *J. Am. Chem. Soc.* **1980**, *102*, 7211.
- ³¹ Huisgen, R.; Szeimies, G.; Möbius, L.; *Chem. Ber.* **1967**, *100*, 2494.
- ³² Scheiner, P.; Schomaker, J. H.; Deming, S.; Libbey, W. J.; Novak, G. P. *J. Am. Chem. Soc.* **1965**, *87*, 306.

³³ Stork, G.; Brizzolara, A.; Landesman, H.; Szmuszkovicz, J.; Terrell, R. *J. Am. Chem. Soc.*
1963, *85*, 207.

Chapter 6

1,3-Dipolar cycloaddition reactivities of perfluorinated aryl azides with enamines and strained dipolarophiles^a

ABSTRACT: The reactivities of enamines and pre-distorted (strained) dipolarophiles towards perfluoroaryl azides (PFAAs) were explored experimentally and computationally. Kinetic analyses indicate that PFAAs undergo 3+2 cycloadditions with enamines up to four orders of magnitude faster than phenyl azide reacts with these dipolarophiles. DFT calculations were used to identify the origin of this rate acceleration. Orbital interactions between the cycloaddends are larger due to the relatively low-lying LUMO of PFAAs. The triazolines resulting from PFAA-enamine cycloadditions rearrange to amidines at room temperature, while 3+2 cycloadditions of enamines and phenyl azide yield stable, isolable triazolines. The 1,3-dipolar cycloadditions of norbornene and DIBAC also show increased reactivity towards PFAAs over phenyl azide, but are slower than enamine-azide cycloadditions.

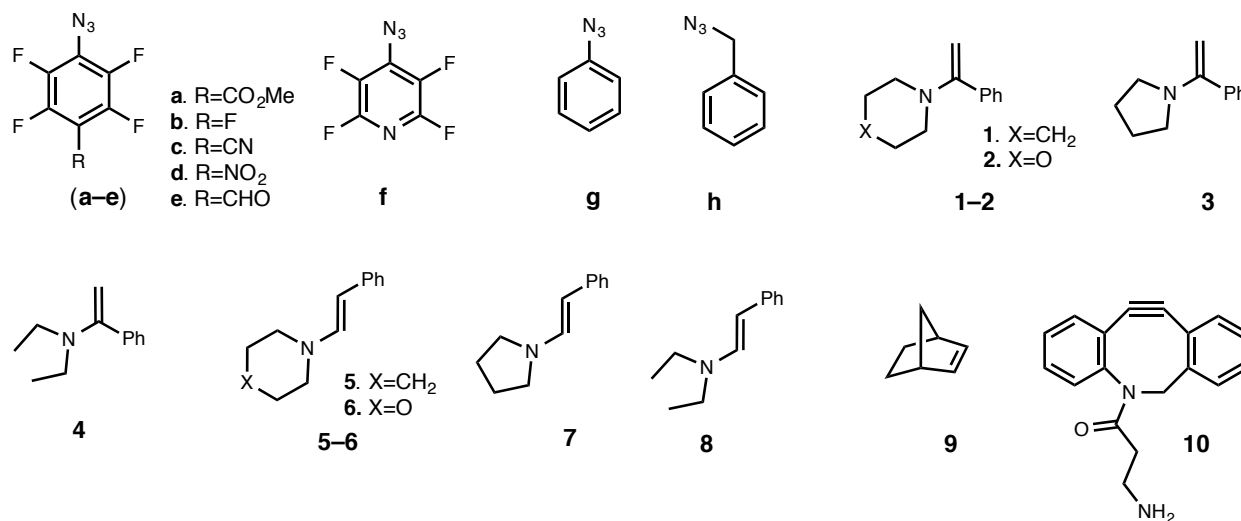
^a Reprinted with permission from *Journal of the American Chemical Society* **2014**, *137*, 8, 2958–2966. Copyright 2014 American Chemical Society. Authors are S. Xie, Steven Alexander Lopez, Olof Ramström, Mingdi Yan, and K. N. Houk

Introduction

Perfluorinated aryl azides (PFAAs) have been extensively utilized for the functionalization of materials and surfaces¹ and for photoaffinity labeling.² PFAAs are easily converted to nitrenes by photolysis or thermolysis. They are also relatively electrophilic due to the presence of strongly electronegative fluorine atoms. PFAAs have been further used as photocoupling agents, primarily by the Yan group, to functionalize surfaces and nanomaterials³ and are relatively stable to elevated temperatures. Here we report a theoretical and experimental exploration of the 1,3-dipolar cycloadditions of PFAAs to expand the scope of reagents that can be used for surface functionalization.

Huisgen discovered 1,3-dipolar cycloadditions of azides in the 1960s.⁴ Meldal and Sharpless independently developed the click reaction of azides and terminal alkynes that requires Cu-catalysis. The resulting triazoles are formed efficiently and regioselectively,^{5,6} and have since increased interest in the cycloaddition.⁷ Azide-alkyne cycloadditions, particularly those involving strained alkynes, now constitute a key bioorthogonal reaction used to label biomolecules *in vivo*.⁸ Initial calculations on 1,3-dipolar cycloadditions of PFAAs predicted that these electron-deficient aryl azides would undergo rapid cycloadditions with electron-rich dipolarophiles such as enamines. We explored substituent effects on several aryl azides with various *p*-electron withdrawing groups (EWGs) (**a–f**) in cycloadditions to enamines (**1–8**), norbornene (**9**), and DIBAC (**10**) (Scheme 1). The rates for these cycloadditions are compared to those for ambiphilic azides **g** and **h**.

Scheme 1. Scope of azides and dipolarophiles for the (3+2) cycloadditions studied here.



Computational Methods

All computations were carried out with *Gaussian09*.⁹ Reactants, transition states, and products were optimized with the density functional M06-2X¹⁰ using the 6-31G(d) basis set with an ultrafine grid, consisting of 590 radial shell and 99 grid points per shell.¹¹ M06-2X has been found to give reliable energetics for cycloadditions involving main group elements.¹² Normal vibrational mode analysis confirmed all stationary points to be minima (no imaginary frequencies) or transition states (one imaginary frequency). Zero point energy and thermal corrections were computed from unscaled frequencies for the standard state of 1 M and 298.15 K. Truhlar's quasiharmonic correction was applied for entropy calculations by setting all frequencies less than 100 cm⁻¹ to 100 cm⁻¹.^{13,14} Input structures for these computations were generated using Gaussview.

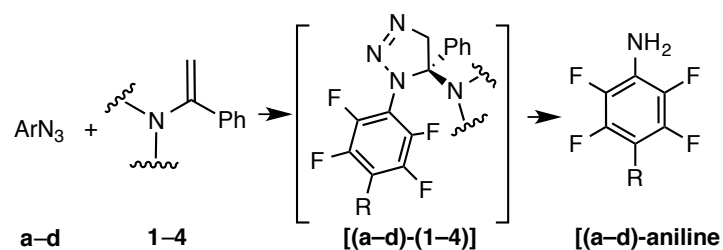
Results/Discussion

The rate constants for these 1,3-dipolar cycloadditions were determined in CDCl_3 at 25 °C with a 2:1 ratio of azide to dipolarophile. Most reactions were monitored by $^1\text{H-NMR}$ or $^{19}\text{F-NMR}$ spectroscopy, and the second order rate constants (k_c) were found based on the triazoline or triazole formation rate. Detailed information about the kinetic studies we performed can be found in the experimental section and in the Supporting Information.¹⁵

Acetophenone-Derived Enamine Cycloadditions

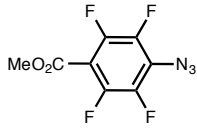
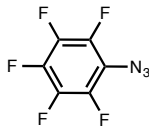
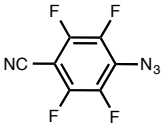

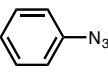
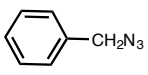
The reaction of acetophenone enamines and PFAAs gave perfluoroanilines as the major products (60–90% isolated yields) on the basis of $^{19}\text{F-}$ and $^1\text{H-NMR}$ spectroscopy.⁹ These triazolines decomposed to perfluoroanilines by a mechanism for which the mechanism is not known with certainty (Scheme 2).¹⁶

Scheme 2. Cycloadditions of PFAAs and acetophenone enamines.



The k_c for the cycloadditions of azides to enamine **1** are listed in Table 1. These data are presented as a plot of triazoline concentration vs. time in the Supporting Information.⁹

Table 1. Rate constants (k_c) for the (3+2) cycloadditions of (**a-d**, **g**, and **h**) to **1**.^a

Azide	k_c ($10^{-2} \text{M}^{-1} \text{s}^{-1}$)	k_{rel}^b	$\Delta G_{\text{exp}}^{\ddagger c}$ (kcal mol^{-1})
	1.41 ± 0.04	16,300	20.0 ± 0.1
	0.126 ± 0.05	1,450	21.0 ± 0.1
	11.8 ± 0.06	135,000	18.4 ± 0.1
	15.9 ± 0.4	185,000	18.2 ± 0.1
	$0.867 \pm 0.04 \times 10^{-4}$	1	25.3 ± 0.1
	n.d.	–	–

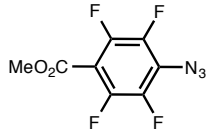
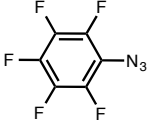
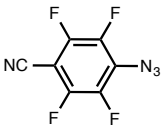
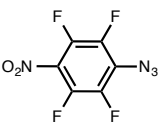

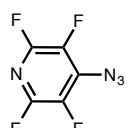
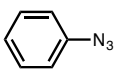
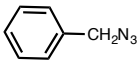
^aConditions: [Azide]:[Enamine] 2:1, ¹H- and ¹⁹F-NMR in CDCl₃, 293.0 K, Figure S2-S6. ^b $k_{\text{rel}} = k_c(\mathbf{a-h})/k_c(\mathbf{g})$. ^cCalculated from Eyring equation. ^dNo cycloaddition detected by NMR.

Phenylacetaldehyde-Derived Enamine Cycloadditions

Scheme 3 shows the 1,3-dipolar cycloadditions of (**a-f**), to enamines (**5-8**) under ambient conditions. Intermediate triazolines bearing a perfluoroaryl group undergo N₂-extrusion and rearrange (observed by ¹H-NMR) to afford amidines (Scheme 3).

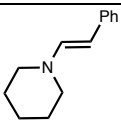
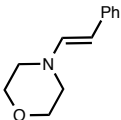
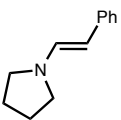
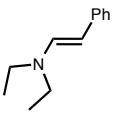
Table 2 gives k_c and the corresponding experimental activation free energies ($\Delta G_{\text{exp}}^\ddagger$). Rate constants for cycloadditions were found in the same manner as for reactions of acetophenone-derived enamines. However, triazolines [(a-g)-(5-8)] decompose to form amidines [(a-g)-(5-8)]'.

Table 2. Rate constants (k_c) for the (3+2) cycloadditions of azides (a–h) and phenylacetaldehyde piperidine enamine **5**.^a

Azide	k_c ($10^{-2} \text{M}^{-1} \text{s}^{-1}$)	k_{rel}^b	$\Delta G_{\text{exp}}^\ddagger^c$ (kcal mol ⁻¹)
	7.22 ± 0.04	9,080	18.7 ± 0.1
	1.05 ± 0.03	1,320	19.8 ± 0.1
	97.2 ± 2.4	122,000	17.2 ± 0.1
	121.6 ± 3.2	153,000	17.0 ± 0.1
	35.9 ± 0.6	45,000	17.7 ± 0.1
	80.8 ± 0.2	102,000	17.3 ± 0.1
	1.85×10^{-3}	1	24.0 ± 0.1^d
	$< 10^{-5} \text{ (f)}$	—	—

The rate constants for the cycloadditions of **5–8** and aryl azides (**a** and **b**) are listed in Table 3. The reactivities of PFAAs with phenylacetaldehyde-derived enamines follow the same trend as that of acetophenone-derived enamines, but have k_c that are 5 to 10 fold greater. This is likely due to the greater steric bulk associated with ketonic enamines. The reaction between **a** and **5** is nearly four orders of magnitude faster than that of phenyl azide. The rate constant for the cycloaddition of 4-nitroperfluorophenyl azide (**d**) and **5** is $1.216 \pm 0.032 \text{ M}^{-1} \text{ s}^{-1}$, which is the fastest for the cycloaddition of an azide with an unstrained dipolarophile. The mechanism of 1,3-dipolar cycloadditions involving enamines and phenyl azide has been explored experimentally by Munk¹⁹ and computationally by Houk.²⁰ The rate constants of the cycloaddition of PFAA **a** and **b** to enamines (**5–8**) were subsequently measured and are listed in Table 3.

Table 3. Rate constants of the cycloadditions of **a** and **b** with **5–8**.^a Relative rate constants are given in parentheses.

Enamine	k_c (a) ($10^{-2} \text{ M}^{-1} \text{ s}^{-1}$)	k_c (b) ($10^{-2} \text{ M}^{-1} \text{ s}^{-1}$)
	7.22 ± 0.04 (11)	1.05 ± 0.03 (11)
	0.639 ± 0.001 (1)	0.098 ± 0.002 (1)
	17.6 ± 0.2 (27)	2.29 ± 0.06 (23)
	10.1 ± 0.1 (16)	1.35 ± 0.03 (14)

^aRates were determined by ¹H- and ¹⁹F-NMR in CDCl₃, [Azide]:[Enamine] 2:1, 293.0K.

The reactivities of enamines towards PFAAs decrease in the following order: **7**, **5**, **6**. Munk *et al.* observed the same trend experimentally for the reactions of phenyl azide with the same substrates.^{13a} Lopez and Houk showed that the reactions of PhN₃ and enamines are concerted and proceed through relatively asynchronous transition structures.¹³ The asynchronicities of the reactions arise from strong orbital interactions of the high-lying enamine HOMO with the LUMOs of phenyl azide, and to a greater extent with the PFAAs studied here. Computationally, both concerted and stepwise mechanisms were considered; the transition structures for both modes of cycloaddition are shown in Figure 2.

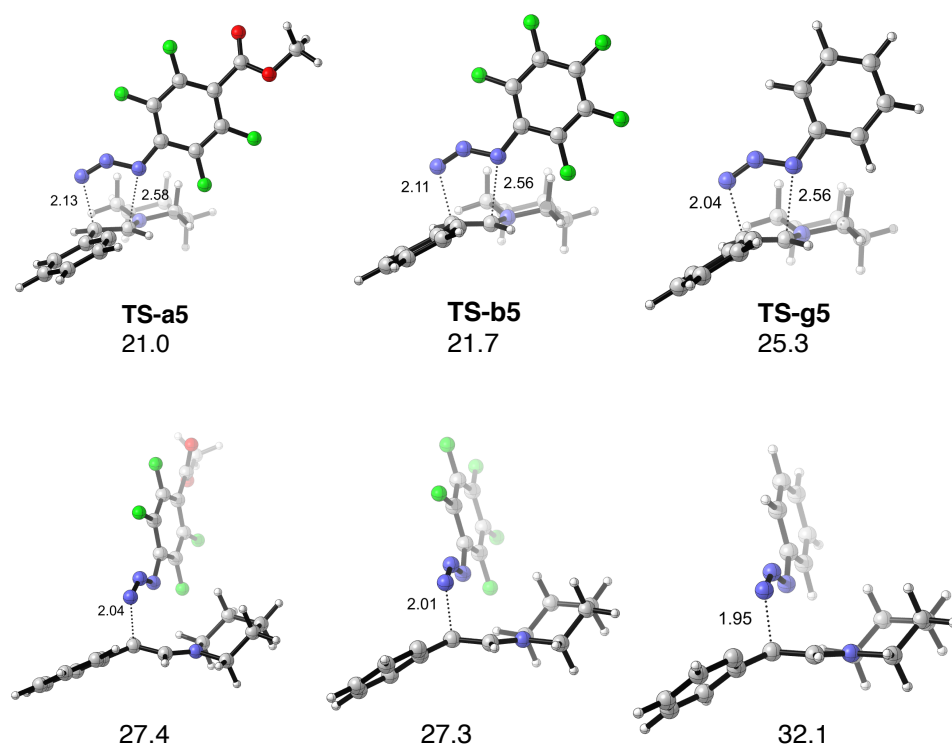


Figure 2. The concerted transition structures for the (3+2) cycloaddition of PFAAs (**a** and **b**) and phenyl azide (**g**) to **5** are in the left column. The stepwise transition structures are in the right column. Computed using M06-2X/6-311+G(d,p)/IEFPCM^{CHCl₃}//M06-2X/6-31G(d)/IEFPCM^{CHCl₃}. Bond lengths are reported in Å, and reported energies, are Gibbs free energies in kcal mol⁻¹ determined assuming a standard state of 1 M and 298.15 K.

The activation free energies for the stepwise cycloadditions are greater than the ΔG^\ddagger of the corresponding concerted transition state by 5–7 kcal mol⁻¹ and will not be considered further. The computed activation free energies for concerted cycloadditions are overestimated by 1–3 kcal mol⁻¹ relative to experimentally-determined rates. However, the qualitative reactivity trends observed experimentally are reproduced computationally.

Figure 2 shows that the activation free energies decrease for the transition structures involving increasingly electron-deficient aryl azides along the series **TS-g5**, **TS-b5**, **TS-a5** ($\Delta G^\ddagger = 25.3$, 21.7, 21.0, respectively). These transition structures are concerted but asynchronous. The transition structures have bond lengths between the β -carbon and terminal azide nitrogen (C_β -N) that are more developed than the other forming bond (C_α -N). The (C_α -N) forming bond lengths (ca. 2.6 Å) are nearly unchanged in these transition structures. The C_β -N forming bond lengths are also similar in **TS-a5** and **TS-b5** (ca. 2.1 Å). This forming bond is notably shorter in **TS-g5**, 2.04 Å.

We utilized the Distortion/Interaction model²¹ to understand the origins of the reactivity difference of PFAAs studied experimentally with enamines and strained dipolarophiles. The activation energy (ΔE^\ddagger) is dissected into distortion energy (ΔE_d^\ddagger) and interaction energy (ΔE_i^\ddagger). Distortion energy is the energy required to distort each of the reactants into their respective transition state geometries, without allowing the fragments to interact. The interaction energy is the energy of interaction between the distorted cycloaddends. It is often a net stabilizing quantity that results from charge transfer of occupied-vacant orbital interactions, electrostatic interactions, polarization, and closed-shell (steric) repulsions. Figure 3 summarizes our findings as a graph of ΔE^\ddagger , ΔE_d^\ddagger (enamine), ΔE_d^\ddagger (azide), and ΔE_i^\ddagger for **TS-a5**, **TS-b5**, and **TS-g5**.

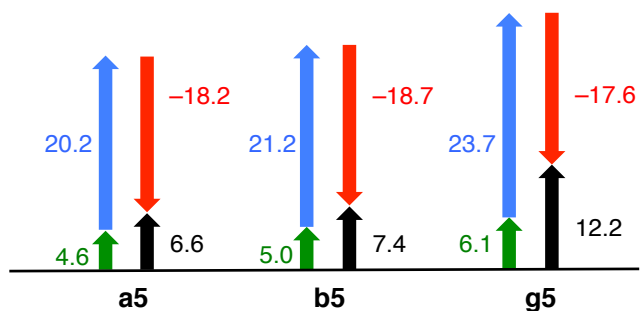


Figure 3. Graph of activation, distortion, and interaction energies for **TS-a5**, **TS-b5**, and **TS-g5**. (black: activation energies, green: distortion energies of dipolarophile, blue: distortion energies of azides, red: interaction energies). Calculated using M06-2X/6-311+G(d,p)/IEFPCM^{CHCl3}//M06-2X/6-31G(d)/IEFPCM^{CHCl3}.

The graph in Figure 3 suggests that **TS-g5** has the highest activation energy because of increased total cycloaddend distortion and reduced interaction between the dipole and dipolarophile. Both components of distortion energy (green and blue) increase from left to right in Figure 3. **TS-g5** occurs latest, which means that the cycloaddends are most distorted from their reactant geometries. A Frontier Molecular Orbital (FMO) analysis can be used to understand how interaction energies contribute to the activation energies of these reactions. Figure 4 shows the computed molecular orbitals of enamine **5** and azides **a**, **b**, and **g**.

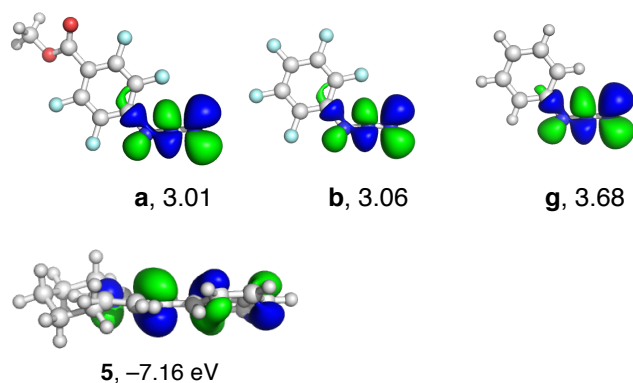


Figure 4. Computed LUMOs of azides **a**, **b**, **g** and the HOMO of enamine **5**. Orbital energies are reported in eV and calculated using HF/6-31G(d)//M06-2X/6-31G(d)/IEF-PCM^{CHCl3}.

The major stabilizing orbital interaction is between the HOMO of enamine **5** and the LUMO of **a**, **b**, and **g**. Perfluorination of the phenyl ring substantially lowers the azide LUMO energies of **a** and **b**, resulting in smaller HOMO-LUMO gaps and stronger FMO interactions.

1,3-Dipolar Cycloadditions of Norbornene and PFAAs

Motivated by the use of strained alkenes in bioorthogonal reactions, we explored the reactivity of norbornene towards PFAAs, (**a–c**, **f**), phenyl azide (**g**) and benzyl azide (**h**) (Scheme 4). Additions to norbornene are fast and *exo* stereoselective. At 25 °C, PFAAs react with norbornene faster than does phenyl azide. Rate constants for these reactions are summarized in Table 4.

Scheme 4. (3+2) cycloadditions of phenyl and benzyl azides to norbornene.

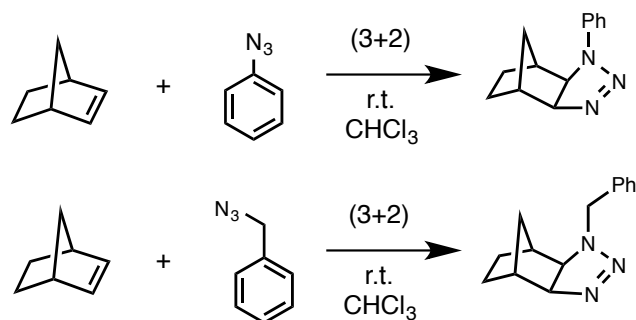
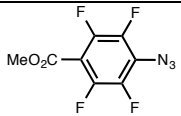

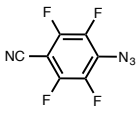
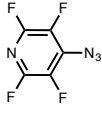
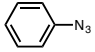
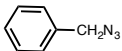


Table 4. Azide-norbornene (3+2) cycloaddition rate constants and corresponding activation free energies.^a

Azide	k_c ($10^{-4} \text{ M}^{-1} \text{ s}^{-1}$)	k_{rel}^b	$\Delta G^{\ddagger c}$ (kcal mol ⁻¹)
	9.13 ± 0.06	60	21.3 ± 0.1
	4.08 ± 0.03	27	21.8 ± 0.1
	28.0 ± 0.2	185	20.7 ± 0.1
	30.9 ± 0.2	205	20.6 ± 0.1
	0.151 ± 0.022	1	23.7 ± 0.1
	0.0184 ± 0.002	0.12	25.0 ± 0.1

^aConditions: [Azide]:[Norbornene] 2:1, ¹H- and ¹⁹F-NMR in CDCl₃, 294.7 K, Figure S20-S25.

^b $k_{\text{rel}} = k_{c(\text{a-h})}/k_{c(\text{g})}$. ^cCalculated from Eyring equation ($k_B = 1$).

Representative transition structures **TS-a9**, **TS-b9**, and **TS-g9** are shown in Figure 5. The transition structures are concerted, but slightly asynchronous. The bond length between the carbon and terminal azide nitrogen (C–N_{term}) is slightly shorter than that of the carbon and internal nitrogen (C–N_{int}) for each of these transition structures.

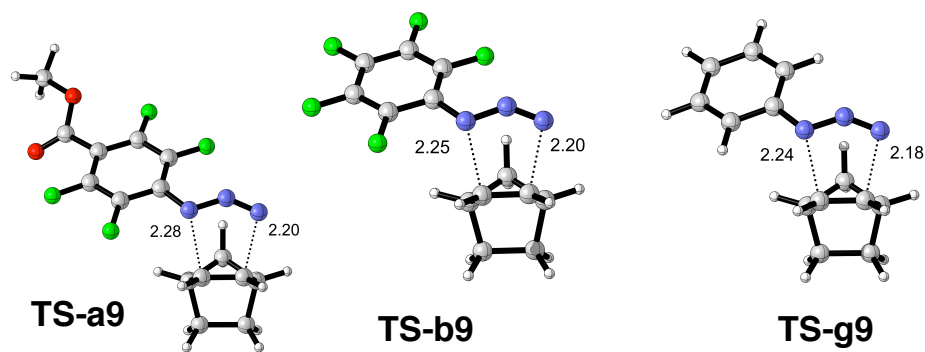


Figure 5. The transition structures for the (3+2) cycloadditions of norbornene (**9**) and **a**, **b**, and **g**. Computed using M06-2X/6311+G(d,p)/IEFPCM^{CHCl₃}//M06-2X/31G(d)/IEFPCM^{CHCl₃}.

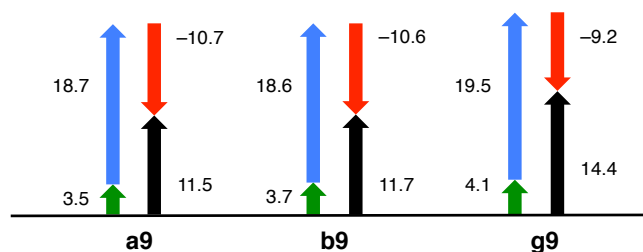


Figure 6. Graph of activation, distortion, and interaction energies for **TS-a9**, **TS-b9**, **TS-g9**. (black: activation energies, green: distortion energies of dipolarophile, blue: distortion energies of azides, red: interaction energies). Calculated using M06-2X/6-311+G(d,p)/IEFPCM^{CHCl₃}//M06-2X/6-31G(d)/IEFPCM^{CHCl₃}.

The ΔE^\ddagger of **TS-a9** and **TS-b9** are lower in energy (11.5 and 11.7 kcal mol⁻¹, respectively) than **TS-g9** (14.4 kcal mol⁻¹). The higher ΔE^\ddagger for PhN₃ cycloadditions arise from increased distortion energies and less favorable interaction energies. The ΔE_d^\ddagger of **TS-a9** and **TS-b9** are nearly identical (22.2 and 22.3 kcal mol⁻¹) and increase to 23.6 kcal mol⁻¹ in **TS-g9**. The newly-forming bonds in **TS-g9** are more developed than **TS-a9** or **TS-b9**, which require additional distortion of the cycloaddends to reach the geometries of the transition structures. The interaction energies are more favorable for **TS-a9** and **TS-b9** (-10.7 and -10.6, respectively) than **TS-g9** (-9.2 kcal mol⁻¹). The dominant FMO interaction is that of the dipole LUMO and the relatively high-lying HOMO (ca. -7.79 eV) of norbornene. The reactions with the greatest interaction energies involve the most electrophilic dipole, azide **a**.

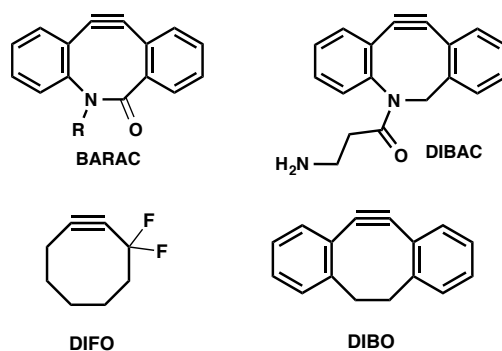
Reactivity enhancement by predistortion vs. orbital effects

Perfluorophenyl azide reacts with enamine **5** 25-fold faster than norbornene (**9**) ($k_c = 1.05 \times 10^{-2}$ and $4.08 \times 10^{-4} \text{ M}^{-1} \text{ s}^{-1}$, respectively). The distortion/interaction model was used to understand why orbital effects outweigh norbornene predistortion. The ΔE^\ddagger for **TS-b5** and **TS-b9** are 7.4 and 11.7 kcal mol⁻¹, respectively; the distortion energies are 26.1 and 22.3 kcal mol⁻¹, respectively. The double bond of norbornene is pyramidalized and resembles the *exo* transition structure (*i.e.*, the reaction is distortion accelerated).^{13a} The interaction energies for **TS-b5** and **TS-b9** are -18.7 and -10.6 kcal mol⁻¹, respectively. The HOMO of norbornene is not as high-lying as **5**, and does not interact strongly with the LUMO of **b**. The enhanced interaction energy component overrides norbornene predistortion.

Cycloadditions of DIBAC

In addition to examining norbornene as a dipolarophile in these cycloadditions, the cycloaddition of PFAAs with other pre-distorted dipolarophiles, including benzocyclooctynes bioorthogonal reagents like DIBAC,²² DIBO,²³ DIFO,²⁴ and BARAC were explored. These strained alkynes are used as bioorthogonal probes to label cell-surface azido glycans (Scheme 5).

Scheme 5. Some cyclooctynes DIBO, DIBAC, DIFO, and BARAC known to participate in bioorthogonal reactions.



BARAC shows the greatest reactivity towards benzyl azide cycloadditions ($0.96 \text{ M}^{-1} \text{ s}^{-1}$).²⁵ Computations by the Houk group have explained how predistortion and substituent effects control the reactivities of BARAC and its derivatives.²⁶ Here we performed cycloadditions of PFAAs, phenyl, and benzyl azide to DIBAC (**10**). Experimental observations using ¹H- and ¹⁹F-NMR for product **a-10** (Figure. S32) indicated a mixture of regioisomers in a ratio of 1:0.4. Attempts to assign the identity of the isomers however proved inconclusive. Rate constants were measured and are shown in Table 5.

Scheme 6. The regioisomeric products resulting from the reaction of **10** with azides (**a**, **b**, or **g**).

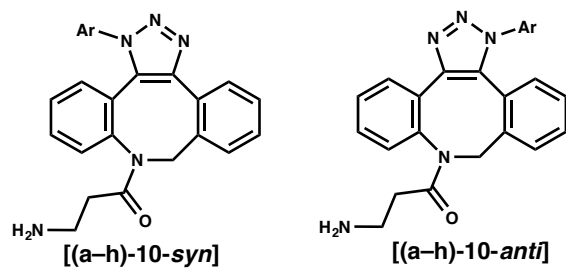
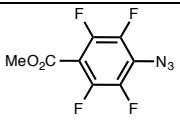
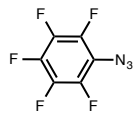
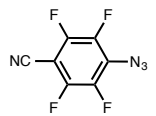
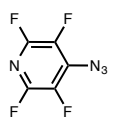
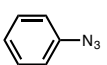
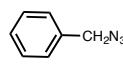


Table 5. Azide-DIBAC (**10**) cycloaddition rate constants^a and corresponding activation free energies.^a

Azide	k_c ($10^{-2} \text{ M}^{-1} \text{ s}^{-1}$)	k_{rel}^b	$\Delta G^{\ddagger c}$ (kcal mol^{-1})
	4.88 ± 0.11	1.96	19.0 ± 0.1
	11.1 ± 0.4	4.45	18.5 ± 0.1
	4.28 ± 0.1	1.72	19.1 ± 0.1
	2.58 ± 0.05	1.03	19.4 ± 0.1
	2.49 ± 0.03	1	19.4 ± 0.1
	21.9 ± 0.3	8.8	18.1 ± 0.1

^aConditions: [Azide]:[DIBAC] 2:1, ¹H- or ¹⁹F-NMR in CDCl₃, 294.7 K. Figure S26-S31. ^b k_{rel} : relative rate $k_c/k_{c(g)}$. ^cCalculated from Eyring equation ($k_B = 1$).

DIBAC is more reactive with PFAAs than with PhN₃ and is not regioselective. We use the M06-2X density functional to understand the reactivity differences of aryl azides towards **10** with model dibenzoazacyclooctyne, **11**. The global minimum of **11** is shown in Figure 7.

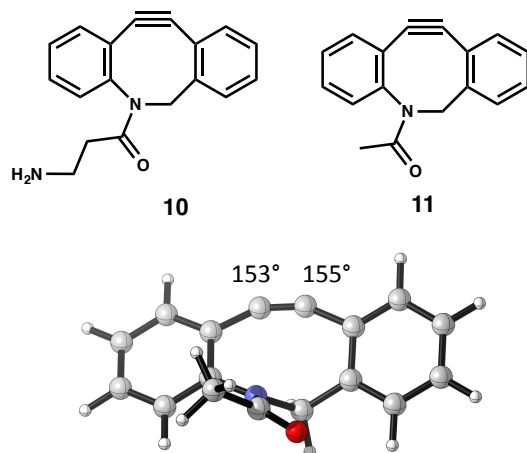


Figure 7. The lowest energy conformer of dibenzocyclooctyne **11**. The alkyne bond angles are reported in degrees.

As expected, the amide isomerization is facile at room temperature. We computed twelve possible transition structures (differing in *syn/anti* orientation of azide and *s-trans/s-cis* amide conformation, and three conformations of the aryl ring for the reaction of **a**, **b**, and **g** with **11** (See SI for higher energy transition structures). Table 6 shows the activation free energies for the regioisomeric transition structures for the reactions of azides **a**, **b**, and **g** to **11**. The lowest energy transition structures for the *syn* and *anti* approaches of the azide [TS(**g11-syn**) and TS(**g11-anti**)] are shown in Figure 8.

Table 6. The activation free energies for the cycloadditions involving **a**, **b**, and **g** to **11**. Activation free energies are reported in kcal mol⁻¹. Computed free energies in solution are for the standard state of 1 M and 298.15 K.

Azide	$\Delta G_{syn}^{\ddagger}$	$\Delta G_{anti}^{\ddagger}$
	23.4	24.1
	22.2	22.8
	24.0	24.0

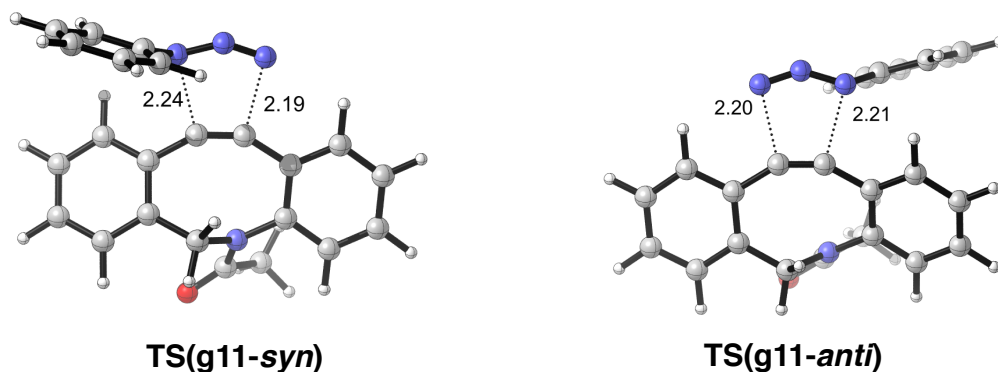


Figure 8. Lowest energy *syn* and *anti* transition structures for the cycloadditions of **g** to **11**. Bond lengths are reported in Å and energies in kcal mol⁻¹. Computed free energies in solution are for the standard state of 1 M and 298.15 K using M06-2X/6-311+G(d,p)/IEFPCM^{CHCl3}//M06-2X/6-31G(d)/IEFPCM^{CHCl3}.

These transition structures are almost perfectly synchronous. The C-N bond lengths range only from 2.19–2.24 Å. While computations do not quantitatively reproduce experimental activation free energies, the experimental reactivity trends are reproduced by theory. Our calculations show that the ΔG^\ddagger for **TS(a11-*syn*)** and **TS(b11-*syn*)** are lower in energy than the corresponding *anti* transition states by 0.7 and 0.6 kcal mol⁻¹, respectively. These results suggest that there should be a small preference for the *syn* regioisomers for PFAAs. The ΔG^\ddagger for **TS(g11-*syn*)** and **TS(g11-*anti*)** are identical, which should result in a 1:1 mixture of *syn* and *anti* regioisomers.

To understand why PFAAs are more reactive than phenyl azide in cycloadditions involving DIBAC, distortion/interaction analyses were performed on **TS(a11-*syn*)**, **TS(b11-*syn*)**, and **TS(g11-*syn*)** (Figure 9).

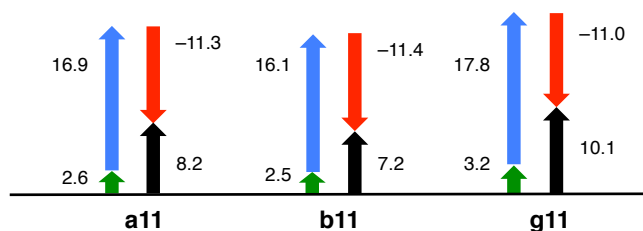


Figure 9. Graph of activation, distortion, and interaction energies for **TS-a11**, **TS-b11**, and **TS-g11**. (black: activation energies, green: distortion energies of dipolarophile, blue: distortion energies of azides, red: interaction energies). Calculated using M06-2X/6-311+G(d,p)/IEFPCM^{CHCl3}//M06-2X/6-31G(d)/IEFPCM^{CHCl3}.

The interaction energies are nearly constant, and the distortion energies control the small difference in reactivities.

Conclusion

We have experimentally and computationally explored the 1,3-dipolar cycloaddition of PFAAs to enamines and strained dipolarophiles (norbornene and DIBAC). Perfluorination of phenyl group of these aryl azides accelerates cycloadditions to all of the substrates studied here. This is due to improved orbital interactions with the relatively low-lying LUMO of PFAAs. Despite the predistortion of norbornene, PFAAs prefer to react with enamines because of the much more favorable interaction energies. These cycloadditions give triazolines as intermediates that rearrange at room temperature to give amidines, while cycloadditions involving enamines and phenyl azide yield isolable triazolines. The mechanism of triazoline decomposition is currently being investigated.

Acknowledgement

Sheng Xie performed all of the experiments. Dr. Yan and Ramstrom oversaw Sheng's work.

Experimental Methods

Materials. Azides, ketonic enamines, and aldehydic enamines were synthesized using reported procedures.^{27,28} All compounds were stored at $-20\text{ }^{\circ}\text{C}$ and compound purity was assessed by $^1\text{H-NMR}$ before performing kinetic studies. Norbornene (bicyclo[2.2.1]hept-2-ene, 99%) and DIBAC (dibenzocyclooctyneamine, >94.5%) were purchased from Sigma-Aldrich, and were used as received. In kinetic studies, CDCl_3 was filtered through K_2CO_3 and treated over molecular sieves. The amount of water in the purified CDCl_3 was 0.3 ppm measured by 756 KF Coulometer, which was <1 mole% enamines used in all kinetic studies.

Cycloaddition reaction between azide and enamine (Schemes 2 and 3). The following describes the reaction between PFPA **a** and enamine **5**. Other reactions were carried out using the same protocols. To a solution of **5** (1.0 mmol) in THF (1.0 mL), a solution of **a** (1.1 mmol) in THF (1.0 mL) was added dropwise while stirring at room temperature. Reaction progress was monitored by NMR spectroscopy. Upon a reaction's completion (8-12 hours), the solvent was removed under reduced pressure and the residual mixture was purified by flash column chromatography (hexanes/EtOAc= 9:1, R_f = 0.27) yielding (**a-5**)' as a white powder (390 mg, 95%). Alternatively, the reactions could be carried out in methanol (1.5-3 mL) using a slight excess of enamines (1.1 eq). In this case, the amidine product precipitated out from the solution within 12 hours and the product was separated by filtration (isolated yields > 70% for all amidines).

Cycloaddition between azide and norbornene (Scheme 4). The following describes the reaction of azide **c** with norbornene **9**. Reactions of other azides followed the same protocol. To a solution of norbornene **9** (1.25 mmol) in hexanes (2-4 mL), azide **c** (1.00 mmol) was added. The

solution was set at room temperature without stirring until a white solid started to form. When TLC indicated full conversion of the azide, the mixture was cooled to $-20\text{ }^{\circ}\text{C}$, filtered, and the solid was washed with a small amount of hexanes to afford the product as a white solid (270 mg, 87%).

Cycloaddition reaction between azide and DIBAC. In a typical reaction, a solution of DIBAC in CDCl_3 (9.0 mM) was added into a solution of azide (18 mM). The reactions were followed by NMR. The products were not isolated, and only characterized by NMR as presented in the kinetic studies.

Kinetic studies. Kinetic experiments were conducted using NMR following similar protocols reported in the literature.^{12,15,19} In a typical experiment, a solution of azide in deuterated solvent was mixed with an equal volume of the dipolarophile in an NMR tube at a mole ratio of 2:1. The ^1H - or ^{19}F -NMR spectra of the sample were recorded on a Bruker AVANCE (400 MHz or 500 MHz) spectrometer every 1.5-5 minutes. The acquisition time for a typical experiment was 30 seconds for ^1H -NMR and 18 seconds for ^{19}F -NMR. In the ^1H -NMR studies, the peaks of the dipolarophile were monitored, which decreased as the reaction proceeded. In the ^{19}F -NMR studies, the F signals in PFPAs and the cycloaddition products were followed. Each reaction was allowed to proceed to 10% - 90% conversion. Every experiment was repeated at least three times.

To calculate the rate constant of the cycloaddition reaction, the conversion-time curve was constructed. The curves were then fit to the standard second-order kinetic model using the statistic software GraphPad prism (see SI for detailed calculations). The characteristic peaks of

the intermediates and products can be found in corresponding datasheets in the supporting information.

Acknowledgements

K. N. Houk, O. Ramstrom, and M. Yan were the project directors. S. Xie performed all of the experiments. Steven Alexander Lopez performed all the calculations and wrote the majority of the manuscript. We thank the National Science Foundation (NSF CHE- 1059084) for financial support of this research. The computations were performed on the UCLA IDRE Hoffman2 cluster.

References

-
- ¹ (a) Cai, S.; Nabity, J. C.; Wybourne, M. N.; Keana, J. F. W. *Chem. Mater.* **1990**, *2*, 631. (b) Yan, M.; Cai, S.; Wybourne, M. N.; Keana, J. F. W., **1994**, *5*, 151. (c) Yan, M.; Cai, S.; Keana, J. F. W. *J. Org. Chem.* **1994**, *59*, 5951. (d) Yan, M.; Ren, J. *Chem. Mater.* **2004**, *16*, 1627. (e) Joester, D.; Klein, E.; Geiger, B.; Addadi, L. *J. Am. Chem. Soc.* **2006**, *128*, 1119.
- ² (a) Schnapp, K. A.; Poe, R.; Leyva, E.; Soundararajan, N.; Platz, M. S., *Bioconjug. Chem.* **1993**, *4*, 172. (b) Kapfer, I.; Jacques, P.; Toubal, H.; Goeldner, M. P., *Bioconjug. Chem.* **1995**, *6*, 109. (c) Tate, J. J.; Persinger, J.; Bartholomew, B., *Nucleic. Acids. Res.* **1998**, *26*, 1421. (d) Baruah, H.; Puthenveetil, S.; Choi, Y. A.; Shah, S.; Ting, A. Y., *Angew. Chem., Int. Ed.* **2008**, *47*, 7018. (e) Jung, M. E.; Chamberlain, B. T.; Ho, C. L.; Gillespie, E. J.; Bradley, K. A., *ACS. Med. Chem. Lett.* **2014**, *5*, 363.
- ³ (a) Liu, L. H.; Yan, M. *Acc. Chem. Res.* **2010**, *43*, 1434. (b) Pastine, S. J.; Okawa, D.; Kessler, B.; Rolandi, M.; Llorente, M.; Zettl, A.; Frechet, J. M. *J. Am. Chem. Soc.* **2008**, *130*, 4238. (c) Park, J.; Yan, M. *Acc. Chem. Res.* **2013**, *46*, 181. (d) Chen, X.; Ramström, O.; Yan, M., *Nano. Res.* **2014**, *7*, 1381.
- ⁴ Huisgen, R. *Angew. Chem., Int. Ed.* **1963**, *2*, 565.
- ⁵ (a) Rostovtsev, V. V.; Green, L. G.; Fokin, V. V.; Sharpless, K. B. *Angew. Chem., Int. Ed.* **2002**, *41*, 2596. (b) Agnew, H. D.; Rohde, R. D.; Millward, S. W.; Nag, A.; Yeo, W. S.; Hein, J. E.; Pitram, S. M.; Tariq, A. A.; Burns, V. M.; Krom, R. J.; Fokin, V. V.; Sharpless, K. B.; Heath, J. R. *Angew. Chem., Int. Ed.* **2009**, *48*, 4944.
- ⁶ Tornøe, C. W.; Christensen, C. and Meldal, M. *J. Org. Chem.* **2002**, *67*, 3057.

⁷ Brase, S.; Gil, C.; Knepper, K.; Zimmermann, V. *Angew. Chem., Int. Ed.* **2005**, *44*, 5188.

⁸ (a) Sletten, E. M.; Bertozzi, C. R. *Angew. Chem., Int. Ed.* **2009**, *48*, 6974. (b) Bertozzi, C. R. *Acc. Chem. Res.* **2011**, *44*, 651.

⁹ Frisch, M. J.; Trucks, G. W.; Schlegel, H. B.; Scuseria, G. E.; Robb, M. A.; Cheeseman, J. R.; Scalmani, G.; Barone, V.; Mennucci, B.; Petersson, G. A.; Nakatsuji, H.; Caricato, M.; Li, X.; Hratchian, H. P.; Izmaylov, A. F.; Bloino, J.; Zheng, G.; Sonnenberg, J. L.; Hada, M.; Ehara, M.; Toyota, K.; Fukuda, R.; Hasegawa, J.; Ishida, M.; Nakajima, T.; Honda, Y.; Kitao, O.; Nakai, H.; Vreven, T.; Montgomery, J. A., Jr.; Peralta, J. E.; Ogliaro, F.; Bearpark, M.; Heyd, J. J.; Brothers, E.; Kudin, K. N.; Staroverov, V. N.; Kobayashi, R.; Normand, J.; Raghavachari, K.; Rendell, A.; Burant, J. C.; Iyengar, S. S.; Tomasi, J.; Cossi, M.; Rega, N.; Millam, J. M.; Klene, M.; Knox, J. E.; Cross, J. B.; Bakken, V.; Adamo, C.; Jaramillo, J.; Gomperts, R.; Stratmann, R. E.; Yazyev, O.; Austin, A. J.; Cammi, R.; Pomelli, C.; Ochterski, J. W.; Martin, R. L.; Morokuma, K.; Zakrzewski, V. G.; Voth, G. A.; Salvador, P.; Dannenberg, J. J.; Dapprich, S.; Daniels, A. D.; Farkas, O.; Foresman, J. B.; Ortiz, J. V.; Cioslowski, J.; Fox, D. J.; Gaussian 09, revision C.01; Gaussian Inc.: Wallingford, CT, 2010

¹⁰ Zhao, Y.; Truhlar, D. G. *Theor. Chem. Acc.* **2008**, *120*, 215.

¹¹ Wheeler, S. E.; Houk, K. N. *J. Chem. Theory Comput.* **2010**, *6*, 395.

¹² Zhao, Y.; Truhlar, D. G. *Acc. Chem. Res.* **2008**, *41*, 157.

¹³ Zhao, Y.; Truhlar, D. G. *Phys. Chem. Chem. Phys.* **2008**, *10*, 2813.

¹⁴ Ribeiro, R. F.; Marenich, A. V.; Cramer, C. J.; Truhlar, D. G. *J. Phys. Chem. B.* **2011**, *115*, 14556.

¹⁵ The supporting information can be accessed free of charge on pubs.acs.org.

-
- ¹⁶ The decomposition of the triazolines was furthermore accompanied by a rapid color change from light yellow to dark red as well as the evolution of gas after 20-60 minutes reaction time.
- ¹⁷ (a) Fusco, R.; Bianchetti, G.; Pocar, D. *Gazz. Chim. Ital.* **1961**, *91*, 933. (b) Fusco, R.; Bianchetti, G.; Pocar, D.; Ugo, R. *Chem. Ber.* **1963**, *96*, 802. (c) Shea, K. J.; Kim, J-S. *J. Am. Chem. Soc.* **1992**, *114*, 4846.
- ¹⁸ Contini, A.; Erba, E. *RSC. Adv.* **2012**, *2*, 10652.
- ¹⁹ Meilahn, M. K.; Cox, B.; Munk, M. E. *J. Org. Chem.* **1975**, *40*, 819.
- ²⁰ (a) Lopez, S. A.; Munk, M. E.; Houk, K. N. *J. Org. Chem.* **2013**, *78*, 1576. (b) Jones, G. O.; Houk, K. N. *J. Org. Chem.* **2008**, *73*, 1333.
- ²¹ Ess, D. H.; Houk, K. N. *J. Am. Chem. Soc.* **2007**, *129*, 10646.
- ²² Debets, M. F.; van Berkel, S. S.; Schoffelen, S.; Rutjes, F. P.; van Hest, J. C.; van Delft, F. L. *Chem. Commun.* **2010**, *46*, 97.
- ²³ Ning, X.; Guo, J.; Wolfert, M. A.; Boons, G.-J.; *Angew. Chem., Int. Ed.* **2008**, *47*, 2253.
- ²⁴ Baskin, J. M.; Prescher, J. A.; Laughlin, S. T.; Agard, N. J.; Chang, P. V.; Miller, I. A.; Lo, A.; Codelli, J. A.; Bertozzi, C. R. *Proc. Natl. Acad. Sci. U.S.A.* **2007**, *104*, 16793.
- ²⁵ Jewett, J. C.; Sletten, E. M.; Bertozzi, C. R. *J. Am. Chem. Soc.* **2010**, *132*, 3688.
- ²⁶ Gordon, C. G.; Mackey, J. L.; Jewett, J. C.; Sletten, E. M.; Houk, K. N.; Bertozzi, C. R.; *J. Am. Chem. Soc.* **2012**, *134*, 9199.

²⁷ (a) Keana, J. F. W.; Cai, S. X. *J. Org. Chem.* **1990**, *55*, 3640. (b) Chapyshev, S. V. *Chem. Heterocycl Compd.* **2001**, *37*. (c) Berger, O.; Kaniti, A.; van Ba, C.; Vial, H.; Ward, S.; Biagini, G.; Bray, P.; O'Neill, P. *ChemMedChem* **2011**, *6*, 2094. (d) Serwinski, P.; Esat, B.; Lahti, P.; Liao, Y.; Walton, R.; Lan, J. *J. Org. Chem.* **2004**, *69*, 5247. (e) Jin, L. M.; Xu, X.; Lu, H.; Cui, X.; Wojtas, L.; Zhang, X. P. *Angew. Chem., Int. Ed.* **2013**, *52*, 5309.

²⁸ (a) Carlson, R.; Nilsson, Å.; Carlström, K.; Sköldefors, H.; Wilking, N.; Theve, N. *Acta Chem Scand. B* **1984** *38*, 49. (b) Amat, M.; Cantó, M.; Llor, N.; Escolano, C.; Molins, E.; Espinosa, E.; Bosch, J. *J. Org. Chem.* **2002**, *67*, 5343.

Chapter 7

Substituent Effects on Rates and Torquoselectivities of Electrocyclic Ring Openings of *N*-Substituted-2-Azetines^a

ABSTRACT: Transition structures for the conrotatory electrocyclic ring opening reactions of *N*-substituted-2-azetines were computed with the M06-2X density functional at the 6-31+G(d,p) level of theory. A wide range of substituents from π acceptors (e.g., CHO, CN) to π donors (NMe₂, OMe) were explored. Acceptor substituents delocalize the nitrogen lone pair and stabilize the reactant state of 2-azetines, while donors destabilize the 2-azetine reactant state. The conrotatory ring opening is torquoselective, the transition state for the outward rotation of the *N*-substituent and inward rotation of the nitrogen lone pair is preferred. This transition structure is stabilized by an interaction between the nitrogen lone pair and the vacant π^* orbital. The activation free energies are linearly related to the reaction free energies and the Taft σ_R^0 parameter.

Introduction

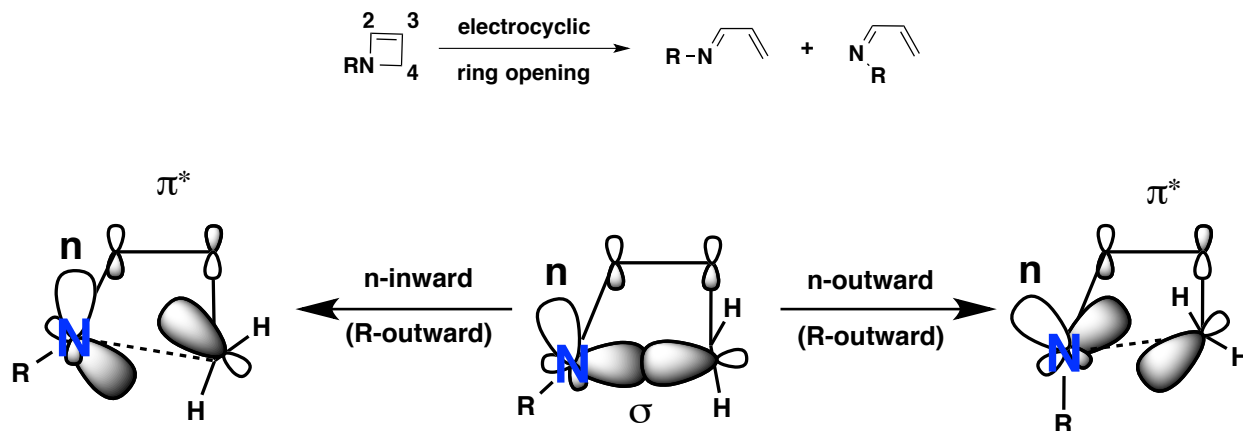
Cyclobutenes undergo thermal conrotatory 4π electrocyclic ring opening reactions to afford 1,3-butadienes.¹ Substituents may rotate “inward” or “outward” in their reactions. A preference for one diastereomeric transition state is called torquoselectivity.² The term was coined in the 1980s because ring opening involves twisting or torque of the breaking single bond. This selectivity has been shown to arise from interactions between the substituent orbitals and those of the breaking bond. Donors rotate outward to avoid repulsive filled-filled interactions

^a Reprinted with permission from *Journal of Organic Chemistry* **2014**, 79, 6189–6195. Copyright 2014 American Chemical Society. Authors are Steven Alexander Lopez and K. N. Houk

with the HOMO of cyclobutene upon inward rotation. Acceptors have low-lying vacant orbitals and the best acceptors (CHO, $-\text{SiR}_3$, GeR_3) preferentially rotate inward.

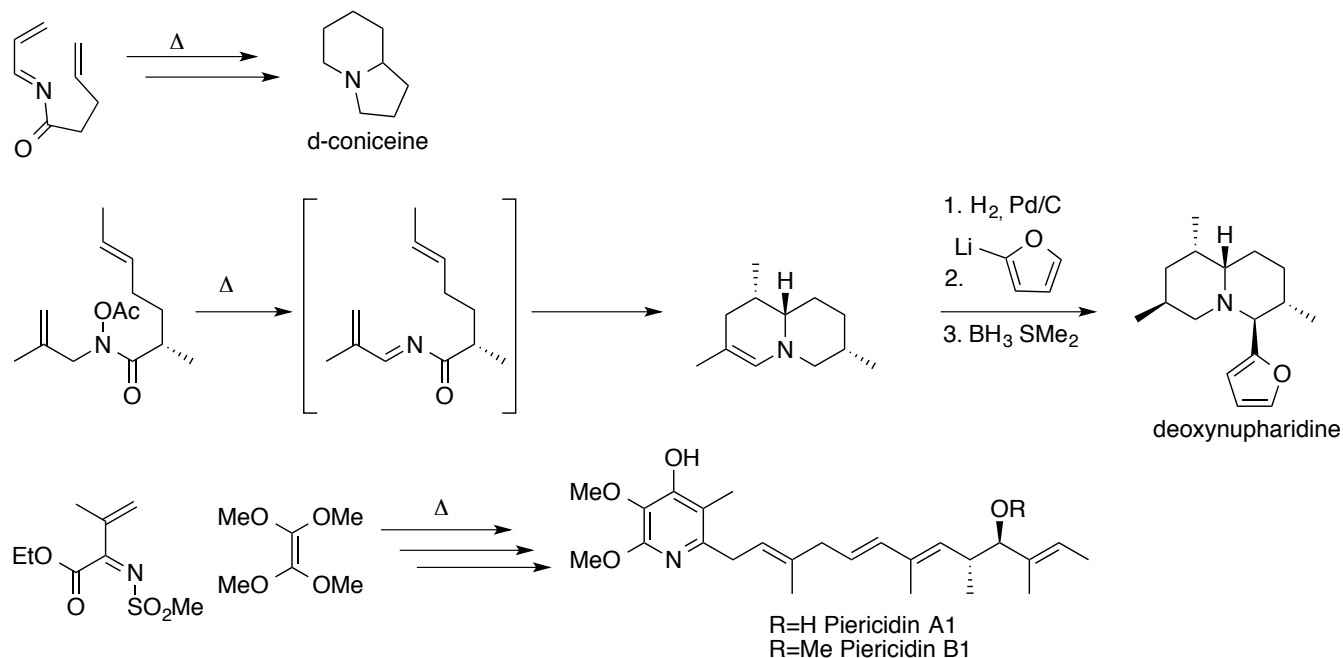
Our group published DFT calculations on the torquoselectivities of 2-azetines (also known as 1,2-dihydroazete) and carbocyclic derivatives. The N-H greatly prefers to rotate outward while the nitrogen lone pair rotates inward (Scheme 1).³ This preference results from an interaction of the nitrogen lone pair with the azetine π^* (LUMO) orbital in the transition state upon inward rotation of the nitrogen lone pair. The other mode of conrotatory ring opening has the *N*-substituent rotating inward and nitrogen lone pair rotating outward, which diminishes interaction of the lone pair with the π^* orbital. Chattaraj *et al.* published DFT calculations on the electrocyclic ring opening reaction rates of related heterocyclic unsaturated four-membered rings, including unsubstituted 2-azetines.⁴ They also report a strong preference for the outward rotation of heteroatom substituents and inward rotation of the heteroatom lone pair. This was explained using activation hardness theory⁵ (Δn^*), which analyzes reactivity based on the energy change of frontier molecular orbitals from reactant to transition state. De Kimpe *et al.* studied the ring opening reaction of various 3-chloro-2-azetines experimentally and with DFT calculations. They established that aryl groups at the 4-position stabilize the transition states and result in significantly more facile ring opening reactions.⁶ Scheme 1 shows the possible products upon ring opening and a diagram of the frontier molecular orbital interactions for both modes of conrotatory ring opening transition structures.

Scheme 1. Inward rotation of the lone pair (**n**) on nitrogen (left). Outward rotation of the lone pair on nitrogen (right).



We have explored how *N*-substituents affect the conversion rate of 2-azetines to 1-azadienes. The 1-azadienes are electron-deficient and can participate in hetero-Diels-Alder cycloadditions with inverse electron-demand. This cycloaddition is the key step in the synthesis of many heterocyclic targets⁷ such as δ -coniceine⁸, and piericidin A1 and B1⁹ (Scheme 2). The 1-azadienes have been shown to react regio- and chemoselectively in asymmetric (4+2), (3+2), and (2+2) cycloadditions as 2π or 4π components.¹⁰ Relatively stable 2-azetines have *N*-substituents that are strong π acceptors. Jung⁸ and Bott¹¹ report syntheses for an *N*-acyl-2-azetidine and *N*-nitro-2-azetidine, respectively. Barluenga and coworkers have recently reported the synthesis of an *N*-nosyl-2-azetidine utilizing Cu-catalysis.¹² After this paper was accepted and was undergoing review, *N*-acyl-2-azetines were reported to participate in a bioorthogonal reaction¹³ with tetrazines.¹⁴

Scheme 2. Natural products synthesized using 1-azadienes in inverse electron-demand Diels-Alder reactions.



Computational Methods

All computations were carried out with GAUSSIAN 09.¹⁵ Reactants, transition states, and products were optimized with the density functional M06-2X¹⁶ using the 6-31G+(d,p) basis set with an ultrafine grid.¹⁷ M06-2X has been found to give more reliable energetics than B3LYP¹⁸ for cycloadditions involving main group atoms.¹⁹ Vibrational analysis confirmed all stationary points to be minima (no imaginary frequencies) or transition structures (one imaginary frequency). Thermal corrections were computed from unscaled frequencies for the standard state of 1atm and 298.15 K. Truhlar's quasiharmonic correction was applied for entropy calculations by setting all frequencies to 100 cm^{-1} when they are less than 100 cm^{-1} .^{20,21}

Results and Discussion

We first describe the effects of *N*-substituents on the geometries of 2-azetines. The structures of the following 2-azetines were computed for the following *N*-substituents: dimethylamino, methoxy, fluoro, chloro, trifluoromethyl, methyl, vinyl, cyano, acetyl, nitro, sulfonyl, and formyl. Figure 1 shows the optimized geometries for the series of these 2-azetines. The pyramidalization angle, defined as $180^\circ - \text{the } C_3C_2NR \text{ dihedral angle}$, is shown below each structure (Figure 1). This angle is 55° (half of 109.5°) in a perfect tetrahedral geometry. The substituents are divided into three classes C, X, and Z as first defined by Houk.²² These refer to conjugating groups (C), donors (X), and acceptors (Z), respectively.

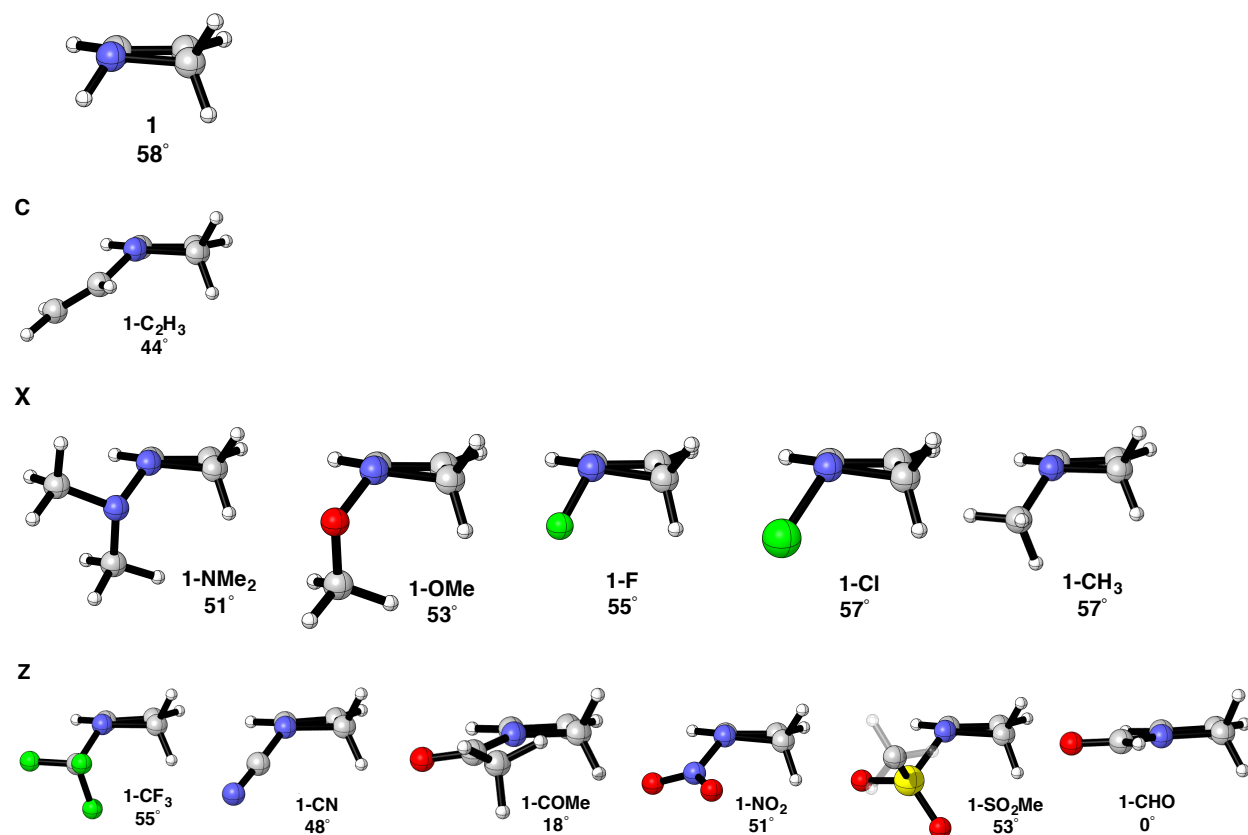
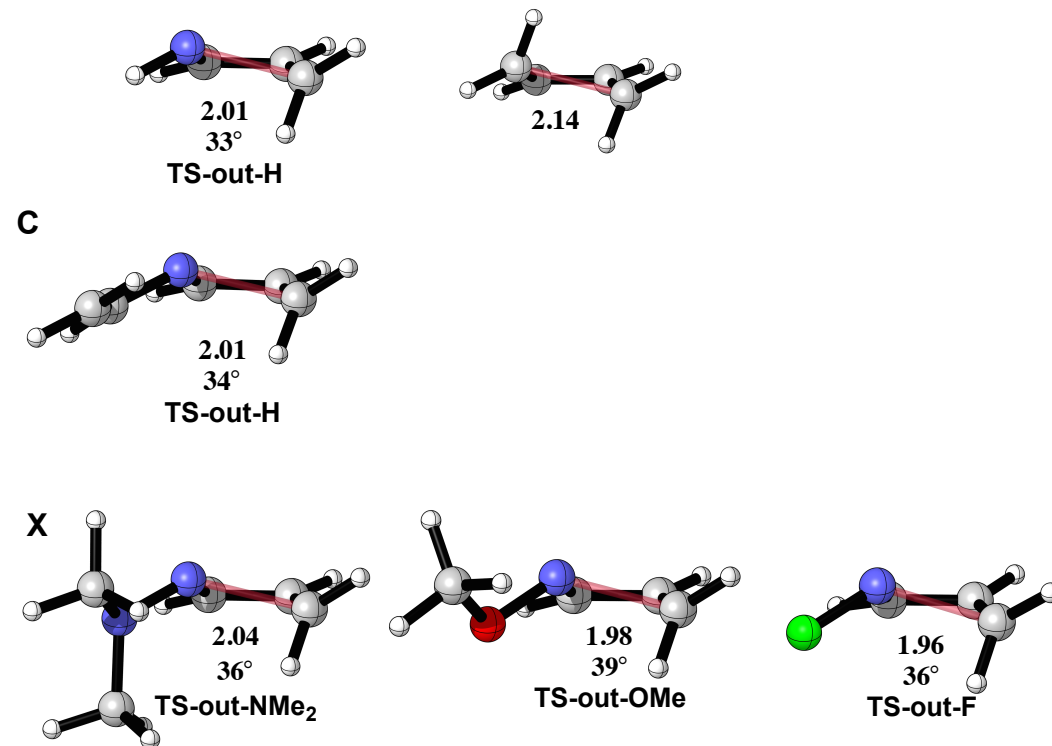


Figure 1. The optimized geometries of *N*-substituted-2-azetines (**1-R**). The pyramidalization angle is reported in degrees.

The pyramidalization angle ranges from 0–61°. With the exception of acyl groups, which prefer planar or almost planar geometries, other substituents do not differ substantially in the reactant geometry. Conjugating and strong π acceptors are able to delocalize the nitrogen lone pair, promoting planarization (e.g. **1-CHO**). While the angle changes only to 44° with *N*-vinyl, it is reduced to 18° with *N*-COCH₃ and 0° in *N*-CHO.

Transition Structures

Both conrotatory transition structures were located for each of the *N*-substituted-2-azetines. Figures 2 and 3 show the 2-azetine lone-pair-in, substituent-out and lone-pair-out, substituent-in transition structures, respectively. These transition states will be referred to as “out” and “in” throughout the text. The cyclobutene transition structure for ring opening is shown in both figures for comparison.



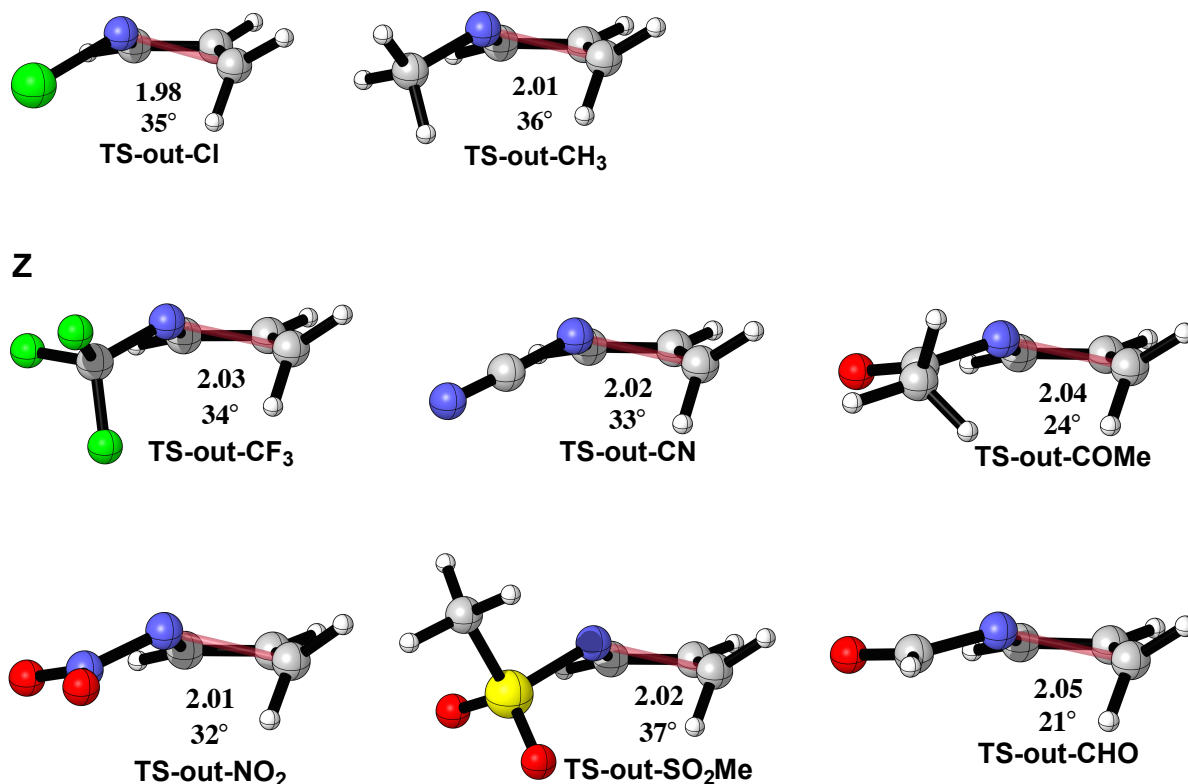
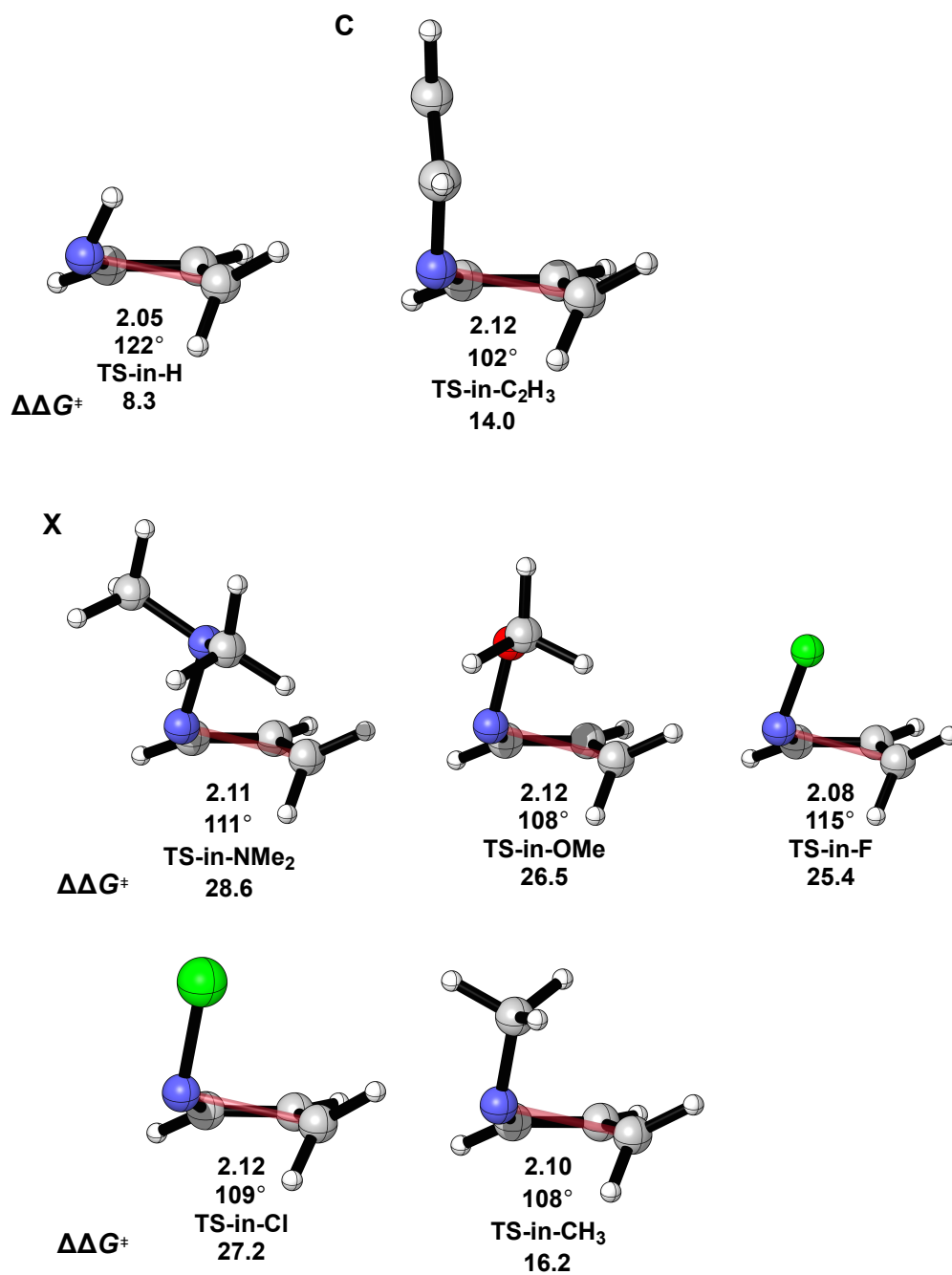


Figure 2. Electro-cyclic conrotatory ring opening lone-pair-in, substituent-out transition structures. Breaking CC or CN bond lengths are reported in Å. The pyramidalization angle is reported in degrees.

The breaking CN bond lengths are quite similar for these transition structures (1.96 – 2.05 Å). As expected, CN bond lengths are shorter than the breaking CC bond length in the cyclobutene ring opening reaction (2.14 Å). In the “out” transition states, *N*-substituents that can conjugate with the nitrogen lone pair retain planarity from reactant to transition state (e.g. **TS-out-CHO**, **TS-out-NO₂**, **TS-out-CN**, **TS-out-COMe**). All of the transition structures are planarized relative to the reactant, with the exception of the *N*-acyl-2-azetines. **1-COMe** and **1-CHO** become slightly more pyramidalized in the transition state because the nitrogen lone pair can also delocalize into the CC π^* orbital. A Natural Bond Orbital analysis, (NBO version 3²³) which supports our $n_{\text{N}}-\pi^*_{\text{CC}}$ orbital effect hypothesis. The $n_{\text{N}}-\pi^*_{\text{CC}}$ orbital interaction is

significantly higher for the “out” transition states than for the “in” transition states, the interaction is greatly reduced because of the nitrogen lone pair is pointed outward. The “in” transition structures are shown in Figure 3.



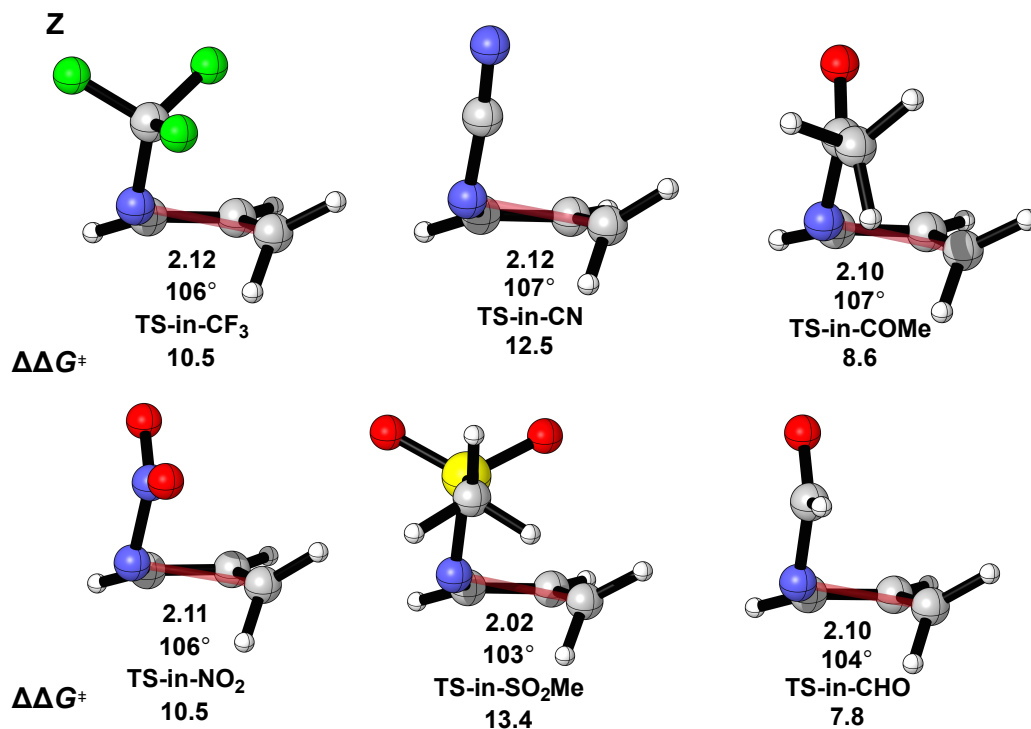


Figure 3. Electrocyclic conrotatory ring opening lone-pair-out, substituent-in transition structures. Breaking CC or CN bond lengths are reported in Å. The pyramidalization angle is reported in degrees. The energies of these transition structures to that of the outward rotation (Figure 2) are given in kcal mol⁻¹ and are shown below each structure.

These transition structures show the *N*-substituent rotated inward. The pyramidalization angles range from 102–122°. Overall, the transition structures with *N*-donor substituents have larger pyramidalization angles, which to minimize destabilizes filled-filled orbital interactions with the breaking CN σ bond of the 2-azetines. The “in” transition structures also have similar σ bond-breaking distances (2.05 – 2.12 Å), which are slightly longer than the “out” transition structures. The preference for the “out” transition structure ($\Delta\Delta G^\ddagger$) shown in Figure 3 are largest for donor substituents and smallest for acceptors. This is related to the well-studied orbital interactions in electrocyclic ring opening reactions of 3-substituted cyclobutenes.²⁴

Three “out” transition structures for azetidine ring openings are overlaid with the transition structures of identically substituted 3-substituted-cyclobutenes and for the “in” transition

structures of *N*-substituted-2-azetines and 3-substituted cyclobutenes with the same substituents (Figure 4).

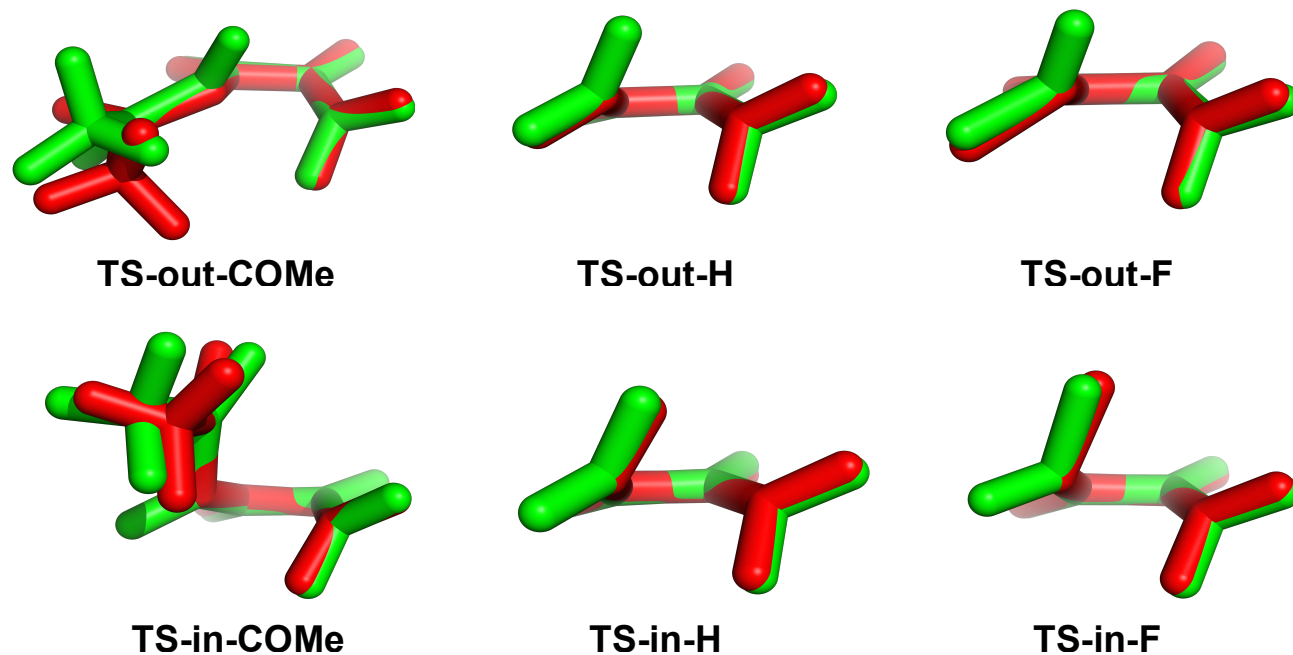


Figure 4. Overlaid “out” and “in” transition structures are shown in the top and bottom rows, respectively for selected *N*-substituted-2-azetines (red) and 3-substituted-cyclobutenes (green).

Figure 4 demonstrates the structural similarity of 2-azetine transition structures of *N*-substituted -2-azetines and the analogous 3-substituted cyclobutenes, except for a slight rotation of the acetyl group. This shows that the interaction of the substituent orbitals with the breaking σ bond (HOMO) are important for 2-azetines as well as cyclobutenes.

Reactivity

The activation barriers for the transition structures shown in Figures 2 and 3 and the experimentally determined Taft σ_R^0 parameters are shown in Table 1. The Taft σ_R^0 parameter is an experimentally determined substituent constant that measures the resonance effect of the substituent.²⁵ The π donors have $\sigma_R^0 < 0$ and π acceptors have $\sigma_R^0 > 0$. Table 1 is arranged from best donor to best acceptor according to σ_R^0 .

Table 1. Activation free energies for both diastereomeric transition structures of the electrocyclic ring opening reactions of azetines. The activation barriers are given in kcal mol⁻¹. $\Delta G_{\text{out}}^\ddagger$ and $\Delta G_{\text{in}}^\ddagger$ refer to the activation barriers corresponding to transition structures where the *N*-substituent rotates outward or inward.

<i>N</i> -R	$\Delta G_{\text{out}}^\ddagger$	$\Delta G_{\text{in}}^\ddagger$	σ_R^0	<i>N</i> -R	$\Delta G_{\text{out}}^\ddagger$	$\Delta G_{\text{in}}^\ddagger$	σ_R^0
NMe ₂	18.3	46.9	-0.56	CF ₃	32.2	42.7	0.10
OMe	15.3	41.8	-0.43	CN	27.5	40.1	0.13
F	20.9	46.3	-0.34	COMe	35.4	44.0	0.16
Cl	21.5	48.7	-0.23	NO ₂	30.0	44.8	0.16
CH ₃	29.5	45.7	-0.13	SO ₂ Me	27.9	41.3	0.19
C ₂ H ₃	29.2	43.2	-0.01	CHO	36.3	44.1	0.23
H	30.4	38.7	0				

The *N*-substituent prefers to rotate outward, while the nitrogen lone pair rotates inward, regardless of the *N*-substituent ($\Delta G_{\text{out}}^\ddagger \ll \Delta G_{\text{in}}^\ddagger$). However, the activation free energies for outward rotation of the substituent strongly depend on the nature of the *N*-substituent: donors

result in low activation barriers, while acceptors result in high barriers. $\Delta G^{\ddagger}_{\text{out}}$ values range from 15.3 to 36.3 kcal mol⁻¹, while the range of $\Delta G^{\ddagger}_{\text{in}}$ is more compressed: 38.7 – 48.7 kcal mol⁻¹.

The large range of $\Delta G^{\ddagger}_{\text{out}}$ is the result of reactant state stabilization of the 2-azetines. Delocalization of the lone pair with an acceptor (e.g. **1-CHO**) stabilizes the reactant, whereas donors destabilize the reactants because of a filled-filled orbital interaction between the nitrogen lone pair and the substituent (e.g. **1-F**). Destabilized reactants require the least amount of energy to reach the transition state, where the nitrogen lone pair is delocalized into the π^* orbital of the alkene. Stabilized reactants require more energy to reach the transition state; because the nitrogen lone pair can be delocalized into the acceptor orbital and the π_{CC}^* . This is demonstrated by plotting $\Delta G^{\ddagger}_{\text{out}}$ with respect to σ_{R}^0 (Figure 5).

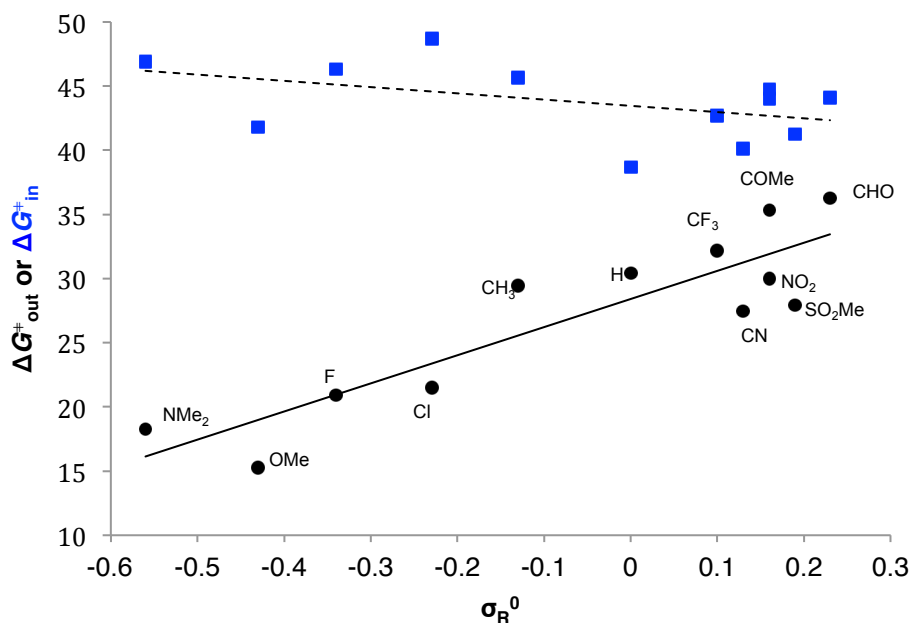


Figure 5. Computed $\Delta G^{\ddagger}_{\text{out}}$ (black circles) and $\Delta G^{\ddagger}_{\text{in}}$ (blue squares) plotted against the Taft σ_{R}^0 parameter. $\Delta G^{\ddagger}_{\text{out}} = 21.9\sigma_{\text{R}}^0 + 28.4$; $R^2=0.79$. $\Delta G^{\ddagger}_{\text{out}}$ corresponds to lone pair in, substituent out. $\Delta G^{\ddagger}_{\text{in}} = -4.9\sigma_{\text{R}}^0 + 43.4$; $R^2=0.20$. $\Delta G^{\ddagger}_{\text{in}}$ refers to lone pair out, substituent in.

Figure 5 shows a reasonably good ($R^2=0.79$) linear relationship between $\Delta G^{\ddagger}_{\text{out}}$ and σ_{R}^0 . On the other hand, the correlation is poorer between $\Delta G^{\ddagger}_{\text{in}}$ and σ_{R}^0 ; the activation energy is high, and only gradually decreases as the π acceptor character of the substituent increases. The data in Figure 5 were used to compute ρ values were computed from $\log(k_{\text{R}}/k_{\text{H}})$ vs. σ_{R}^0 plots (Figures S1 and S2). The ρ value for the “out” transition structures is -16.1 . The very large magnitude and sign of ρ means that the reactivity is very sensitive to the character of the *N*-substituent. There is no significant charge difference from reactant to transition state, but in reactants, the substituents interact strongly with the lone pair on nitrogen, but in the transition state mainly with the σ_{CN}^* acceptor orbital of the breaking bond. The ρ value for the “in” transition structures is 3.6 , which indicates low sensitivity to the *N*-substituent and a small increase in the interaction with the nitrogen lone pair in the transition state.

The relationship of reactivity and σ_{R}^0 was compared to that of the frequently-studied ring opening reaction of 3-substituted-cyclobutenes.¹⁹ We computed the activation free energies for the ring opening reaction with the same methods used for the azetines. A plot of $\Delta G^{\ddagger}_{\text{out}}$ or $\Delta G^{\ddagger}_{\text{in}}$ vs. σ_{R}^0 is shown in Figure 6 to evaluate the sensitivity of the reactivity of 3-substituted cyclobutenes to the nature of the substituent.

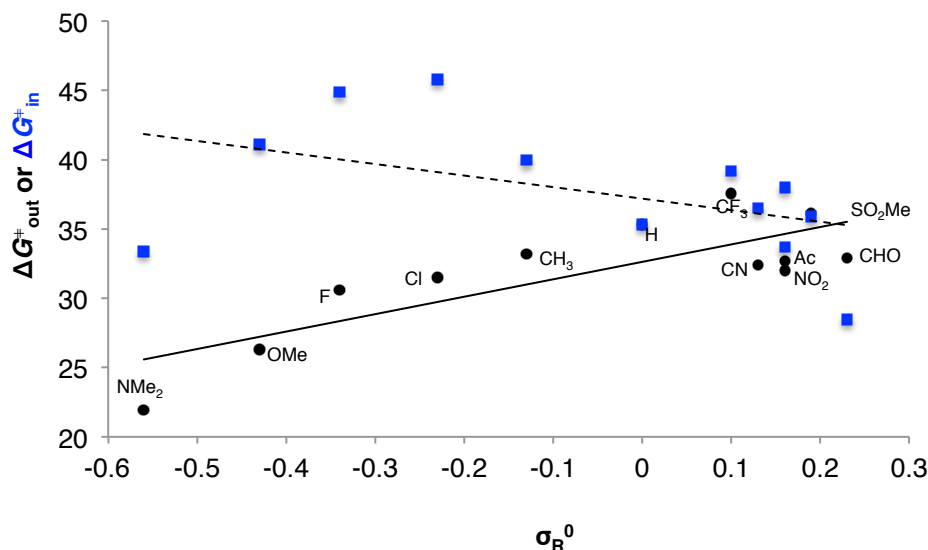


Figure 6. Computed ΔG^*_{out} (black circles) and ΔG^*_{in} (blue squares) plotted against Taft σ_R^0 for the ring-opening reaction of 3-substituted cyclobutenes. $\Delta G^*_{\text{out}} = 12.6\sigma_R^0 + 32.6$; $R^2=0.64$. ΔG^*_{out} is for outward rotation of the substituent. $\Delta G^*_{\text{in}} = -8.3\sigma_R^0 + 37.2$; $R^2=0.21$. ΔG^*_{in} is for inward rotation of the substituent.

Previous calculations established that $\Delta G^*_{\text{in}} - \Delta G^*_{\text{out}}$ correlates well with σ_R^0 . In Figure 6, the ΔG^*_{in} and ΔG^*_{out} are plotted individually for cyclobutenes. The ρ values were computed for the 3-substituted cyclobutenes in Figure 6. The magnitude of ρ is lower for the carbocyclic ring opening than for that the “out” transition structures of 2-azetines ($\rho = -9.1$ vs. -16.1 , respectively). The ρ value for the “in” transition states is 6.1, but the correlation is very poor. The difference in ρ is due to the direct resonance interaction between the substituent and the nitrogen lone pair. This interaction is not possible in the carbocyclic cases and only the substituent stabilization of the breaking σ bond remains. Donors favor outward rotation substantially by interaction with the σ^*_{CC} orbital of the breaking bond, while there is no clear trend for inward rotation due to substantial closed shell repulsion for donors that is overridden by acceptor stabilization upon inward rotation.

Inward rotation of the *N*-substituent causes the lone pair to rotate outward, where it cannot interact with the π^* LUMO of the azetene. Reactivity gradually increases as the substituent changes from a strong donor to a strong acceptor. The poor correlation between $\Delta G_{\text{in}}^\ddagger$ and σ_{R}^0 for cyclobutenes is consistent with a previous study where we established that even strong acceptors (e.g. NO_2) prefer to rotate outwards for 3-substituted cyclobutenes.^{23h} Competing steric and electronic effects in the transition states erodes the preference for “in” transition structures for cyclobutenes and 2-azetines substituted with acceptors. A plot of $\Delta G_{\text{in}}^\ddagger - \Delta G_{\text{out}}^\ddagger$ for cyclobutene ring opening and σ_{R}^0 is shown in Figure 7.

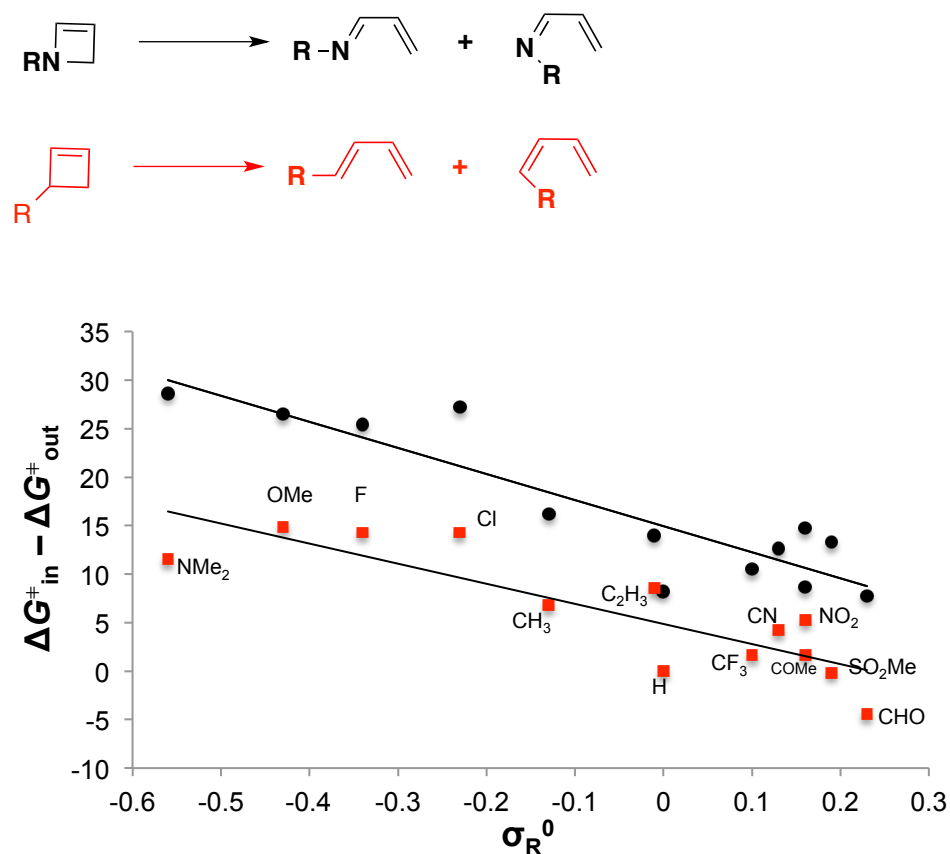


Figure 7. Activation barrier difference plotted against Taft σ_{R}^0 values for the electrocyclic ring opening of 3-substituted cyclobutenes (red squares) and *N*-substituted-2-azetines (black circles). The linear regression equations are $\Delta G_{\text{in}}^\ddagger - \Delta G_{\text{out}}^\ddagger = -20.7\sigma_{\text{R}}^0 + 4.9$; $R^2=0.73$ and $\Delta G_{\text{in}}^\ddagger - \Delta G_{\text{out}}^\ddagger = -26.9\sigma_{\text{R}}^0 + 15.0$; $R^2=0.82$, respectively.

Although the correlation of $\Delta G_{\text{in}}^{\ddagger} - \Delta G_{\text{out}}^{\ddagger}$ with σ_{R}^0 is relatively good for the 3-substituted cyclobutenes, the correlation of individual values of $\Delta G_{\text{in}}^{\ddagger}$ and $\Delta G_{\text{out}}^{\ddagger}$ with σ_{R}^0 is poor. This was previously shown by our group^{23h} and we now find a nearly identical relationship between $\Delta G_{\text{in}}^{\ddagger} - \Delta G_{\text{out}}^{\ddagger}$ and σ_{R}^0 for *N*-substituted-2-azetines. Figure 7 shows a larger R^2 value for the 2-azetines, likely due to the increased resonance interaction between the substituent and nitrogen lone pair, relative to the cyclobutene cases. The role of reactant stabilization on reactivity was further assessed by calculating the reaction free energies for the conversion of 2-azetines to 1-azadienes. Table 2 shows the reaction energies corresponding to **2-out-(a-m)** and **2-in-(a-m)**.

Table 2. The reaction energies for the ring opening reactions of 2-azetines. Energy values reported in kcal mol⁻¹.

<i>N</i> -R	ΔG_{out}	ΔG_{in}	<i>N</i> -R	ΔG_{out}	ΔG_{in}
NMe ₂	-24.4	-18.7	CF ₃	-16.2	-10.0
OMe	-28.3	-27.7	CN	-19.1	-17.4
F	-21.6	-17.5	COMe	-10.9	-8.1
Cl	-19.8	-16.9	NO ₂	-13.8	-10.9
CH ₃	-19.4	-14.8	SO ₂ Me	-17.4	-7.4
C ₂ H ₃	-19.3	-14.5	CHO	-9.5	-7.0
H	-18.8	-17.5			

Table 2 shows that the reaction free energies corresponding to **2-out-(a-m)** and **2-in-(a-m)** are all exergonic [(-9.5 to -28.3 kcal mol⁻¹) and (-7.0 to -27.7 kcal mol⁻¹)], respectively. The *trans*-1-azadienes resulting from outward rotation are all more stable than the *cis* cases. When the *N*-substituent is a π acceptor, the reactant is stabilized and the reaction free energies are least

exergonic for the formation of **2-out-(a-m)** and **2-in-(a-m)** [(-9.5 to -19.1 kcal mol⁻¹) and (-7.0 to -17.4 kcal mol⁻¹)]. π -Donor substituents result in more exergonic reactions for **2-out-(a-m)** and **2-in-(a-m)** [(-17.5 to -28.3 kcal mol⁻¹) and (-17.5 to -27.7 kcal mol⁻¹)]. Figure 8 shows plots of $\Delta G_{\text{out}}^{\ddagger}$ vs. ΔG_{out} and $\Delta G_{\text{in}}^{\ddagger}$ vs. ΔG_{in} for the ring opening reactions of *N*-substituted-2-azetines to understand the relationship between reactivity and reaction energies for both modes of conrotatory ring opening reactions.

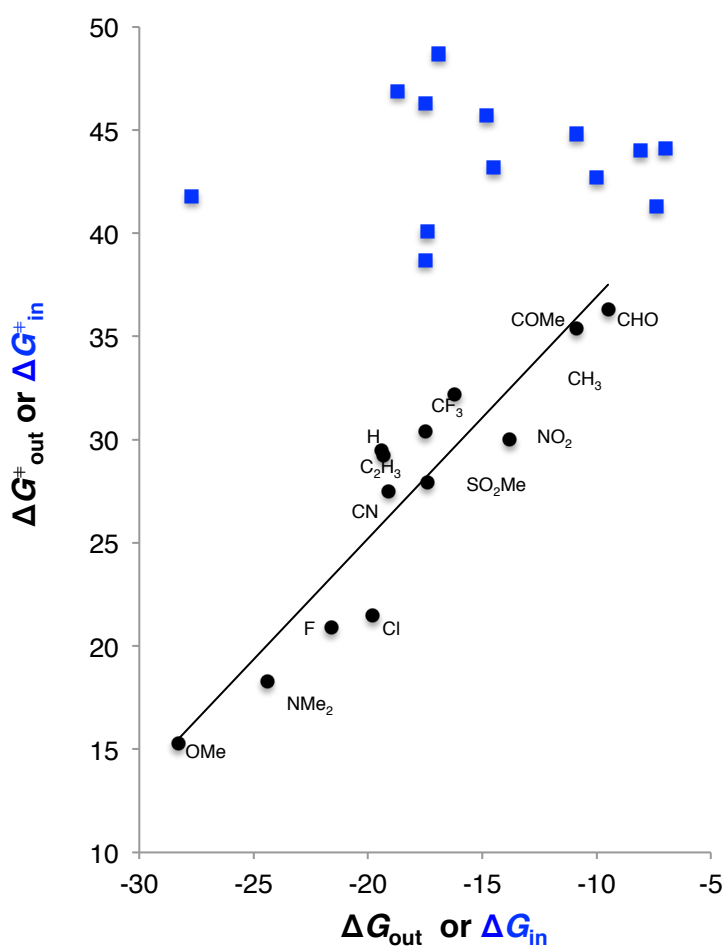


Figure 8. Computed $\Delta G_{\text{out}}^{\ddagger}$ (black circles) and $\Delta G_{\text{in}}^{\ddagger}$ (blue squares) plotted against ΔG_{out} or ΔG_{in} for the ring opening of 2-azetines. $\Delta G_{\text{out}}^{\ddagger} = 1.17\Delta G_{\text{out}} + 48.6$; $R^2=0.86$. $\Delta G_{\text{out}}^{\ddagger}$ corresponds to the substituent rotating outward. $\Delta G_{\text{in}}^{\ddagger} = 0.01\Delta G_{\text{in}} + 43.9$; $R^2=0.00$. $\Delta G_{\text{in}}^{\ddagger}$ refers to the substituent rotating inward.

Figure 8 shows that for outward rotation, there is a large range of reaction energies for the substituents studied here. The activation free energies corresponding to “in” does not depend on the reaction energy because the substituent influences the reactant and transition state energies similarly.

Donors destabilize *N*-substituted 2-azetines, effectively decreasing the energy required to reach the transition state. The reaction energies are more negative when the substituent is a π donor. Acceptors stabilize 2-azetines by delocalizing the nitrogen lone pair, which corresponds to higher activation free energies and reduced exergonicities. The rates of electrocyclic ring openings are controlled by a reactant state effect.

Conclusion

The origins of the torquoselectivities and reactivities of the electrocyclic ring opening reactions of 2-azetines were determined. The lone-pair-in, substituent-out transition structures are always lower in energy than the lone-pair-in, substituent-in transition structures. The torquoselectivities for these reactions result from the interaction of the nitrogen lone pair with the π^* orbital of the 2-azetine ($n_N - \pi^*_{CC}$) upon outward rotation of the substituent. The energies of 2-azetines are strongly affected by the nature of the *N*-substituent. A linear correlation was found to exist between ΔG^\ddagger and ΔG_{rxn} for the “out” transition structures. Acceptors stabilize the reactant state by delocalizing the nitrogen lone pair, while donors destabilize the reactant state due to unfavorable filled-filled orbital interactions. The transition structures are much less sensitive to the nature of the *N*-substituent and the large range of activation free energies depends on the reactant state energies of the 2-azetines. Further computational studies regarding the utility of substituted 2-azetines as chemical reporters in bioorthogonal reactions is ongoing.

Acknowledgements

K. N. Houk was the project director. Steven Alexander Lopez performed all the calculations and wrote the majority of the manuscript. We thank the National Science Foundation (NSF CHE-1059084) for financial support of this research. The computations were performed on the UCLA IDRE Hoffman2 cluster.

References

-
- ¹ a) Woodward, R. B.; Hoffmann, R. *J. Am. Chem. Soc.* **1965**, *87*, 395. b) Vogel, E. *Angew. Chem.* **1954**, *66*, 640.
- ² a) Kirmse, W.; Rondan, N. G.; Houk, K. N. *J. Am. Chem. Soc.* **1984**, *106*, 7989. b) Rondan, N. G.; Houk, K. N. *J. Am. Chem. Soc.* **1985**, *107*, 2099.
- ³ Walker, M.; Hietbrink, B. N.; Thomas IV, B. E.; Nakamura, K.; Kallel, E. A.; Houk, K. N. *J. Org. Chem.* **2001**, *66*, 6669.
- ⁴ Jaccob, M.; Jem, I. S.; Giri, S.; Venuvanalingam, P.; Chattaraj, P. K. *J. Phys. Org. Chem.* **2011**, *24*, 460.
- ⁵ Zhou, Z.; Parr, R. G. *J. Am. Chem. Soc.* **1990**, *112*, 5720.
- ⁶ Mangelinck, S.; Speybroeck, V. Van; Vansteenkiste, P.; Waroquier, M.; de Kimpe N. *J. Org. Chem.* **2008**, *73*, 5481.
- ⁷ Monbaliu, J-C M.; Masschelein, K. G. R.; Stevens, C. V. *Chem. Soc. Rev.* **2011**, *40*, 4708.
- ⁸ Jung, M. E.; Choi, Y. M. *J. Org. Chem.* **1991**, *56*, 6729.
- ⁹ Schnermann, M. J.; Boger, D. L. *J. Am. Chem. Soc.* **2005**, *127*, 15704.
- ¹⁰ Ma, C.; Gu, J.; Teng, B.; Zhou, Q-Q; Li, R.; Chen, Y-C. *Org. Lett.* **2013**, *15*, 6206.

¹¹ Marchand, A. P.; Rajagopal, D.; Bott, S. G.; Archibald, T. G. *J. Org. Chem.* **1994**, *59*, 1608.

¹² Barluenga, J.; Riesgo, L.; Lonzi, G.; Tomas, M.; Lopez, L. A. *Chem. Eur. J.* **2012**, *18*, 922.

¹³ Debets, M. F.; v. Hest, J. C. M.; Rutjes, F. P. J. T. *Org. Biomol. Chem.* **2013**, *11*, 6439 and references therein.

¹⁴ Engelsma, S. B.; Willems, L. I.; v. Paaschen, C. E.; v. Kasteren, S. I.; van der Marel, G. A.; Overkleeft, H. S.; Filippov, D. V. *Org. Lett.* **2014**, ASAP, DOI:10.1021/ol501049c

¹⁵ Frisch, M. J.; Trucks, G. W.; Schlegel, H. B.; Scuseria, G. E.; Robb, M. A.; Cheeseman, J. R.; Scalmani, G.; Barone, V.; Mennucci, B.; Petersson, G. A.; Nakatsuji, H.; Caricato, M.; Li, X.; Hratchian, H. P.; Izmaylov, A. F.; Bloino, J.; Zheng, G.; Sonnenberg, J. L.; Hada, M.; Ehara, M.; Toyota, K.; Fukuda, R.; Hasegawa, J.; Ishida, M.; Nakajima, T.; Honda, Y.; Kitao, O.; Nakai, H.; Vreven, T.; Montgomery, J. A., Jr.; Peralta, J. E.; Ogliaro, F.; Bearpark, M.; Heyd, J. J.; Brothers, E.; Kudin, K. N.; Staroverov, V. N.; Kobayashi, R.; Normand, J.; Raghavachari, K.; Rendell, A.; Burant, J. C.; Iyengar, S. S.; Tomasi, J.; Cossi, M.; Rega, N.; Millam, J. M.; Klene, M.; Knox, J. E.; Cross, J. B.; Bakken, V.; Adamo, C.; Jaramillo, J.; Gomperts, R.; Stratmann, R. E.; Yazyev, O.; Austin, A. J.; Cammi, R.; Pomelli, C.; Ochterski, J. W.; Martin, R. L.; Morokuma, K.; Zakrzewski, V. G.; Voth, G. A.; Salvador, P.; Dannenberg, J. J.; Dapprich, S.; Daniels, A. D.; Farkas, O.; Foresman, J. B.; Ortiz, J. V.; Cioslowski, J.; Fox, D. J.; Gaussian 09, revision C.01; Gaussian Inc.: Wallingford, CT, 2010

¹⁶ Zhao, Y.; Truhlar, D. G. *Theor. Chem. Acc.* **2008**, *120*, 215.

¹⁷ Wheeler, S. E.; Houk, K. N. *J. Chem. Theory Comput.* **2010**, *6*, 395.

¹⁸ a) Becke, A. D. *J. Chem. Phys.* **1993**, *98*, 5648. b) Stephens, P. J.; Devlin, F. J.; Chabalowski, C.; Frisch, M. J. *J. Phys. Chem.* **1994**, *98*, 11623.

¹⁹ Zhao, Y.; Truhlar, D. G. *Acc. Chem. Res.* **2008**, *41*, 157.

-
- ²⁰ Zhao, Y.; Truhlar, D. G. *Phys. Chem. Chem. Phys.* **2008**, *10*, 2813.
- ²¹ Ribeiro, R. F.; Marenich, A. V.; Cramer, C. J.; Truhlar, D. G. *J. Phys. Chem. B.* **2011**, *115*, 14556.
- ²² Houk, K. N. *J. Am. Chem. Soc.* **1973**, *95*, 4092.
- ²³ NBO Version 3.1, E. D. Glendening, A. E. Reed, J. E. Carpenter, and F. Weinhold
- ²⁴ Rudolf, K.; Spellmeyer, D. C.; Houk, K. N. *J. Org. Chem.* **1987**, *52*, 3708. b) Houk, K. N.; Spellmeyer, D. C.; Jefford, C. W.; Rimbault, C. G.; Wang, Y.; Miller, R. D. *J. Org. Chem.* **1988**, *53*, 2125. c) Buda, A. B.; Wang, Y.; Houk, K. N. *J. Org. Chem.* **1989**, *54*, 2264. d) Kallel, E. A.; Wang, Y.; Spellmeyer, D. C.; Houk, K. N. *J. Am. Chem. Soc.* **1990**, *112*, 6759. e) Niwayama, S.; Houk, K. N. *Tetrahedron Lett.* **1992**, *33*, 883. f) Nakamura, K.; Houk, K. N. *Heterocycles* **1993**, *35*, 631. g) Evanseck, J. D.; Thomas, B. E. IV; Spellmeyer, D. C.; Houk, K. N. *J. Org. Chem.* **1995**, *60*, 7134. h) Niwayama, S.; Kallel, E. A.; Spellmeyer, D. C.; Sheu, C.; Houk, K. N. *J. Org. Chem.* **1996**, *61*, 2813. i) Niwayama, S.; Kallel, E. A.; Sheu, C.; Houk, K. N. *J. Org. Chem.* **1996**, *61*, 2517. j) Dolbier, W. R., Jr.; Koroniak, H.; Houk, K. N.; Sheu, C. *Acc. Chem. Res.* **1996**, *29*, 471. k) *J. Am. Chem. Soc.* **1992** *114*, 1157. l) Matsuya, Y.; Ohsawa, N.; Hideo, N. *J. Am. Chem. Soc.* **2006**, *128*, 412. m) Ibrahim-O.; M. *Tetrahedron Lett.* **2010**, *51*, 3610.
- ²⁵ Taft, R. W.; Lewis, I. C. *J. Am. Chem. Soc.* **1958**, *80*, 2436.

Chapter 8

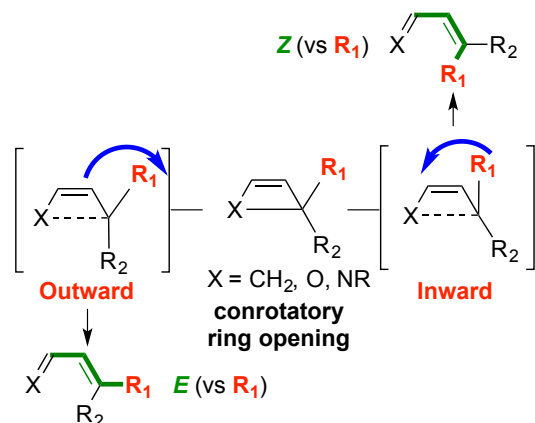
Mono-, di- and trifluoroalkyl substituent effects on the torquoselectivities of cyclobutene and oxetene electrocyclic ring openings

ABSTRACT: The reactivities and torquoselectivities of electrocyclic ring opening reactions of trifluoromethyl substituted cyclobutenes (Houk *et al.* *J. Am. Chem. Soc.* 2003, 125, 5072-5079) and oxetenes (Mikami *et al.* *J. Am. Chem. Soc.* 2011, 133, 20092–20095) were studied with M06-2X density functional theory. The torquoselectivities of a series of mono-, di-, and trifluoromethyl cyclobutenes and oxetenes result from the interplay of a favorable orbital interactions and closed-shell repulsions. When the substituent rotates inward, there can be a favorable interaction between the breaking σ_{CC} or σ_{CO} bond and the σ_{CF}^* orbital ($\sigma_{CO} \rightarrow \sigma_{CF}^*$) of the fluoroalkyl group for mono- and difluoromethyl oxetenes. The preference for rotation of a fluoroalkyl group is diminished for trifluoromethyl oxetenes because closed-shell repulsions between the breaking σ_{CO} bond and substituent orbitals compete with the $\sigma_{CO} \rightarrow \sigma_{CF}^*$ interaction.

Introduction

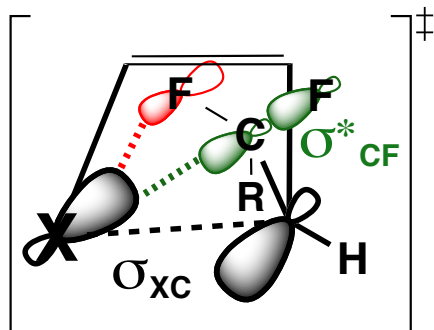
Cyclobutenes undergo thermal conrotatory 4π electrocyclic ring opening reactions to afford 1,3-butadienes.¹ Substituents may rotate “inward” or “outward” during the course of reaction; a preference for one of these diastereomeric transition states is called torquoselectivity.² This selectivity has been shown to arise from interactions between the substituent orbitals and those of the breaking bond. Donors rotate outward to avoid repulsive filled-filled interactions with the HOMO of cyclobutene upon inward rotation. Acceptors have low-lying vacant orbitals, and the best acceptors (CHO, $-\text{SiR}_3$, $-\text{GeR}_3$) preferentially rotate inward. The reactivities and torquoselectivities of four-membered heterocycles such as 2-azetines,³ oxetenes, and thietes⁴ have received renewed attention. These cyclobutenes and heterocyclic derivatives can be designed to undergo ring-opening reactions to afford functionalized dienes and heterodienes stereoselectively. The trifluoromethyl group is of great importance in synthetic organic chemistry⁵ and medicinal⁶ chemistry because of its unique steric and electronic properties.⁷ While major strides have been made in late-stage functionalization of heteroaromatic substrates with the CF_3 group, stereoselective functionalization of tri- and tetrasubstituted alkenes are quite limited.⁸ Recent work by Mikami *et al.* fills this void in the literature by utilizing a torquoselective electrocyclic ring opening reaction of oxetenes⁹ (Scheme 1) inspired by earlier reports by Houk *et al.* on the electrocyclic ring opening of 3-trifluoromethyl cyclobutene.¹⁰

Scheme 1. 4π -Electrocyclic ring opening of carbocyclic and heterocyclic four membered rings.



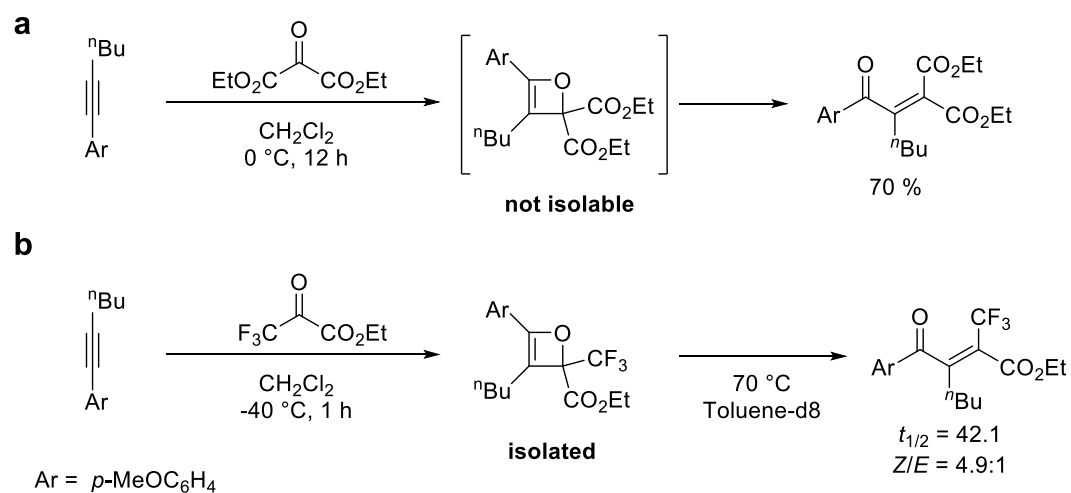
Thermal 4π -electrocyclic ring openings proceed via conrotation of the termini to form the corresponding dienes, in accordance with the Woodward-Hoffmann rules.¹¹ The 3-trifluoromethyl cyclobutenes undergo slightly torquoselective electrocyclic ring opening reactions with inward rotation of the trifluoromethyl group.¹⁰ Mikami and coworkers report high torquoselectivities for the electrocyclic ring opening of 3-trifluoroalkyloxetenes (>75% inward-rotation product). These studies suggest that a through-space orbital interaction between the breaking σ_{CO} orbital with the σ_{CF}^* orbital of the trifluoromethyl group is responsible for the preference of inward rotation in oxetenes. Scheme 2 shows this orbital interaction in transition structures where the fluoroalkyl group rotates inwards. The favorable ($\sigma_{CO} \rightarrow \sigma_{CF}^*$) interaction is shown in green, and unfavorable closed-shell repulsions between the fluorine lone pair orbitals and the breaking σ_{CO} orbital (${}^nF-\sigma_{CO}$) are shown in red. The interplay of these effects will be discussed in the second part of this report for oxetenes (**11–18**).

Scheme 2. Orbital interactions upon inward rotation of the fluoroalkyl substituent



Scheme 2 shows the relative stability of trifluoromethyl-substituted oxetenes at ambient conditions. In contrast, other oxetenes undergo rapid electrocyclic ring opening to afford α,β -unsaturated carbonyl compounds without isolation of the oxetene intermediates (Scheme 3).^{5a}

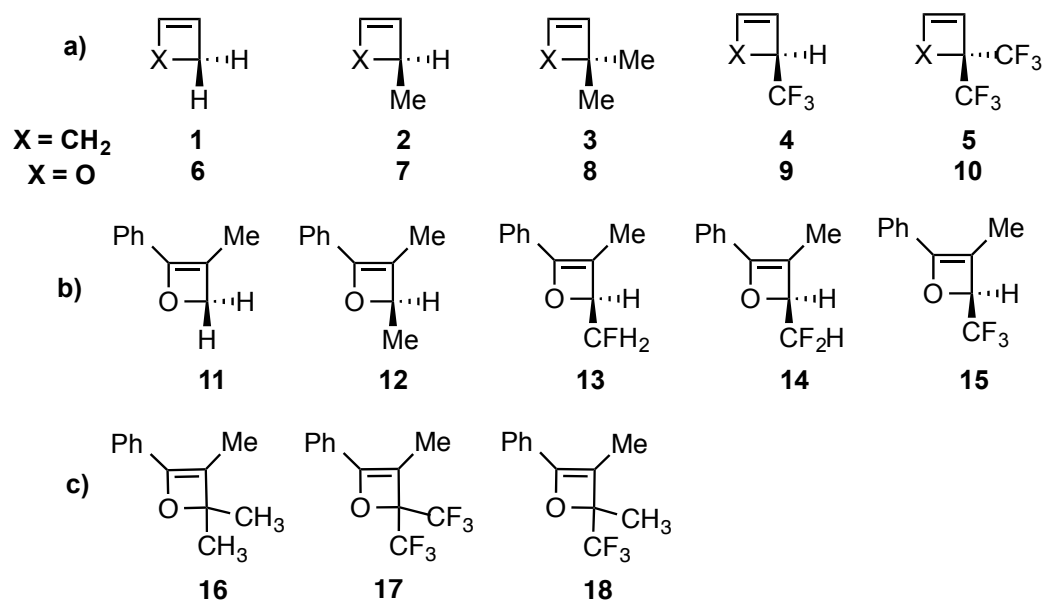
Scheme 3. Synthesis of oxetenes via a [2+2] cycloaddition and subsequent ring opening reaction.



We have applied density functional theory to understand the origin of reactivities and torquoselectivities of mono-, di-, and trifluoromethyl oxetenes. Scheme 4 shows the scope of cyclobutenes and oxetenes studied here. The electrocyclic ring opening reaction of oxetenes and cyclobutenes without alkenyl substituents (**1–10**), 2-phenyloxetenes bearing mono-, di-, and tri-

fluoromethyl groups at the 4-position (**11–18**), and 2-phenyloxetenes disubstituted at the 4-positions were studied to determine the origin of the reactivities and torquoselectivities.

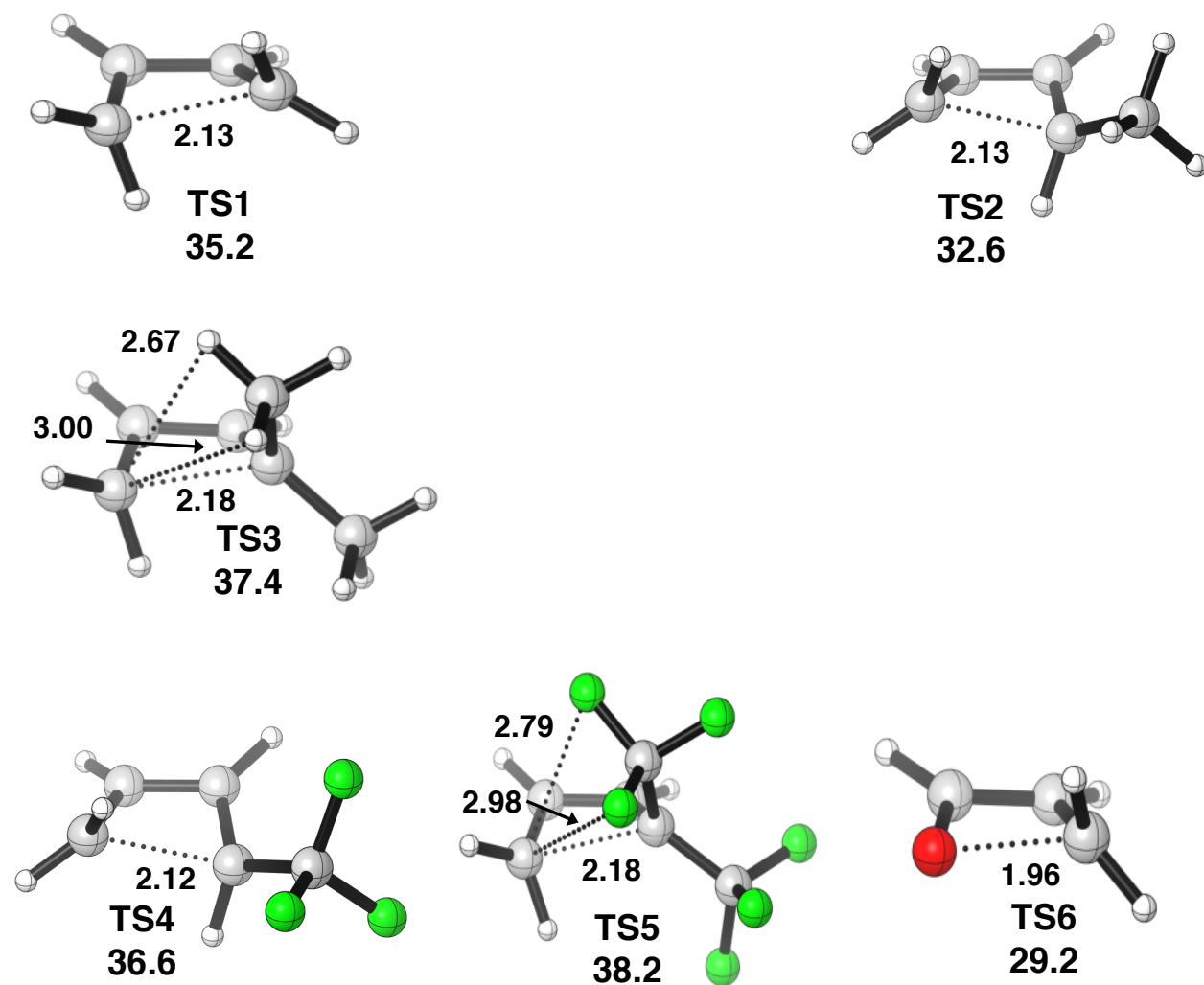
Scheme 4. Mono- and di-substituted cyclobutene and oxetene derivatives.



Computational Methods

All computations were carried out with Gaussian09 Rev.D01.¹² Reactants, transition states, and products were optimized with the density functional M06–2X using the 6-31+G(d,p) basis set and the IEF–PCM¹³ model for toluene to correct for solvent effects. Vibrational analysis confirmed all stationary points to be minima (no imaginary frequencies) or transition structures (one imaginary frequency). Thermal corrections were computed from unscaled frequencies for the standard state of 1 atm and 298.15 K.

The lowest energy transition structures for both modes of conrotation for parent cyclobutenes (**1–5**) and oxetene derivatives (**6–10**) are given in Figure 1. For all transition structures, possible steric clashes are indicated by dotted black lines for contacts with radii less than the sum of their van der Waal radii.¹⁴ The disfavored transition structures are given in the Supporting Information with their activation free energies.



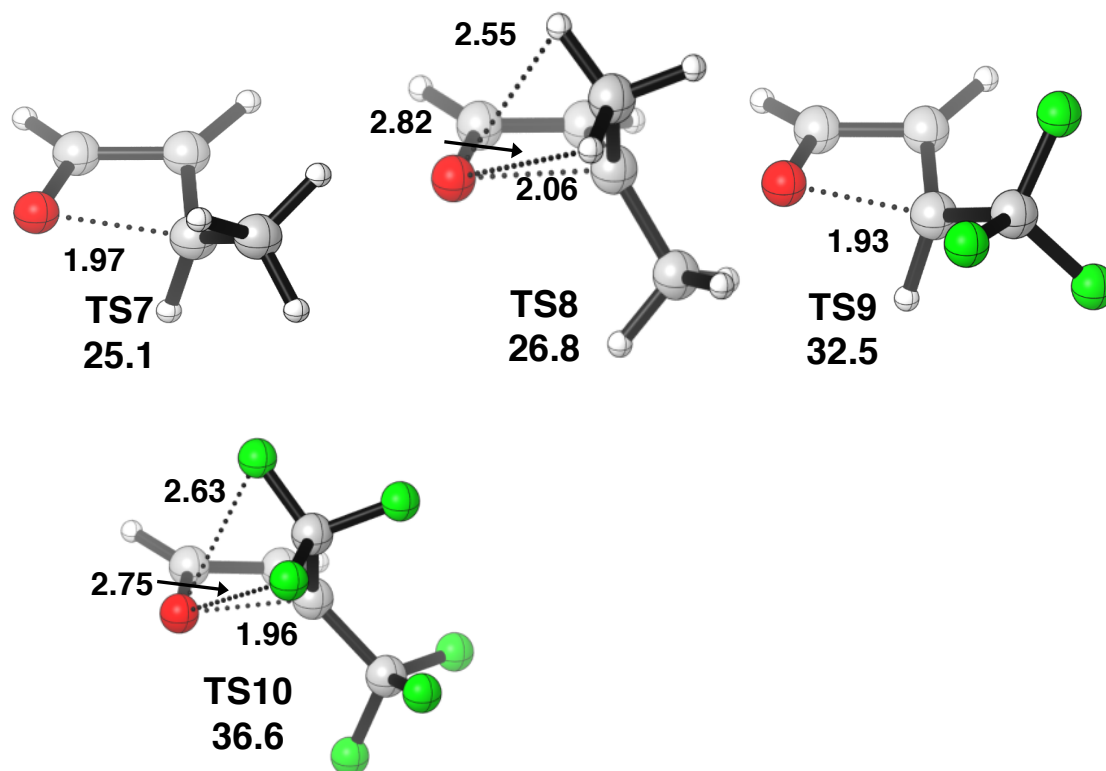


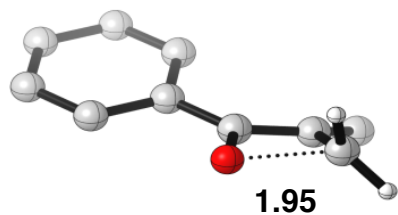
Figure 1. Optimized transition structures of model cyclobutenes and oxetenes. Distances and energies are reported in Ångstroms and kcal mol⁻¹, respectively.

The breaking C–C bond lengths range from 2.13–2.18 Å in the carbocyclic transition structures [TS(1–5)]. The activation free energy (ΔG^\ddagger) of cyclobutene is 35.2 kcal mol⁻¹. The 3-methylcyclobutene is torquoselective for the “out” transition structure and has a lower activation free energy ($\Delta G^\ddagger = 32.6$ kcal mol⁻¹) than cyclobutene. The 3-trifluoromethylcyclobutene also prefers to rotate outward, but is predicted to undergo electrocyclic ring opening much more slowly ($\Delta G^\ddagger = 36.6$ kcal mol⁻¹). The preference for the “out” transition state is due to the decreased steric congestion in that mode of conrotatory ring opening. The disubstituted cyclobutenes (**3** and **5**) have relatively bulky substituents (CF₃ and CH₃), and their transition states feature relatively long C–C and C–O breaking bond lengths (2.18 Å) to minimize closed-shell re-

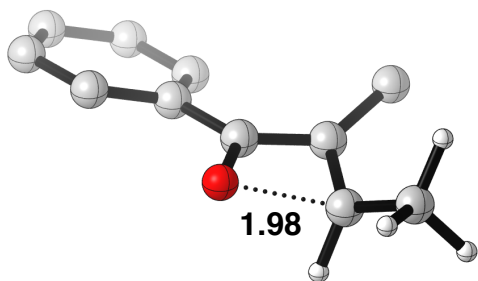
pulsion between the substituents and the breaking σ_{CC} orbital. The unavoidable steric clashes in **TS3** and **TS5** result in relatively high activation free energies (37.4 and 38.2 kcal mol⁻¹, respectively).

The oxetene transition structures have C–O breaking bond lengths that range from 1.96–2.06 Å, somewhat shorter than those of the carbocyclic transition structures. The oxetenes have activation free energies that are 4–10 kcal mol⁻¹ lower than those of the cyclobutene derivatives. The difference is large for the parent and alkyl-substituted cases, but lowest for the trifluoromethyl-substituted oxetenes. The electrocyclic ring opening of 4-methyl oxetene (**7**) and 4-trifluoromethyl oxetene (**9**) both prefer outward rotation of the substituent, and have activation free energies of 25.1 and 32.5 kcal mol⁻¹, respectively. 3,3-disubstituted oxetenes (**8** and **10**) have relatively high activation barriers due to unavoidable closed-shell substituent– σ_{CO} interactions in these transition states.

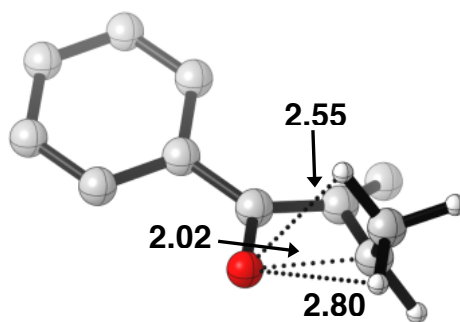
In this section, we report transition structures for 2-phenyl-substituted oxetenes and evaluate how different fluoroalkyl groups affect the reactivities and torquoselectivities of oxetenes (**11–15**). The transition structures for both modes of conrotatory ring opening, and corresponding activation free energies are shown in Figure 2.



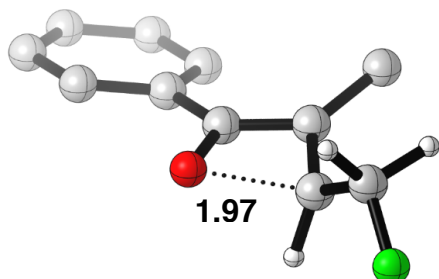
TS11
30.2



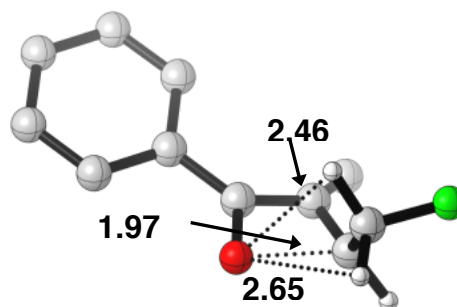
TS12-out
26.8



TS12-in
32.6



TS13-out
29.0



TS13-in
31.6

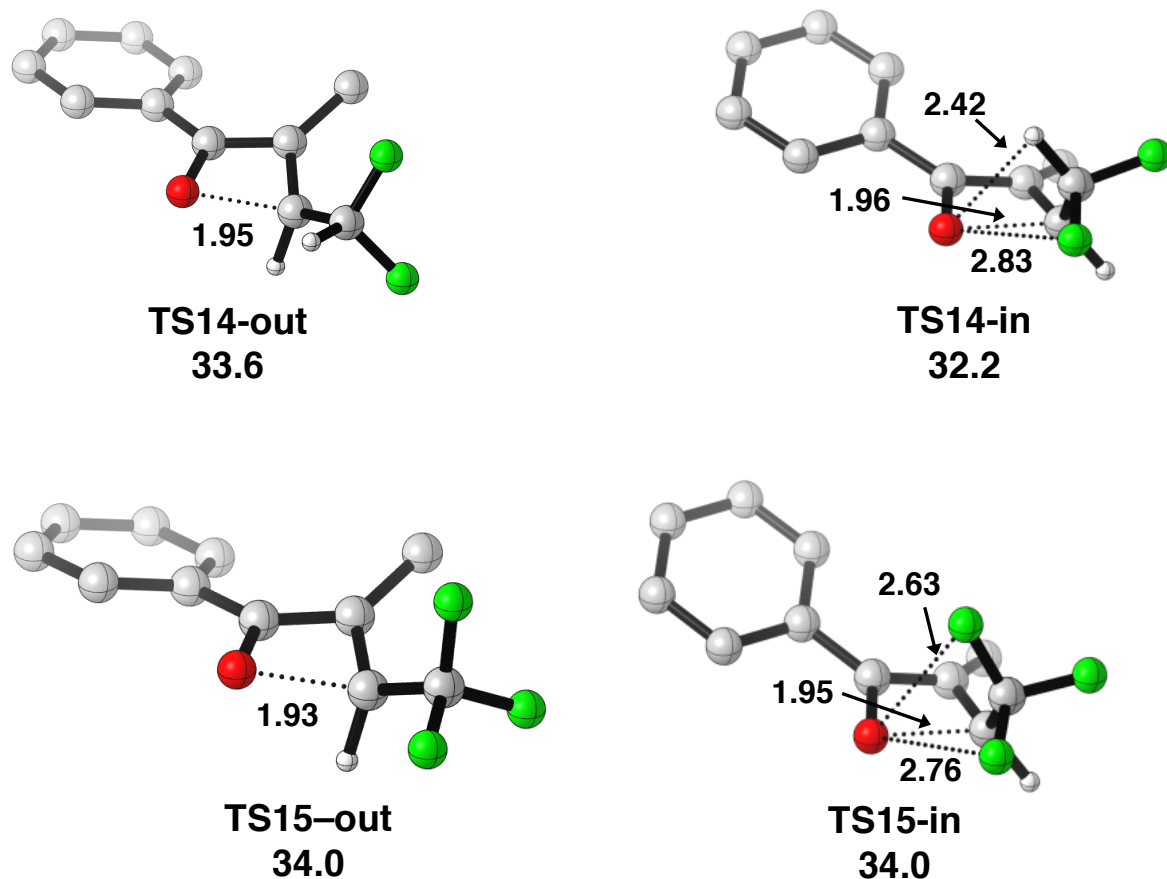


Figure 2. The two transition structures for conrotatory electrocyclic ring openings of **11–15**. Distances and energies are reported in Ångstroms and kcal mol⁻¹, respectively.

Reactivity

The 2-phenyloxetenes have higher activation free energies by ~1 kcal mol⁻¹ relative to the parent oxetene. The breaking C–O bond length in these transition structures range from 1.95 to 2.02 Å; they are relatively unchanged from those of the **TS(6–10)** without the phenyl. The 4-monosubstituted oxetenes bearing substituents with increasing σ -acceptor character have higher activation barriers along the series **12**, **13**, **14**, **15** (30.3 to 34.0 kcal mol⁻¹). The 3.7 kcal mol⁻¹ increase in activation free energy makes the ring opening of **15** approximately 500 fold slower

than **12**, which is in line with the elevated temperatures required for the ring opening of **15** (70 °C; Scheme 3).

Torquoselectivity

Torquoselectivity is the difference in activation free energies between the two modes of conrotation ($\Delta\Delta G^\ddagger$). The electrocyclic ring opening of 4-methyl-substituted oxetene **12** is predicted to be the most facile of the reactions shown in Figure 3. The ΔG^\ddagger of **TS12-out** is 26.0 kcal mol⁻¹, and is predicted to be the most torquoselective for outward rotation of CH₃ ($\Delta\Delta G^\ddagger = 5.8$ kcal mol⁻¹). The ΔG^\ddagger for the ring opening of monofluoromethyloxetene **13** is 2.2 kcal mol⁻¹ higher and less torquoselective, but still favors the outward rotation of CH₂F by 2.6 kcal mol⁻¹. The decreased torquoselectivity stems from the stabilization of the “in” transition structure via a through-space interaction ($\sigma_{\text{CO}} \rightarrow \sigma_{\text{CF}}^*$) between the σ_{CO} orbital and the σ_{CF}^* orbital ($\sigma_{\text{CO}} \rightarrow \sigma_{\text{CF}}^*$). The C–F bond in **TS13-in** is oriented to maximize $\sigma_{\text{CO}} \rightarrow \sigma_{\text{CF}}^*$. The **TS14-in** of the trifluoromethyl case is raised by 3.2 kcal mol⁻¹ vs. **13**, but is lower in energy than **TS14-out** by 1.4 kcal mol⁻¹. Thus, the ring opening of **14** is torquoselective for inward conrotation; the energy of the σ_{CF}^* orbital is lower than that of **13** because of the additional geminal fluorine, and the $\sigma_{\text{CO}} \rightarrow \sigma_{\text{CF}}^*$ becomes more favorable. The activation free energies of the trifluoromethyl case, **TS15-out** and **TS15-in**, are both 34.0 kcal mol⁻¹. This reaction is not torquoselective because in **TS15-in** there is a competition of the $\sigma_{\text{CO}} \rightarrow \sigma_{\text{CF}}^*$ effect and unavoidable closed-shell repulsions between fluorine lone pair orbitals (ⁿF) and (σ_{CO}), upon inward rotation. These interaction lengths are 2.63 Å and 2.76 Å, which are less than the sum of the oxygen and fluorine van der Waal radii (2.99 Å).¹⁴ The geometry of **TS15-out** does not allow for $\sigma_{\text{CO}} \rightarrow \sigma_{\text{CF}}^*$ stabilization. An NBO analysis

shows that the $\sigma_{\text{CO}} \rightarrow \sigma_{\text{CF}}^*$ is present when the alkylfluoro substituents rotate inwards (See Supporting Information).

We also explored a number of reactions of 4,4-disubstituted substrates. These substituents are mono-, di-, and trifluoromethyl groups like **12** – **15** (CH_2F , CHF_2 , and CF_3 , respectively). The subsequent discussion will focus on the ring opening of 4,4-dimethyloxetene (**16**), 4,4-bistrifluoromethyloxetene (**17**), and 4-methyl-154-trifluoromethyloxetene (**18**). The transition structures and activation free energies for these reactions are given in Figure 3. The transition structures, coordinates, and energies of the other 4,4-disubstituted oxetenes can be found in the Supporting Information.

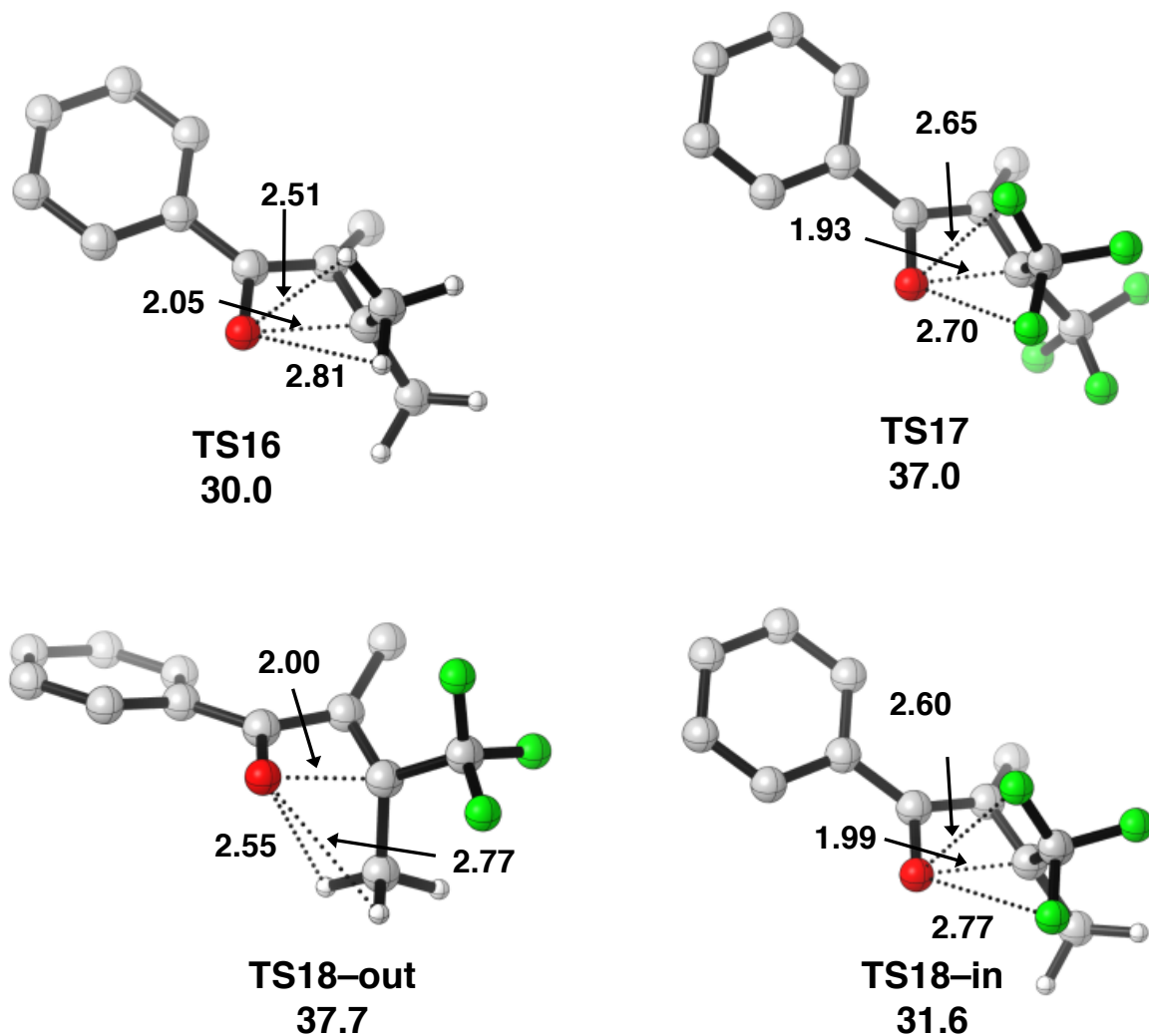


Figure 3. The transition structures for the electrocyclic ring opening reactions of disubstituted oxetenes **16–18**. Distances and energies are reported in Ångstroms and kcal mol⁻¹, respectively. Computed using M06-2X/6-31+G(d,p)/PCM^{tol}.

The 4,4-disubstituted oxetenes have generally higher activation free energies than the 4-monomonsubstituted oxetenes. The ΔG^\ddagger of **TS16** and **TS17** are 30.0 and 37.0 kcal mol⁻¹, respectively. The ΔG^\ddagger for 4-methyloxetene (**12**) and 4-trifluoromethyloxetene (**15**) are 26.8 and 34.0 kcal mol⁻¹, respectively. These barriers are higher by ~ 3 kcal mol⁻¹ because unavoidable closed-shell repulsions (^oF- σ_{CO}) make the transition states more unfavorable. The electrocyclic ring opening

of **18** can involve either outward rotation of CH₃ and inward rotation of CF₃ (**TS18-out**) or inward rotation of CH₃ and outward rotation of CF₃ (**TS18-in**). The ΔG^\ddagger for the favored transition state (**TS18-in**) is 31.6 kcal mol⁻¹. This ring opening is very torquoselective ($\Delta\Delta G^\ddagger = 6.1$ kcal mol⁻¹) because of simultaneously favorable outward rotation of CH₃ and inward rotation of CF₃. Inward rotation of CF₃ facilitates $\sigma_{\text{CO}} \rightarrow \sigma_{\text{CF}}^*$, while avoiding closed-shell repulsions between methyl hydrogens with σ_{CO} .

Conclusion

The reactivities of oxetene electrocyclic ring openings are controlled by the electronic character of the substituent of 4-substituted oxetenes. Oxetene ring opening is accelerated when the substituent at the 4-position is a σ -donor; σ -acceptors cause the ring opening to occur less readily. and the interplay of ${}^n\text{F}-\sigma_{\text{CO}}$ and $\sigma_{\text{CO}} \rightarrow \sigma_{\text{CF}}^*$ upon inward rotation of the fluoroalkyl substituent. The torquoselectivities are controlled by a competition of $\sigma_{\text{CO}} \rightarrow \sigma_{\text{CF}}^*$ effect and unfavorable closed-shell repulsions. Our calculations suggest that 4-difluoromethyloxetenes prefer inward rotation because the favorable $\sigma_{\text{CO}} \rightarrow \sigma_{\text{CF}}^*$ orbital effect outweighs closed shell repulsions in the transition state.

References

¹ (a) Woodward, R. B.; Hoffmann, R. *J. Am. Chem. Soc.* **1965**, *87*, 395. (b) Vogel, E. *Angew. Chem.* **1954**, *66*, 640.

² (a) Kirmse, W.; Rondan, N. G.; Houk, K. N. *J. Am. Chem. Soc.* **1984**, *106*, 7989. (b) Rondan, N. G.; Houk, K. N. *J. Am. Chem. Soc.* **1985**, *107*, 2099.

³ Lopez, S. A.; Houk, K. N. *J. Org. Chem.* **2014**, *79*, 6189-6195. (b) Walker, M.; Hietbrink, B. N.; Thomas, B. E., IV; Nakamura, K.; Kallel, E. A.; Houk, K. N. *J. Org. Chem.* **2001**, *66*, 6669. (c) Mangelinck, S.; Speybroeck, V. V.; Vansteenkiste, P.; Waroquier, M.; de Kimpe, N. *J. Org. Chem.* **2008**, *73*, 5481.

⁴ Jaccob, M.; Jem, I. S.; Giri, S.; Venuvanalingam, P.; Chattaraj, P. K. *J. Phys. Org. Chem.* **2011**, *24*, 460. H. Yu, W. Chan, J. D. Goddard, *J. Am. Chem. Soc.* **1990**, *112*, 7529.

⁵ (a) Kirsch, P.; *Modern Fluoroorganic Chemistry: Synthesis, Reactivity, Applications*; Wiley-VCH, **2013**. (b) Ojima, I.; *Fluorine in Medicinal Chemistry and Chemical Biology*; Wiley-Blackwell, **2009**. (c) Begue, J. P.; Delpon, D. B.; *Bioorganic and Medicinal Chemistry of Fluorine*; Wiley-Blackwell, **2008**.

⁶ (a) Wang, J.; Sánchez-Roselló, M.; Luis, Aceña, J. L.; Pozo, C.; Sorochniky, A. E.; Fustero, S.; Solochonok, V. A.; Liu, H. *Chem. Rev.* **2014**, *114*, 2432–2506. (b) Purser, S.; Moore, P. R.; Swallow, S.; Gouverneur, V. *Chem. Soc. Rev.*, **2008**, *37*, 320–330.

⁷ O'Hagan, D. *Chem. Soc. Rev.* **2008**, *37*, 308–319.

⁸ The most popular ways to construct the stereoselective fluoromethyl substituted alkene derivatives are stereospecific substitution to the sterically-pure alkene precursors: (a) He, Z.; Luo, T.; Hu, M.; Cao, Y.; Hu, J. *Angew. Chem., Int. Ed.*, **2012**, *51*, 3944–3947. (b) Zine, K.; Petriguet, J.; Thibonnet, J.; Abarbri, M. *Synlett*, **2012**, 755–759. (c) Takeda, Y.; Shimizu, M.; Hiyama, T. *Angew. Chem., Int. Ed.* **2007**, *46*, 8659–8661. (d) Liu, X.; Shimizu, M.; Hiyama, T. *Angew. Chem., Int. Ed.* **2004**, *43*, 879–882. (e) Aikawa, K.; Nakamura, Y.; Yokota, Y.; Toya, W.; Mikami, K. *Chem. Eur. J.* **2015**, *21*, 96–100.

⁹ (a) Aikawa, K.; Hioki, Y.; Shimizu, N.; Mikami, K. *J. Am. Chem. Soc.* **2011**, *133*, 20092–20095. (b) Aikawa, K.; Shimizu, N.; Honda, K.; Hioki, Y.; Mikami, K. *Chem. Sci.* **2014**, *5*, 410–415.

¹⁰ (a) Lee, P. S.; Zhang, X.; Houk, K. N. *J. Am. Chem. Soc.* **2003**, *125*, 5072–5079. (b) Niwayama, S.; Kallel, A. K.; Spellmeyer, D. C.; Sheu, C.; Houk, K. N. *J. Org. Chem.* **1996**, *61*, 2813–2825.

¹¹ Woodward, R. B.; Hoffmann, R. *Angew. Chem., Int. Ed.* **1969**, *8*, 781–932.

¹² Frisch, M. J.; Trucks, G. W.; Schlegel, H. B.; Scuseria, G. E.; Robb, M. A.; Cheeseman, J. R.; Scalmani, G.; Barone, V.; Mennucci, B.; Petersson, G. A.; Nakatsuji, H.; Caricato, M.; Li, X.; Hratchian, H. P.; Izmaylov, A. F.; Bloino, J.; Zheng, G.; Sonnenberg, J. L.; Hada, M.; Ehara, M.; Toyota, K.; Fukuda, R.; Hasegawa, J.; Ishida, M.; Nakajima, T.; Honda, Y.; Kitao, O.; Nakai, H.; Vreven, T.; Montgomery, J. A., Jr.; Peralta, J. E.; Ogliaro, F.; Bearpark, M.; Heyd, J. J.; Broth-

ers, E.; Kudin, K. N.; Staroverov, V. N.; Kobayashi, R.; Normand, J.; Raghavachari, K.; Rendell, A.; Burant, J. C.; Iyengar, S. S.; Tomasi, J.; Cossi, M.; Rega, N.; Millam, J. M.; Klene, M.; Knox, J. E.; Cross, J. B.; Bakken, V.; Adamo, C.; Jaramillo, J.; Gomperts, R.; Stratmann, R. E.; Yazyev, O.; Austin, A. J.; Cammi, R.; Pomelli, C.; Ochterski, J. W.; Martin, R. L.; Morokuma, K.; Zakrzewski, V. G.; Voth, G. A.; Salvador, P.; Dannenberg, J. J.; Dapprich, S.; Daniels, A. D.; Farkas, O.; Foresman, J. B.; Ortiz, J. V.; Cioslowski, J.; Fox, D. J. Gaussian 09, revision C.01; Gaussian Inc.: Wallingford, CT, 2010.

¹³ Cances, E.; Mennucci, B.; Tomasi, J. *J. Chem. Phys.* **1997**, *107*, 3032.

¹⁴ Bondi, A. *J. Phys. Chem.* **1964**, *68*, 441.

Chapter 9

How alkyl side chains on BTTT materials control OFET performance

Abstract

The effects of substituting *n*-hexyl alkyl chains on oligomers of poly(2,5-bis-(3-*hexyl*thiophen-2-yl) thieno[3,2-*b*]thiophenes) (BTTT) were explored theoretically and experimentally. Substituted and unsubstituted monodisperse oligomers of BTTT were characterized by molecular structure, variations in solid-state packing, and thin film morphology with single crystal X-ray diffraction (SCXRD). The crystal structures of BTTT oligomers without side chains are nearly linear and have thiophene sulfurs that point away from those in the fused thiophene core (*Anti*). The BTTT oligomers with alkyl side chains prefer the *Syn* conformation and deviate substantially from planarity. This conformational preference was investigated with gas phase DFT calculations. The unsubstituted BTTT oligomers have an intrinsic preference for the *Anti* conformation due to S-S repulsions. Those with side chains prefer the adjacent nonplanar *Syn* conformations, due to repulsions between the side chains and thiophene destabilize the *Anti* conformation. BTTT oligomers with side chains show superior charge transport performance to those without side chains in thin film field effect transistors (TF-FETs). Molecular dynamics and charge-carrier dynamics simulations reveal that dispersive interactions between alkyl side chains promote crystal packing. The reduced disorder results in improved charge transport.

Introduction

P3HT, PBTTT, and PQT12 are prototypical benchmark polymers for exploration of structure-property relations and represent the most studied class of organic semiconductors, polythiophenes. Studies of these materials show that control of microstructure is directly correlated to performance.¹ Various additives and processing techniques have been explored as attempts to control critical morphologic parameters,^{1c,2} yet the molecular structure is the principle and most fundamental handle to tune morphology.^{1c,1d,3} This motivates a rigorous exploration in search of a deeper understanding of structure-property relations in these systems. Ultimately, this will provide unprecedented insight for experimental design, both in synthetic design and material processing techniques. Specifically, facile side chain modification and the available variety of sizes, shapes, and chemistries make them particularly well suited for meaningful structure-property studies.^{3d}

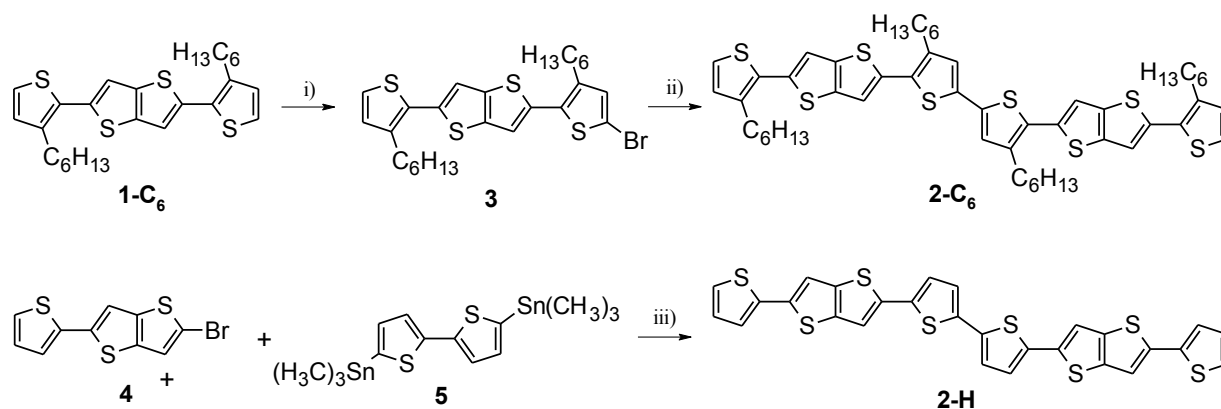
Primarily, side-chains are incorporated to enable solution processing of otherwise insoluble organic semiconductors.^{1d,3d} This is of particular importance in polymeric systems where thermal evaporation is not feasible. Unfortunately, polymer systems are plagued by frustrated packing and present a convoluted picture of local crystallization and conformations.⁴ This inherently limits the use of side-chain studies in the polymer systems where they are needed most. Conversely, recent oligomer studies demonstrate remarkable insight into crystal packing and nano-scale morphology.^{5,6} An oligomer-based structure-property study provides a well-controlled model system to explore the subtle changes in packing and morphology within the corresponding polymer.^{3c,6-7} pBTTT in particular provides an excellent, benchmark system for study.⁸ pBTTT differs from other polythiophenes by its high degree of crystallinity, strong tendencies to interdigitate in the solid state, and unique ability to intercalate with PCBM.⁸ These

particular self-assembly properties are well suited for this study because they manifest directly from molecular structure where the side chain plays an integral role.⁹

In a recent review of oligothiophene-based organic semiconductors,¹⁰ we acknowledged a substantial effect of substitution on the crystal packing, thin film properties, and device performance. Specifically, substitution type, location, and density directly affect backbone conformation, crystal structure, and charge transport properties.^{3b,10} Additionally, we note that thin film morphologies may differ from the bulk crystal. Processing conditions (solvent choice, casting conditions, sheering, etc.) have been employed to gain access to other polymorphs and thin film morphologies.¹⁰ Non-bonding interactions are of particular importance in these systems and are an intrinsic driving force for the changes observed in crystal packing upon substitution or alternative processing.^{3a-3c} Recent computational studies of non-bonding interactions has been able to help assess preferred packing conformations.^{3a-c,11,12}

The goal of this publication is to provide a meaningful structure-property study using oligomers as both standalone and model systems for probing microstructure as a function of chemical structure. To accomplish this, we leverage single crystal X-Ray diffraction to gain insights about the thin film morphology and, in tandem with computational chemistry, evaluate other accessible conformations/polymorphs. The computational validation of other conformations is particularly important in polymeric systems where relationship between conformational preference and disorder is largely speculative.¹² In this publication, we focus on a set of substituted and unsubstituted BTTT monomers and dimers (Scheme 1) to advance our understanding of the forces that drive self-assembly in both the bulk crystal and the thin film of the BTTT system.

Experimental



Scheme 1. Synthetic route for dimer synthesis of **2-C₆**, **1-H**, and **2-H**.^[cite lei] Reaction conditions: i) NBS, CHCl₃/CH₃COOH (50:50, vol), 0 °C to rt; ii) Pd(0)(PPh₃)₄, hexamethylditin, toluene, reflux 12 hrs.

Scheme 1 shows synthetic routes for dimer synthesis. The monomers **1-H**, **1-C₆**, and **2-C₆** were synthesized according to literature procedure.¹³ **1-C₆**: commercially available 2-bromo-3-alkylthiophene undergoes a Stille coupling with the bis(trimethyl)tinthienothiophene core to afford the **1-C₆** in high yield. **1-H**: 2-bromothiophene undergoes Stille coupling with bis(trimethyl)tinthienothiophene. **2-C₆**: **1-C₆** is monobrominated with NBS and subsequently dimerized by Stille coupling with hexamethylditin. The alkylated materials and intermediates were purified by column chromatograph and single crystals were grown from slow evaporation of hexanes. **1-H** purification was performed by sublimation at 220 °C under reduced pressure. Crystals suitable for X-Ray analysis were grown in physical vapor transport (PVT). Due to prevalent solubility issues with the unsubstituted dimer and its precursors, an alternate synthetic path was established to synthesize **2-H** in several steps.

2-(trimethylstannyl)-thiophene (**4**) was coupled to the 2,6-dibromothiophene (**5**) via Stille coupling to yield the monosubstituted product **6**, 2-bromo-6-thiophenyl-thienothiophene. The reaction mixture was then purified by column chromatography and **6** was coupled to the 5,5'-bis(trimethylstannyl)-bithiophene (**8**) via Stille coupling in toluene to afford **2-H**. The **2-H** product was purified by washing with toluene and then cold chlorobenzene followed by sublimation and physical vapor transport at 270-300 °C under vacuum. This material was processable with boiling trichlorobenzene at low concentrations (<1mg/mL).¹⁴

The UV-Vis absorptions of the compounds in chloroform solution and thin films are summarized in Table 1. Figure 1 shows the absorption spectra of the BTTT oligomers in chloroform and thin film.

Electrochemical and optical properties

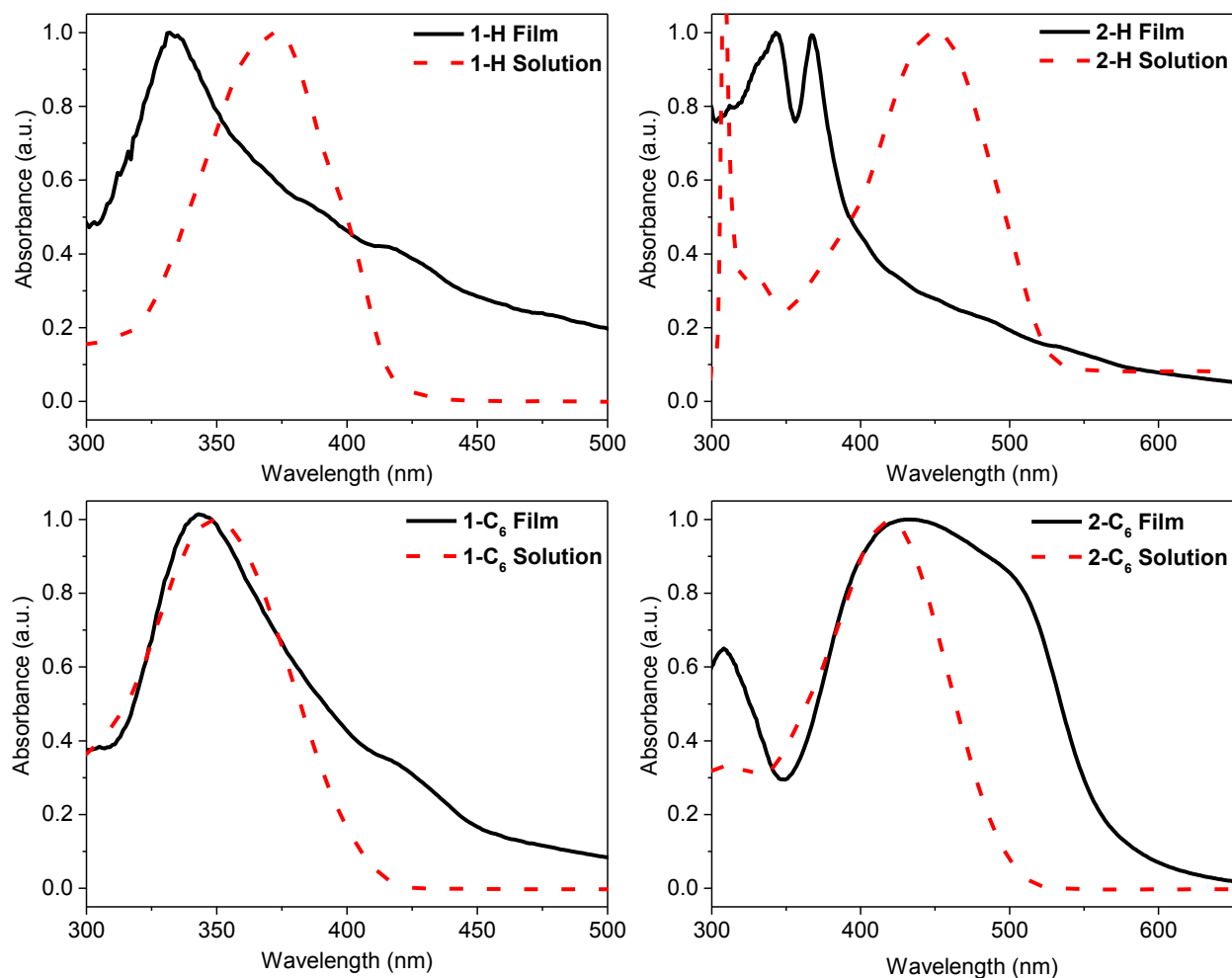


Figure 1. Normalized UV-Vis spectra of the materials in chloroform (dashed red) and thin film on glass (solid black): a-d) **1-H**, **2-H**, **1-C₆**, **2-C₆**, respectively.

The solution maximum absorption of **1-H** is red shifted relative to **1-C₆** (373 and 350 nm, respectively) because **1-H** is nearly planar. In the solid state, the blue shift observed in the maximum absorption of the **1-H** is much larger than the **1-C₆** (42 nm and 8 nm, respectively). **1-H** forms a stronger-coupled H-aggregate and has a larger blue shift. H-aggregation in both monomers is also responsible for the Davydov splitting (shoulder at 409 nm) in the solid state.

The dimers (Figure 1b and 1d) show a red-shifted absorption compared to the monomers due to the extended conjugation. Similar to the solution phenomena observed in the monomers, the **2-H** has a red shifted maximum absorption compared to the **2-C₆** because it is more planar in solution. The solid state of the **2-H** is also strongly blue shifted from its solution state spectra due to H-aggregation. The solid state spectra of the **2-C₆** shows blue shifted maximum absorption (11 nm shifted) compared to the solution spectra. However, the solid state **2-C₆** absorption broadens substantially from the solution spectra and additional lower energy absorption is evidence of J-aggregation.^{14a}

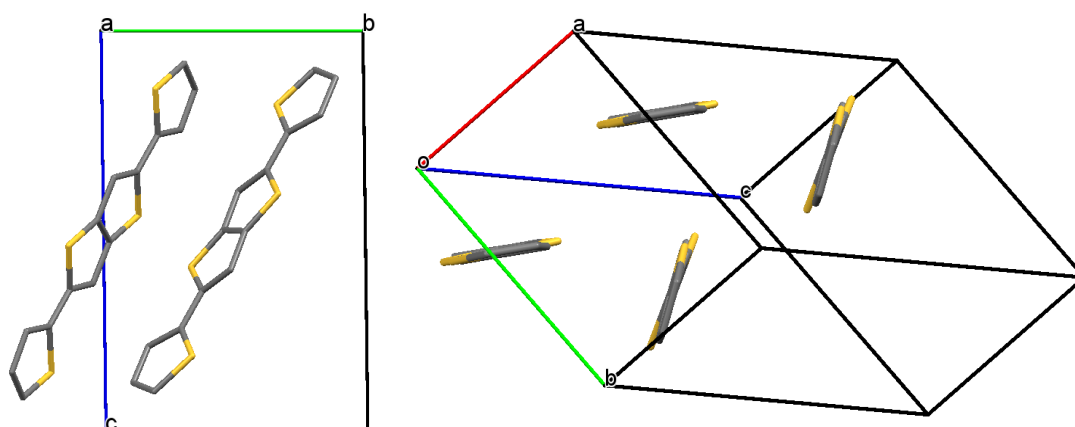
We first computed the frontier molecular orbitals to assess the HOMO-LUMO gaps of **1-C₆**, **2-C₆**, **1-H**, and **2-H** based on the B97D geometries. These results show that incorporating alkyl side chains raise the HOMO energies of the BTTT systems studied here. This qualitatively corresponds to a decrease in the bandgaps for the monomers and dimers (2.5eV vs. 3.0eV and 2.4eV vs. 3.0eV, respectively). The optical band gap was determined by using the absorption edge from the solution spectra. Cyclic voltammetry studies were performed in chloroform with 0.1M TBAPF₆ and a scan rate of 100 mV/s to determine ionization potentials (IPs) of these oligomers. Table 1 shows the electrochemically determined IP from the onset of oxidation as compared to ferrocene.

Table 1. Optical properties, electrochemical data, and DFT calculated energies.

Material	λ_{\max} Soln ^a [nm]	λ_{\max} Film ^b [nm]	OpBG ^c [eV]	IP ^d [eV]	EA ^e [eV]	HOMO ^f [eV]	LUMO ^f [eV]
1-H	373	331	3.0			-5.10	-2.07
2-H	450	343,367	2.4			-4.90	-2.10
1-C₆	350	343	3.0	-5.4	-2.4	-5.16	-1.35
2-C₆	421	432	2.5	-5.3	-2.6	-5.02	-1.80

^aAbsorptions were measured from thin films on glass. ^bAbsorption was measured from chloroform solution. ^cDetermined from onset of absorption in the solution UV-Vis. ^dDetermined by cyclic voltammetry (CV) in chloroform. ^eEstimated from the sum of OpBG and IP. ^fDetermined using B3LYP/6-31G(d)//B3LYP/6-311G(d,p).

Figure 2 shows the crystal structure of **1-H**. Figure 3 shows the crystal structures of **1-C₆** and **2-C₆**.

**Figure 2.** Crystal packing of **1-H** showing the unit cell along the A-axis (a) and the herringbone packing (b).

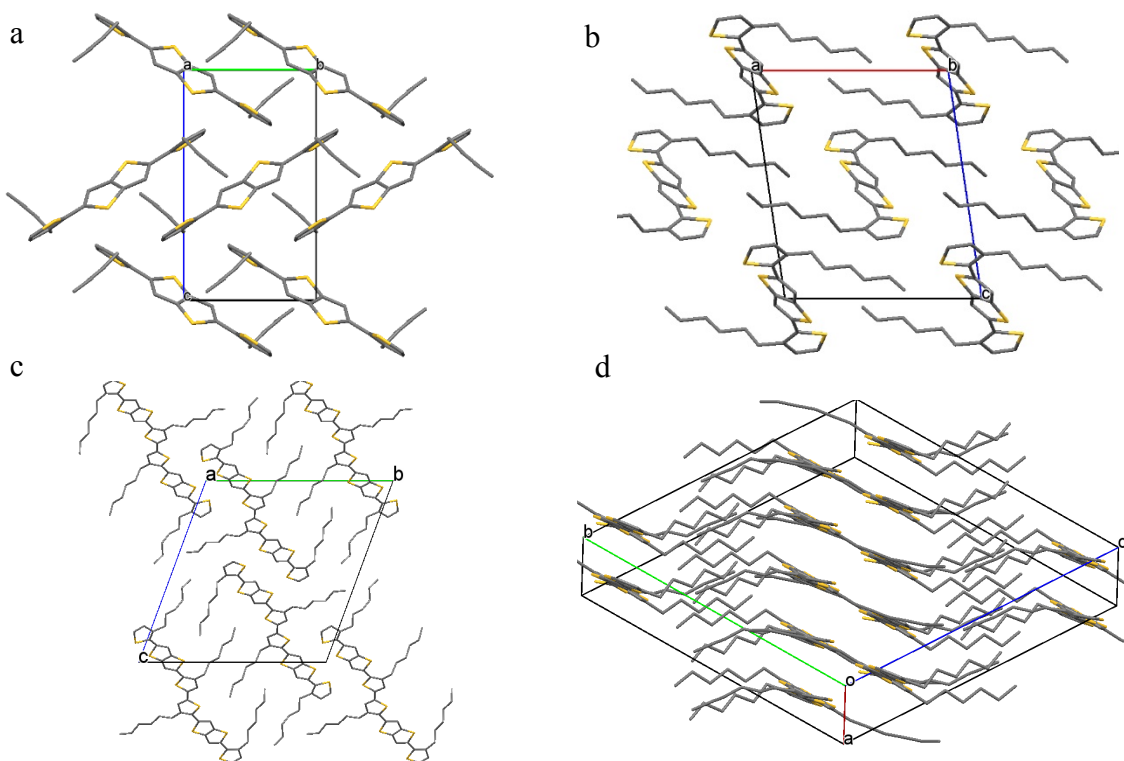


Figure 3. Crystal packing of **1-C₆** (a, b) along the unit cell A-axis (a) and B-axis (b) and **2-C₆** (c, d) along the unit cell A-axis (c) and illustrate π stacking (d).

1-H packs in a triclinic P-1 space group with a unit cell that contains two C_2 -symmetric half-molecules (Figure 2a and 2b). **1-H** adopts a highly planar, *Anti-Anti* conformation and the characteristic herringbone packing motif observed for other unsubstituted thiophenes systems.³⁰ The **1-H** has slightly slipped edge to face interactions along the long-axis with π -planes at 63° . A suitable crystal of **2-H** could not be made for SCXRD. MD simulations suggest that side chains are necessary for stable crystal structures because they provide extended dispersive interactions that result in more highly-ordered crystal structures.

1-C₆

Figures 3a and 3b show that **1-C₆** has a $P2_1/n$ space group and an end-to-face herringbone packing motif. The C-H- π interaction occurs between terminal thiophenes with the long-axes

perpendicular; the interplanar angle is 63°. The backbones of symmetry equivalent molecules interact via C–H and S–H interactions and the intermolecular distance does not support strong π - π interactions. The terminal thiophenes are both in the *Syn* conformation and are coplanar but deviate from planarity by 38°.

2-C₆ packs in a P-1 space group and contains both *Anti* and *Syn* terminal thiophenes in a single molecule (Figures 3c and 3d). The π - π distance in Figure 3d is 3.5 Å, which suggests a modest π - π dispersive interaction. This unique packing is quite planar; alkyl chains curve out from the core. The hexyl side chains curve in the same direction, opposite to the side with one chain present.

Conformational analysis of monomeric BTTT systems

Wheeler *et al.* report highly accurate torsional potentials for bithiophene, bifuran, and biselenophene and a benchmark of twelve common density functionals based on focal point analyses.¹⁵ They conclude that M06-2X¹⁶ is the most reliable functional for bithiophene, but the performance is not guaranteed for larger oligomers such as **BTTT** and **1-R**. They find that B97D has an average error in predicted energies of only 0.21 kcal mol⁻¹ over a large range of basis sets, for bithiophene. Gas phase calculations were carried out using the density functional B97D¹⁷ with the def2-TZV¹⁸ basis set for **1-H** and **1-C₆**. In order to avoid computing all the accessible conformers of hexyl groups, we truncated the alkyl group to a methyl (**1-Me**) or an ethyl (**1-Et**) side chain. Energies were obtained from single-point calculations on the B97D geometries employing the B97D functional and the large def2-QZVP basis set.¹⁹ Scheme 2 shows the three possible near-planar conformations of BTTT groups upon rotation of both single bonds.

Scheme 2. **1-R** Nomenclature of three near-planar conformers of (R=H, Me, Et).

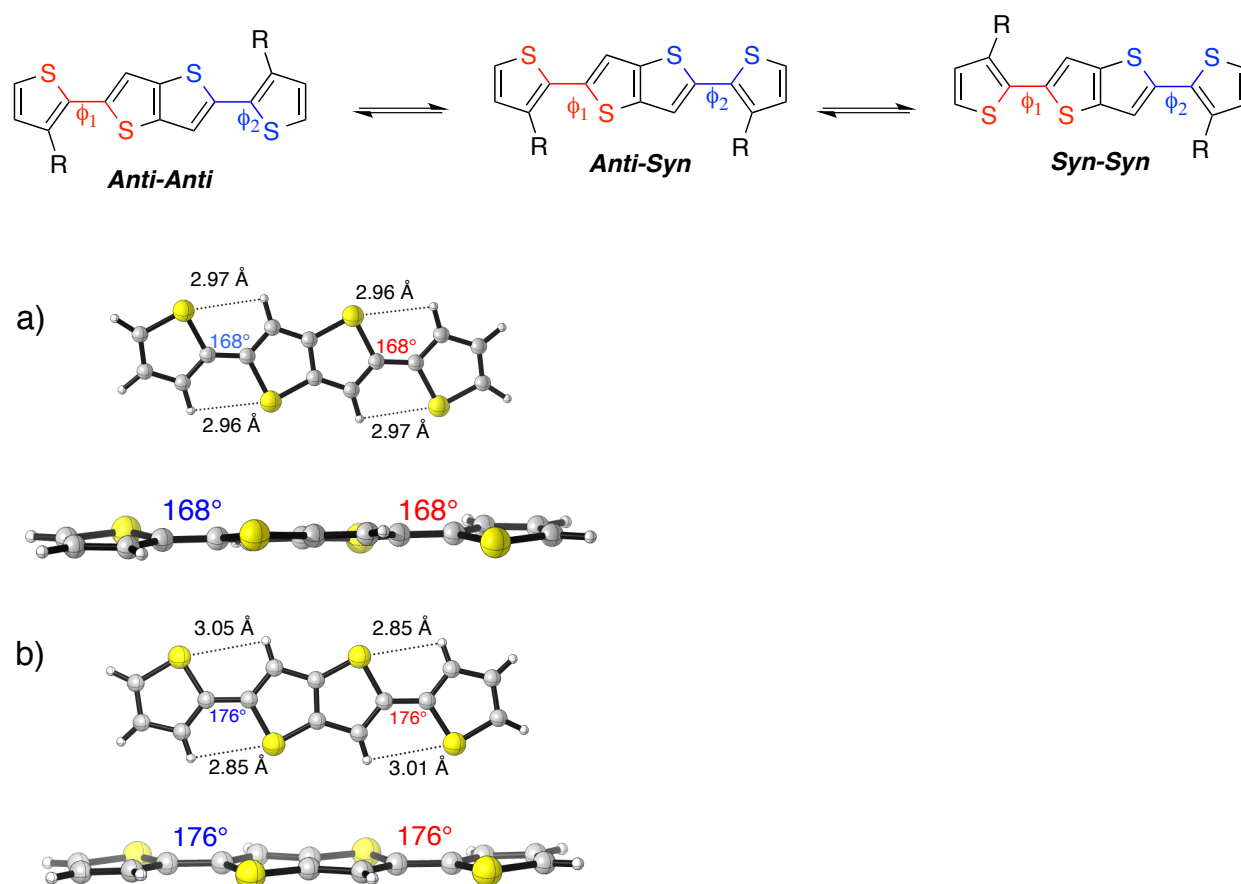


Figure 4. Top and side view of **1-H**. a) Computed structure and b) experimental crystal structure.

The computed *Anti-Anti* global minimum is very similar to the X-ray crystal structure refined by Briseño *et al.*, but the torsional angles ϕ_1 and ϕ_2 are both 8° less than those measured in the crystal structure. The S-H_{aryl} distances (indicated by the dotted lines) are 0.07 and 0.11 Å longer in the computed structures. The backbone of the computed structure is less planar and the S-H interaction lengths are therefore elongated in the gas phase. The greater planarity of **1-H** in the crystal is presumably due to crystal packing. The other computed near-planar conformers (*Anti-Syn* and *Syn-Syn*) of are shown in Figure 5.

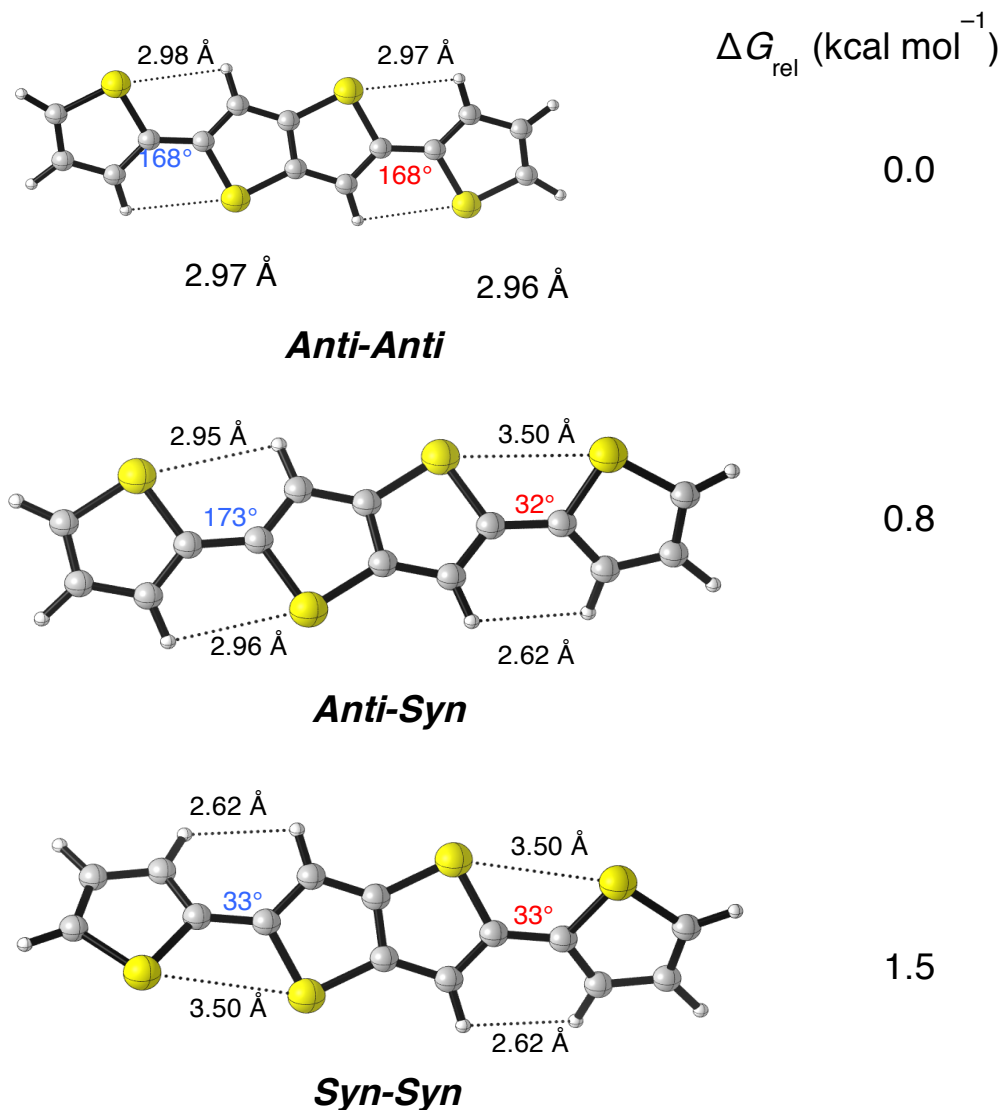


Figure 5. The optimized gas phase conformers of **1-H**. SCCS dihedral angles are shown in blue and red. The H–H and H–S distances are indicated for *Anti-Syn* and *Syn-Syn* conformers, and reported in Angstroms. Computed by B97D/def2-TZV.

The SCCS dihedral angles of *Anti-Anti* are equal and the backbone is nearly planar (168°). When the sulfurs point in the same direction, S–S repulsion causes the SCCS dihedral angle to distort further from planarity in both the *Anti-Syn* (32°) and *Syn-Syn* (33°) conformers. We evaluated possible H–H and H–S steric effects in the structures shown in Figure 2. The H–H

distance is longer than twice the van der Waals radius²⁰ (r_{vdw}) for hydrogen (2.40 Å) for all conformers. The H–S interaction distance is longer than the sum of the hydrogen and sulfur r_{vdw} (3.00 Å). The S–S distance is 3.50 Å, which is less than twice the r_{vdw} of S (3.60 Å). These results suggest that these possible steric effects are small or negligible and S–S repulsion controls the intrinsic preference for the *Anti-Anti* conformer of **1-H**.

2-C₆

The *Anti-Anti* conformer of **1-H** is favored in the gas and solid phases, but the alkyl side chains alter this preference. Briseño *et al.* observe that the crystal structure of **1-C₆** is *Syn-Syn* (Figure 6).

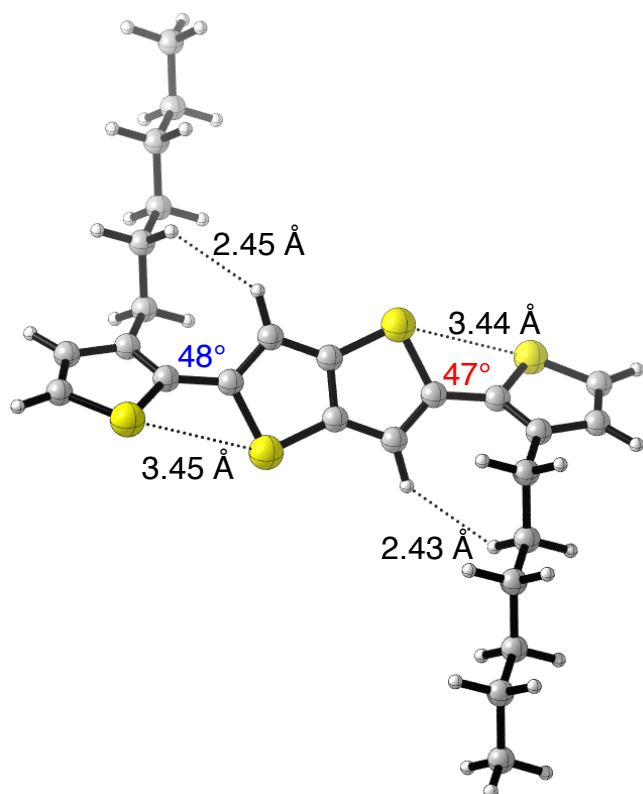


Figure 6. Crystal structure of **1-C₆**.

Heeney *et al.*⁹ used an experimental and theoretical approach to understand the origin of paracrystalline disorder in poly BTTT. They employed simplified calculations by modeling the important steric effects of the tetradecyl side chain as an ethyl group. In line with this, we shortened the hexyl side chain to an ethyl group, and also performed the same calculations on a methyl-substituted **BTTT** system **1-Me**. Figure 7 shows the three computed near-planar conformers of **1-Et**.

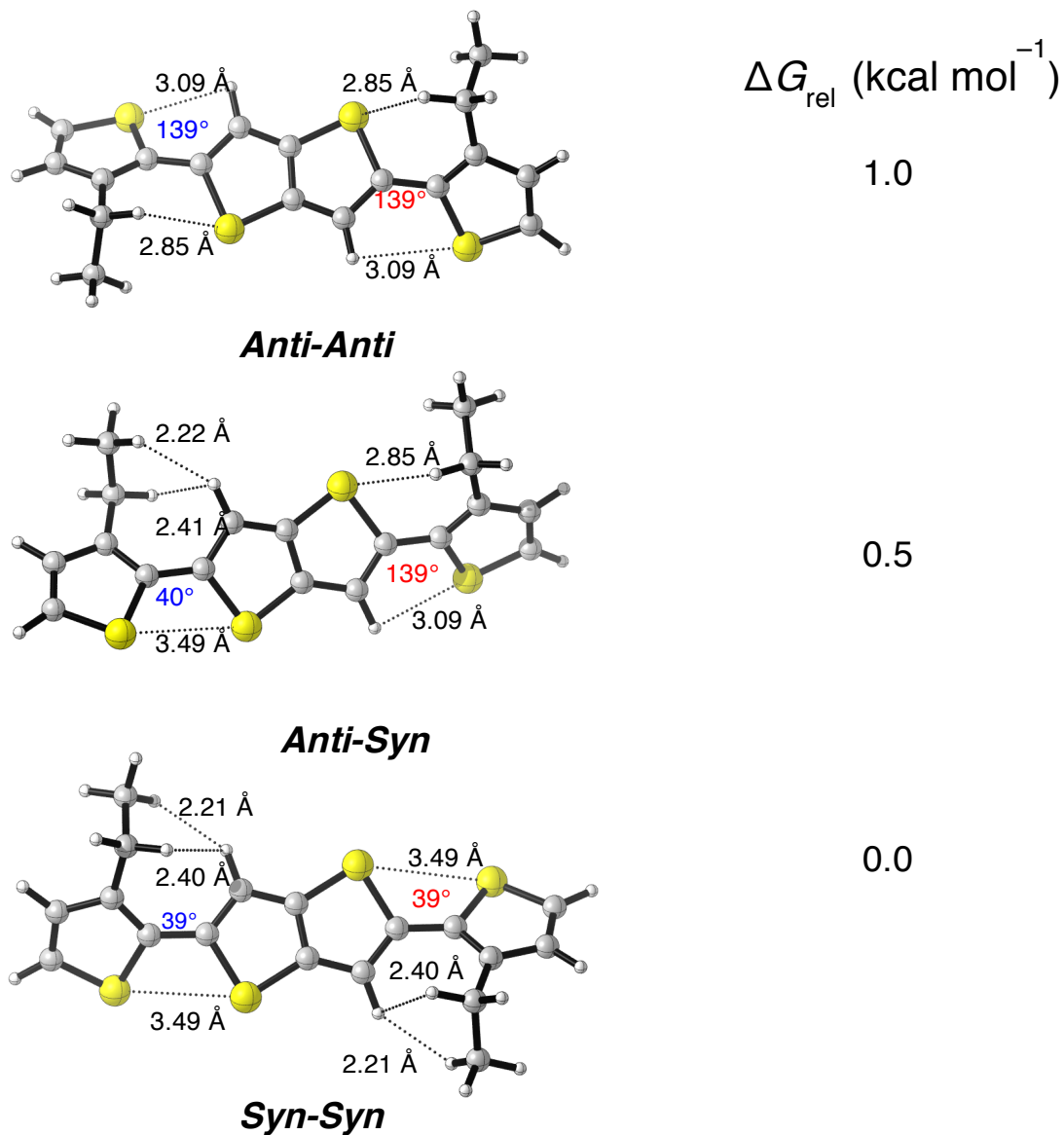


Figure 7. The optimized gas phase conformers of **1-Et**. SCCS dihedral angles are shown in blue and red. The H_{alk}-S distances are indicated for *Anti-Anti* and *Anti-Syn* conformers. The H_{alk}-H_{aryl} distance is indicated with the dotted line for the *Syn-Syn* conformer. All distances are reported in Angstroms computations with B97D/def2-TZV.

The alkyl substituents cause substantial deviation from planarity. The SCCS dihedral angles of the *Anti-Anti* conformer of **1-Et** are both 139°, about halfway between planar (180°) and perpendicular (90°). An unfavorable ($H_{\text{alk}}-S$) steric interaction causes this large deviation from planarity. *Anti-Anti* is now 1.0 kcal mol⁻¹ higher in energy than *Syn-Syn*, because there are two $H_{\text{alk}}-S$ steric interactions (2.85 Å); the sum of r_{vdw} of sulfur and hydrogen is 3.00 Å. Our calculations show that the $H_{\text{aryl}}-S$ distance is 3.09 Å, which is longer than the sum of the sulfur and hydrogen r_{vdw} . Therefore, we do not expect this interaction to be a factor in controlling the conformational preferences of **1-Hex**. The *Anti-Syn* conformer is lower in energy than *Anti-Anti* by 0.5 kcal mol⁻¹ because of one of the $H_{\text{alk}}-S$ interactions is not possible in this conformation. The S-S (3.5 Å) and $H_{\text{alk}}-H_{\text{aryl}}$ repulsions (2.21 Å) are overridden by the $H_{\text{alk}}-S$ clash. $2r_{\text{vdw}}$ of hydrogen and sulfur are 2.40 Å and 3.60 Å, respectively. The *Syn-Syn* conformer is the lowest energy conformer because there is no clash between the alkyl group and S. The *Syn-Syn* conformer of **1-Et** has a similar SCCS dihedral to the *Syn-Syn* conformer of **1-H** (39° vs. 33°). The computed free energies of the three conformers for **1-H**, **1-Me**, and **1-Et** are summarized in Table 2. The ϕ_1 and ϕ_2 for each conformer of **1-H**, **1-Me**, and **1-Et** are given in Table 3.

Table 2. The computed relative free energies for the three conformers of **1-H**, **1-Me**, and **1-Et**. Computed using B97D/def2-QZVP//B97D/def2-TZV, values are in kcal mol⁻¹.

R	<i>Anti-Anti</i>	<i>Anti-Syn</i>	<i>Syn-Syn</i>
H	0.0	0.8	1.5
Me	0.8	0.3	0.0
Et	1.0	0.5	0.0

The *Syn-Syn* conformer is the global minimum for **1-Me** and **1-Et**. These model systems show that when alkyl groups are present, the unfavorable alkyl-S steric interaction outweighs S–S repulsion. The SCCS dihedral angles for all computed structures are shown in Table 3.

Table 3. The two SCCS dihedral angles (ϕ_1 and ϕ_2) of the three computed conformers of **1-H**, **1-Me**, and **1-Et**. Computed using B97D/def2-QZVP//B97D/def2-TZV, values are in degrees.

R	<i>Anti-Anti</i> SCCS (ϕ_1, ϕ_2)	<i>Anti-Syn</i> SCCS (ϕ_1, ϕ_2)	<i>Syn-Syn</i> SCCS (ϕ_1, ϕ_2)
H	168, 168	173, 32	33, 33
Me	149, 149	145, 38	38, 38
Et	139, 139	139, 40	39, 39

We computed the torsional potential for **1-H** and **1-Me** to understand how the unfavorable steric and orbital effects described above contribute to the overall torsional potentials about ϕ_1 and ϕ_2 (Figure 8).

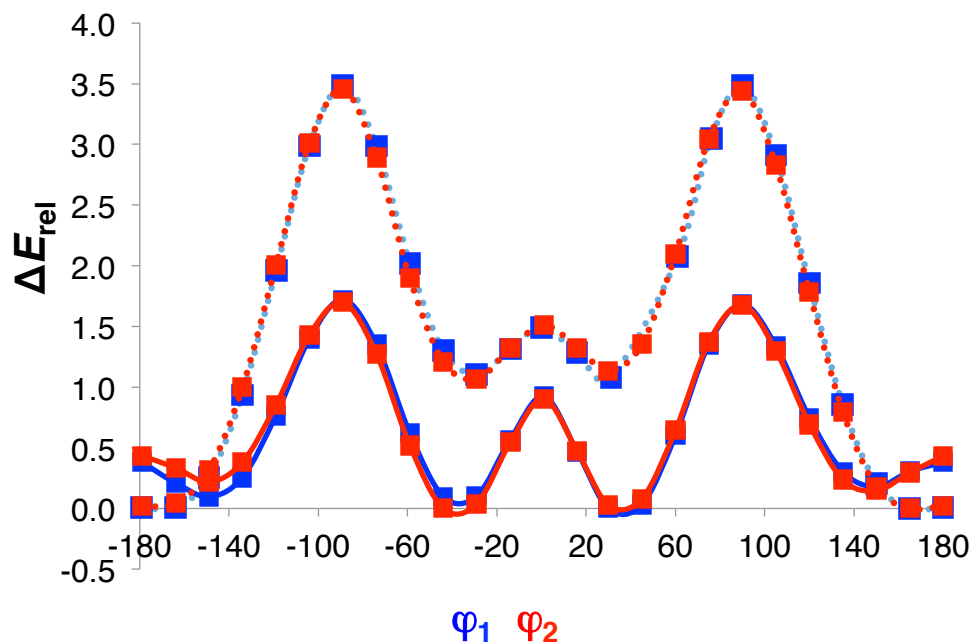


Figure 8. Torsional potentials (kcal mol⁻¹) for SCCS torsion (in degrees) for **1-H** and **1-Me**. Blue potentials represent the interconversion of *Anti-Anti* to *Anti-Syn* and red potentials represent the interconversion of *Anti-Syn* to *Syn-Syn*. Computed using B97d/def2-QZVP//B97d/def2-TZV.

The rotations all exhibit maxima at $\pm 90^\circ$ and 0° , which are the transition states for rotation. In line with the conformational preferences of **1-Et**, the lowest energy conformer of **1-Me** is *Syn-Syn*, and S–S repulsion causes substantial deviations from planarity.

Thin film morphologies and device performance

GIXD

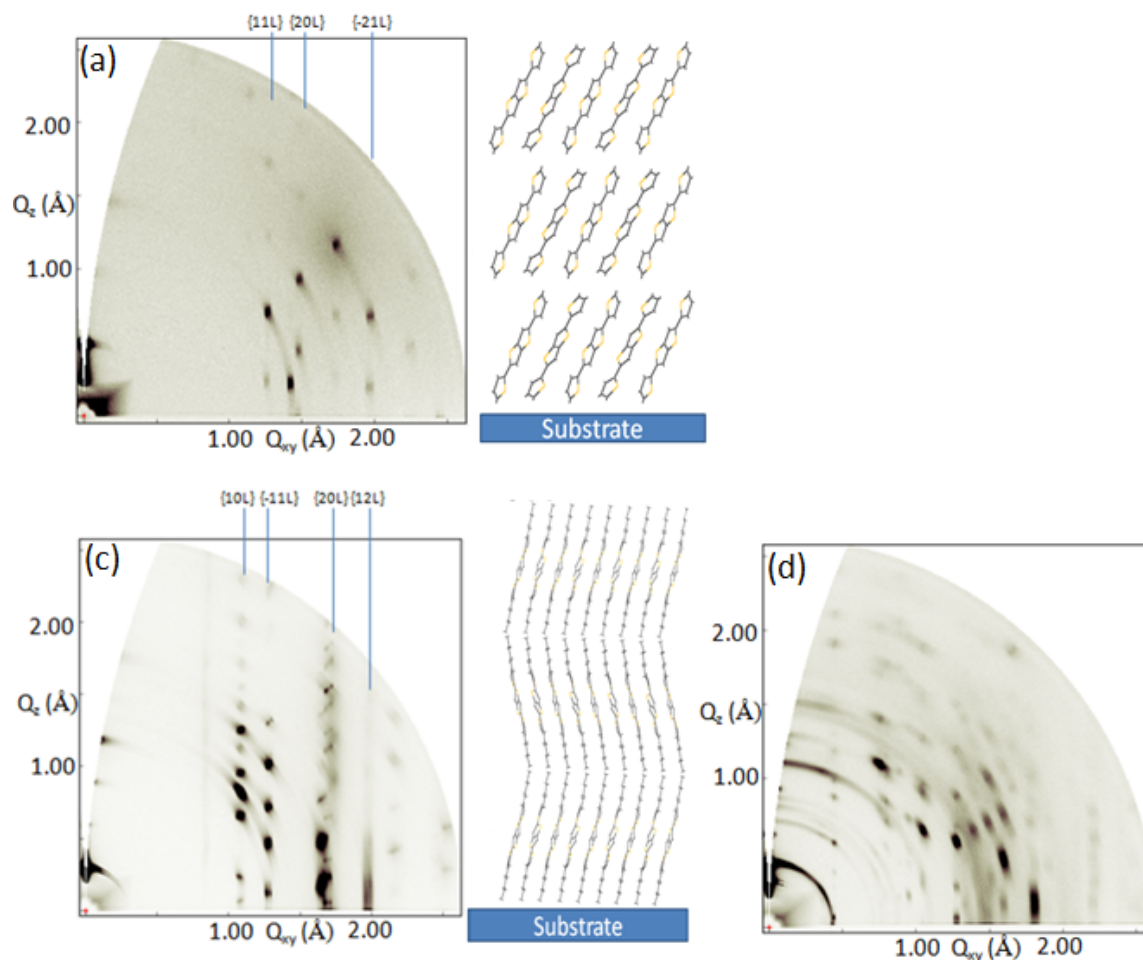


Figure 9. GIXD images and corresponding packing cartoons of oligothiophenes on Si substrates by spin-casting from chloroform solution: (a) **1-H**, (c) **1-C₆**, and (d) **2-C₆**.

Molecular packing in thin films can greatly differ from the bulk crystal structures. Grazing incidence X-ray diffraction (GIXD) is a powerful scattering technique that can provide details about the crystalline packing in thin films of organic semiconductors. GIXD allows for the molecular packing in both the out-of-plane (q_z) and in-plane (q_{xy}) directions to be probed. GIXD experiments were performed on thin film samples of oligothiophenes to study the influence of increasing length of oligomers and side chains on the thin film morphology, and compare the morphology to the bulk crystal packing. Figure 9 shows the GIXD patterns of

oligothiophene films spin coated on Si substrates. As shown in Figure 9a, **1-H** packs in a 2D herringbone structure with several Bragg rods that are vertically arranged on the substrate. The diffraction pattern can be indexed to a unit cell with dimensions: $a = 8.59 \text{ \AA}$, $b = 5.64 \text{ \AA}$, $c = 13.21 \text{ \AA}$, $\alpha = 77.6^\circ$, $\beta = 89.8^\circ$, $\gamma = 82.4^\circ$. These values compare very similar with the bulk unit cell, which indicates that the thin film packing is the same of the bulk, with an edge-on packing with the oligomer backbone perpendicular to the substrate. The **1-C₆** thin film packing greatly differs from the bulk. The thin film has a unit cell with dimensions: $a = 7.58 \text{ \AA}$, $b = 7.71 \text{ \AA}$, $c = 21.71 \text{ \AA}$, $\alpha = 75.6^\circ$, $\beta = 94.3^\circ$, $\gamma = 99.8^\circ$. Compared to the 2D bulk packing, the thin film packing is more one dimensional, in what resembles a classic "edge-on" lamellar packing with alkyl chains aligning perpendicular to the substrate.

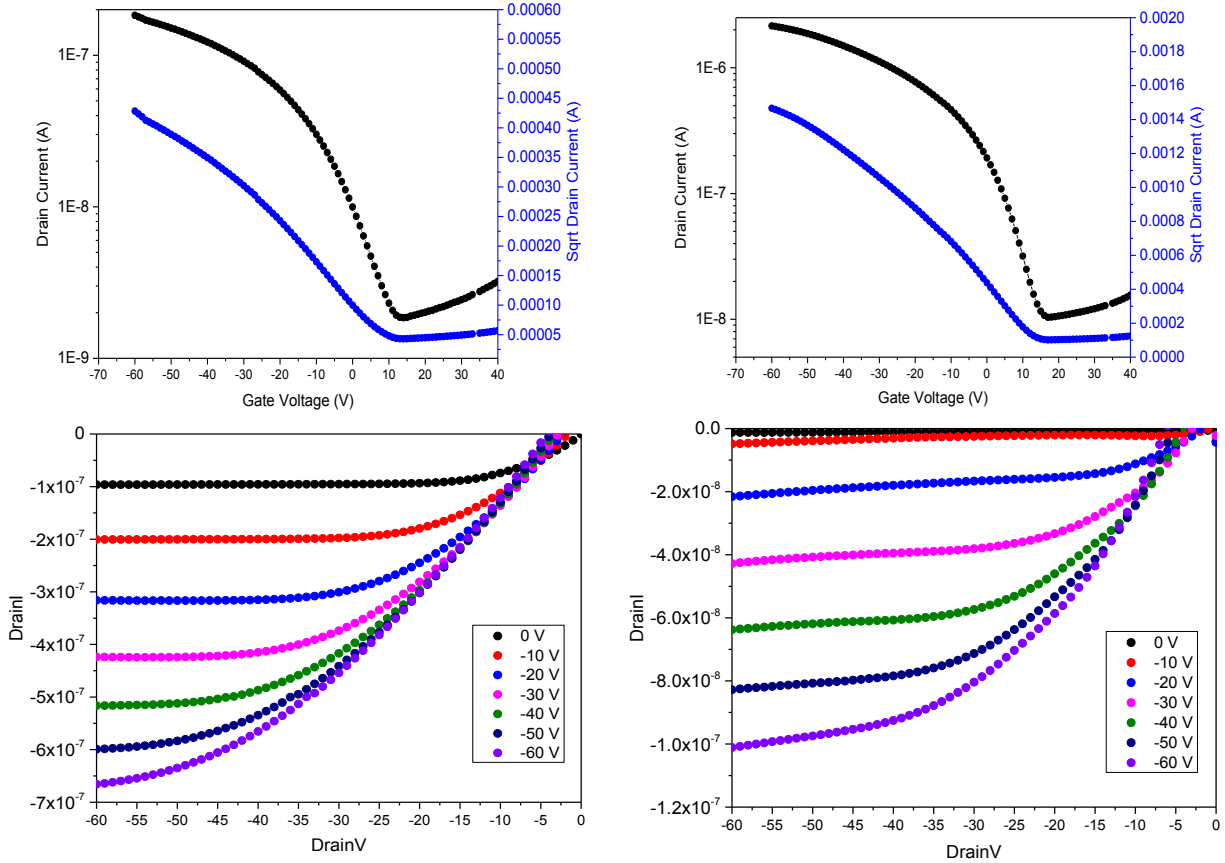


Figure 10. The transfer/square root of current characteristics of (a) **1-C₆** and (b) **2-C₆** and output characteristics of (c) **1-C₆** and (d) **2-C₆** BG-BC thin film transistors.

Electrical measurements were performed in ambient conditions using a standard probe station. Thin film OFETs were fabricated in a bottom-gate, bottom contact geometry by spin coating 10 mg/ml solution of oligothiophenes in chloroform at 3000 rpm for 60 s. The hole mobilities calculated in the saturated regime, threshold voltages, and current on/off ratios can be seen in Figure 10. **1-C₆** has a hole mobility of $2.64 \times 10^{-4} \text{ cm}^2/\text{Vs}$, when the backbone length is increased in **2-C₆** the mobility increases to $3.21 \times 10^{-3} \text{ cm}^2/\text{Vs}$.

Mobility simulations and Discussion

The morphologies were simulated using classical molecular dynamics (MD) simulations (with AMBER²¹) and charge-carrier dynamics using kinetic Monte Carlo²² (kMC) simulations (using VOTCA²³), based on Marcus Theory.²⁴ We calculated the charge-transport properties, reorganization energies (λ), energetic disorder, electronic-coupling distributions and the hole-mobilities (μ) for the BTTT oligomers computed here. The reorganization energies are calculated by the four-point rule²⁵ using the B3LYP²⁶ density functional using the 6-311G(d,p) basis set. The energetic disorder is obtained from the distribution of site-energy differences calculated by Thole²⁷ model. The electronic-coupling between molecular dimers are calculated using ZINDO²⁸ semi-empirical method.

The initial configurations are constructed as multiple copies of the unit cells in three crystallographic directions (Figure 11). We used 1560, 1536 and 1536 molecules for **1-H**, **1-C₆**, and **2-C₆** respectively. The initial crystals are equilibrated at 300 K in an NPT ensemble for 6 *ns* followed by a production run lasting 10 *ns*. The predicted morphologies are shown in Figure 12, and the C₆H₁₃ side-chains are shown as green sticks for clarity. kMC simulations are performed on snapshots of the MD trajectories based on Marcus theory.

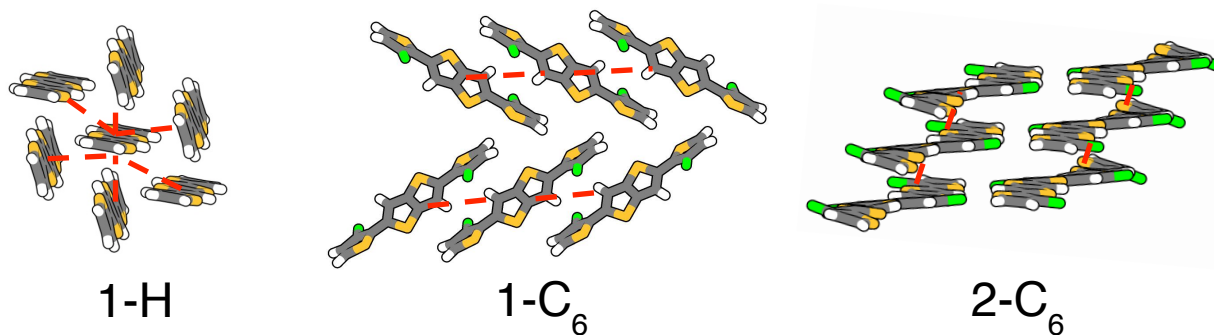


Figure 11. Crystal structures of **1-H**, **1-C₆**, and **2-C₆** with principal electron transport direction indicated in red.

Devices were fabricated using these materials and hole mobilities were measured for **1-H**, **1-C₆**, and **2-C₆**. Briseño *et al.* could not measure mobility for **1-H**, while mobilities for **1-C₆**, and **2-C₆** are 6.2×10^{-4} and $1.3 \times 10^{-3} \text{ cm}^2/\text{Vs}$, respectively. We sought to understand the origin of this large difference of charge-transport properties by employing molecular dynamics simulations. Figure 12 shows the initial configurations (left) and the snapshots of representative morphologies of **1-H**, **1-C₆**, and **2-C₆** materials (right). Under each of these snapshots is the paracrystalline order parameter $g = \delta/\bar{d}$. Here, δ is the standard deviation and \bar{d} is average of intermolecular distance distributions between oligomer centroids within the snapshot. Paracrystallinity is a measure of total disorder in organic crystals and defining the crystalline phase.²⁹

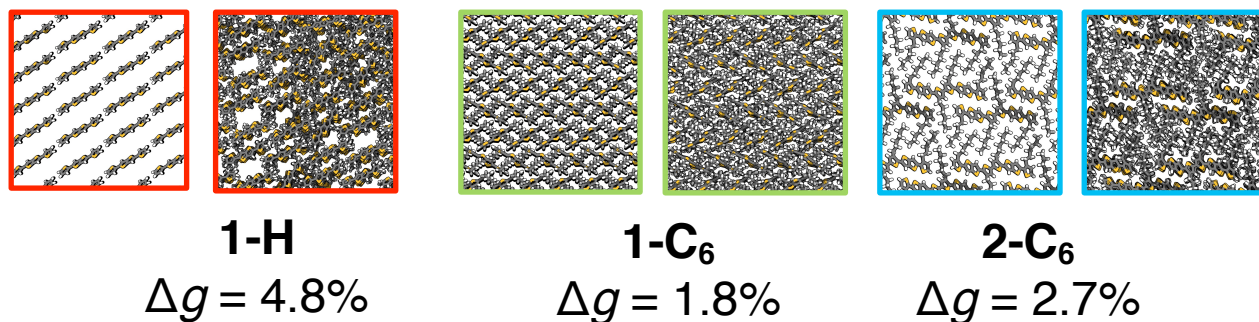


Figure 12. Snapshot crystal configurations before (left) and after (right) introducing thermal disorder with Amber molecular dynamics. **1-H** (red), **1-C₆** (green), **2-C₆** (blue)

The **1-H** morphology is visibly disordered, and exhibits a large number of defects. However, **1-C₆** and **2-C₆** morphologies are quite unchanged after MD equilibration. These have paracrystallinity values of 1.8% and 2.7% respectively, while that of **1-H** is 4.8%. The hexyl sidechains are critical to the structural integrity of the crystal. Dispersive interactions between the alkyl chains provide a packing force that maintains order within the crystal. In **1-H**, this interaction is not possible and the crystal is substantially disordered. The structural disorder in **1-H** greatly affects the electronic landscape of these thin films. The energetic disorder parameter can be understood by computing the site energy differences. The site-energy difference is defined as the difference between HOMO energies of the system during charge-transfer reactions. The distributions of site-energies of the equilibrated morphologies are shown in Figure 13.

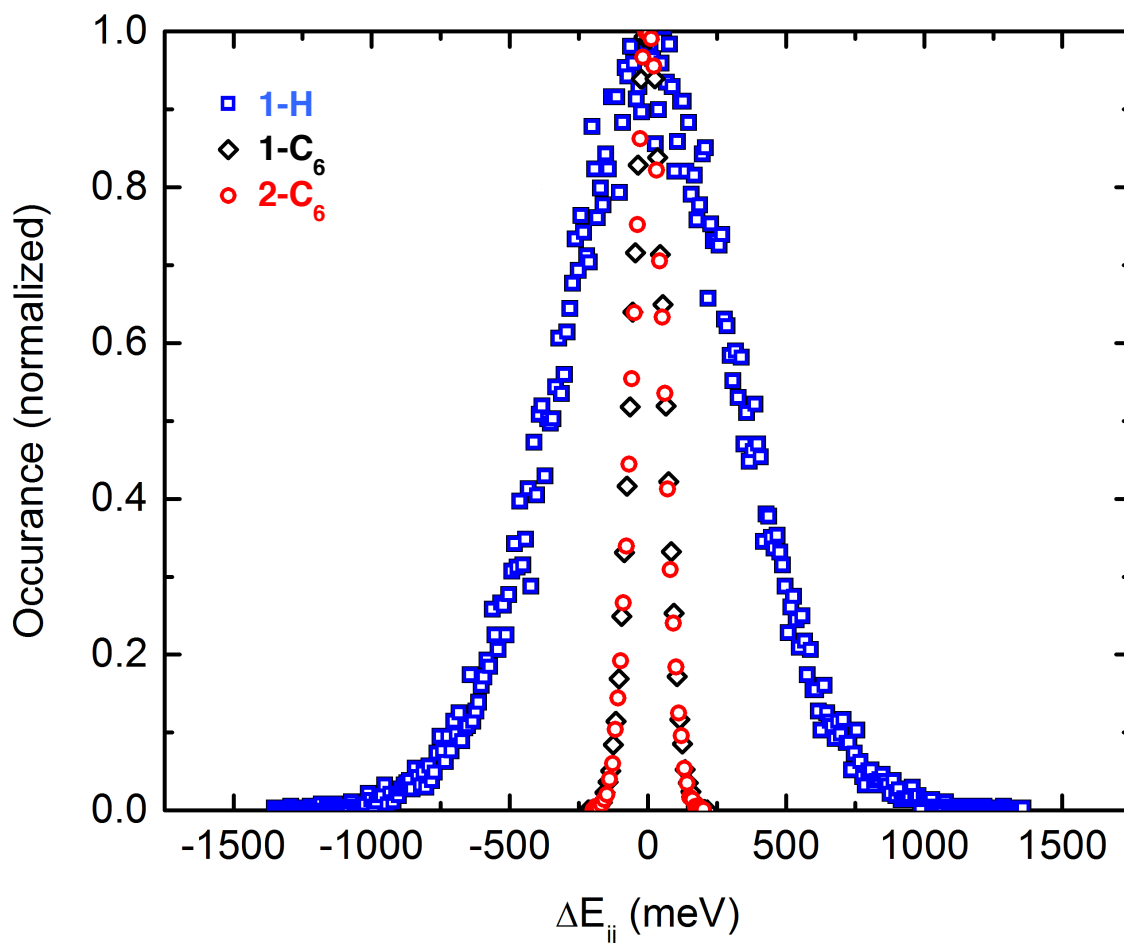


Figure 13. Plot of site energies for **1-H** (blue), **1-C₆** (black), and **2-C₆** (red).

The energetic disorder (σ) is the standard deviations of the data distributions in Figure 13. The σ of **1-H** is higher than those of **1-C₆** and **2-C₆** (334 meV vs. ~ 55 meV). The highly disordered morphology of **1-H**, greatly increases the number of possible hopping sites, which often decreases the charge-transport efficiency. The highly disordered morphology at 300 K is consistent with unfavorable site-energies of **1-H**. The reorganization energies (λ), energetic disorders (σ) and the calculated and measured hole-mobilities (μ) for the BTTT oligomers are summarized in Table 4.

Table 4. Experimental (μ_{exp}), computed hole mobilities (μ_{calc}), reorganization energy (λ , meV), and electronic coupling (J , meV) for **1-H**, **1-C₆**, and **2-C₆**.

	1-H	1-C₆	2-C₆
μ_{exp}	n/a	6.2×10^{-4}	1.3×10^{-3}
μ_{calc}	$\sim 10^{-7}$	1.0×10^{-3}	6.3×10^{-3}
λ	420	618	630
J	6.0	170	104

The predicted hole mobilities (μ_{calc}) follow the trend of measured hole mobilities (μ_{expt}) and are all within one order of magnitude of μ_{expt} . This is in line with our previous study that established a methodology by which hole mobilities can be computed within an order of magnitude of the experimental mobility.³⁰ The **1-H** thin film device exhibited no conductivity and the μ_{calc} is $\sim 10^{-9}$ cm²/Vs. This result is surprising based on the reorganization energies alone, which are somewhat smaller than **1-C₆** and **2-C₆**. MD simulations reveal that crystal packing is poor in **1-H** because it does not benefit from inter-sidechain dispersive interactions. The disorder manifests itself in much low electronic coupling between hopping sites (6 meV vs. 10² meV) and decreased charge-transport efficiency due to the greatly increased number of hopping sites. The mobilities of **1-C₆** and **2-C₆** are 2.64×10^{-4} and 3.21×10^{-3} cm²/Vs, respectively. We postulate that the nearly ten-fold higher mobility of **2-C₆** over **1-C₆** results from additional packing forces possible from additional alkyl sidechains in the dimer, relative to the monomer.

Conclusion

We synthesized unsubstituted and hexyl-substituted BTTT oligomers. These materials were characterized as single crystals and thin films. **1-H** adopts the in the *Anti-Anti* confirmation, while **1-C₆** adopts a *Syn-Syn* conformation. Gas phase DFT calculations reveal that unfavorable S–S closed-shell repulsions a minimized in the *Anti-Anti* confirmation. The *Syn-Syn* conformation is preferred for **1-C₆** because unfavorable H_{aryl}-H_{alkyl} overwhelms the preference for the sulfurs to point in opposite directions. The **2-C₆**, however, clearly demonstrates that the solid-state packing is a much more complex interaction space. The **2-C₆** single crystal structure shows a nearly planar backbone with both *Anti* and *Syn* conformational thiophenes. Molecular dynamics simulations and hole mobility calculations reveal that **1-H** shows poor performance because of the highly inefficient charge-transport network. This network is substantially better in **1-C₆** and **2-C₆** because the alkyl side chains on these oligomers provide an important packing force, which results in a crystal that is much more highly ordered and capable of transporting charge.

Acknowledgements

All of the experiments were carried out by B. Cherniawski, E. K. Burnett, L. Zhang (Briseño group). S. C. B. Mansfield did x-ray crystallography.

References

-
- ¹ (a) Noriega, R.; Rivnay, J.; Vandewal, K.; Koch, F. P. V.; Stingelin, N.; Smith, P.; Toney, M. F.; Salleo, A. *Nat. Mater.* **2013**, *12*, 1038–1044. (b) Sirringhaus, H. *Adv. Mater.* **2014**, *26*, 1319–1335. (c) Mei, J.; Diao, Y.; Appleton, A. L.; Fang, L.; Bao, Z. *J. Am. Chem. Soc.* **2013**, *135*, 6724–6746. (d) Beaujuge, P. M.; Fréchet, J. M. J. *J. Am. Chem. Soc.* **2011**, *133*, 20009–20029. (e) Salleo, A.; Kline, R. J.; DeLongchamp, D. M.; Chabinyc, M. L. *Adv. Mater.* **2010**, *22*, 3812–3838. (f) Zaumseil, J.; Sirringhaus, H. *Chem. Rev.* **2007**, *107*, 1296–1323. (g) Virkar, A. A.; Mannsfeld, S.; Bao, Z.; Stingelin, N. *Adv. Mater.* **2010**, *22*, 3857–3875. (h) Mas-Torrent, M.; Rovira, C. *Chem. Rev.* **2011**, *111*, 4833–4856. (i) Sirringhaus, H.; Brown, P. J.; Friend, R. H.; Nielsen, M. M.; Bechgaard, K.; Spiering, A. J. H. **1999**, 685–688.
- ² (a) Baklar, M. A.; Koch, F.; Kumar, A.; Domingo, E. B.; Campoy-Quiles, M.; Feldman, K.; Yu, L.; Wobkenberg, P.; Ball, J.; Wilson, R. M.; McCulloch, I.; Kreouzis, T.; Heeney, M.; Anthopoulos, T.; Smith, P.; Stingelin, N. *Adv. Mater.* **2010**, *22*, 3942–3947. (b) Mas-Torrent, M.; Rovira, C. *Chem. Rev.* **2011**, *111*, 4833–4856.
- ³ (a) Jackson, N. E.; Savoie, B. M.; Kohlstedt, K. L.; Olvera de la Cruz, M.; Schatz, G. C.; Chen, L. X.; Ratner, M. a. *J. Am. Chem. Soc.* **2013**, *135*, 10475–10483. (b) Facchetti, A.; Yoon, M.; Stern, C. L.; Hutchison, G. R.; Ratner, M. A.; Marks, T. J. *J. Am. Chem. Soc.* **2004**, *126*, 13480–13501. (c) Marsh, H. S.; Jankowski, E.; Jayaraman, A. *Macromolecules* **2014**, *47*, 2736–2747. (d) Lei, T.; Wang, J.; Pei, J. *Chem. Mater.* **2014**, *26*, 594–603.
- ⁴ Lim, J. A.; Liu, F.; Ferdous, S.; Muthukumar, M.; Briseno, A. L. *Mater. Today* **2010**, *13*, 14–24.

-
- ⁵ Zhou, C.; Liang, Y.; Liu, F.; Sun, C.; Huang, X.; Xie, Z.; Huang, F.; Roncali, J.; Russell, T. P.; Cao, Y. *Adv. Funct. Mater.* **2014**, ASAP.
- ⁶ Briseno, A. L.; Mannsfeld, S. C. B.; Shamberger, P. J.; Ohuchi, F. S.; Bao, Z.; Jenekhe, S. a.; Xia, Y. *Chem. Mater.* **2008**, *20*, 4712–4719.
- ⁷ (a) Meier, H.; Stalmach, U.; Kolshorn, H. **1997**, 379–384. (b) Chen, P.; Lalancette, R. A.; Jäkle, F. *J. Am. Chem. Soc.* **2011**, *133*, 8802–8805. (c) Zade, S. S.; Bendikov, M. *Chemistry* **2007**, *13*, 3688–3700. (d) Zade, S. S.; Zamoshchik, N.; Bendikov, M. *Acc. Chem. Res.* **2011**, *44*, 14–24.
- ⁸ McCulloch, I.; Heeney, M.; Bailey, C.; Genevicius, K.; Macdonald, I.; Shkunov, M.; Sparrowe, D.; Tierney, S.; Wagner, R.; Zhang, W.; Chabiny, M. L.; Kline, R. J.; McGehee, M. D.; Toney, M. F. *Nat. Mater.* **2006**, *5*, 328–333.
- ⁹ Fei, Z.; Pattanasattayavong, P.; Han, Y.; Schroeder, B. C.; Yan, F.; Kline, R. J.; Anthopoulos, T. D.; Heeney, M. *J. Am. Chem. Soc.* **2014**, 1–4.
- ¹⁰ Zhang, L.; Colella, N. S.; Cherniawski, B. P.; Mannsfeld, S. C. B.; Briseno, A. L. *ACS Appl. Mater. Interfaces* **2014**, *6*, 5327–5343.
- ¹¹ DeLongchamp, D. M.; Kline, R. J.; Lin, E. K.; Fischer, D. A.; Richter, L. J.; Lucas, L. A.; Heeney, M.; McCulloch, I.; Northrup, J. E. *Adv. Mater.* **2007**, *19*, 833–837.
- ¹² Northrup, J. *Phys. Rev. B* **2007**, *76*, 245202.

-
- ¹³ Wang, L.; Zhang, X.; Zhang, J.; Tian, H.; Lu, Y.; Geng, Y.; Wang, F. *J. Mater. Chem. C* **2014**, *2*, 9978–9986.
- ¹⁴ (a) Zhang, X.; Côté, A. P.; Matzger, A. J. *J. Am. Chem. Soc.* **2005**, *127*, 10502–10503. (b) Zhang, X.; Johnson, J. P.; Kampf, J. W.; Matzger, A. J. *Chem. Mater.* **2006**, *18*, 3470–3476.
- ¹⁵ Bloom, J. W. G.; Wheeler, S. E. *J. Chem. Theory Comput.* **2014**, *10*, 3647.
- ¹⁶ Zhao, Y.; Truhlar, D. *Theor. Chem. Acc.* **2008**, *120*, 215.
- ¹⁷ Grimme, S. *J. Comput. Chem.* **2006**, *27*, 1787.
- ¹⁸ Schafer, A.; Huber, C.; Ahlrichs, R. *J. Chem. Phys.* **1994**, *100*, 5829.
- ¹⁹ Weigend, F.; Furche, F.; Ahlrichs, R. *J. Chem. Phys.* **2003**, *119*, 12753.
- ²⁰ Bondi, A. *J. Phys. Chem.* **1964**, *68*, 441.
- ²¹ Salomon-Ferrer, R.; Gtz, A. W.; Poole, D.; Le Grand, S.; Walker, R. C. *J. Chem. Theory. Comput.* **2013**, *9*, 3878–3888.
- ²² Ruehle, V.; Lukyanov, A.; May, F.; Schrader, M.; Veho, T.; Kirkpatrick, J.; Baumeier, B.; Andrienko, D. *J. Chem. Theory. Comput.* **2011**, *7*, 3335–3345.
- ²³ Ruehle, V.; Junghans, C.; Lukyanov, A.; Kremer, K.; Andrienko, D. *J. Chem. Theory. Comput.* **2009**, *5*, 3211–3223.
- ²⁴ (a) Marcus, R. A. *J. Chem. Phys.* **1956**, *24*, 966–978. (b) Marcus, R. A. *Rev. Mod. Phys.* **1993**, *65*, 599–610.
- ²⁵ Kippelen, B.; Bredas, J.-L. *Energy Environ. Sci.* **2009**, *2*, 251–261.
- ²⁶ Becke, A. D. *J. Chem. Phys.* **1993**, *98*, 5648–5652.
- ²⁷ Thole, B. T. *Chem. Phys.* **1981**, *59*, 341–350.
- ²⁸ Ridley, J.; Zerner, M. *Theor. Chim. Acta* **1973**, *32*, 111–134.

²⁹ Noriega, R.; Rivnay, J.; Vandewal, K.; Koch, F. P.; Stingelin, N.; Smith, P.; Toney, M. F.; Salleo, A. *Nat. Mat.* **2013**, *12*, 1038–1044. (b) Rivnay, J.; Noriega, R.; Kline, R. J.; Salleo, A.; Toney, M. F. *Phys. Rev. B* **2011**, *84*, 045203.

³⁰ Yavuz, I.; Martin, B. M.; Park, J.; Houk, K. N. *J. Am. Chem. Soc.* **2015**, *137*, 2856.